Towards injectable theranostic platforms: magnetic peptide-based supramolecular hydrogels with drug-delivery, MRI reporting and hyperthermia

Teresa Sousa Pereira

UMinho | 2021

University of Minho
School of Sciences

Teresa Sousa Pereira

Towards injectable theranostic platforms: magnetic peptide-based supramolecular hydrogels with drug-delivery, MRI reporting and hyperthermia capabilities.

March 2021

University of Minho
School of Sciences

Teresa Sousa Pereira

Towards injectable theranostic platforms: magnetic peptide-based supramolecular hydrogels with drug-delivery, MRI reporting and hyperthermia capabilities.

Master's Dissertation
Medicinal Chemistry

Performed under supervision of
Professor Dr. José Alberto Martins
Dr. Manuel Bañobre-Lopez

March 2021

Acknowledgments

This thesis year was the best year of my academic life, because of the work, but mainly because of the people I met and worked with.

I want to say thank you so much to professor Dr. José Alberto, of university of Minho, and to Dr. Manuel Bañobre, of INL, as my research supervisors, by all support and knowledge shared throughout this year and by all excellent opportunities it has given me. I want also to express my gratitude, to professor Dr. Paula Margarida Ferreira, of university of Minho, by all ideas and advices shared that also contribute to the good development of this thesis.

I also want to express my appreciation to all the people that contributes to this work. Dr. Loic of PIEP of University of Minho, by the rheological studieds; Dr. David Pereira of pharmacy faculty of University of Porto, by the toxicity studies; Dr. José Sereno and Professor Dr. Antero Abrunhosa of the ICNAS, by the *in vivo* studies. Thank you so much for the time available.

I would also to recognize the role of the Chemical center of the university of Minho for providing the resources and the access to the investigation areas needed to the realization of this thesis. Important to refer the contribut of the Elisa Pinto and Vania Azevedo of the NMR network, the biological engineering center of the university of Minho and the C.A.C.T.I. of university of Vigo. I want also to recognize the contribution of the FCT with a funding project PTDC/QUI-QOR/29015/2017.

My gratitude to all the people I met in this year and made it better. Sofia Teixeira, for all the support and for our long conversations; André Lopes and Diana Brandão for the incredible friendship. Without them, this would not be so amazing.

I want to say thank you to my boyfriend, José Duarte, by all support even when I was stressed, for all the love he gives me and makes me feel so special, giving me the strength to continue this walk.

Last but not least, I want to say thank you to my parents and to my aunt for the opportunity they gave me to be able to study and achieve my goals, and for all the support that I received during this year, sometimes so hard, and without them I would have given up. It is also important to refer the love and support that my little babys (my pets) give me every day.

And finally, thank you God for always walking beside me.

This year was a great success!

STATEMENT OF INTEGRITY

I hereby declare having conducted this academic work with integrity. I confirm that I have not used plagiarism or any form of undue use of information or falsification of results along the process leading to its elaboration. I further declare that I have fully acknowledged the Code of Ethical Conduct of the University of Minho.

Towards injectable theranostic platforms: magnetic peptide-based supramolecular hydrogels with drug-delivery, MRI reporting and hyperthermia capabilities

Abstract

Self-assembled peptide-based hydrogels are the novel paradigm biomaterials: synthetic versatility and amenability to automation, high water content and fibril structure, biocompatibility and degradability and responsiveness to environmental stimuli.

A new family of di- and tri-peptide succinic acid *N*-capped dehydropeptide hydrogelators (suc-Xaa-ΔPheOR and suc-Xaa-Xaa-ΔPheOR; suc - succinic acid, Xaa - Phe or 3-(2-naphthyl)-L-alanine; R- Me or H) was prepared and characterised. Self-assembly (UV-Vis, fluorescence and CD spectroscopy), hydrogelation and rheological studies demonstrated the succinic acid *N*-capped hydrogels display excellent elasticity, thermal and mechanical stability and recovery properties. Magnetic hydrogels, with incorporation of SPION (0.4 *wt* %, 14 *wt* %$_{\text{Fe}}$ SPION), retain the fibril network structure and self-healing properties of the non-magnetic hydrogels. These materials were characterised as potential Contrast Agents (CA) for T_{2w} MRI by relaxometry (1.5 T, 60 MHz, 37 °C) and MRI (3 T, 120 MHz, 37 °C) phantoms and $T_{1,2}$ relaxation maps. The magnetic hydrogels display significant concentration-dependent T_{2w} contrast enhancement and relaxivity (r_2, $\text{mM}^{-1}\text{s}^{-1}$) values similar to the SPION preparation. Paramagnetic hydrogels, with incorporated Gd^{3+} complexes, display concentration-dependent T_{1w} contrast enhancement, and relaxivity values (r_1, $\text{mM}^{-1}\text{s}^{-1}$) comparable to the Gd complexes in solution. The heating efficacy of the magnetic hydrogels (0.4 *wt* %, 14 *wt* %$_{\text{Fe}}$ SPION) was evaluated by the parameter Specific Absorption Rate (*SAR*, H = 250 G, f = 869 Hz). Despite a moderate *SAR* reduction, comparing to the SPION preparation, the magnetic hydrogels attain temperatures (~ 50 °C) suitable for cancer hyperthermia. Non-magnetic (0.4 *wt* %) and magnetic hydrogels (0.4 *wt* %, 14 *wt* %$_{\text{Fe}}$ SPION) were tested as nanocarriers for drug deliver with model drugs: methyl orange dye (negative charge), methylene blue dye (positive charge) and the antibiotic ciprofloxacin (zwitterionic structure at neutral pH). The release mechanism was identified as Fickian diffusion. The magnetic hydrogel suc-NapPheΔPheOMe (0.4 *wt* %, 14 *wt* %$_{\text{Fe}}$ SPION) was injected into a mouse xenograft tumour model (cell line CT26). T_{2w} MRI monitoring confirmed that the hydrogel was retained by the tumour over the experiment duration (3 days). The work carried out in this thesis represents a decisive step towards the development of magnetic self-assembled peptide-based hydrogels as theranostic cancer platforms.

Keywords: succinic acid *N*-capped dehydropeptides; self-assembly; hydrogels; SPION; Hyperthermia; MRI; drug-delivery; cancer theranostics.

Desenvolvimento de plataformas teranósticas injetaveis: hidrogéis magnéticos supramoleculares baseados em peptídos com capacidade de entrega de fármacos, IRM e hipertemia magnética

Resumo

Hidrogeis baseados na auto-associação peptídica são os novos biomateriais: versatibilidade de síntese e amenidade para automação, alto teor de água e estrutura fibrilar, biocompatibilidade, degradabilidade e resposta a estimulos ambientais.

Uma nova família de hidrogeladores di- e tri-peptidicos *N*-protegidos com anidrido sucínico (suc-Xaa-ΔPheOR and suc-Xaa-Xaa-ΔPheOR; suc – anidrido sucínico, Xaa - Phe or 3-(2-naftil)-L-alanina; R-Me or H) foi preparada e caracterizada. Estudos de auto-associação (UV-Visivel, fluorescência e dicroísmo circular), hidrogelação e reologia mostraram que os hidrogeis *N*-protegidos com anidrido sucínico exibem excelente elasticidade, estabilidade térmica, mecânica e recuperação. Os hidrogéis magnéticos (com SPION) (0.4 *wt* %, 14 *wt* %$_{\text{Fe}}$ SPION), mantêm estrutura em rede fibrilar e propriedades de auto-regeneração dos hidrogéis não magnéticos. Estes materiais foram caracterizados como potenciais agentes de contraste (AC) para T_{2p} IRM por relaxometria (1.5 T, 60 MHz, 37 °C) e por IRM (3 T, 120 MHz, 37 °C) e mapas de relaxação $T_{1,2}$. Os hidrogéis magnéticos apresentam aumento de contraste T_{2p} dependente da concentração e relaxividades (r_2, mM^{-1}s^{-1}) semelhantes às dos SPION. Hidrogeis paramagnéticos com complexos de Gd^{3+} incorporados demostram um aumento de contraste T_{1p} dependente da concentração e relaxividades (r_1, mM^{-1}s^{-1}) comparáveis às do complexo em solução. A eficácia de aquecimento dos hidrogeis magnéticos (0.4 *wt* %, 14 *wt* %$_{\text{Fe}}$ SPION) foi avaliada pela taxa de absorção específica (*TAE*, H= 250 G, f= 869 Hz). Apesar de uma redução moderada do *TAE*, comparativamente aos SPION em solução, os hidrogéis magnéticos alcançam temperaturas (~50 °C) adqueadas para hipertermia do cancro. Os hidrogeis não magnéticos (0.4 *wt* %) e magnéticos (0.4 *wt* %, 14 *wt* %$_{\text{Fe}}$ SPION) foram testados como nano-transportadores para entrega de fármacos com as drogas modelo: o corante alaranjado de metil (carga negativa), o corante azul de metileno (carga positiva) e o antibiótico ciprofloxacina (estrutura zwiteriónica a pH neutro). O mecanismo de libertação foi identificado como difusão de Fickian. O hidrogel magnético suc-NapPheΔPheOMe (0.4 *wt* %, 14 *wt* %$_{\text{Fe}}$ SPION) foi injetado num rato (cell line CT26). Monitorização T_{2p} IRM confirmou que o hidrogel foi retido pelo tumor durante a experiência (3 dias).

Esta tese é uma contribuição para o desenvolvimento de plataformas de hidrogeis magnéticos baseados na auto-associação de desidropeptidos.

Palavras-chave: desidropeptídos N-protegidos com acido sucinico; auto-associação; hydrogeis; SPION; hipertermia; IRM; entrega de fármacos; teranóstico de cancro.

Index

Index of figures

Index of tables

Abbreviatures

3D	three dimensional
Cbz	benzyloxycarbonyl
Cgc	critical gelation concentration
DMSO	dimethyl sulfoxide
DMF	dimethyl formamide
LMWG	low molecular-weight gelation
G’	shear storage modulus
G’’	loss modulus
ω	angular frequency
FF	diphenylalanine
Fmoc	fluorenylmethyloxycarbonyl
Nap	naphthalene
MNPs	magnetic nanoparticles
SPION	superparamagnetic iron oxide nanoparticles
IONP	iron oxide nanoparticles
MRI	magnetic resonance imaging
Fe_3O_4	magnetite
γ Fe_2O_3	maghemite
PEG	polyethylene glycol
DMSA	dimercaptosuccinic acid
RGD	arginylglycylaspartic acid
SSPIO	standard superparamagnetic iron oxide nanoparticles
USPIO	ultra-small superparamagnetic iron oxide nanoparticles
DOTA	1,4,7,10-Tetraazacyclododecane-1,4,7,10-tetraacetic acid
DTPA	diethylenetriaminepentaacetic acid
CA	contrast agent
SAR	specific absorption rate
SLP	specific loss power
AC	alternating current
DMSO-d6	deuterated dimethylsulfoxide
DMAP	4-dimethylaminopyridine

DCM	dichlorometane
Boc$_2$O	*tert*-butyl dicarbonate
CD	circular dichroism
LOX	lysyl oxidase
CDCl$_3$	deuterated cloroform
Npx	Naproxene
SBM	solomon-Bloenbergen-Morgan
NSAID	nonsteroidal anti-inflammatory drug
TEA	triethylamine
NMR	nuclear magnetic ressonance
GdL	D-glucono-δ-lactone
TEM	transmission electron microscopy
TLC	thin layer chromatography
TFA	trifluoroaceti acid
T	tesla
TMG	*N,N,N',N'*- tetramethylguanidine
Rf	radiofrequency
B_0	magnetic field
$T_{1,2}$	relaxation time constant
$R_{1,2}$	relaxation rates
$r_{1,2}$	relaxivity
Gd	gadolinium
Mn	manganese
Fe	ferro
τ_R	correlation time
τ_M	residence time of the coordinated water molecule
τ_D	translational correlation time
τ_N	Nèel relaxation time

Chapter 1

Introduction

1.1 Physical and supramolecular hydrogels

The nanotechnology paradigm has an extraordinary impact across all areas of science and technology.[1] Functional materials, with hierarchical nanostructuring, show tremendous potential for a wide range of applications (electronics, biotechnology, biomedicine and medicine) which are expected to have far-reaching social implications.[2]

Hydrogels are viscoelastic solid-like materials with high water content, generally above 99 %. High water content allied to biocompatibility and tuneable structure and function and responsiveness to external stimuli, make hydrogels the new archetype.[3] In hydrogels, water molecules are trapped by a tridimensional network of fibrillar structures. Synthetic and natural polymers originate hydrogels *via* physical (reversible) and/or chemical (irreversible) crosslinking of long oligomer chains.[4] Polymer-based hydrogels can be classified into two main groups: physical and chemical hydrogels. Physical hydrogels are characterized by a 3D network of entangled polymer chains, driven by non-covalent interactions (hydrogen bonding, ionic interactions, *van der Walls* and hydrophobic interactions).[5] A chemical hydrogel is formed by covalent cross-linking of polymer chains.[4] In general, physical hydrogels display reversibility and responsiveness to external stimuli thanks to the non-covalent nature of the array of interactions responsible for gelation. Reversibility and self-healing properties are fundamental for applications that require injection of hydrogels. Hydrogel formation *in vivo* can be triggered by specific physiological conditions such as temperature (thermoresponsive hydrogels) or pH changes (pH responsive hydrogels). Alternativelly, injectable hydrogels are broken, i.e. undergo gel-to-solution phase transition in response to pressure (shear-thining, tixotropic hydrogels), but show recovery (self-healing) following injection (**Figure 1**).[6]

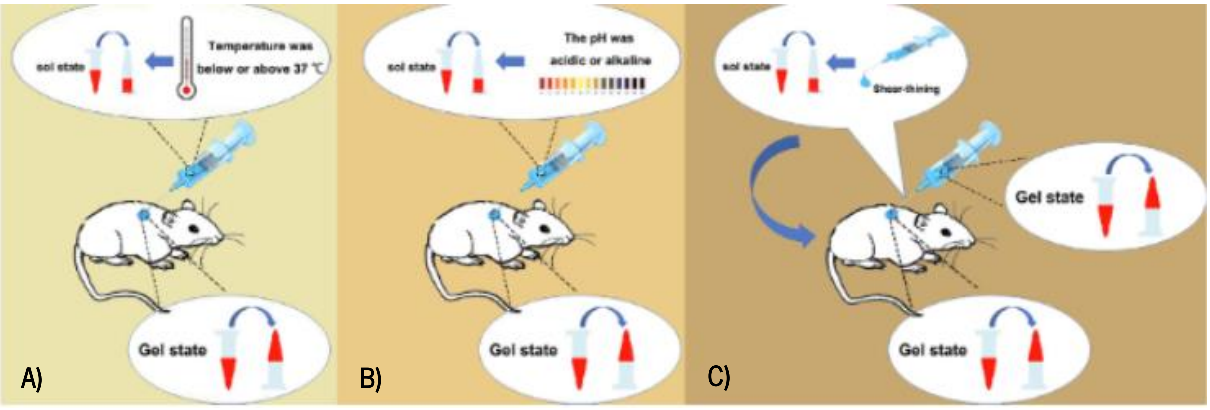

Figure 1 Stratagies for hydrogel injection *in vivo*: **A**) thermo-sensitive hydrogels; **B**) pH-responsive hydrogels; **C**) thixotropic hydrogels.[6]

In physical gels, gel-to-solution phase transition can be triggered by a range of physical and chemical external stimuli: pH, ionic strength, electric fields, light, pressure, sound or the presence of specific molecules. These stimuli change the balance of non-covalent molecular interactions within the hydrogel network which result in rearrangement of the polymer network. pH-responsive hydrogels are particularly suited for delivery of bioactive agents to specific organs owing to organ-specific pH values, e.g. stomach, intestine, liver tumours, blood vessels and vagina.[7] Despite suitable rheological properties, reversibility and self-healing and responsiveness, *in vivo* applications of polymeric hydrogels are limited by degradability and biocompatibility and imunogenicity problems.[8] Supramolecular, also known as self-assembled hydrogels, are a sub-class of physical hydrogels formed by low molecular weight hydrogelators (LMWH). Self-assembled hydrogels have become, in recent years, the prototype biomaterials: high water content, above 99.5 %, excellent biocompatibility, biodegradability, tuneable responsiveness, specific biological functions and synthetic practicability. Peptides are the most effective low molecular weight hydrogelators due to the structural variety of amino acids with side chains able to engage in a variety of intermolecular non-covalent interactions: electrostatic interactions, hydrogen bonding, hydrophobic and *van der walls* interactions and π-π stacking interactions. Stimulus-triggered self-assembly of peptide molecules into fibril structures (tubes, ribbons, etc), followed by physical entanglement, originates highly hydrated porous networks similar to the extracellular matrix. The non-covalent nature of the molecular interactions responsible for gelation warrants responsiveness to a wide variety of stimuli, pH, ionic strength, electric fields, light, pressure, sound or the presence of specific molecules. Peptide-based self-assembled hydrogels have found many applications: as intelligent carriers for delivery of therapeutic agents (drugs, genes, proteins), as promising matrices for repair and regeneration of tissues and organs.[9]

Self-assembled hydrogels

Molecular peptide self-assembly can occur under thermodynamic or kinetic control conditions (**Figure 2**).[10]

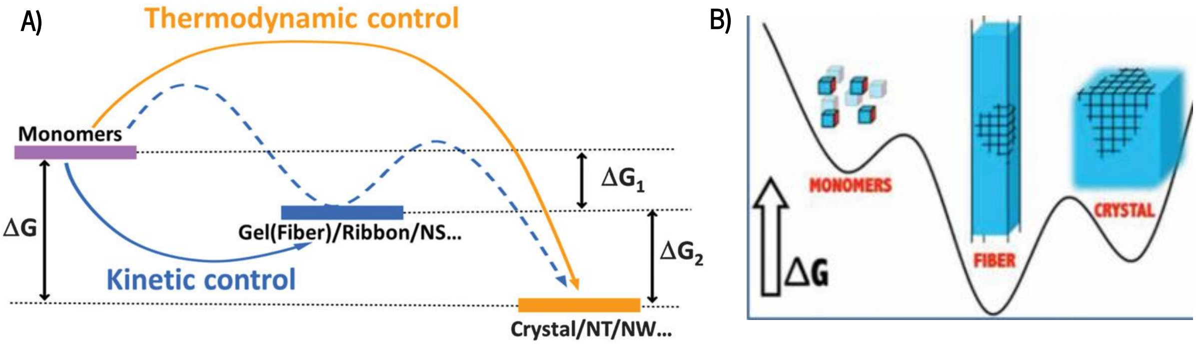

Figure 2 Schematic representation of self-assembly pathways under thermodynamic and kinetic control conditions (**A**); stability of the different self-assembled structures states (**B**).[11]

Monomer self-assembly triggered by external stimuli, e.g. pH, temperature shifts, counter-ions, concentration and solvents effects, produces kinetically trapped structures (hydrogels, nanotubes, spheres, ribbons) stabilised by an ensemble of weak non-covalent interactions. Therefore, obtaining kinetic structures requires a narrow set of experimental conditions which do not allow to surpass the energy barrier to the minimum energy state, thermodynamic state (**Figure 2**).[11]

Low molecular weight peptide hydrogelators undergo self-assembly into kinetically trapped nano-micro structures (fibres, ribbons, etc) which upon entanglement entrap high amounts of water, thus originating hydrogels.[12] Hydrogel formation from low molecular weight peptide gelators requires a trigger, *i.e.* a change of experimental conditions, *e.g.* pH, heating-cooling cycles, solvent polarity, that disturb the balance of the array of non-covalent interactions which keep the hydrogelator in solution. The trigger conditions result in reduction of the hydrogelator molecular solubility. The majority of low molecular weight peptides have ionisable groups, which endow them with pH-dependent solubility properties. LMWH display in general higher solubility in water-miscible organic solvents (DMSO, DMF) than in water. Solvent polarity changes, resulting insolubility reduction, can be attained by water dilution of concentrated hydrogelator solutions. Hydrogelator solubility can also be directly manipulated by heating-cooling cycles. Structural modifications, usually the removal of charged solubilising groups from pro-hydrogelator molecules, can have also a dramatic effect on solubility (**Figure 3**).[13]

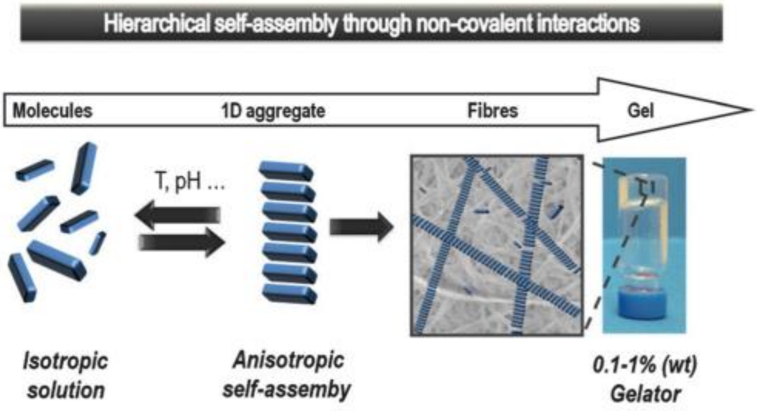

Figure 3 Schematic representation of the self-assembly of a gelator into a fibrous network resulting in a self-supporting gel.[101]

The formation of self-assembled (supramolecular) hydrogels is a hierarchical process: the self-assembly of hydrogelator molecules into one-dimension fibre-type structures, driven by an ensemble of weak non-covalent intermolecular interactions, is followed by fibre entanglement. Bulk hydrogels result from water entrapment by the fibrous network.[13]

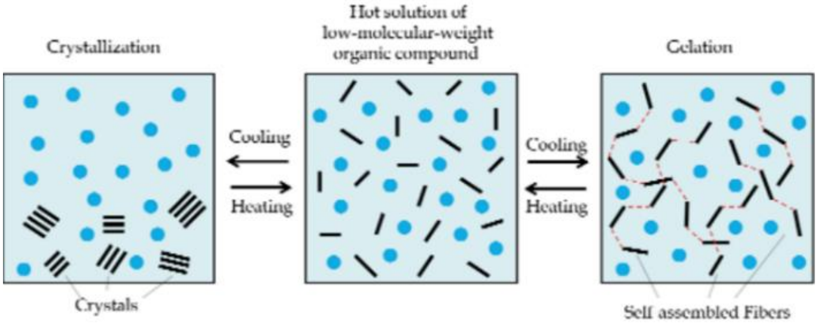

Figure 4 Hierarchical assembly across different length scales in low molecular weight hydrogels.[13]

Self-assembled hydrogels based on LMWG usually display characteristic mechanical properties, distinct from those presented by synthetic and biopolymer-based hydrogels. The hydrogels tend to break at relatively low strains and often display thermo-reversibility, melting and re-forming on warming and cooling, respectively (**Figure 4**).[13,14]

Hydrogels are characterised by the viscoelastic parameters shear storage modulus (G’) and loss modulus (G’’). From the practical point of view hydrogels are usually characterised by studying the dependence of the shear storage modulus (G’) and loss modulus (G’’) on the angular frequency (ω) (**Figure 5**).[15]

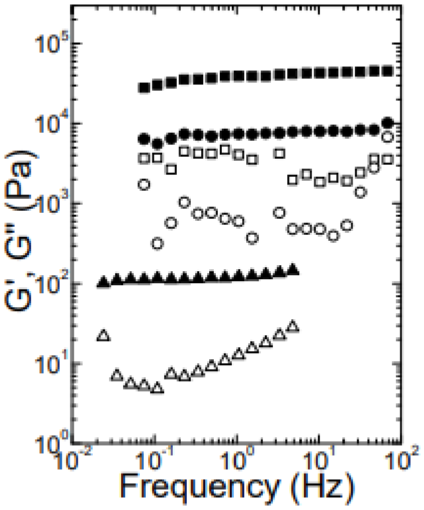

Figure 5 Frequency dependence of shear storage modulus (G') and loss modulus (G'') for a peptide-based self-assembled hydrogel (solid symbols: G'; empty symbols: G").[15]

For hydrogels, the ratio between G'(ω) (elasticity) and G''(ω) (viscosity) is typically of the order of magnitude G´/G´´~10.[16]

LMWH are generally composed of both hydrophilic and hydrophobic regions. Hydrophilic molecular spots ensure compatibility with water, while hydrophobic regions drive the self-assembly in water *via* hydrophobic collapse.[13] The amphyphylic nature of LMWH results in molecular self-assembly into well-defined supramolecular architectures: micelles, vesicles, fibres, tubes, sheets, etc (**Figure 6**).[17]

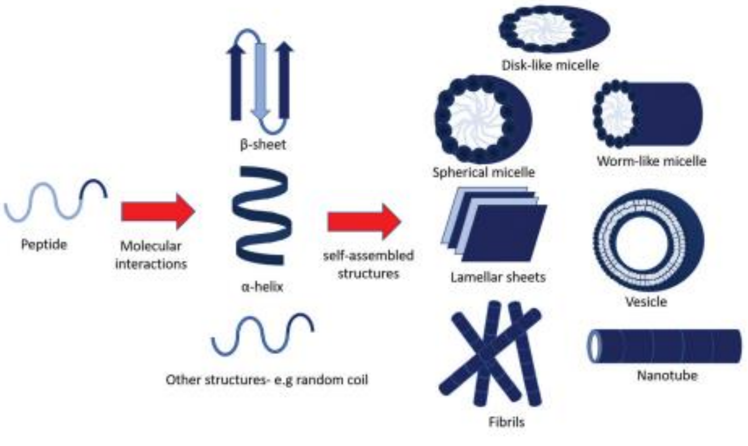

Figure 6 Self-assembly of peptidegelators into different supramolecular architectures.[102]

Low molecular weight peptides containing aromatic residues self-assemble in water into a variety of nano-architectures. The diphenylalanine (PhePhe; FF) dipeptide, a fragment of the Alzheimer's β-amyloid polypeptide, is one of the simplest, but still the most powerful gelating *motif* explored for molecular self-assembly (**Figure 7**).[11]

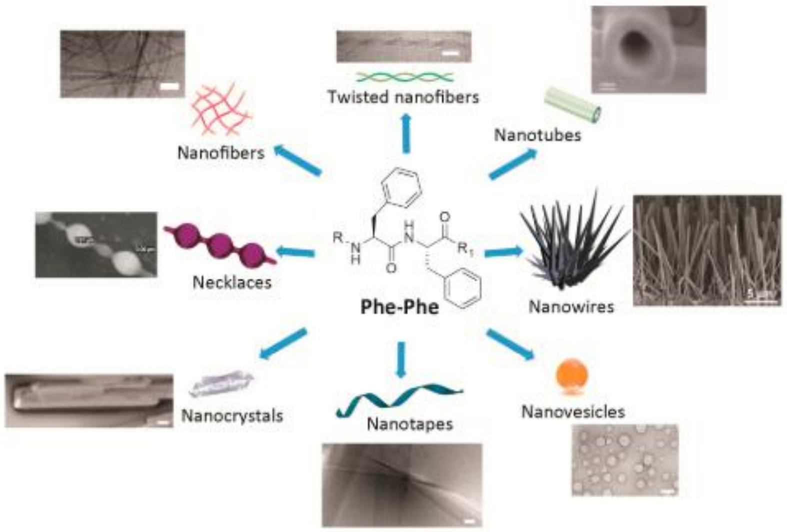

Figure 7 Diverse nanomorphologies formed by self-assembly of peptides containing the Phe-Phe dipeptide *motif*.[22]

Self-assembled hydrogels were obtained by self-assembly of unprotected PhePhe dipeptide structures.(**Figure 8**).[18,19]

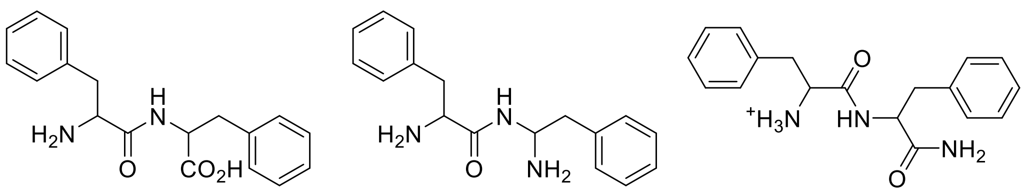
1 2 3

Figure 8 Examples of unprotected PhePhe dipeptide structures that afford hydrogels: **1**) NH_2PhePheOH; **2**) NH_2PhePheNH_2; **3**) NH_3^+PhePheNH_2.[18,19]

N-capped dipeptide PhePhe structures are the most extensively studied low molecular weight peptide gelators. Aromatic bulky *N*-capping groups fluorenylmethyloxycarbonyl (Fmoc), benzyloxycabonyl (Cbz, *Z*) and naphthalene-derived groups (naproxen, 2-naphythyl acetic acid) contribute π-π stacking interactions to the array of non-covalent interactions displayed by the dipeptide PhePhe resulting in high gelation propensity in water (**Figure 9**).[20,21]

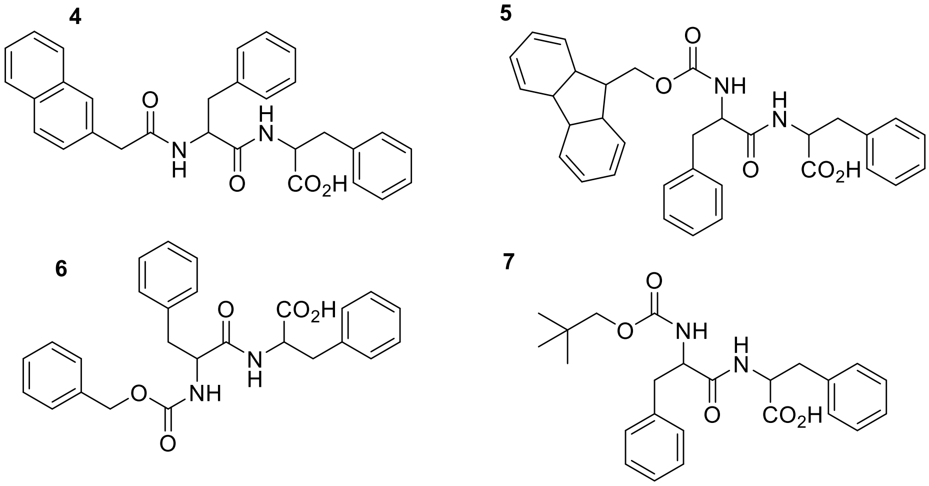

Figure 9 Illustrative examples of low molecular weight gelators containing the *N*-capped PhePhe *motif*. **4**) *N*-Naphthylalanine-PhePheOH; **5**) *N*-Fmoc-PhePheOH; **6**) *N*-Cbz -PhePheOH; **7**) *N*-Boc-PhePheOH.[20,21]

The use of peptides *in vivo*, as pharmaceutics, is hampered by fast degradation by endogenous proteases. Incorporation of synthetic amide bond mimics (isosteres) and replacement of canonical amino acid residues by non-canonical equivalents improves peptide resistance towards proteolysis.[22] Incorporation of *D*-amino acids, β-amino acids and dehydroamino acids residues into peptides are successful strategies to improve peptide stability *in vivo*. Our research group explored extensively low molecular weight peptides (di- and tripeptides) containing dehydroamino acids (dehydrophenylalanine- ΔPhe, dehydroaminobutyric acid- ΔAbu and dehydroalanine- ΔAla) residues as powerful hydrogelators resistant to proteolysis (**Figure 10** and **Figure 11**).[23,24]

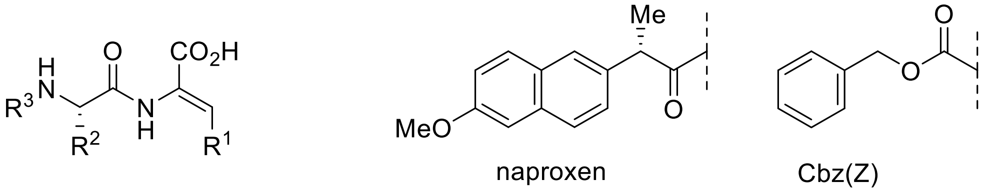

R^1 - H dehydroalanine
- Me dehydroaminobutyric acid
- Phe dehydrophenylalanine

R^2 - cannonical aa residue: Phe, Lys, Tyr, Asp, Met
R^3 - naproxen, Cbz (Z)

Figure 10 General structure of *N*-capped dehydropeptide-based hydrogelators developed by Ferreira and Martins research group at University of Minho.

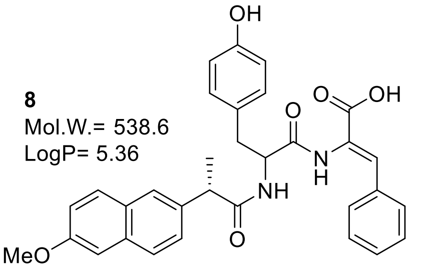

8
Mol.W.= 538.6
LogP= 5.36

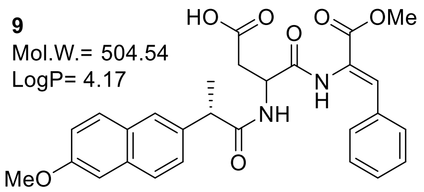

9
Mol.W.= 504.54
LogP= 4.17

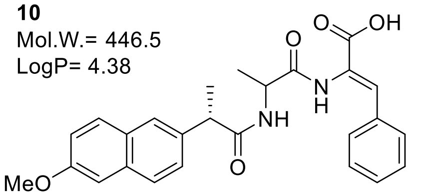

10
Mol.W.= 446.5
LogP= 4.38

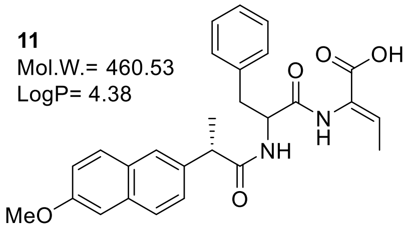

11
Mol.W.= 460.53
LogP= 4.38

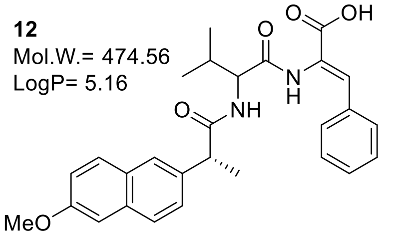

12
Mol.W.= 474.56
LogP= 5.16

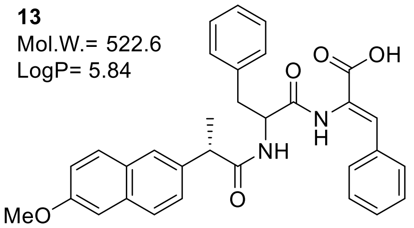

13
Mol.W.= 522.6
LogP= 5.84

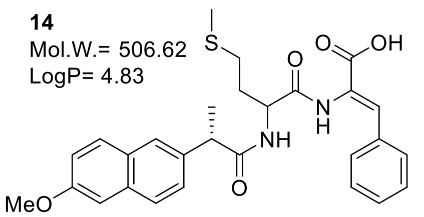

14
Mol.W.= 506.62
LogP= 4.83

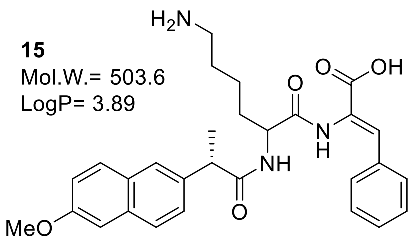

15
Mol.W.= 503.6
LogP= 3.89

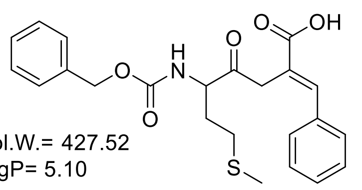

16
Mol.W.= 427.52
LogP= 5.10

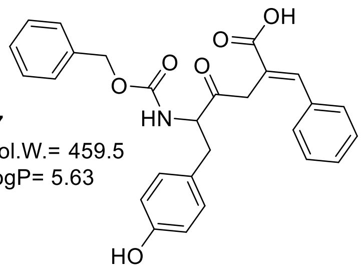

17
Mol.W.= 459.5
LogP= 5.63

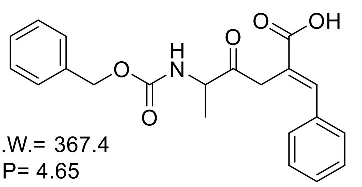

18
Mol.W.= 367.4
LogP= 4.65

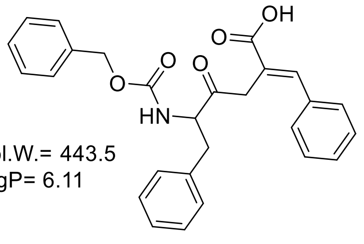

19
Mol.W.= 443.5
LogP= 6.11

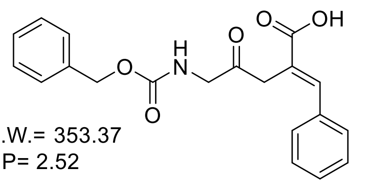

20
Mol.W.= 353.37
LogP= 2.52

Figure 11 Illustrative examples of of dehydropeptidehydrogelators synthesized in our research group. **8**- Npx-L-Tyr-Z-ΔPheOH; **9**- Npx-L-Asp-Z-ΔPheOMe; **10**- Npx-L-Ala-Z-ΔPheOH; **11**- Npx-L-Phe-Z-ΔAbuOH; **12**- Npx-L-Val-Z-ΔPheOH; **13**- Npx-L-Phe-Z-ΔPheOH; **14**- Npx-L-Met-Z-ΔPheOH; **15**- Npx-L-Lys-Z-ΔPheOH; **16**- Cbz-L-Met-Z-ΔPheOH; **17**- Cbz-L-Tyr-Z–ΔPheOH; **18**- Cbz-L-Ala-Z–ΔPheOH; **19**- Cbz-L-Phe-Z–ΔPheOH; **20**- Cbz-L-Gly-Z–ΔPheOH.[15,23,24]

Table 1 Critical gelation concentration (*cgc*), gelations conditions and applications devised for the hydrogels represented in **Figure 11**.

Hydrogelator	Cgc (*wt*%)	Gelation conditions	Applications	Refs
8	0.4	0.3 *wt*% GdL	Drug release, anti-inflammatory	15
9	0.8	0.3 *wt*% GdL	Drug release, anti-inflammatory	15
10	0.4	PBS/Heating (60 °C)-cooling	Drug release	23
11	0.4	PBS/Heating (60 °C)-cooling	Drug release	23
12	0.6	NaOH (1 M)/HCl (1 M)	Drug release	23
13	0.8	NaOH (1 M)/HCl (1 M)	Drug release	23
14	0.5	0.4 *wt*% GdL	Drug release, anti-inflammatory	24
15	0.5	pH13 buffer	Drug release, anti-inflammatory	24
16	0.1	0.5 *wt*% GdL	Drug release	24
17	0.2	0.5 *wt*% GdL	Drug release	24
18	–	No gel	—	24
19	0.1	0.5 *wt*% GdL or cool/heating	Drug release	24
20	–	No gel	—	24

Dehydropeptides *N*-capped with bulky aromatic groups, associate high gelation propensity, low critical gelation concentrations, to proteolytic stability. Moreover, the hydrogels display pH values in the physiological pH range (5 - 7) which is ideal for biological applications. Insight into the effect of the *N*-capping group on the self-assembly was obtained by spectroscopic techniques (UV-Vis and Fluorescence spectroscopy and CD spectroscopy). The aromatic *N*-capping group together with other aromatic groups on the dehydropeptide molecules are the self-assembly drivers by intermolecular π-π stacking interactions.[23,24]

The diblock peptide **21**, containing a dehydropeptide gelator block and the linear RGD (Arg-Gly-Asp) epitope, revealed good gelation properties. *In silico* studies indicate that the molecular construct retains $\alpha_5\beta_3$-integrin binding affinity. This result suggests that naproxen *N*-capped dehydropeptide gelators are suitable for building functional diblock hydrogelators for gel applications that require molecular recognition of cell receptors (**Figure 12**).[25,26]

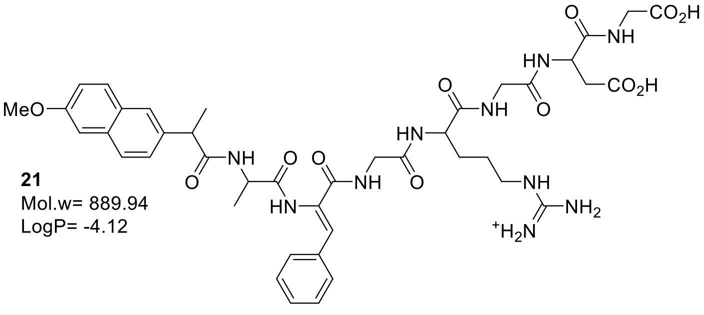

21
Mol.w= 889.94
LogP= -4.12

Figure 12 Structure of the diblock hydrogelator **Npx-L-Ala-ΔPhe**-Gly-Arg-Gly-Asp-Gly-OH.

The naproxen *N*-capped dehydrodipeptides retain the NSAID (NonSteroidal Anti-Inflammatory Drug) properties of naproxen. Moreover, the hydrogelators display new pharmacological properties - as LOX (Lysyl OXidase) and proteasome inhibitors, as novel chemical entities not related to naproxen.[27]

1.2 Magnetic nanoparticles

Physico-chemical properties of magnetic nanoparticles

Magnetic nanoparticles (MNPs), in particular superparamagnetic iron oxide nanoparticles (SPION), are promising platforms for applications in biomedicine: magnetic cell separation and biomolecule isolation, cell mechanics and tumour progression dynamics, *in vivo* stem cells tracking, drug delivery, Magnetic Resonance Imaging (MRI) contrast enhancement and hyperthermia.[28,29] SPION can be synthesized by wet chemical methodologies with controlled size and shape and narrow polydispersity. Moreover, the chemical synthesis usually allows coating the iron oxide core with an organic shell by a one-pot procedure.[30] SPION typically display core-shell architecture - an iron oxide core and a hydrophilic coating shell (**Figure 13**).[31]

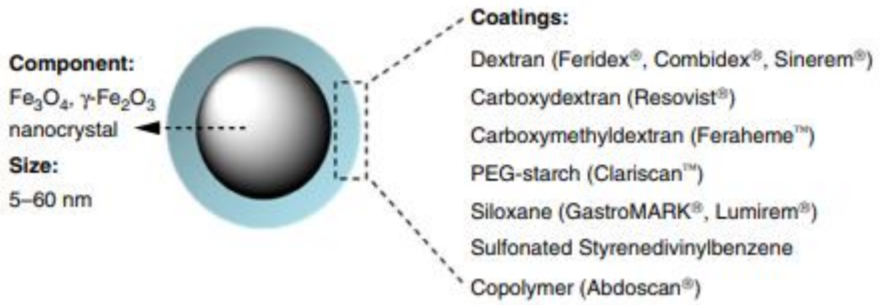

Figure 13 Scheme of a hydrophilic core-shell SPION architecture.[31]

The SPION core can be magnetite (Fe_3O_4) and/or maghemite (γ Fe_2O_3). Oxidation of the SPION core, by exposure to oxygen or oxidizing agents, converts the magnetite (Fe_3O_4) magnetic phase into maghemite (γ Fe_2O_3) (**Figure 14**).[32,33]

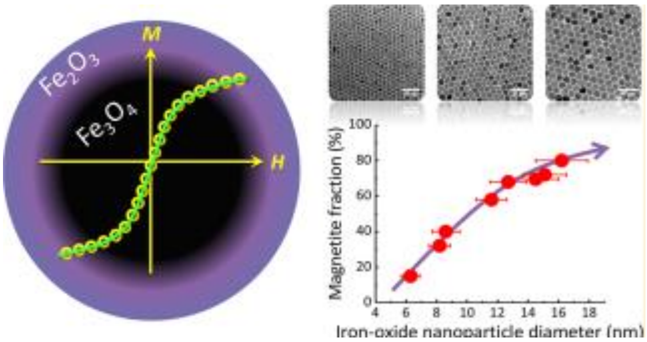

Figure 14 Illustration of the oxidation of the magnetite (Fe_3O_4) core into maghemite (γ Fe_2O_3).[33]

The (inevitable) *in vitro/in vivo* oxidation of the external surface of the magnetite core has a significant impact on the magnetic properties of SPION, particularly important for small nanoparticles.

The surface functionalization of the iron oxide cores with organic shell prevents nanoparticle aggregation by electrostatic and/or steric repulsion, contributing to higher colloidal stability and preventing nonspecific protein adsorption and clearance by macrophages. Tailoring the properties of the SPION to specific applications by engineering a functional – coating agent is still a difficult task. The most widely used coatings for SPION are based on polyethylene glycol (PEG), polysaccharide polymers, dextran, chitosan and starch, poly(L-lactic acid), polyacrylic acid, silica, dimercaptosuccinic acid (DMSA), citrate, oleate or oleic acid.[28]

SPION can be classified into three main categories according to hydrodynamic diameter: oral SPION (300 – 3.5 mm), standard SPION (SSPIO) (50 – 150 nm) and ultra-small SPION (USPIO), with hydrodynamic diameter under 50 nm. The fate of SPION *in vivo* is determined, amongst other properties, by their hydrodynamic size. SPION 10 – 100 nm in size is considered optimal for intravenous administration. Nanoparticles with hydrodynamic diameter above 200 nm are sequestered by the organs of the reticulo-endothelial system (liver and spleen) while those with diameter above 10 nm show fast renal clearance.[28]

Magnetic properties of SPION

Ferro(ferri)magnetic nanoparticles with core size (4 - 18 nm) smaller than the size of a magnetic domain, can form stable colloidal suspensions. As each crystal of ferro- or ferri-magnetic material in the colloid is fully magnetized, the nanoparticles become nanomagnets made of fully magnetized single domains.[34]

The magnetic energy of a nanomagnet in a magnetic field depends on the direction of its magnetization vector with respect to the crystallographic directions. The directions that minimize the magnetic energy are called anisotropy directions or easy axes (**Figure 15**).[34]

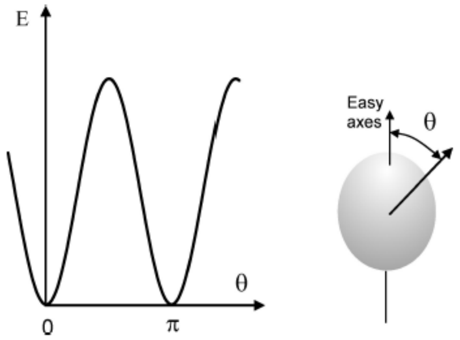

Figure 15 Dependence of the magnetic energy of a nanomagnet in a magnetic field on the tilt angle (θ) between the magnetization vector and the easy axes.[34]

Figure 15 shows that the magnetic energy increases with the tilt angle between the magnetic moment vector and the easy directions. The amplitude variation of this curve, called anisotropy energy, depends on the crystal volume and the anisotropy constant (**Equation 1**).

$$E = K * V * sin^2\theta \qquad \textbf{Equation 1}$$

K is the anisotropy constant and *V* is the crystal volume.

The anisotropy energy, being proportional to crystal volume, increases very rapidly with crystal size. It is determined also by the chemical composition and the crystallographic structure (magnetic phase) of the nanomagnet. The anisotropy constant (*K*) varies also with the shape and surface structure of the crystal. A crystal with spherical shape has no anisotropy energy The anisotropy constant is further influenced by nanoparticles´ aggregation/self-assembly, which results in a reduction of inter-crystal distance (**Figure 16**).[34,35]

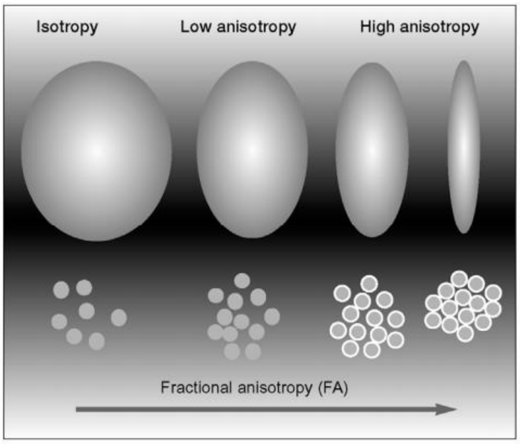

Figure 16 Schematic representation of magnetic nanoparticles with different anisotropy states.[35]

In high anisotropy conditions crystal magnetization is locked in the easy axes as the Boltzman law favours the directions with lower magnetic energy. Following a perturbation, the magnetization returns to equilibrium *via* two different relaxation mechanisms: Néel relaxation or Brownian relaxation (**Figure 17**).[36]

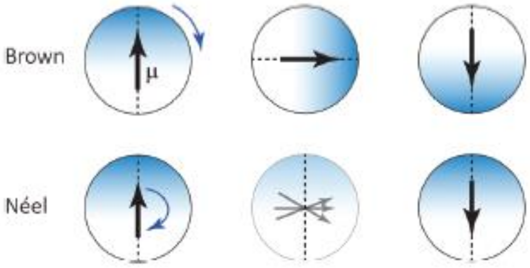

Figure 17 Schematic representation of the *Brownian* and *Nèel* relaxation mechanisms.[36]

In the *Brownian* motion, the changes of the ferrofluid magnetization are the result of rotation of the whole nanoparticles whereas the internal magnetization remains fixed with respect to the crystal lattice (**Equation 2**).[37]

$$\tau_B = \frac{3nV_h}{kT} \qquad \textbf{Equation 2}$$

η represents fluid viscosity, V_h is the particle hydrodynamic volume, k is the *Boltzmann's* constant and T is the *Kelvin* temperature.

The *Nèel* relaxation time is determined by fluctuations that arise from jumps of the magnetic moment between different easy directions.[34] (**Equation 3**).

$$\tau_N = \tau_0(E)e^{\frac{E}{kT}} \qquad \textbf{Equation 3}$$

E is the total anisotropy energy, k is the Boltzman constant, and T is the absolute temperature. $\tau_0(E)$ is the pre-exponential factor of the Nèel relaxation time expression.

At high temperatures and low anisotropy (energy) conditions ($E << kT$) the *Nèel* relaxation time is dominated by the pre-exponential term. The dependence of the parameter τ_0 on the anisotropy energy, indicates that $\tau_0(E)$ decreases as the anisotropy energy increases. USPIO magnetite particles with radius bellow 4 nm fulfil low anisotropy conditions at room temperature. In contrast, in high anisotropy energy conditions ($E >> kT$) the Nèel relaxation time is dominated by the exponential factor.

Increasing the anisotropy energy (*E*) results in a steep increase of the relaxation time.[34] In some magnetic fluids the return of the magnetization to the equilibrium state is determined by both *Nèel* and *Brownian* relaxation. In these conditions the global magnetic relaxation rate is determined by the sum of the *Nèel* and *Brownian* relaxation rates (**Equation 4**), (**Figure 18**).[34,38]

$$\frac{1}{\tau} = \frac{1}{\tau_N} + \frac{1}{\tau_B}$$ **Equation 4**

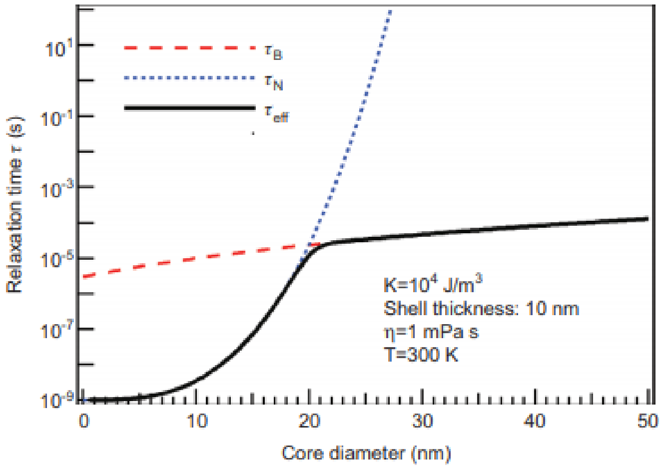

Figure 18 Contributions of the *Nèel* and *Brownian* relaxation times to the global relaxation time.[38]

The *Brownian* component of the magnetic relaxation is proportional to crystal volume, while *Nèel* relaxation is an exponential function of nanoparticles´ volume. Thus, the relaxation rate of small nanoparticles (diameter bellow 5 nm) is dominated by *Nèel* relaxation, whereas the relaxation rate of larger nanoparticles (diameter above *circa* 8 nm) is dominated by *Brownian* relaxation - viscous rotation of the whole nanoparticles.

Superparamagnetic nanoparticles display magnetization only in the presence of a magnetic field. The magnetization (*M*) of a material represents the resulting magnetic moment (μ) per unit volume (*V*) (**Equation 5**).[39]

$$M = \frac{d\mu}{dV}$$ **Equation 5**

Magnetization measurements must be performed above the blocking temperature or at temperatures below which a hysteresis can be observed. In these conditions, the magnetic relaxation time is roughly equal to the measurement time. Fast magnetic relaxation allows the system to be at thermodynamic equilibrium at all times so that the magnetization curve is perfectly reversible (**Figure 19**).[34,40]

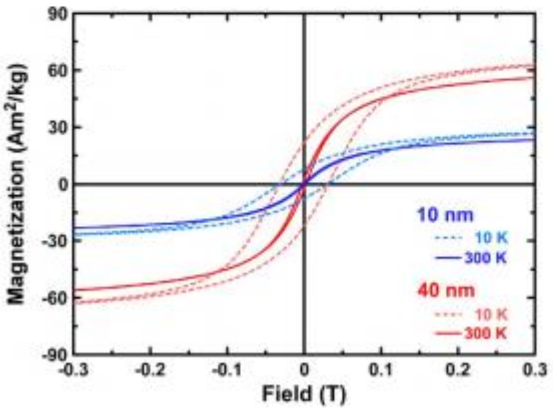

Figure 19 Magnetization curves for superparamagnetic nanoparticles as a function of applied magnetic field: samples with different sizes (10 nm and 40 nm) measured at 10 and 300 K.[40]

The magnetic field dependence of the magnetization is proportional to the *Langevin* function. **(Equation 6)**.[41]

$$M = M_s * L(x)$$ **Equation 6**

M is the magnetization at a specific magnetic field strength, *M_s* is the saturated magnetization, and *L(x)* is the *Langevin* function.

The *Langevin* function takes into acount a *Boltzman* distribution of all possible energy levels for all orientations of the particles´ magnetization moment. (**Equation 7**).[41]

$$L(x) = \left[\coth(x) - \frac{1}{x}\right]; x = \frac{M_s V B_o}{kT}$$ **Equation 7**

M_s is the saturated magnetization, *V* is the nanoparticles volume and *B_o* is the magnetic field strength.

The heterogeneity, high polydispersity, of nanoparticles preparations results in a reduction of the saturation magnetization. Synthetic pathways that afford nanoparticles displaying narrow size dispersity are in high demand.[42] In general, the saturation magnetization of nanoparticles is lower than that of the corresponding bulk material. Moreover, the saturation magnetization decreases sharply with the reduction of the nanoparticles size.[39]

Spinel ferrites

Iron oxide nanoparticles display a spinel structure with general formula MFe_2O_4: M represents a divalent M^{2+} cation (Fe, Mn, Co, Fe, Ni or Zn) (**Figure 20**).[43]

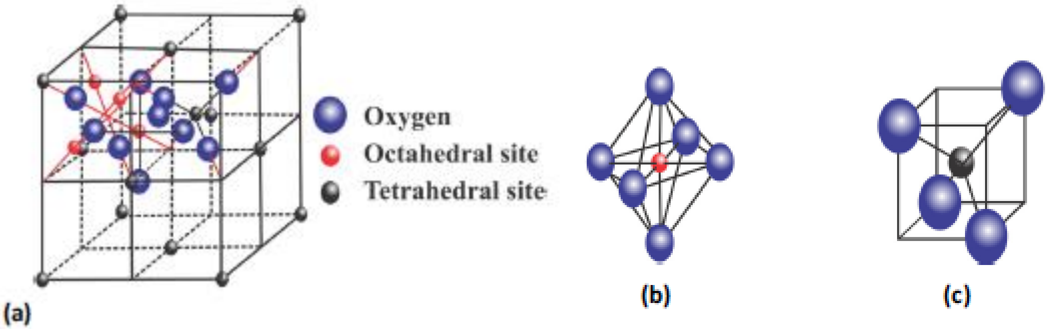

Figure 20 Illustration of a spinel ferrite: **a)** unit cell of spinel structure; **b)** Octahedral site; **c)** Tetrahedral site.[44]

The oxygen atoms display cubic close packing, with the M and Fe cations occupying tetrahedral and octahedral lattice sites. The cubic unit cell is formed by 56 atoms: 32 oxygen anions distributed in a cubic close-packed structure and 24 cations occupying 8 of the 64 available tetrahedral sites (A sites) and 16 of the 32 available octahedral sites (B sites).[44] It is possible to find three types of spinel structures: normal, inverse, and mixed spinel structure. The normal spinel has divalent cations occupying tetrahedral sites and iron cations occupying octahedral sites. In an inverse spinel, divalent cations occupy octahedral sites, while iron cations are distributed equally between tetrahedral and octahedral sites (**Figure 21**).[43]

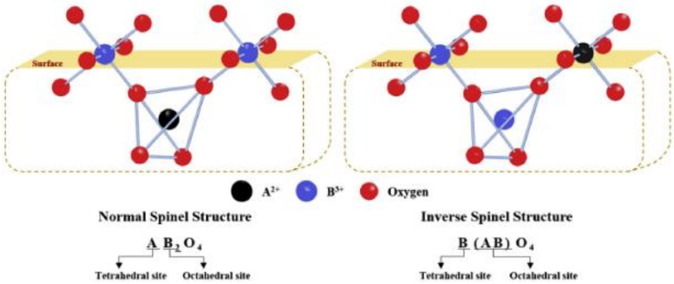

Figure 21 Schematic representation of a normal and an inverse spinel structure.[43]

Many applications, ranging from storage media and magnetic memory devices, to magnetic bio-separations, magnetic targeting, drug delivery, cancer hyperthermia and magnetic resonance imaging (MRI) were reported for spinel ferrite nanoparticles with controlled size and specific shapes.[45] Magnetite (Fe_3O_4) displays an inverse spinel structure with the oxygen anions forming a face-centred cubic crystal system. All tetrahedral sites are occupied by Fe^{3+} cations and the octahedral sites are occupied by both

Fe^{3+} and Fe^{2+} cations. The magnetic moment of magnetite is determined by the magnetic moment of the Fe^{3+} cations, with 4 unpaired electrons in the 3*d* shell.[46] Magnetite is the most relevant ferrite for clinic applications owing to suitable magnetic properties, namely superparamagnetism and high saturation magnetization, and established biocompatibility.

Mixed spinel ferrites of generic formulation MFe_2O_4 (M = Mn, Co, Fe, Ni or Zn, represent transition metals ions) display enhanced magnetic properties comparing to magnetite: higher saturation magnetization and size and shape dependent magnetic properties (**Figure 22**).[45,47]

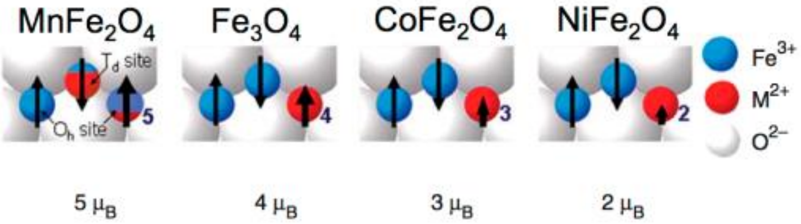

Figure 22 Schematic representation of spin alignment in mixed spinel ferrites with general formula MFe_2O_4 (M^{2+}= Mn, Fe, Co and Ni).[47]

Mixed spinel ferrites allay display a non-zero magnetic moment due to the uncompensated spin of the M^{2+} metal ions. The magnetic moment of the M^{2+} metal ion, mainly determined by the number of umpaired electrons, determines the magnetic properties of mixed spinel ferrite nanostructures.[48]

The saturation magnetization (M_s, 2 *T*) of mixed spinel ferrites MFe_2O_4 (M^{2+} = Mn, Co, Fe, Ni or Zn) $Ms_{Mn>Fe>Co>Ni>Zn}$ parallels the periodic arrangement of the M^{2+} cations and the number of unpaired electrons. The saturation magnetization of nanoparticles reaches that of the bulk material as the nanoparticles´ size increases. The contribution of the disordered surface spin layer to the nanoparticles magnetic moment becomes less important as the nanoparticles size increases (lower surface curvature, spin canting effects).[45]

Additionally, spin-orbit coupling, which induces large magnetocrystalline anisotropy, leads to an increase of the blocking temperature in an order of Zn < Ni < Mn < Fe < Co (**Figure 23**).[45]

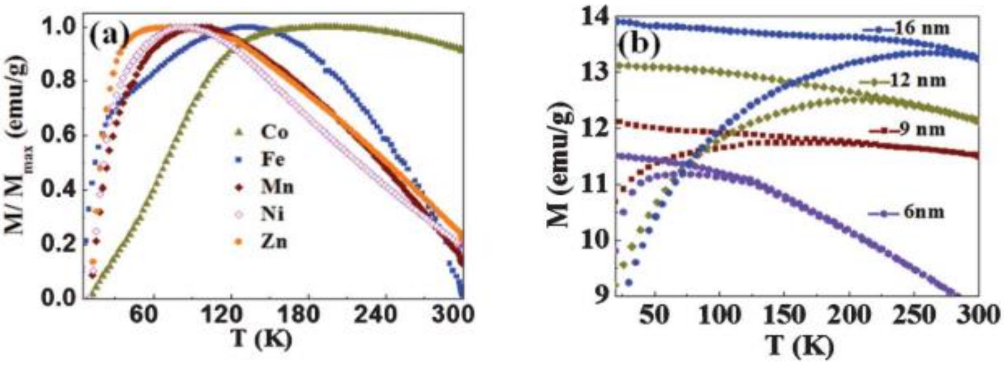

Figure 23 Normalised magnetization curves for nanoparticles with mixed spinel ferrite structure MFe_2O_4: **a**) effect of the M^{2+} metal ion on the magnetization for nanoparticles with the same size (6 nm); **b**) effect of the nanoparticles´size on the magnetization for nanoparticles with the same spinel structure (MFe_2O_4).

The blocking temperature increases also with the nanoparticle size (**Figure 23**).[45] The linear behaviour of the magnetization with the temperature results from enhancement of the magneto-crystalline anisotropy energy for the larger particle sizes.

In addition to composition and size, shape (anisotropy) tailoring is also a powerful strategy to enhance the magnetic properties of nanoparticles. There are procedures reported in the literature for synthesis of nanoparticles with a high degree of size control. Shape control is much more challenging. Procedures for preparation of nanoparticles with on-demand shape are rare. Moreover, joint optimization of nanoparticles´ size and shape is a formidable challenge. Nanoparticle self-assembly and controlled aggregation are also feasible strategies for optimization of the magnetic properties of nanoparticles.[45]

1.3 SPION and Gd^{3+} chelates as Contrast Agents for MRI

MRI was established in the last decades as one of the most powerful diagnostic imaging tools in medicine and biomedicine. MRI makes use of benign non-ionising radiation - radiofrequencies and magnetic fields, which makes repeated imaging innocuous. MRI images can be obtained with sub-millimetre spatial resolution, high anatomical contrast, and outstanding capability of differentiating soft tissues. The main limitation of MRI is low detection sensitivity, inherent to the nuclear magnetic resonance (NMR) phenomenon, which precludes clear distinction (contrast) between the region of interest (disease) and the background (normal tissues).[49] Human MRI imaging using magnetic fields above 3 *T* is not in current use due to excessive radiofrequency burden for patients. Contrast Agents (CA) improve the detection sensitivity of MRI by shortening the relaxation times ($T_{1,2}$) of the water protons in their vicinity. MRI CA are water relaxation catalysts. MRI contrast results from the magnetic properties of the CA. Paramagnetic chelates (Gd^{3+} and Mn^{2+}) and superparamagnetic nanomaterials (Fe_3O_4, FePt, and Gd_2O_3) can be used as MRI contrast agents.[50]

MRI is based on the Nuclear Magnetic Resonance (NMR) phenomenon. In the presence of an externally applied static magnetic field B_0 the spins of magnetic nuclei (^1H, ^{19}F) assume non-random parallel and antiparallel orientations in relation to the magnetic field orientation. The parallel orientation is energetically more favourable (lower energy) than the antiparallel orientation. Thus, an equilibrium state, with a small excess spin population aligned with the field, is rapidly attained according to the *Boltzmann* law. The excess spin population combines into a net magnetic field or net magnetisation (M), which at equilibrium is aligned along the positive z axis (along B_0) with the value M_0. Signal intensity in NMR and MRI is proportional to the net magnetization, which is determined by the strength of the applied magnetic field and the properties of the magnetic nucleus: natural abundance and giromagnetic ratio. When the equilibrium net magnetization is perturbed by a radiofrequency pulse (*rf*), the spins begin to move away from the B_0 alignment. This movement is caused by a much slower rotation about the applied *rf* field, B_1, which rotates in the xy plane at the same frequency as the Larmor frequency, appearing as an additional static field to the rotating net magnetisation vector (M). The net magnetisation rotates around both B_0 and B_1 fields, and, as a result, the net magnetisation follows a spiral path from its alignment with the z axis towards a rotational motion in the xy plane.[51]

The return of the magnetization to the equilibrium state is described by two relaxation mechanisms - longitudinal (spin-lattice) and transverse (spin-spin) relaxation, characterized by relaxation time constants T_1 and T_2, respectively (**Figure 24A** and **24B**).[51]

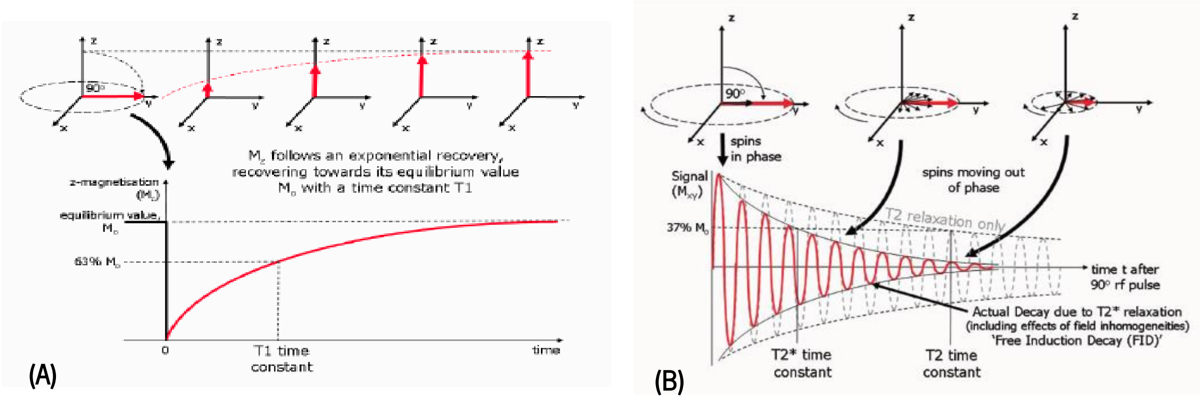

Figure 24 $T_{1,2}$ relaxation mechanisms following a 90° (π/2) pulse: **A)** T_1 relaxation mechanism; **B)** T_2 relaxation mechanism.[51]

T_1 (s) is the time required for recovery of 63 % of the longitudinal magnetization following the *rf* pulse.[52] The transversal relaxation, also known as spin-spin relaxation, arises from energy exchange between the spinning protons. The T_2 (s) relaxation time represents the actual time required for the transversal magnetization to decrease to 37 % of its starting value.[52]

The MRI signal is a combination of the T_1 and T_2 relaxation times of the water protons of tissues acquired in volume elements (*voxel*). MRI contrast arises from the intrinsically different relaxation times $T_{1,2}$ of the water protons of tissues and differences in water abundance. MRI CA are magnetic water relaxation catalysts, which reduce selectively the relaxation times of the water protons in their vicinity. The CA used for MRI usually reduce both the T_1 and T_2 relaxation times of the water protons. Nonetheless, the overall effect is generally more pronounced on either T_1 or T_2. Selective reduction of T_1 results in signal intensity enhancement, which translates into bright MRI images - positive contrast agents.[49] T_2 shortening results in signal intensity reduction which translates into dark images and negative contrast enhancement. The relaxation rates, $R_{1,2}$ (s^{-1}) ($R_{1,2} = 1/T_{1,2}$ (s^{-1})) measure the rate of recovery of the longitudinal magnetization (R_1) and the rate of loss of transversal magnetization (R_2) of the water protons. CA efficacy is assessed by the parameter relaxivity ($r_{1,2}$, $mM^{-1}s^{-1}$), defined as the selective enhancement of the relaxation rates ($R_{1,2}$, s^{-1}) of the water protons produced by 1 mM concentration of (para)magnetic species (Gd, Mn, Fe, SPION, organic radicals) (**Equation 8**).[49]

$$R_{1,2\,(obs)} = R_{1,2o} + r_{1,2}C \qquad \textbf{Equation 8}$$

$R_{1,2o}$ represents the relaxation rates measured before adding the CA, C represents the concentration of the (para)magnetic species (Gd, Mn, Fe, organic radicals).

Relaxivities ($r_{1,2}$, $mM^{-1}s^{-1}$) are generally calculated from the slope of the graphical representation of $R_{1,2}$ (s^{-1}) *vs* CA concentration (C, mM).[50] The (r_2/r_1) ratio determines CA effectiveness in relation to the predominant imaging (negative/positive) modality. In general, the higher the ratio r_2/r_1, higher is T_2 imaging efficacy and the lower the r_2/r_1, higher is T_1 imaging efficacy. As rule of thumb, T_2 CA display ratios r_2/r_1 *circa* 10 and T_1 CA display r_2/r_1 ratios < 5.[49]

Complexes of paramagnetic Gd^{3+} ions are the most effective T_1 CA for contrast-enhanced MRI examinations in the clinical setting: Gd^{3+} ions display high paramagnetism ($4f^7$, seven unpaired electrons) and long electronic relaxation times. Free, unchelated Gd^{3+} ions are acutely toxic. Complexation of Gd^{3+} ions with polydentate ligands reduces toxicity, allows tailoring the pharmaco-kinetic properties of chelates and can add targeting ability to the complexes. Octadentate poly(aminocarboxylate) macrocyclic (DOTA-type) and linear (DTPA-type) ligands form complexes with Gd^{3+} ions with high thermodynamic stability and kinetic inertness. Several Gd-based CA were in use over the last decades for human contrast-enhanced MRI (**Figure 25**).[53,54]

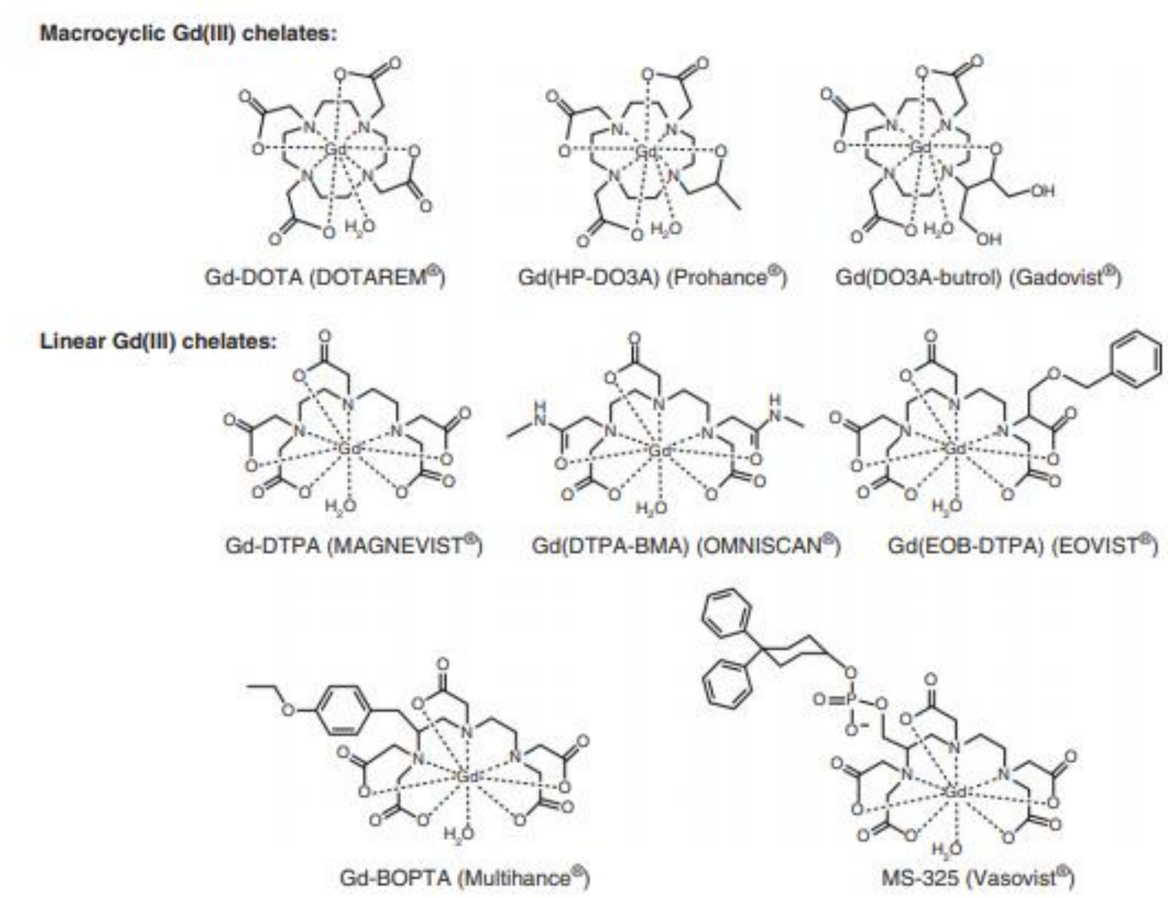

Figure 25 Gd^{3+} complexes currently used at clinical diagnosis.[54]

Fast chelate elimination via kidney filtration, reduces the provability of complex demethylation and Gd-associated toxicity.

Macrocyclic gadolinium-based contrast agents (especially Dotarem) display higher thermodynamic and kinetic stability than their linear DTPA-based counterparts thanks to the macrocycle effect. High thermodynamic stability and kinetic inertness ensures that chelate dissociation rate *in vivo* is lower than the complex elimination rate from the body. Therefore, Gd^{3+} release becomes negligible during the *in vivo* residence time of the gadolinium complex.[50] In fact, the condition Nephrogenic Systemic Fibrosis (NSF) was mainly associated to linear Gd-based CA in individuals with compromised renal function. Insufficient chelate kinetic stability associated to long lifetimes *in vivo* resulted in extensive complex demethylation and severe kidney damage. More recently, the appearance of hyperintense brain areas in patients submitted to Gd-based CA enhanced MRI raises concerns about Gd release and accumulation in the brain.[55]

Manganese (Mn^{2+}) based complexes are under intense research as alternatives to Gd-based CA. The Mn^{2+} ion exhibits physical and magnetic properties similar to Gd^{3+}: high spin quantum number (5 unpaired electrons, S = 5/2), long longitudinal electronic relaxation times and fast water exchange kinetics (**Figure 26**).[56]

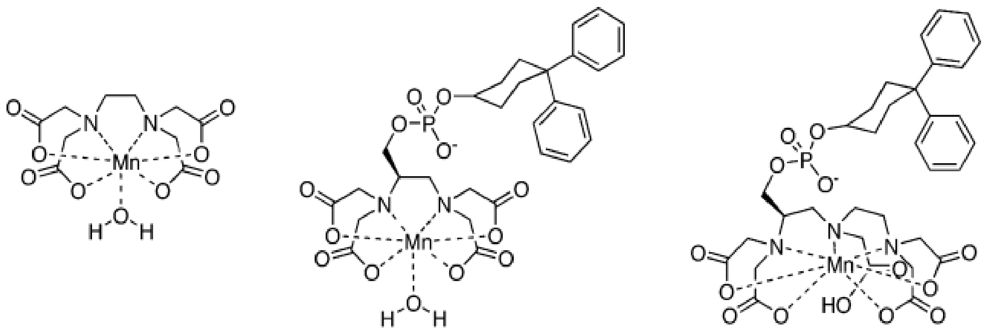

$[Mn(EDTA)(H_2O)]^{2-}$ **MnL1** **MnL2**

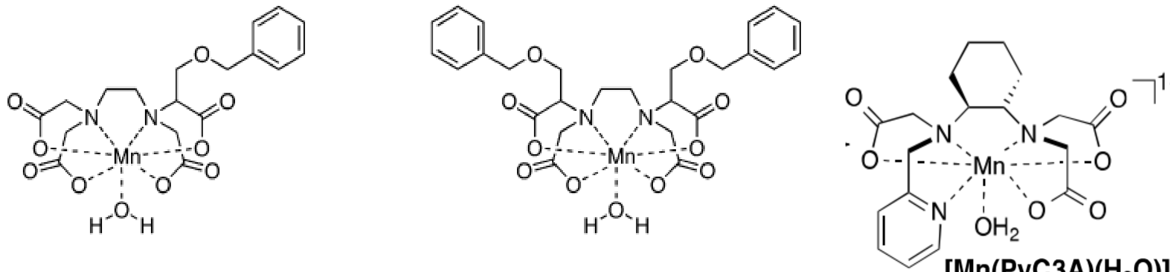

$[Mn(EDTA(BOM))(H_2O)]^{2-}$ **$[Mn(EDTA(BOM)_2)(H_2O)]^{2-}$** **$[Mn(PyC3A)(H_2O)]^{-}$**

Figure 26 Mn^{2+} complexes proposed as potential contrast agents for MRI.[56]

Ligand design for complexation of Mn^{2+} ions is more difficult that for Gd^{3+} due to a difficult compromise between inner sphere complex hydration and complex stability. Nonetheless, complex stability requisites are not as stringent as for Gd^{3+} as Mn is an essential trace element. Mn released form Mn-based CA is rapidly taken by liver and eliminated. Still, concerns about neurologic toxicity associated to Mn release from Mn-based CA is prone to limit the wide use of Mn^{2+} chelates as human CA in a near future.[56]

Relaxation mechanism for paramagnetic complexes

The Solomon-Bloenbergen-Morgan physical-chemical model describes the relaxation of the water protons catalysed by paramagnetic complexes (**Figure 27**).[53,49,57]

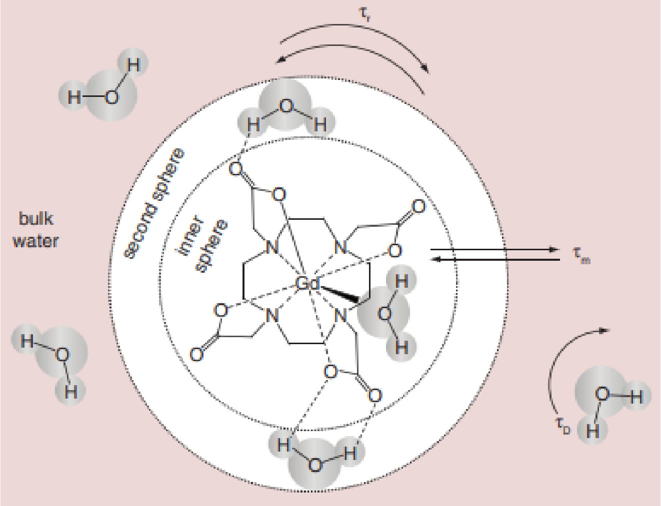

Figure 27 Schematic representation of the molecular parameters that govern the relaxivity of paramagnetic complexes.[57]

According to this model, the relaxivity of paramagnetic complexes is determined by parameters intrinsic to the metal ion (paramagnetism and electronic relaxation times) and parameters related to the water exchange properties and rotational dynamics of the complex. The majority of CA are metal complexes (Gd^{3+}, Fe^{3+}, Mn^{2+}) with polydentate ligands that do not saturate the coordination sphere of the metal ion but leave one (or more) free positions for direct water coordination. Gd^{3+} has coordination number 9, thus complexes with octadentate poly(aminocarboxylate) DOTA- and DTPA-type ligands display a water molecule directly coordinated to the metal ion. The region in close vicinity to the coordinated metal ion can be divided into inner sphere and outer sphere. The inner-sphere water molecules are directly coordinated to Gd^{3+} ion, while the outer-sphere (bulk water molecules) are diffusing in the chelate near environment. A second sphere, where water molecules are hydrogen bonded to the chelating unit, can be considered in some cases.[57]

Dipolar coupling, between the nuclear spin of the water protons of the coordinated water molecule and the spin of the unpaired electrons of the metal ion, results in shortening of the relaxation times of the coordinated water protons. The extent of dipolar coupling is determined by the rotational correlation time (τ_R) of the complex; the residence time (τ_M, $\tau_M = 1/k_{ex}$) of the coordinated (inner sphere) water molecule; the distance (d) between the metal ion and the protons of the coordinated water molecule and the relaxation times ($T_{1,2}$) of the metal ion electron spin. The dipolar coupling is modulated by the correlation parameter τ_{Ci} (**Equation 9**).[49]

$$\frac{1}{\tau_{Ci}} = \frac{1}{\tau_R} + \frac{1}{\tau_M} + \frac{1}{\tau_{Si}} \qquad \text{Equation 9}$$

τ_{Si} is the electron relaxation correlation time for the electronic spin associated with the paramagnetic ion.

The outer sphere contribution is modulated by the translational correlation time (τ_D) ($\tau_D = d/D$): D is the relative diffusion constant (m^2/s) of the water molecules and the paramagnetic complex and d represents the distance of closest approach between the complex and the diffusing water molecules. The relaxivity of Gd^{3+} complexes is mainly determined by inner-sphere relaxation. Outer-sphere relaxation becomes important for complexes without inner-sphere hydration.[49]

The design of high relaxivity complexes focuses on the optimization of the parameters τ_R, τ_M and q, the number of coordinated water molecules in the inner-sphere, via ligand design.[53] The research group developed strategies for attaining high relaxivities *via* simultaneous optimization of the main parameters that govern relaxivity, τ_R and k_{ex} and q. Synthetic routes for chelators, whose Gd^{3+} complexes display fast water exchange, within the range considered ideal for attaining high relaxivities at intermediate fields, were developed by the research group. Pendant groups on the chelators were used for complex functionalization: with lipophilic moieties for BSA association and self-assembly into micellar structures, with thiol groups for decoration of gold nanoparticles and quantum dots. All these strategies rely on simultaneous optimization of the water exchange rate and on slowing down the rotational dynamics of chelates in solution.[58,59,60,58]

Superparamagnetic nanoparticles as MRI CA

Iron Oxide Nanopaticles (IONP) are an established class of MRI CA owing to high biocompatibility and tuneable magnetic properties. Moreover, the hyperthermia properties of IONP allow combining therapeutic and MRI imaging capabilities in the same nanoparticle platform. Magnetite (Fe_3O_4) is the magnetic phase mostly used for T_2 MRI owing to strong T_2 effect and high ratio r_2/r_1.[50]

The magnetic susceptibility of SPION generates perturbations in the magnetic field around the nanoparticles which stimulates energy exchange between the water protons spins resulting in faster loss of transversal phase coherence (spin dephasing). The result is a faster decline of the water protons transversal magnetization in the presence of SPION, i.e. T_2 relaxation time shortening. This effect, reminiscent of the outer-sphere relaxation mechanism for paramagnetic complexes, is determined by parameters intrinsic to the nanoparticles - magnetic core size and magnetic moment (determine the nanoparticles saturation magnetization), and SPION concentration; parameters describing the interaction of the SPION with the surrounding water environment - diffusion coefficient and number of water molecules (protons) within the dephasing region, in the vicinity of the nanoparticles core magnetic moment, distance between the water protons and the SPION magnetic core and the dynamics of water exchange between the water molecules within the nanoparticle´s field and the bulk water molecules; instrumental parameters - magnetic field strength and applied radiofrequency (**Equation 10a,b**).[34]

$$R_2 = \frac{1}{T_2} = \left(\frac{256\pi^2\gamma^2}{405}\right) V M_S^2 a^2 / D(1 + \frac{L}{a}) \qquad \textbf{Equation 10a}$$

$$\frac{1}{\tau_C} = \frac{1}{\tau_D} + \frac{1}{\tau_N} \qquad \tau_D = \frac{d2}{D} \qquad \omega\tau_C < 1 \qquad \textbf{Equation 10b}$$

γ is the proton gyromagnetic ratio, V is the volume fraction (concentration) of nanoparticles, Ms is the nanoparticles saturation magnetization, a is the diameter of the nanoparticle core, D is the diffusion coefficient of the water protons, and L is the thickness of an impermeable surface coating. ω is the proton *Larmour* frequency, dependent on the magnetic field B_0 and γ is the proton giromagnetic ratio. τ_C is a global correlation time, τ_D is the water proton diffusion time and τ_N is the Nèel relaxation time.

R_2 is modulated by two parameters: τ_D - water translational correlation time and τ_N- Nèel relaxation time (**Equation 10b**).[34] **Equation 10b**, describes the effect of the magnetic field and of the radiofrequency on the nanoparticles relaxivity. Knowing the global relaxation time (τ_C) it is possible to predict the ability of fluctuations of the local magnetic field to relax the nuclear spins of the water protons. For nanoparticles in the motional averaging regime, typically with iron oxide cores with diameter d < 35 nm, R_2 has a linear dependence on the volume fraction (concentration) of nanoparticles. The dependence of the relaxivity on the nanoparticle´s core size is predominantly a consequence of the scaling of the diffusion timescale with $\tau_D = d^2/D$.[34]

Preparation of high relaxivity SPION requires optimization of experimental conditions which favour a large core size, thus displaying high magnetization, and an extended dephasing region around the nanoparticles, containing a large amount of slow diffusing water molecules. Therefore, SPION physical-chemical properties, core and shell size, magnetic composition and nanoparticle self-assembly/agglomeration determine the performance of the SPION as CA for MRI.[34] The increase of r_2 relaxivity with the size of SPION is a well-established strategy to obtain high relaxivity. However, there is a size limit, *circa* 20 nm, beyond which there is a break of the superparamagnetic regime and the nanoparticles become prone to aggregation under magnetic irradiation, owing to coercivity and remanent magnetization. In general, the saturation magnetization and logically the relaxivity displayed by mixed spinel ferrites (MFe_2O_4; M^{2+}= Mn, Fe, Co, Ni, Zn) parallels the magnetic moment of the M^{2+} ion. Manganese ferrite nanoparticles display much higher, by almost a *factor* 2, relaxivity than magnetite nanoparticles with the same size.(**Figure 28**).[50,57]

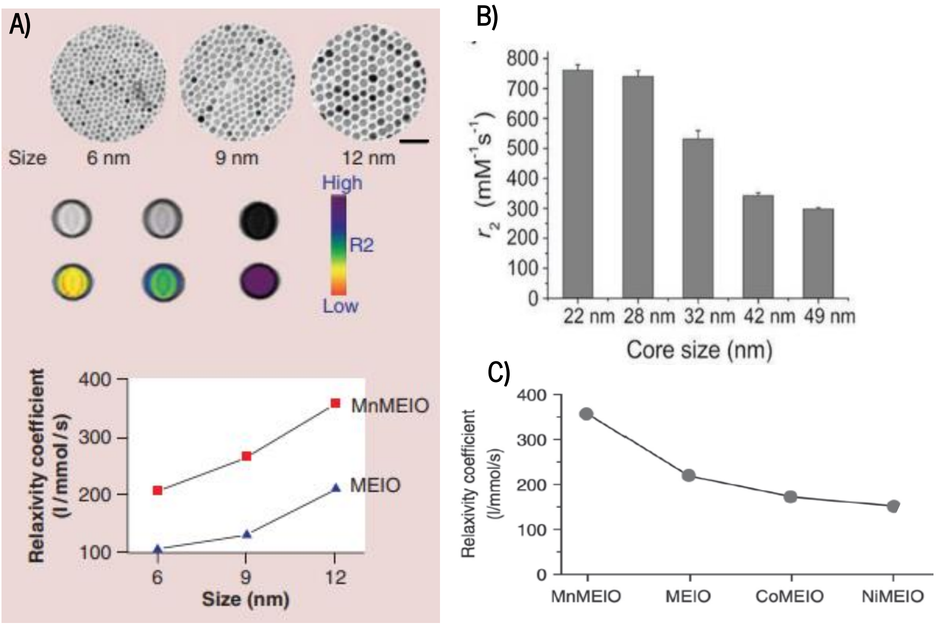

Figure 28 Effect of the nanoparticle´s size: **A**) core size < 20 nm and **B**) core size > 20 nm; and magnetic core composition in r_2 relaxivity **C**).[57]

Despite superb magnetic properties and performance as T_2 MRI CA, concerns about Mn toxicity *in vivo* are likely to limit the translation of Mn ferrite nanoparticles into clinical use.[50]

The strong magnetic fields produced by SPION used as T_2 CA perturb T_1 relaxation, thus attaining high r_2 values and high r_2/r_1 ratios. The reduction of magnetization for small nanoparticles is detrimental for T_2 but beneficial for T_1 - weighted MRI.[50] Ultrasmall superparamagnetic iron oxide nanoparticles (USPIO) can be used as effective T_1 contrast agents.

A coating is fundamental to guaranty colloidal stability and to protect the surface of the nanoparticles from water erosion. The transversal relaxation rate R_2 is inversely proportional to the nanoparticles coating thickness (**Equation 10a**). R_1 is not significant affected by shell thickness. The magnetic field induced by magnetic nanoparticles decreases with the distance away from the core. Thick surface coatings can result in significant losses of transversal relaxivity owing to reduction of the extension of the dephasing region around the nanoparticles core. However, surface hydrophilic ligands that interact with water molecules promote relaxivity enhancements owing to reduction of the water diffusion coefficient. Crosslinked and reticulated hydrophilic polymer shell structures may reduce the diffusion coeficient of water molecules within polymeric shells leading to relaxivity enhancement.[47] Strong hydrogen bonding of water molecules to the coating shell can even result in water "immobilization". Fast exchange between the immobilized water molecules and the bulk water can result in very high relaxivity enhancements.

Stimuli-responsive magnetic nanoparticle self-assembly has attracted much attention as a smart strategy for attaining high relaxivity. The most common effect of nanoparticle aggregation on r_2 relaxivity is a significant relaxivity reduction comparing to the non-aggregated state. Random nanoparticle aggregation is likely to result in aggregates which display lower magnetic moment than the non-aggregated state. On the other hand, magnetic dipole-oriented aggregates are prone to display considerable relaxivity enhancements.[61]

1.4 Magnetic hyperthermia

Magnetic induction hyperthermia is based on the exposure of magnetic nanoparticles to alternating (AC) magnetic fields. Heat generation can result from magnetic hysteresis loss and from *Nèel* and *Brownian*-relaxation mechanisms. Hyperthermia tumour therapy is very attractive due to the benign nature of magnetic fields allied to depth-independent, non-invasive and localized external actuation. Tumour cells are more heat-sensitive than non-tumours cells, temperatures around 41 °C are lethal to cancer cells.[62]

Specific absorption rate (*SAR*, W/g_{Fe}) also named specific loss power (*SLP*) is the main parameter used to quantify heat generation by magnetic nanoparticles (**Equation 11**).

$$SAR = \frac{C}{m_{Fe}/m_{sol}} \frac{dT}{dt} \qquad \textbf{Equation 11}$$

C is the specific heat capacity of the sample; dT/dt is the tangent to the temperature-time curve at $t = 0$ and m_{Fe}/m_{sol} is the nanoparticles Fe concentration expressed as *wt* %.

The *SAR* of magnetic nanoparticles is usually determined by the calorimetric method (**Figure 29**).[63,64]

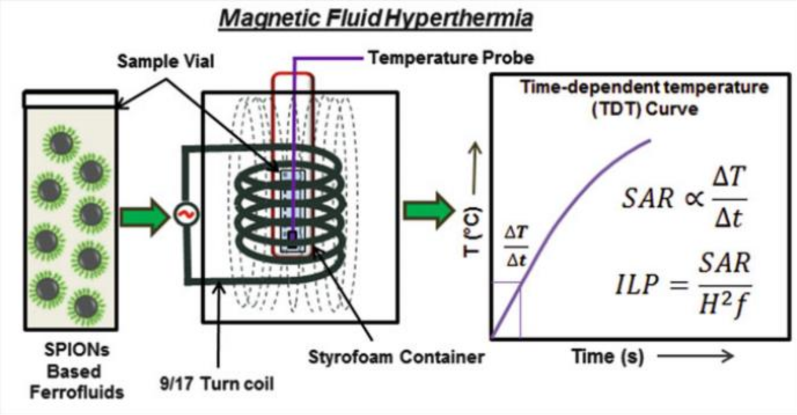

Figure 29 Schematic diagram of the calorimetric method for the determination of the *SAR* parameter.[64]

Oxide magnetic materials with low electrical conductivity, heat under AC irradiation due to loss processes during the reorientation of the magnetization - *Nèel* relaxation or frictional forces if the particle can rotate in a medium of low viscosity- *Brownian*-relaxation (**Equation 12**).[65]

$$SAR = a\frac{4\mu_0 M_s H_{max}}{\rho}f \qquad \textbf{Equation 12}$$

μ_0 is the vacuum permittivity, M_S is the saturation magnetization, H_{max} is the magnetic field amplitude, ρ the mass density of the NPs, f represents the magnetic field frequency and α is a dimensionless factor describing the deviation from a square hysteresis.

The *SAR* value is normalised to the SPION *wt* $\%_{Fe}$ concentration. Therefore, nanoparticles displaying high *SAR* values are sought after because high *SAR* values allows to reduce the amount of magnetic nanoparticles required to attain lethal temperatures inside tumours. According to **Equation 12**, the *SAR* parameter increases linearly with nanoparticles´ saturation magnetization (M_S), which is determined by the nanoparticles composition, size and shape (anisotropy). Moreover, *SAR* is also linearly dependent on the $H_{max}.f$ product. Thus, the normalised *SAR* parameter ILP (ILP= *SAR*/ H^2f) allows to compare the performance of magnetic nanoparticles tested under different magnetic excitation conditions. For practical *in vivo* applications, the parameter $H_{max}.f$ is limited to $H_{max}.f < 5 \times 10^9$ A $m^{-1}s^{-1}$ to avoid nonspecific heating or damage to the human body.[62,57,64]

Simultaneous optimization of nanoparticles´ size and composition, and shape is a powerful strategy to attain high *SAR* values.[62] Anisotropic nanoparticles display dramatic *SAR* enhancements comparing to isotropic spherical nanoparticles (**Figure 30**).

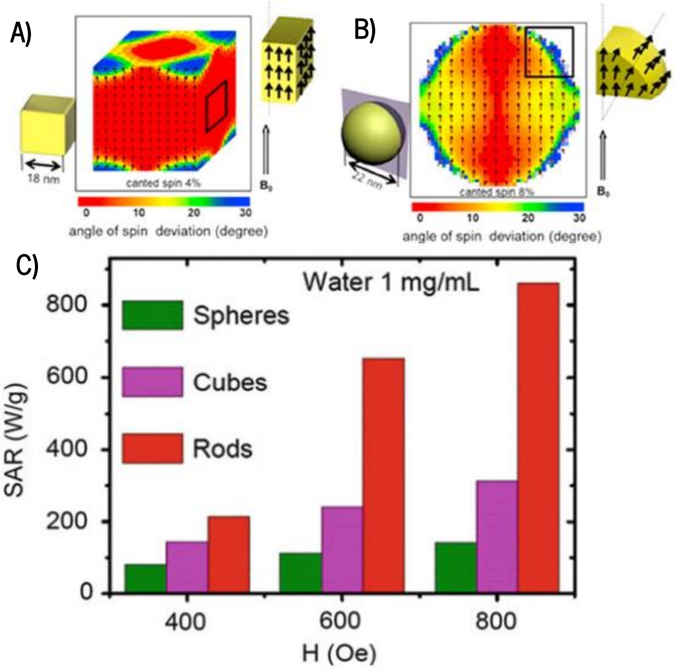

Figure 30 Magnetic spins alignment in different nanoparticles shapes; **a)** cube; **b)** sphere; **c)** effect of the shape over the *SAR* value.[64]

Nanoparticles with a cubic shape display higher anisotropy than spherical nanoparticles. In each cubic surface the spins are aligned in the same direction, whereas in the spherical nanoparticles surface spin canting effects lead to a reduction of the nanoparticles magnetic moment. High *SAR* values can be obtained by modulating the effective anisotropy and not by simply increasing the saturation magnetization of magnetic nanoparticles.[63]

The excitation of a single MNP in magnetic hyperthermia experiment can lead only to a very small temperature increase, about 10^{-9} K. However, a sample with a concentration of the order 10^{9} NPs/cm^{-3} can reach therapeutic temperatures due to nanoparticle´s self-assembly through dipolar interactions (**Figure 31**).[40]

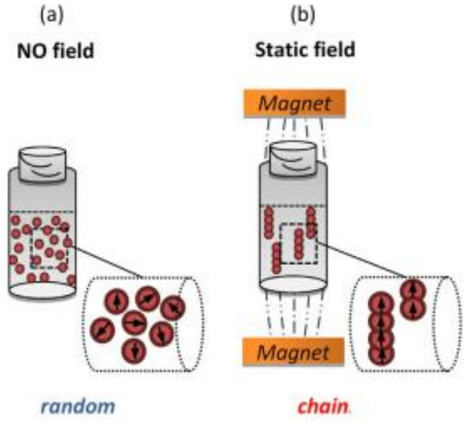

Figure 31 Representation of random **(a)** and ordered **(b)** nanoparticles self-assemblies formed in solution during hyperthermia experiments.[40]

When exposed to an AC field, magnetic nanoparticles can form linear aggregates of magnetic dipole-ordered structures such as chains. Chain-like structures can result in an increase in the heating efficiency of NPs. To maximize the heating efficiency, it is necessary to assemble MNPs into chains with a uniaxial anisotropy, which leads to hysteretic losses that can improve the heat power dissipation process.[63]

Nanoparticle´s size is the single parameter with higher impact on nanoparticles efficacy as MRI CA and hyperthermia sources that can be optimized *via* synthesis. However, for *in vivo* applications nanoparticles´ size is limited by fast clearance by the RES organs, liver and spleen, and by transition from paramagnetism to the ferromagnetic regime when the nanoparticles core size grows above the magnetic single domain threshold ($d < 20$ nm).[62] Therefore, obtaining very high relaxivity/*SAR* magnetic nanoparticles suitable for *in vivo* aplications requires simultaneous optimization of composition, size and shape. Beyond efficacy, it is necessary to take into account the complex interplay between nanoparticles´composition, degradation, elimination and toxicity *in vivo*.

Chapter 2

Results and discussion

2.1 Synthesis

Dehydropeptide hydrogelators

Our research group has developed new methodologies for the preparation of dehydropeptides *N*-capped with aromatic groups (naproxen, 2-naphthyl acetic acid, benzyloxycarbonyl – Cbz, *Z*) as effective hydrogelators - forming hydrogels at low critical gellation concentrations (*cgc*), typically around 4 mg/ml (0.4 *wt* %).[24,25,66,23] Our results, together with the vast literature, enphasise the importance of aromatic residues and π-π stacking interactions on the gelation propensity and elasticity of low molecular weight peptide-based hydrogels - π gelators.[67,11] Aromatic *N*-capping associated to *C*-terminal deprotection endows hydrogelators with solubility in neutral/alkaline conditions and offer the opportunity to trigger gelation by pH dropping. Remarkably, deprotected amino acids and peptides have also been reported as efficacious hydrogelators.[68]

In this work we investigated dehydropeptides lacking an aromatic *N*-capping group as potential hydrogelators. We envisaged that an *N*-terminal succinic acid moiety would still allow manipulating hydrogelators´ solubility through pH adjustment, for gelation purposes, while keeping *C*-terminal methyl ester protection (**Figure 32**).

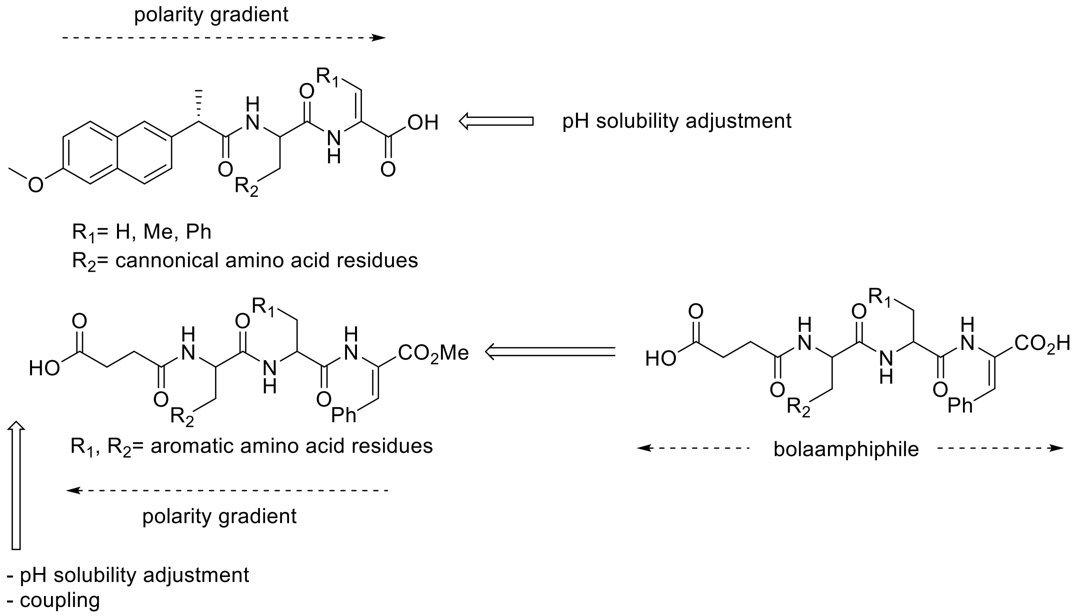

Figure 32 General synthetic strategy for new hydrogelators with a succinic acid capping group.

This approach introduces a polarity reversal in relation to our previous design of *N*-capped *C*-deprotected dehydropeptide hydrogelators.[24,66,23] This strategy offers opportunities for coupling, both in solution and solid-phase conditions, e.g., RGD bioepitopes, allowing facile access to elaborate hydrogels for biomedical applications. Moreover, the startling possibility that bolaamphiphile-type succinic acid *N*-capped *C*-deprotected dicarboxylic acid dehydropeptides could still display self-assembly and hydrogelation properties, was investigated as well.[69]

To test this hypothesis a panel of hydrogelators (**Figure 33**) was synthesised following methodologies developed by the research group (**Figure 34** and **Figure 37**).

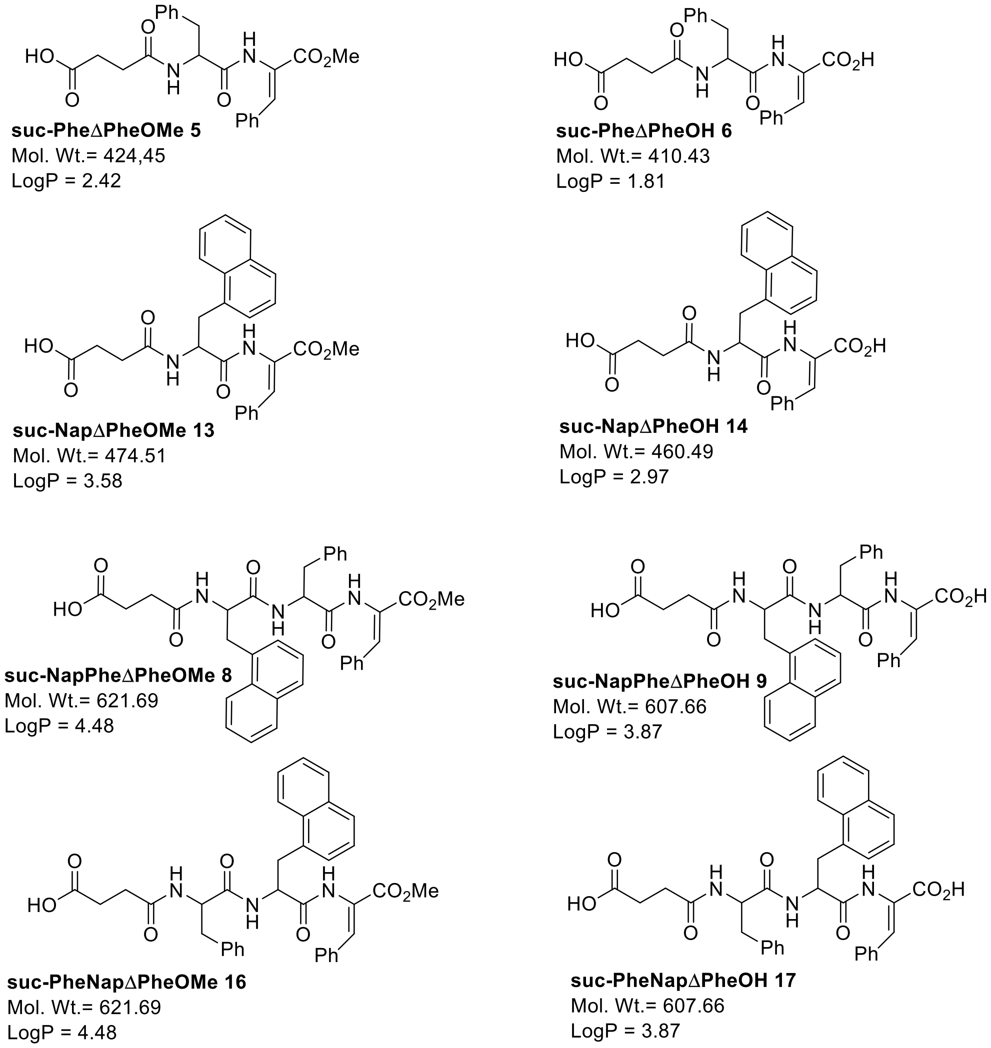

suc-PheΔPheOMe 5
Mol. Wt.= 424,45
LogP = 2.42

suc-PheΔPheOH 6
Mol. Wt.= 410.43
LogP = 1.81

suc-NapΔPheOMe 13
Mol. Wt.= 474.51
LogP = 3.58

suc-NapΔPheOH 14
Mol. Wt.= 460.49
LogP = 2.97

suc-NapPheΔPheOMe 8
Mol. Wt.= 621.69
LogP = 4.48

suc-NapPheΔPheOH 9
Mol. Wt.= 607.66
LogP = 3.87

suc-PheNapΔPheOMe 16
Mol. Wt.= 621.69
LogP = 4.48

suc-PheNapΔPheOH 17
Mol. Wt.= 607.66
LogP = 3.87

Figure 33 Panel of hydrogelators studied in this work. Molecular weight and LogP molecular properties were calculated with the molinspiration online calculator (https://molinspiration.com/cgi-bin/properties).

The Phe-Phe dipeptide *motif* exhibits superb self-assembly propensity.[22] Many low molecular weight peptide-based hydrogels described in the literature feature this *motif*.[70,10] Results from our group suggest that the *analogous* PheΔPhe *motif* displays also enhanced gelation propensity comparing to other dehydipeptide sequences.[24,66,23] Di- and tri- dehydropeptides (**5** and **6**; **8** and **9**) featuring the PheΔPhe *motif* were prepared following strategies developed by the research group (**Figure 34**).

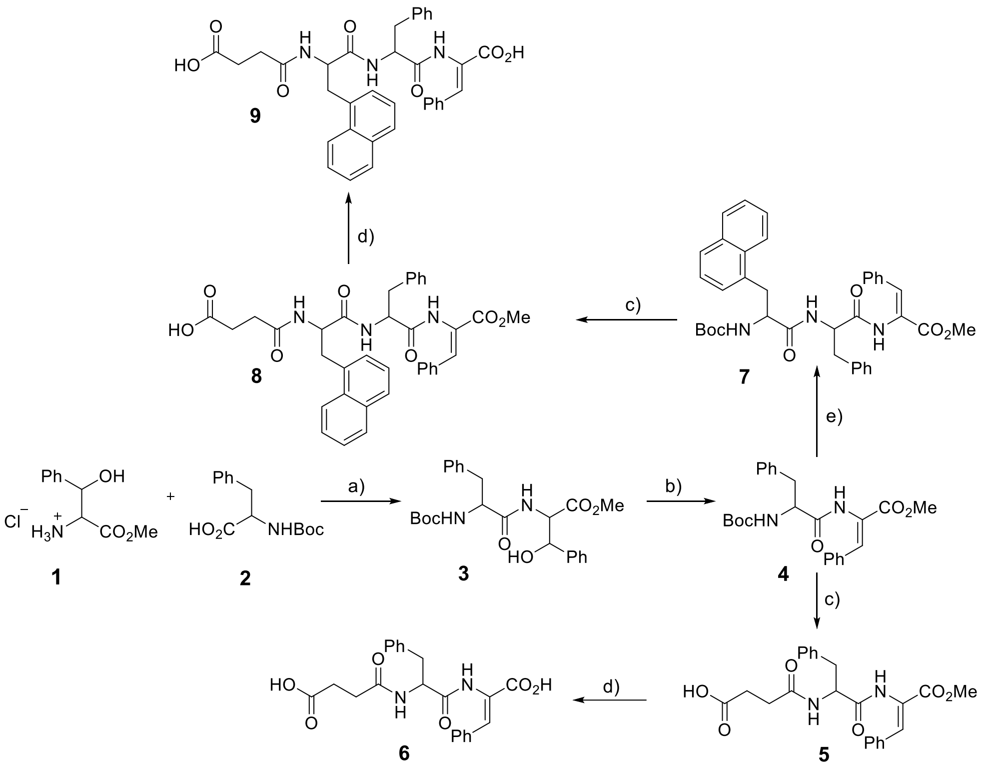

Figure 34 Synthetic pathway for di- and tri-dehydropeptides featuring the PheΔPhe *motif*. (**a**) HBTU, TEA, MeCN; (**b**) (i) Boc_2O, DMAP, dry MeCN, (ii) TMG; (**c**) (i) TFA, (ii) succinic anhydride, pyridine, N_2 atmosphere; (**d**) (i) NaOH (1 M), 1,4-dioxane, (ii) HCl (1 M); **e**) i) TFA, ii) Boc-L-3-(2-Naphtyl)alanine, HBTU, TEA, MeCN.

Orthogonally protected dehydrodipeptide **4**, featuring the PheΔPhe *motif*, was synthesised in 2 steps following procedures described before by the research group. Amide **3** was synthesised in 96 % isolated yield under HBTU coupling conditions in acetonitrile using triethylamine (TEA) as base. The ^1H NMR spectrum of compound **3** is consistent with the proposed structure, showing extensive peak duplication due to formation of a mixture of diasteriomers. Compound **4** was obtained (94 % isolated yield) by dehydration of compound **3** in a one pot two-step procedure using conditions developed by the research group (**Figure 35**).[71]

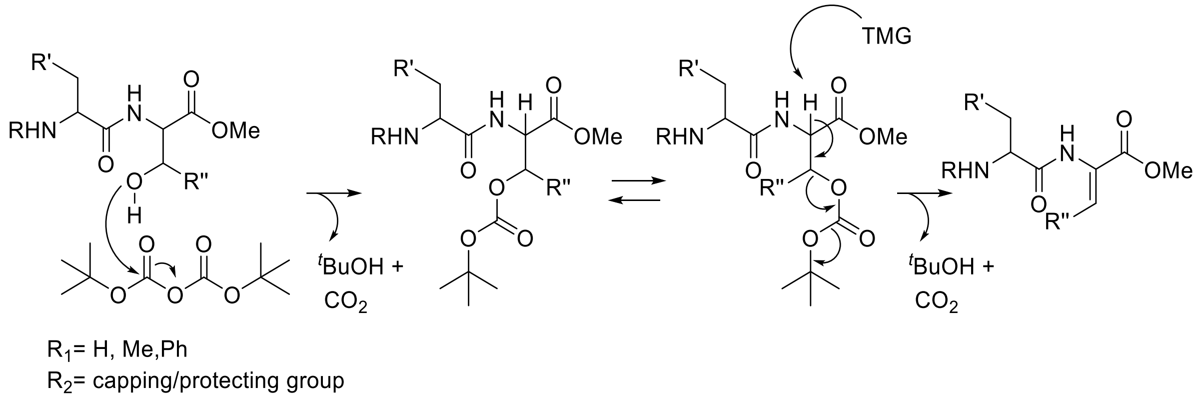

Figure 35 Dehydration mechanism for β-hydroxyamides.

In the first step a carbonate ester of compound **3** is formed by addition of Boc_2O (1.2 molar eq.) and DMAP (10 % mol). The formation of the carbonate ester was followed by ^1H NMR, monitoring the disappearance of the signal assigned to the β-hydroxy group at δ 6.01 ppm and the shift of the signal attributed to the beta proton of the phenylserine moiety at δ 6.68 and 6.89 ppm. When the reaction was deemed complete the elimination was promoted by addition of *N,N,N*` ,*N*`-tetramethylguanidine (TMG). Disappearance of the signal attributed to the CHα proton of the phenylserine moiety marks the reaction completion. Compound **4** was obtained in analytical purity (> 95 % by NMR) simply by acid and base workup. The Boc protecting group of compound **4** was removed selectively with trifluoroacetic acid (TFA) unrevealing the amine function for coupling. Succinic acid functionalization was carried out in neat pyridine using an excess of succinic anhydride (1.5 molar eq). Hydrogelator **5** was obtained in 84 % isolated yield after aqueous workup with diluted HCl (1 M). Saponification of compound **5** in dioxane with NaOH (1 M, 3 molar eq) followed by pH adjustment to *circa* pH 2 afforded compound **6** as a white solid in 78 % yield. Compound **5** and **6** were obtained in 3 and 4 steps, respectively, with 75 and 59 % overall yields.

A large body of evidence, from our research and from the literature, suggests that the self-assembly of low molecular weight peptides is dictated by a delicate balance between hydrophobicity and hydrophilicity and water solubility.[72] Extending the PheΔPhe peptide *motif* with a bulky aromatic amino acid was explored as a strategy to enhance the self-assembly propensity of the succinic acid *N*-capped hydrogelators, especially the di-carboxylic acid hydrogelators which exhibit significantly lower hydrophobicity (LogP) than their *C*-protected analogues (**Figure 33**). The non-proteinogenic Boc-L-3-(2-Naphtyl)alanine (Nap) amino acid was selected for extending the PheΔPhe sequence. The bulky aromatic naphthalene side chain is likely to enhance the self-assembly propensity of the dehydropeptides via π-π stacking interactions and displays interesting spectroscopic properties.[73]

Starting from common precursor **4**, hydrogelator **8** was synthesised in two steps: deprotection of compound **4** (with TFA) and coupling to the protected Boc-L-3-(2-Naphtyl)alanine amino acid under HBTU/TEA conditions; followed by TFA deprotection and reaction with succinic anhydride in pyridine as described for compound **5**. Hydrogelator **9** was obtained by saponification was described for compound **6**. Compounds **8** and **9** were obtained in good yields, 45 and 44 %, over 4 and 5 steps, respectively.

The ^{1}H NMR spectra of the hydrogelators **8** and **9** featuring the PheΔPhe *motif* display some interesting features (**Figure 36**). (see also the ^{1}H and ^{13}C NMR spectra of compounds **5** and **6** in **annex Figure A1**).

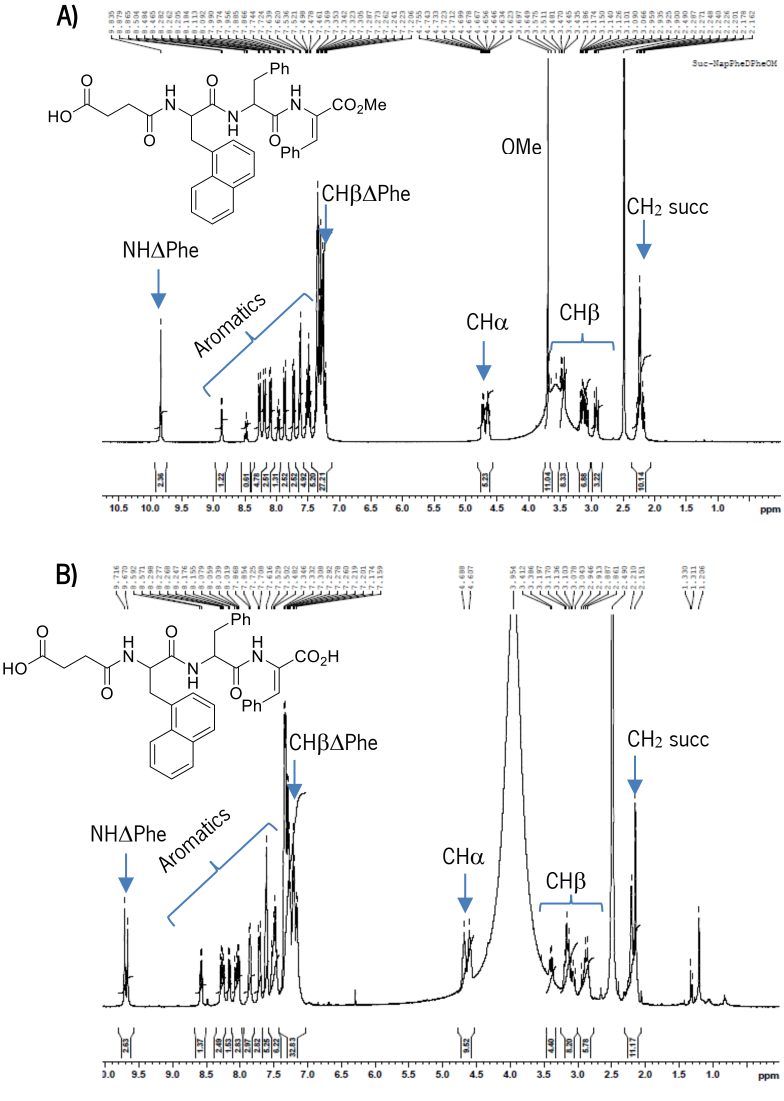

Figure 36 ^{1}H (**A**) and **B**)) NMR spectra of hydrogelators **8** and **9**, respectively.

All signals in the ^{1}H spectra of compound **8** and **9** were assigned using bidimensional HMBC and HMQC techniques.

Di- and tri-dehydropeptide hydrogelators featuring the NapΔPhe *motif* were synthesised also to get insight into the effect of peptide sequence on the self-assembly and gelation properties (**Figure 37**).

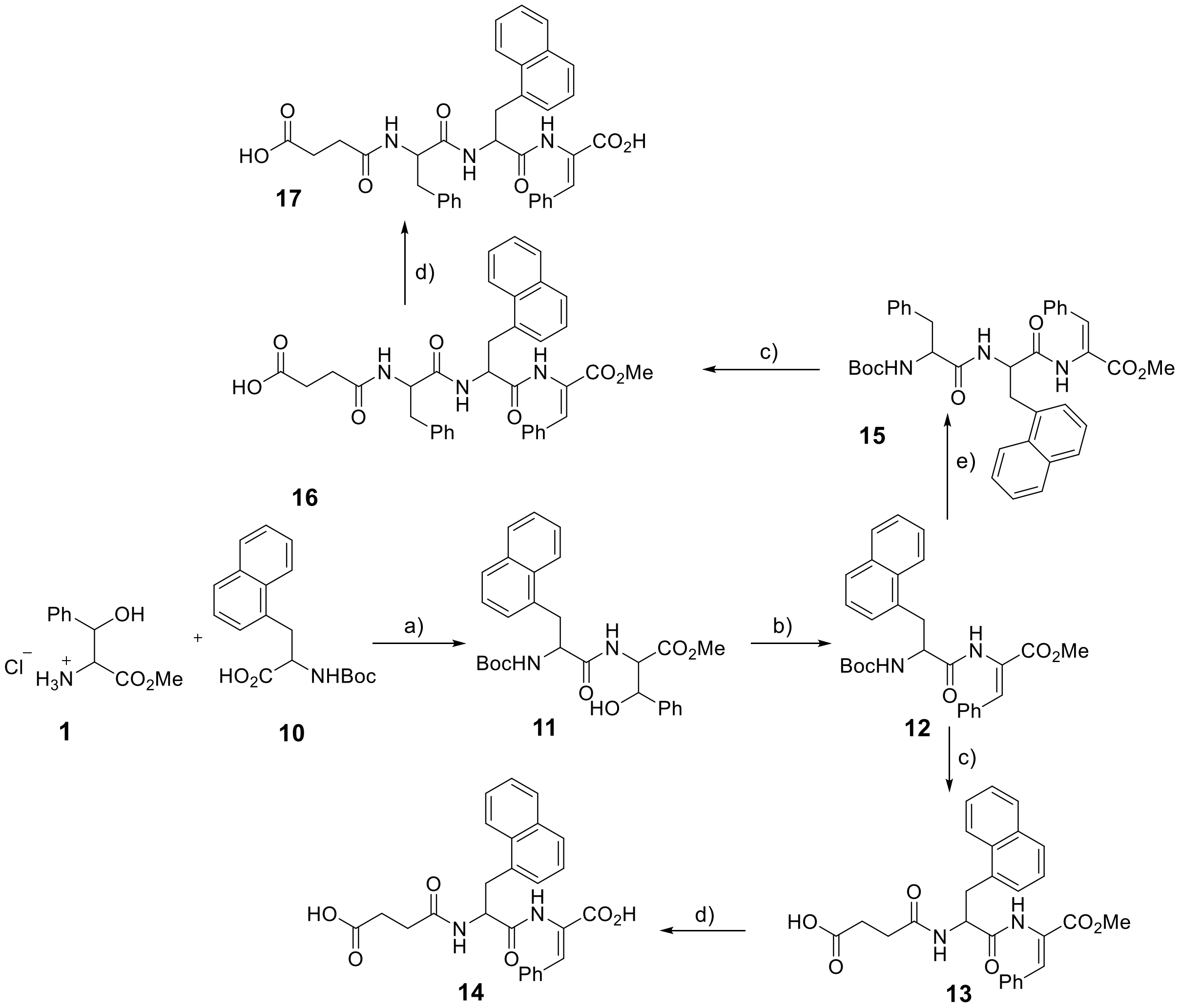

Figure 37 Synthetic pathway for succinic acid *N*-capped for di- and tri-dehydropeptides featuring the NapΔPhe *motif*. (**a**) HBTU, TEA, MeCN; (**b**) (i) Boc_2O, DMAP, dry MeCN, (ii) TMG; (**c**) (i) TFA, (ii) succinic anhydrous, pyridine, N_2 atmosphere; (**d**) (i) NaOH (1 M), 1,4-dioxane, (ii) HCl (1 M); **e**) i) TFA, ii) Boc-Phenylalanine, HBTU, TEA, MeCN.

Protected dehydrodipeptide **12** was synthesised following a sequence similar to that described for dehydrodipeptide **4**. Deprotection and succinoylation afforded hydrogelator **13** in 71 % isolated yield. Saponification of compound **13** under the conditions described for hydrogelator **8** and **5** afforded the dicarboxylic acid hydrogelator **14** in 89 % isolated yield. Dehydrotripeptide **16** was synthesised from the common intermediate **12** in 2 steps involving deprotection and coupling with Boc-Phe followed by deprotection and succinoylation. Dicarboxylic acid hydrogelator **17** was obtained by saponification of compound **16**. ^1H NMR spectra of dehydrotripeptides **14** and **17** are depicted in **Figure 38**. The NMR spectra of hydrogelators **13** and **16** are depicted in **annex Figure A1**.

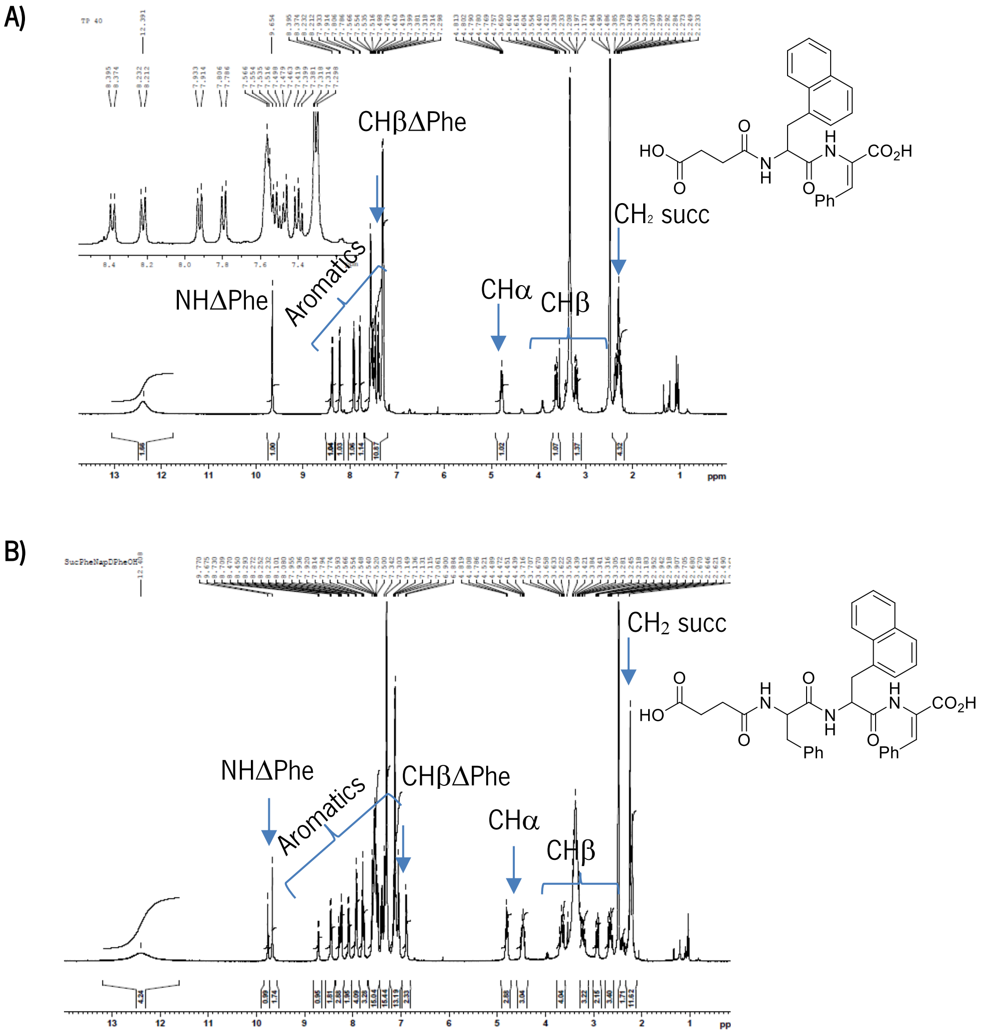

Figure 38 ${}^{1}H$ (**A**) and **B**)) NMR spectra of hydrogelators **14** and **17**, respectively.

The NMR spectra of hydrogelators **14** and **17** were fully assigned by HMQC and HMBC bidimensional techniques.

The focused library of synthesised compounds allows comparing the effect of peptide sequence and composition on the self-assembly, gelation and properties of the hydrogels.

Direct comparasion of hydrogelators **5** and **6** with hydrogelators **13** and **14** can allow to deduce the effect of sequence PheΔPhe vs NapΔPhe on the self-assembly, gelation and properties of the hydrogels. Comparasion of dehydrotripeptides **8** and **9** with hydrogelators **16** and **17** can allow to infer the effect of the sequence on the self-assembly and on the properties of the hydrogels. In fact, hydrogelators **8/9** and **16/17** are isomeric, wich might give insight into the effect of the *motif* PheΔPhe (hydrogelators **8/9**) on the self-assembly and properties of their hydrogels.

Synthesis of Gd^{3+} complexes

Gd^{3+} complexes were prepared for incorporation (co-assembly) into the dehydropeptide-based hydrogels. Paramagnetic hydrogels were studied as potential CAs for MRI (**Figure 39**).

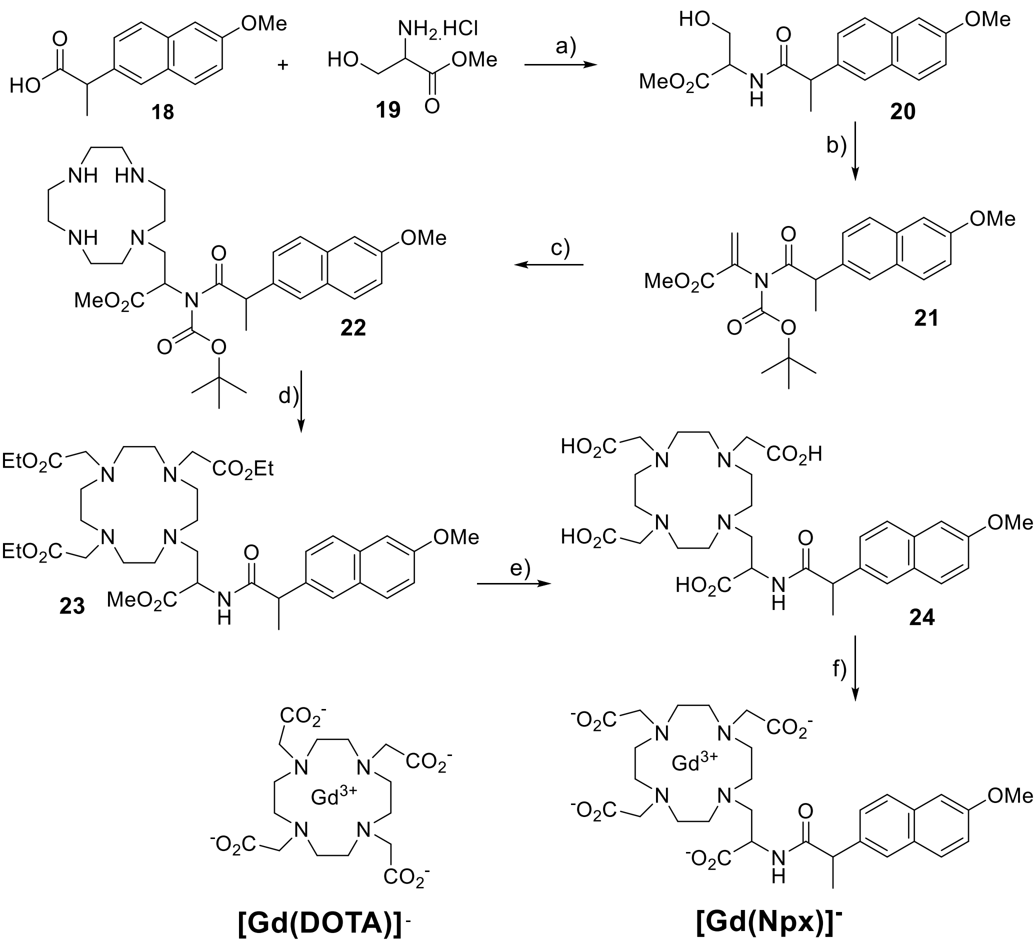

Figure 39 Preparation of the Gd^{3+} complex Gd(Npx) and representation of the Gd(DOTA) complex structure, for incorporation into hydrogels. Experimental conditions: **a)** DCC/HOBT, TEA, DCM; **b)** Boc_2O/DMAP, MeCN; **c)** Cyclen, K_2CO_3/MeCN; **d)** i. TFA/DCM; ii. K_2CO_3, MeCN; iii. ethyl bromoacetate; **e)** i. Dowex-1X2-OH^- H_2O/EtOH; ii. elution with HCl (0,1M); **f)** $GdCl_3$.

The complex $[Gd(DOTA)]^-$ was prepared using the commercially available ligand Na_4(DOTA) and the Gd salt $GdCl_3.6H_2O$, as an archetypical hydrophilic complex.[74] A new complex Gd(Npx) was prepared for evaluating the effect of complex hydrophobicity on the co-assembly with hydrogelators and on the properties of the co-assembled hydrogels as CAs for MRI. The macrocyclic DO3A-type ligand **24**, bearing a pendant propionate arm functionalised with a naproxen (Npx) moiety (naproxen is a non-steroidal anti-inflammatory drug) was prepared following methodologies described by the research group.[60,58,75] Michael addition of dehydroamide **21** to *cyclen* is the key step in this synthetic route (**Figure 40**).

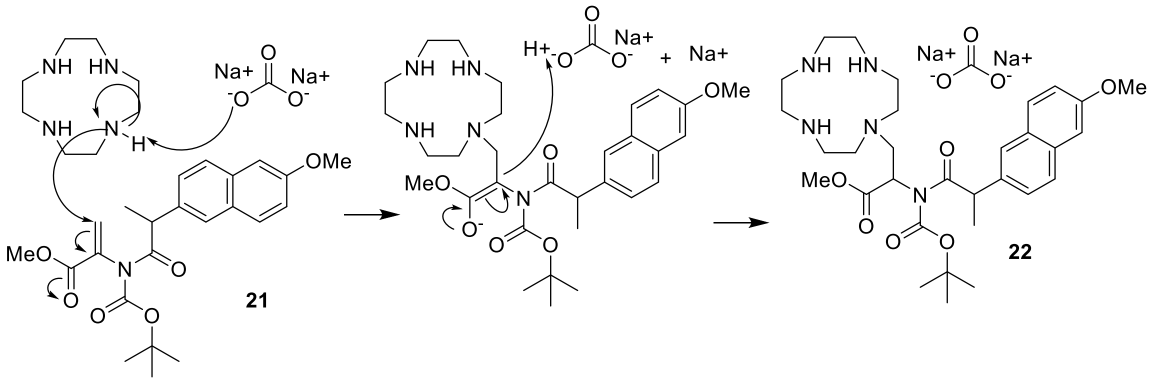

Figure 40 Mechanism for Michael addition of cyclen to dehydroamides.

An excess of *cyclen* (1.5 mol eq) was used to warrant (statistical) mono-functionalization. Boc-amide **21** was prepared in 2 steps following a methodology similar to the one reported above for the preparation of the dehydropeptide hydrogelators. The Boc-amide group on dehydroamide **21** is essential for making it a powerful electrophile in the Michael addition reaction to *cyclen*. The dehydration reaction of amide **20** was carried out with excess Boc_2O (3 molar equivalents) and DMAP (10 % mol) resulting in one pot dehydration and introduction of the Boc-amide group. Mono-functionalised cyclen **22** was per-alkylated with ethyl bromoacetate in acetonitrile using K_2CO_3(s) as base to afford pro-chelator **23**. Npx-conjugate chelator **24** was obtained by saponification of the ester groups with DOWEX-1X2-OH^- resin. The chelator was fully characterised by ^1H spectroscopy and HRMS. (**Figure 41**).

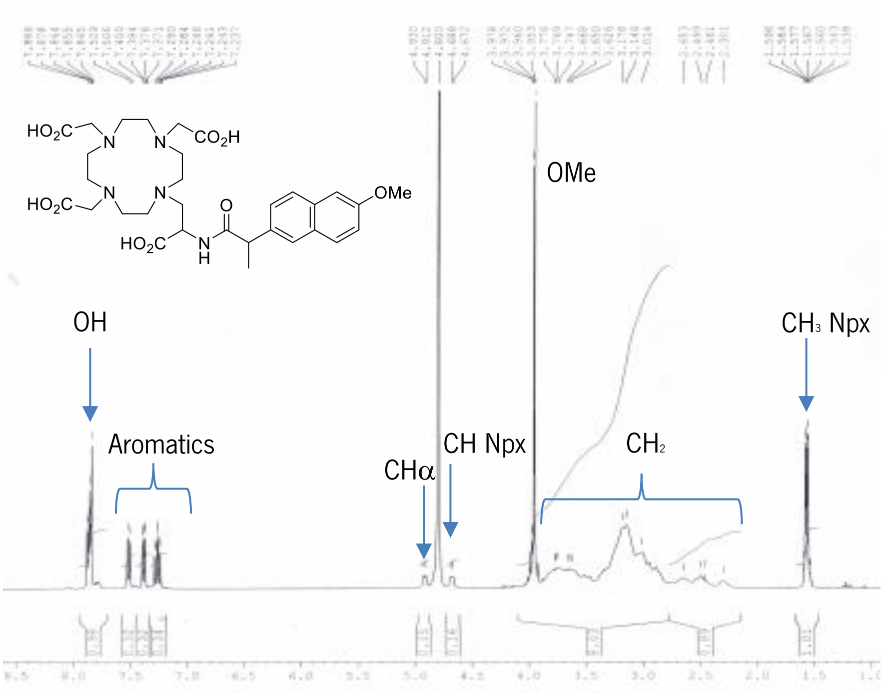

Figure 41 ^{1}H NMR spectrum of the Npx-conjugate DO3A-type chelator **24**.

The NMR spectrum (**Figure 41**) was acquired to the Gd-Npx ligand and all the signals were attributed by the HMBC and HMQC techniques.

2.2 Preparation of hydrogels

Hydrogels were prepared using the *D*-glucono-δ-lactone (GdL) pH drop methodology as reported before by the research group for other dehydropeptide based hydrogels.[23] Hydrogelator suspensions in water were initially adjusted to pH 9 - 10 with NaOH 1 M under magnetic stirring to ensure hydrogelator solubilization. Gelation was triggered by addition of GdL and brief stirring (30 seconds). Solutions were left undisturbed at room temperature over night to allow gelation. Hydrogel formation was confirmed by tube inversion. In this type of experiments the hydrogelator and GdL concentrations are typically reported in *wt*% (% m/v; mg/ml). This notation was adopted in this work and will be used hereafter.

An experimental protocol (see **annex Figure A3**) was set up to determine the optimal gelation conditions. The concentration of the hydrogelators and of the GdL was varied independently in the range 0.05 - 0.4 *wt*% and 0.1 - 0.6 *wt*%, respectively (**Figure 42**).

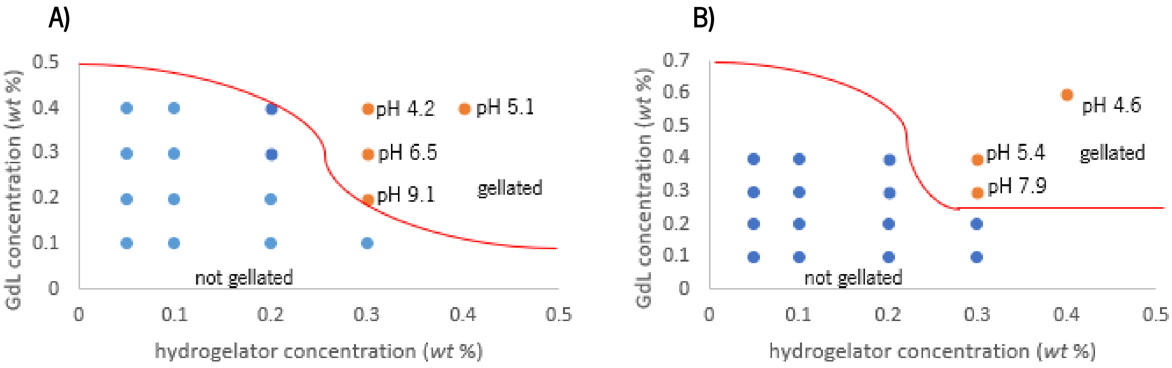

Figure 42 Illustrative phase diagrams for hydrogelation: **A)** hydrogelator suc-NapPheΔPheOMe (**8**); **B)** hydrogelator suc-NapPheΔPheOH (**9**).

The phase diagrams obtained for hydrogels suc-NapPheΔPheOMe (**8**) (**Figure 42A**) and suc-NapPheΔPheOH (**9**) (**Figure 42B**) are illustrative of the gelation conditions found for the methyl ester protected and for the dicarboxylic acid gelator families, respectively (see **annex Figure A4** for the phase diagrams of hydrogelators **5, 6, 13** and **14**). The methyl-ester protected hydrogelators (**5**, **8**, **13** and **16**) afford hydrogels in the concentration range 0.3 - 0.4 *wt* %. In this concentration range hydrogel pH decreases with increasing amounts of GdL. Hydrogels in the physiological pH range can be obtained using equivalent amounts of hydrogelator and GdL. Hydrogels can be obtained also for the dicarboxylic acid hydrogelators (**6**, **9**, **14** and **17**) in the concentration range 0.3 - 0.4 *wt* %. An excess amount of GdL, *circa* 1.5 mass equivalents, is required for gelation. Hydrogel pH decreases with increasing amounts of GdL. Being able to prepare hydrogels with pH values within the physiological pH range is important for prospective *in vitro* and *in vivo* applications. Moreover, gel elasticity is also fundamental for prospective apllications. The gelation studies suggest that hydrogel elasticity increases with hydrogelator concentration. This trend was confirmed by rheological studies (see rheology section). Previous studies from our research group revealed that incorporation of SPION into naproxen *N*-capped dehydropeptide-based hydrogels leads to delayed gelation kinetics and a significant reduction of elasticity. High SPION concentration even prevent gelation.[15] Therefore, anticipating this problem we decided to perform all further studies with hydrogels at 0.4 *wt* % concentration despite slightly acidic pH values. The critical gelation concentration and the best gelation conditions established for the hydrogels are summarized in **Table 2**.

Table 2 Critical gelation concentration (*cgc*) and pH value for hydrogels prepared at 0.4 *wt*%.

Hydrogelator	*cgc* (*wt*%)	GdL (*wt*%)	pH	*wt*%	GdL (*wt*%)	pH
suc-PheΔPheOMe (5)	0.3	0.3	5.7	0.4	0.4	5.5
suc-PheΔPheOH (6)	-	-	-	0.4[b]	0.6	-
suc-NapΔPheOMe (13)	0.3	0.3	5.2	0.4	0.4	5.1
suc-NapΔPheOH (14)	0.3	0.4	5.2	0.4	0.6	4.7
suc-NapPheΔPheOMe (8)	0.3	0.3	6.5	0.4	0.4	5.1
suc-NapPheΔPheOH (9)	0.3	0.4	5.4	0.4	0.6	4.6
suc-PheNapΔPheOMe (16)	0.3	0.3	6.2	0.4	0.4	5.7
suc-PheNapΔPheOH (17)	0.3	0.4	5.3	0.4	0.6	4.6

[b] gel was not formed at the highest hydrogel concentration tested, 0.4 *wt*%.

All hydrogelators, except dipeptide suc-PheΔPheOH (**6**), afforded hydrogels at 0.4 *wt* % concentration as assessed by the inverted tube test (**Figure 43**).

Figure 43 Inverted tube test for hydrogels at 0.4 *wt*% concentration (see **Table 2**). Order of the hydrogels, from left to right: **16**, **17**, **8**, **9**, **13**, **14**, **5**.

Dicarboxilic acid dipeptide suc-PheΔPheOH **(6)** fails to gellate at 0.4 *wt* % concentration, presumably due to too low hydrophobicity comparing to its *C*-protected counterpart suc-PheΔPheOMe (**5**) (LogP 1.81 *vs* 2.42). This is in accordance with literature reports which suggest a hydrophobicity threshold of LogP > 2.6 for peptide self-assembly and formation of self-support hydrogels between 2.6 < LogP < 5.5.[76] The contribution of aromatic π-π stacking interactions seems not to be the limiting factor for self-assembly as hydrogelators **5** and **6** display the same number of aromatic moieties. The naphthylalanine dipeptide suc-NapΔPheOH (**14**), significantly more hydrophobic than hydrogelator **6** (LogP 2.97 *vs* 1.81) affords a hydrogel under the same conditions. Beyond, higher hydrophobicity hydrogelator suc-NapΔPheOH (**14**) is also likely to establish more effective intermolecular π-π stacking interactions than compound **6.** It is difficult to disentangle the contribution of the different non-covalent interactions to self-assembly.

2.3 Preparation of magnetic hydrogels with incorporated SPION

In previous works our research group demonstrated that peptide-based self-assembled hydrogels acquire magnetic properties by incorporation of SPION. SPION endow hydrogels with MRI reporting properties - as efficient CAs for MRI, associated to magnetic hyperthermia and hyperthermia-triggered drug delivery. We proposed that magnetic hydrogels could find relevant biological applications as theranostic cancer agents - allying MRI tumour monitoring to hyperthermia and hyperthermia-triggered drug delivery capabilities.[15] *In vivo* applications of magnetic hydrogels as tumour theranostics can conceptually be accomplished by hydrogel implantation in the tumour resection cavity after surgery, or direct injection into the tumour.[6] Hydrogel implantation allows following the regeneration of the tumour cavity by MRI and performs on-demand drug delivery to the tumour resection margins to guaranty complete elimination of cancer cells and prevent tumour recurrence.[77,78] Direct injection of a magnetic hydrogel loaded with an antitumor drug into the tumour could conceptually allow on-demand synergistic hyperthermia and hyperthermia-triggered drug-deliver (thermo-chemotherapy) combined with MRI monitoring of the therapeutic efficacy. Both tumour implantation and direct injection require hydrogels with injectable properties.[79]

In this Thesis we studied the effect of SPION incorporation on the rheological, MRI reporting and magnetic hyperthermia properties of succinate *N*-capped hydrogels (**5**, **6**, **8**, **9**, **13**, **14**, **16** and **17**) towards the development of injectable self-assembled hydrogels as tumour theranostic platforms.

Superparamagnetic iron oxide nanoparticles (SPION) coated with a polyacrylic acid (PAA) organic shell was used for incorporation into the hydrogels (**Figure 44** and **Table 3**).

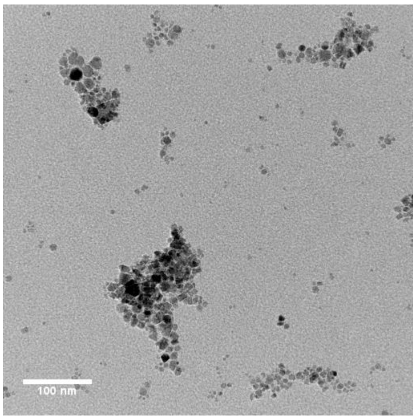

Figure 44 TEM image of the SPION used for incorporation into hydrogels. Scale bar 100 nm.

Table 3 Physico-chemical properties of the SPION used for hydrogel incorporation.

Composition	**Core size (nm)**	**Hydrodynamic Diameter (HD) (HD; nm)**	**Zeta potential (mV)**	**Saturation Magnetisation (M_s; emu/g)**
Fe_3O_4 Magnetite	8	108	- 87.2	88.9

The SPION were used as prepared by the group of Dr. Manuel Bañobre at INL, Braga. The PAA shell endows the nanoparticles with a highly negative zeta potential (- 87.2 mV at pH 7.0) as result of ionization of the carboxylic acid groups. The zeta potential together with the thickness of the PAA shell (steric and electrostatic repulsion) ensures nanoparticle stability in the physiological pH range and under applied magnetic fields. The small (*circa* 8 nm), single domain, magnetite core of the SPION, ensures superparamagnetic properties at room temperature and endows the nanoparticles with dual $T_{1/2}$ MRI reporting properties. The saturation magnetisation of the nanoparticles (88.9 emu/g) is within the range expected for magnetite nanoparticles within this size with high structural quality.

Hydrogels with incorporated SPION were prepared using the GdL pH dropping methodology as described for the non-magnetic hydrogels. The SPION solution was added to pH (9 - 10) adjusted hydrogelator solutions, followed by GdL-triggered gellation. The amount of SPION incorporated into the hydrogels is reported throughout this Thesis as $wt\%_{Fe}$ in relation to the hydrogelator mass ($m_{Fe}/m_{Hydrogelator}$, %).

2.4 Self-assembly studies

UV-Vis and Fluorescence spectroscopy

UV-Vis spectra were acquired for diluted hydrogelator solutions 0.05 *wt* % in phosphate buffer (0.1 M, pH 7.0) in the wavelength range 200 - 400 nm (**Figure 45**).

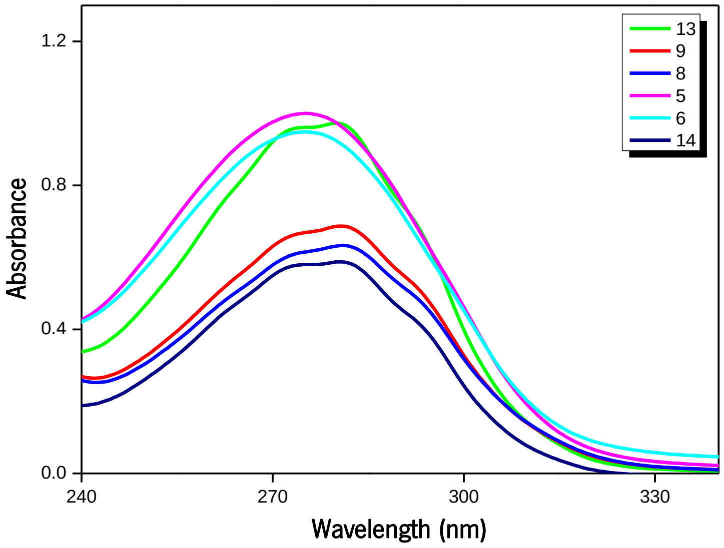

Figure 45 UV-Vis spectra (phosphate buffer, 0.1 mM, pH 7.0) for hydrogelators **5**, **6**, **8**, **9**, **13** and **14** at 0.05 *wt* % concentration.

The UV-Vis spectra of the hydrogelators containing naphthylalanine **8**, **9**, **13** and **14**, with a naphthalene side chain, show a broad absorption band with a fine structure, consisting of two absorption maxima at approximately 272 and 282 nm, attributed to π-π* electronic transitions centred on the aromatic naphthalene group. The dipeptide hydrogelators **5** and **6**, with the PheΔPhe *motif*, show a non-structure broad band with maximum absorption at approximately 276 nm attributed to π-π* electronic transitions centred on the aromatic phenyl group. The molar absorptivity of the hydrogelators seems to be determined both by peptide composition and *C*-terminal deprotection. Interestingly, dehydrodipeptides **5** and **6** bearing the PheΔPhe *motif* and the naphthylalanine protected dehydrodipeptide **13** with the sequence NapΔPhe show the highest absorptivity. Further sequence elongation results in a reduction of the molar absorptivity. This suggests that intramolecular π-π stacking interactions result in absorption reduction.

Fluorescence spectroscopy

pH dependence of hydrogelator´s self-assembly

Fluorescence spectroscopy was used to study the pH dependence of hydrogelator self-assembly, taking advantage of the naphthalene and phenyl groups which can be used as intrinsic fluorescent probes to study molecular aggregation.

Fluorescence spectra (λ_{exc} 280 nm) were acquired (290 - 600 nm) in the pH range 2 - 10 for diluted aqueous solutions of hydrogelators (20 μM) (**Figure 46**). The absorbance of the hydrogelator solutions at the excitation wavelength was kept bellow 0.1 to minimize inner filter effects on fluorescence emission.

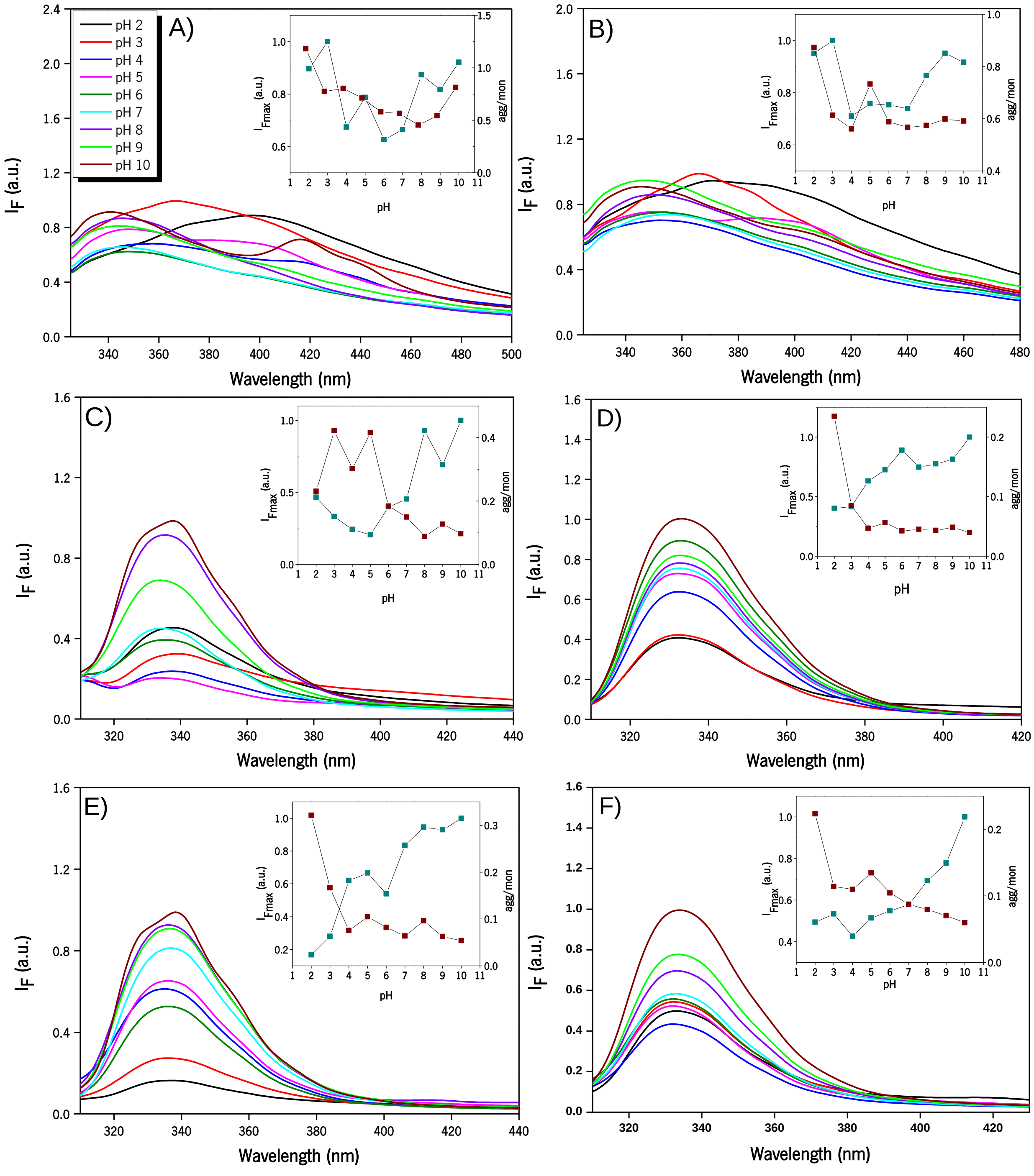

Figure 46 Normalised fluorescence emission spectra (λ_{exc} 280 nm) for hydrogelator solutions (20 μM) in the pH range 2 - 10. Inset: pH dependence of ratio aggregates:monomer (**red squares**) and pH dependence of the intensity of fluorescence maxima (**blue squares**). Hydrogelators: (**A**) suc-PheΔPheOMe (**5**); (**B**) suc-PheΔPheOH (**6**); (**C**) suc-NapPheΔPheOMe (**8**); (**D**) suc-NapPheΔPheOH (**9**); (**E**) suc-NapΔPheOMe (**13**); (**F**) suc-NapΔPheOH (**14**).

Overall, it is noteworthy that the fluorescence emission spectra of the dipeptide hydrogelators suc-PheΔPheOMe/H (**5** and **6**), displaying the PheΔPhe *motif*, show the strongest pH dependence, both in terms of fluorescence intensity and wavelength of maximum emission (**Figure 46A** and **46B**). The fluorescence emission spectra of the dipeptide suc-NapΔPheOMe/H (**13** and **14**) (**Figure 46E** and **46F**) and the tripeptide hydrogelators suc-NapPheΔPheOMe/H (**8** and **9**) (**Figure 46C** and **46D**), bearing the naphthylalanine residue, display weaker pH dependence. The fluorescence emission spectra of hydrogelators **5** and **6** display in the pH range 4 - 10 a main band at 350 nm assigned to the monomer state and a second, less intense band at 420 nm, assigned to the aggregates state (**Figure 46A** and **46B**). The monomer band shows *bathochromic* shift for pH values bellow 4. The pH dependence of the intensity ratio for the aggregates/monomer bands suggests onset of aggregation at pH values around 5 (inset in **Figure 46A** and **46B**). The fluorescence emission spectra of the hydrogelators bearing the naphthylalanine residue (**8**, **9**, **13** and **14**) show similar features: a main band broad at 350 nm, attributed to the monomer state and a much weaker broad band at 420 nm assigned to the aggregates state (**Figure 46C**, **46D**, **46E** and **46F**). The pH dependence of the intensity ratio for the aggregates/monomer bands shows a steep increase for pH values bellow 5 suggesting onset of aggregation at pH 5 (inset in **Figure 46C**, **46D**, **46E** and **46F**). Overall, these results suggest that hydrogelator aggregation is driven by protonation of the carboxylic acid group(s) of the hydrogelator molecules.

Circular Dichroism

Circular Dichroism (CD) spectroscopy is a well-established biophysical tool used to characterize the secondary structure of proteins in solution. This technique is based on the differential absorption of left-handed and right-handed circularly polarised light by chromophores with chiral or asymmetric elements or in chiral environments. The sum of the conformational amide signals of the peptide backbone in the wavelength range 190 - 240 nm results in a spectrum characteristic of the secondary structure (**Figure 47**).[80] α-Helices are characterized by two negative minimums at 208 nm and 222 nm, with equivalent intensity, and a stronger positive maximum at 192 nm, while β-sheets are characterized by a negative minimum at 215 nm and a positive maximum at 198 nm. Random coils display an inverted spectrum, showing a negative minimum at approximately 200 nm and a weak positive maximum at 215 nm. The CD bands originate from π-π* and n-π* transitions at around 200 and 220 nm.[80]

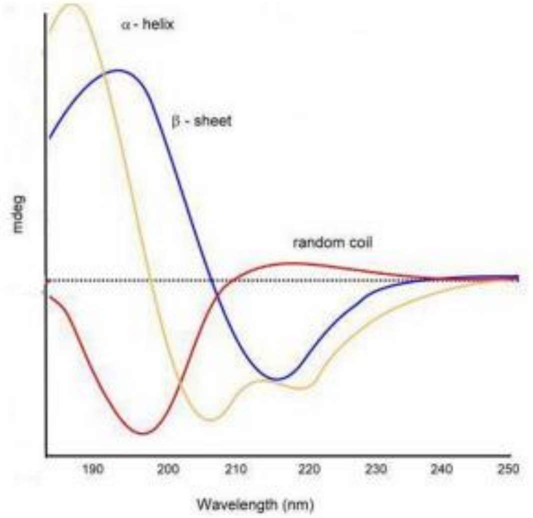

Figure 47 Typical CD spectra for protein secondary structures: α-helix (yellow line), β-sheet (blue line) and random coil (red line).[103]

The hydrogelator samples for CD spectroscopy were prepared by the GdL gelation procedure as described above. CD spectra were acquired with hydrogelator concentrations 0.01 *wt* % due to instrument limitations (**Figure 48**).

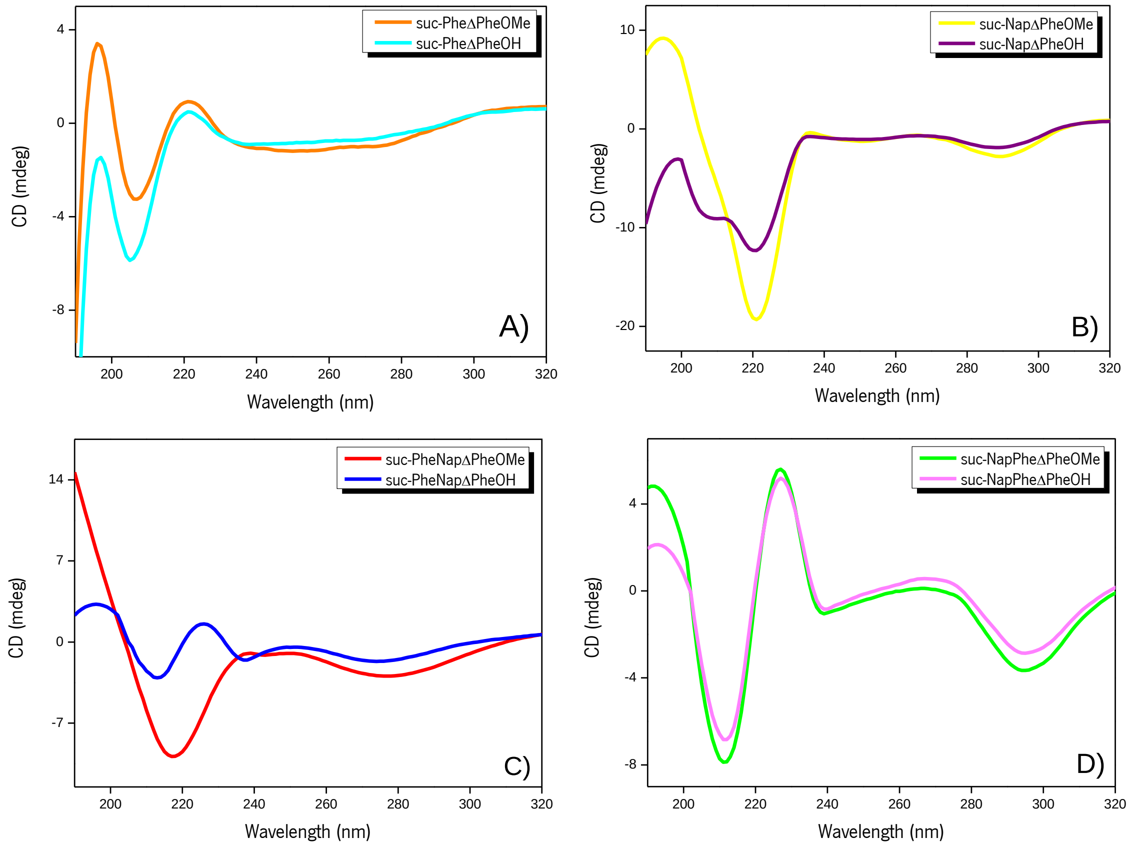

Figure 48 CD spectra of diluted hydrogelator solutions (0.01 *wt* %): (**A**) suc-PheΔPheOMe/H (**5**/**6**); (**B**) suc-NapΔPheOMe/H (**13**/**14**); (**C**) suc-PheNapΔPheOMe/H (**16**/**17**); (**D**) suc-NapPheΔPheOMe/H (**8**/**9**).

In general, with exception of the tripeptide couple suc-PheNapΔPheOMe/H (**16** and **17**) (**Figure 48C**), the deprotection of the *C*-terminal methyl ester group seems to have only a minor effect on the CD spectra of hydrogels with the same sequence, suggesting a similar secondary structure. For the hydrogelator couple suc-PheΔPheOMe/H (**5** and **6**) (**Figure 48A**) the negative minimum at 205 nm and a weak maximum at 220 nm suggests that the peptide backbone adopts predominantly a random coil secondary structure with some minor β-sheet contribution, indicated by the positive maximum at 197 nm. Interestingly, for the hydrogelator couple suc-NapΔPheOMe/H (**13** and **14**) (**Figure 48B**), the positive maximum at approximately 200 nm and the negative minimum at 220 nm suggest predominance of β-sheet secondary structure. The tripeptide hydrogelators suc-PheNapΔPheOMe/H (**16** and **17**) have significantly different CD spectra. The negative minimum at 219 nm in the CD spectrum of hydrogelator **16** is a characteristic β-sheet signature. The CD spectrum of the *C*-protected analogue **17** shows a positive maximum at 200 nm and a negative minimum at 214 nm typical of of β-sheets. The positive maximum at 227 nm suggests random coil contribution to the secondary structure. The CD spectra of both tripeptides suc-NapPheΔPheOMe/H (**8** and **9**) (**Figure 48D**) exhibit a positive maximum at 194 nm and a negative minimum at 214 nm, corresponding to β-sheets with some random coil contribution from the peak at 229 nm.

The CD spectra of the naphthyalanine di- and tri-peptide hydrogelators display a broad band around 280 - 290 nm assigned to chiral naphthalene-centred π-π* transitions, observed also for naproxen *N*-capped dehydropeptides.[23] This band has a minimum around 280 nm for the hydrogelator pair suc-PheNapΔPheOMe/H (**Figure 48C**). *Bathochromic* shift, to minimum around 295 nm, accompanied by intensity enhancement, is observed for the hydrogelators suc-NapΔPheOMe/H (**13** and **14**) (**Figure 48B**) and suc-NapPheΔPheOMe/H (**8** and **9**) (**Figure 48D**). This suggest enhanced π-π stacking and chiral ordering of the naphthalene moieties on the *terminal* naphthylalanine hydrogels comparing to the *interior* naphthylalanine hydrogels.

Owing to instrumental limitations, the CD spectra were acquired with hydrogelator concentrations (0.01 *wt* %) well-below the *cgc* (around 0.3 *wt* %). Therefore, the secondary structure determined by CD is not truly representative of the gel phase but describes the secondary structure of self-assembled fibrils in solution. Increasing the hydrogelator concentration beyond the *cgc* is likely to result in progressive ordering of the β-sheet elements, already seen in the fibrils in solution and a β-sheet secondary structure for the hydrogels. FTIR and Raman spectroscopy experiments, using fully formed hydrogels, can clarify the secondary structure adopted by the hydrogelator molecules on the self-assembled hydrogel fibrils.[24]

2.5 Hydrogel microstructure

The micro- and nanostructure of the hydrogels was characterized by Scanning Transmission Electron Microscopy (STEM). The effect of SPION incorporation on the microstructure of the hydrogels was studied using 0.4 *wt* % hydrogel samples with 14 *wt* % ($m_{Fe}/m_{hydrogelator}$, %) incorporated SPION (**Figure 49**).

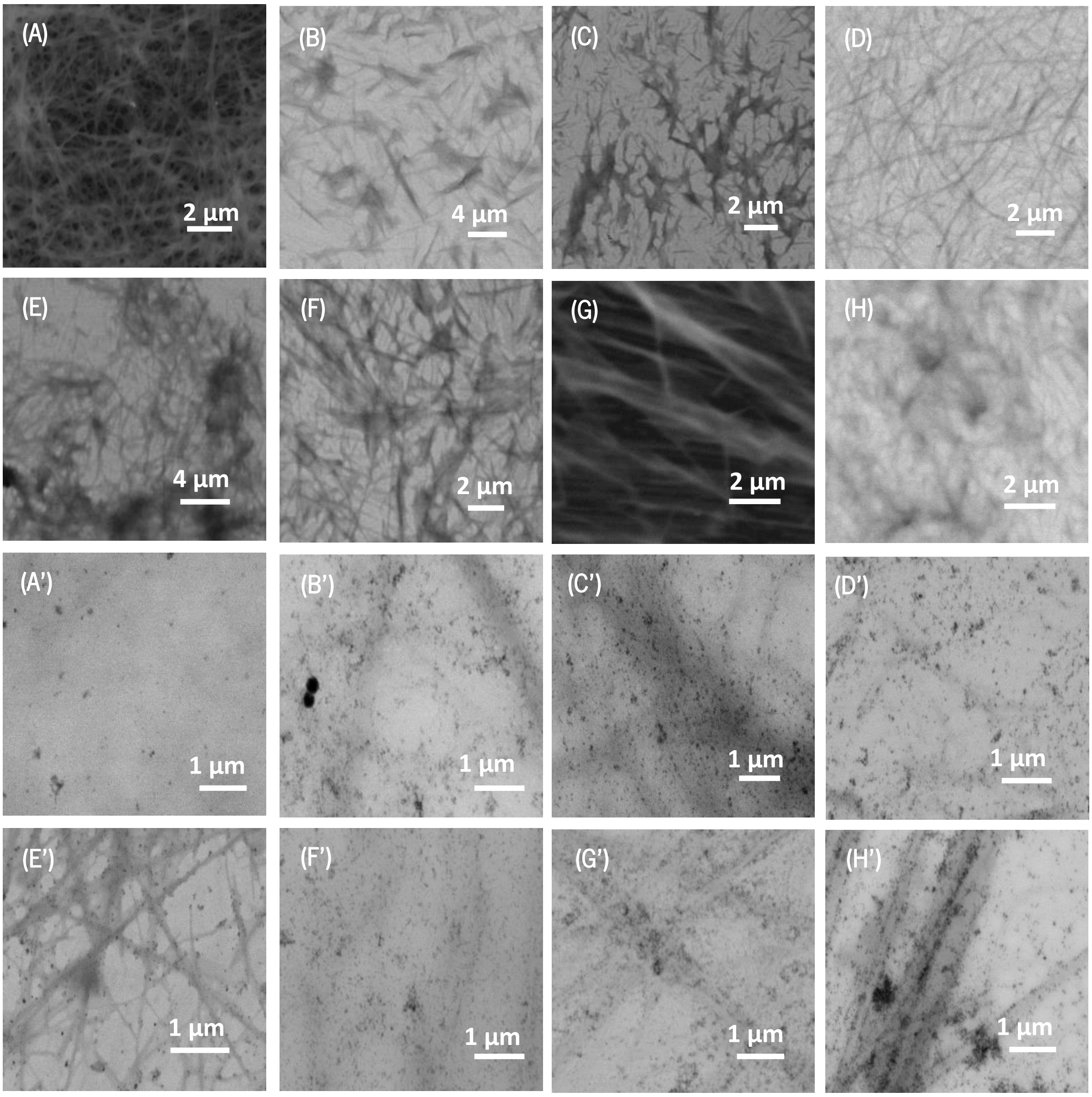

Figure 49 STEM images of (pristine) hydrogels at 0.4 *wt* %: (**A**) suc-NapΔPheOMe (**13**); (**B**) suc-NapΔPheOH (**14**); (**C**) suc-NapPheΔPheOMe (**8**); (**D**) suc-NapPheΔPheOH (**9**); (**E**) suc-PheNapΔPheOMe (**16**); (**F**) suc-PheNapΔPheOH (**17**); (**G**) suc-PheΔPheOMe (**5**); and STEM image of the hydrogelator with 0.4 *wt* % solution: (**H**) suc-PheΔPheOH (**6**). The hydrogels with incorporated SPION (14 *wt* %) are represented by the same word with X'.

STEM images, truly representative of the gel phase, were recorded using hydrogel samples (0.4 *wt* %) deposited onto TEM mesh copper grids. All hydrogels display a fibrilar network although with significant differences regarding fibre thickness, length, entanglement and network density. Hydrogel suc-NapΔPheOMe (**13**) (**Figure 49A**) shows higher density of longer and thinner fibrils, with an average thickness of 35 nm, than its *C*-deprotected counterpart suc-NapΔPheOH (**14**) (**Figure 49B**), composed by a less dense network of shorter and thicker fibres, with an average thickness of 120 nm. For the tripeptide hydrogels suc-NapPheΔPheOMe/H (**8**/**9**) (**Figure 49C/D**), bearing the PheΔPhe *motif*, the dicarboxylic acid suc-NapPheΔPheOH (**9**) (**Figure 49D**) shows a dense network of elongated and thin fibrils (thickness *circa* 25 nm) while the *C*-protected hydrogel suc-NapPheΔPheOMe (**8**) (**Figure 49C**) shows a dense network of thicker fibrils (length *circa* 300 nm and thickness around 28 nm). The tripeptide suc-PheNapΔPheOMe (**16**) (**Figure 49E**) originates hydrogels with thin (*circa* 20 nm diameter) and short fibrils which form agglomerates. Its dicarboxylic acid counterpart suc-PheNapΔPheOH (**17**) (**Figure 49F**) shows a dense network of thin fibrils with an average thickness of 22 nm. The hydrogelator suc-PheΔPheOMe (**5**) (**Figure 49G**) forms a hydrogel with a dense network of seemingly laterally organized tick fibrils (average thickness 29 nm). The viscous solution of hydrogelator suc-PheΔPheOH (**6**) (**Figure 49H**) forms fibrils with an average thickness of 32 nm.

The hydrogels (0.4 *wt* %) with incorporated SPION (14 *wt* %) (all the **Figure 49X'**) retain a fibrilar structure as seen for the pristine hydrogels. There is some evidence of SPION aggregation revealed by the *fractal*-like appearence of the SPION in the images.[81] Interestingly, SPION distribution within the hydrogels seems non-homogeneous, suggesting SPION association with the hydrogel network fibrils.

2.6 Rheological characterization of hydrogels: elasticity, thermal behavior and structural healing after break-up

An experimental protocol was set up to probe gelation kinetics, determine gel elasticity and characterize their thermal sensitivity and self-healing properties, after mechanical breakdown. The steps of the experimental protocol, implemented for characterization of pristine hydrogels (0.4 *wt* %) and hydrogels with incorporated SPION (0.4 *wt* %,14 *wt* $\%_{Fe}$) are illustrated for hydrogelator suc-PheΔPheOMe (**5**) (**Figure 50**).

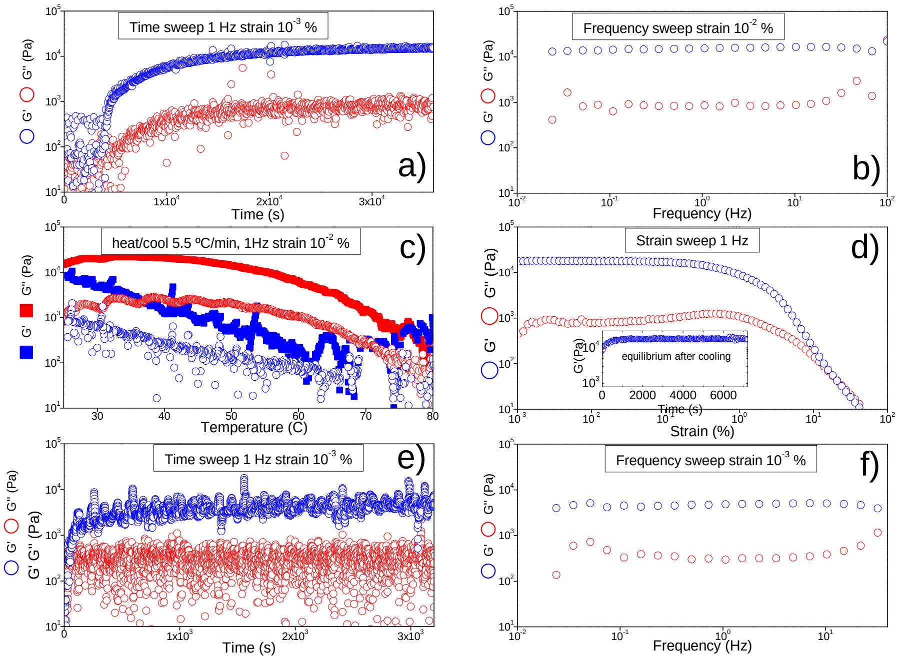

Figure 50 Detailed experimental protocol implemented for the characterization of pristine hydrogels and hydrogels with incorporated SPION (14 *wt* %), illustrated with hydrogelator suc-PheΔPheOMe (**5**): (**a**) gelation kinetics; (**b**) gel elasticity determination; (**c**) thermal sensitivity characterization; (**d**) self-healing properties after mechanical breakdown; (**e**) structural recovery; (**f**) frequency sweep.

Hydrogelator solutions (0.4 *wt* %) were obtained by adjusting under magnetic stirring, water suspensions of hydrogelators to pH *circa* 9 - 10 with NaOH (1 M). Gelation was triggered by addition of GdL followed by immediate loading into the Couette geometry (gap 0.5 mm) of a stress control rotational rheometer (MCR300, Anton Paar). A pre-shear step, consisting on the application of a steady shear rate of 5 s^{-1} for 60 s, was followed by gel setting for 10 hours. Gel setting was monitored by applying a small amplitude oscillatory strain of 10^{-3} % at 1 Hz (**Figure 50a**). The gel setting kinetics was quantitatively described by the parameter t_{half} - time required for the elastic shear modulus G' to attain half of the equilibrium value - G_{eq}. The elastic shear modulus G' (at 1 Hz) was determined from the frequency sweep experiment performed on the equilibrated gel (**Figure 50b**). Next, a thermal cycle (**Figure 50c**) is followed by a 2 h equilibrium period at 25 ° C for allowing gel setting (inset in **Figure 50d**). The thermal reversibility of the gels is quantified by the difference G_{eq} - G_0 (recover time). G_0 (measured at 1 Hz) is the elastic modulus of gels, measured after the 2 hours rest at 25 °C (**Figure 50d**). The strain sweep experiment is also used to compute the critical strain (S_c – mechanical resistance) for gel break-up, defined as the strain where $G'' = G'$, corresponding to a gel-to-solution phase transition, i.e. fluidization of the elastic network in gels. The gel break-up is followed by a structural recovery period which is monitored for 1 hour (**Figure 50e**). The recovery time (t_r) of the gel is defined as the time required for G' to reach 50 % of its equilibrium value following recovery. The elasticity of the healed gel is measured by the elastic modulus G_r (at 1 Hz) during the frequency sweep experiment (**Figure 50f**) and the healing (H – mechanical recovery) of the gel is quantified by $H = G_r / G_0$. A thermo-mechanical healing parameter TMH can be computed by comparing the elastic moduli of equilibrated gels (G_{eq}) and of gels recovered after the strain-induced structural break-down (G_r). The parameter $TMH = G_r / G_{eq}$ offers a comparison between the mechanical spectra of "fresh" and thermo-mechanically treated gels.

The effect of the chemical structure of the hydrogelator molecules on the kinetics of gel structural build up was measured by the characteristic time t_c. Exponential (**Equation 13**) and sigmoidal (**Equation 14**) growth models[82], were used to fit the experimental time dependence of the elastic shear modulus $G'(t)$ to obtain the characteristic time t_c:

$$G'(t) = A + Be^{\frac{-t}{t_c}} \qquad \textbf{Equation 13}$$

$$G'(t) = \frac{\mathrm{A}}{1+\mathrm{e}^{-k(t-t_c)}} \qquad \textbf{Equation 14}$$

Hydrogelator suc-PheNapΔPheOMe (**16**) displays fast gel setting kinetics comparing to all other hydrogelators. A lag time, before the rise in the shear elastic modulus G', which characterizes the slower gel kinetics of all other hydrogelators, is not observed for hydrogelator suc-PheNapΔPheOMe (**16**) (see **annex Figure A5.1**). Accordingly, the gel setting kinetics of compound suc-PheNapΔPheOMe (**16**) was fitted to the exponential model – (**Equation 13**) whilst the kinetic data for all other compounds were fitted to the sigmoidal model (**Equation 14**).

The complete data set for the rheological characterization of pristine hydrogels (0.4 *wt* %, without SPION) and hydrogels with incorporated SPION (0.4 *wt* %, 14 *wt* $\%_{Fe}$) regarding elasticity, thermal behavior and structural healing after break-up, is compiled in **Table 4**.

Table 4 Data for the rheological characterization of pristine hydrogels (0.4 *wt* %, without SPION) and hydrogels with incorporated SPION (0.4 *wt* %, 14 *wt* $\%_{Fe}$).

Hydrogel	t_c (min)	G_{eq} (kPa)	G_{eq} – G_0 (kPa)	S_c (%)	H (%)	TMH (%)	t_r (sec)
suc-PheNapΔPheOMe(16)	121 ± 4[a]	1.2 ± 0.05	-0.40 ± 0.05	51.9 ± 3.6	35.8 ± 7.9	50 ± 12	70 ± 10
with 14 *wt*% SPION	179 ± 7[a]	0.8 ± 0.02	-0.7 ± 0.05	55 ± 7	18.1 ± 0.9	34.0 ± 1.6	500
suc-PheNapΔPheOH(17)	216 ± 1[b]	102.3 ± 5.7	92 ± 5.6	39.1 ± 2.7	12.0 ± 0.8	1.2 ± 0.9	250 ± 30
with 14 *wt*% SPION	437 ± 1[b]	18.3 ± 0.2	2.2 ± 0.3	>100	7.6 ± 0.5	6.6 ± 0.5	35
suc-PheΔPheOMe(5)	210 ± 1[b]	14.8 ± 0.1	-2.4 ± 0.5	19.5 ± 1.3	25.7 ± 1.8	31.1 ± 4.0	300 ± 20
with 14 *wt*% SPION	494 ± 2[b]	19.9 ± 0.7	-44 ± 1	69 ± 5	67.5 ± 2.5	217 ± 15	80
suc-PheΔPheOH(6)	n.a.	n.a	n.a.	n.a.	n.a.	n.a.	n.a.
with 14 *wt*% SPION	no gel	-	-	-	-	-	-
suc-NapPheΔPheOMe(8)	367 ± 1[b]	151 ± 1	140 ± 1	45 ± 3	26.1 ± 1.1	1.8 ± 0.5	370 ± 10
with 14 *wt*% SPION	346 ± 1[b]	116 ± 1.3	98.4 ± 0.8	90 ± 5	6.9 ± 0.3	1.1 ± 0.1	1000 ± 100
suc-NapPheΔPheOH(9)	213 ± 1[b]	45.7 ± 1.6	41.3 ± 1.4	1.1 ± 0.1	22.8 ± 1.7	2.2 ± 0.5	1000 ± 100
with 14 *wt*% SPION	364 ± 1[b]	175 ± 2	163	42 ± 6	40.4 ± 1.1	2.7 ± 0.1	500 ± 100
suc-NapΔPheOMe(13)	212 ± 1[b]	15.5 ± 0.7	-3.9 ± 0.65	63.7 ± 8.5	20.1 ± 0.3	25.2 ± 1.4	300 ± 30
with 14 *wt*% SPION	116 ± 1[b]	5.6 ± 0.1	-10 ± 0.2	55 ± 8	19.5 ± 0.5	7 ± 0.1	140 ± 50
suc-NapΔPheOH(14)	424 ± 2[c]	2.01 ± 0.01	1.5 ± 0.01	>100%	14 ± 2	25.0 ± 0.5	n.a.
with 14 *wt*% SPION	>500	0.45 ± 0.03	0.20 ± 0.04	31 ± 5	20 ± 5	11 ± 3	n.a.

[a]: from fit of equation (**13**) to data [b]: from fit of equation (**14**) to data; [c]$t_{1/2}$ estimate

All studied hydrogelators (**5**, **8**, **9**, **13**, **14**, **16** and **17**), except the hydrogelator suc-PheΔPheOH (**6**), gelled within 10 hours. Incorporation of SPION (14 *wt* $\%_{Fe}$) did not preclude gelation of any other hydrogelator in addition to suc-PheΔPheOH (**6**). The hydrogels display elasticity values ranging from 1.2×10^3 Pa to 1.51×10^5 Pa (**Table 4** and **annex Figure A5.4**). Hydrogels exhibit solid like mechanical spectra with frequency independent shear storage modulus G' which is 10 times larger than the loss shear modulus G''. The latter presents a local minimum at larger frequencies which cannot be fully resolved due to the rheometer's mechanical inertia. However, the increase in gel elasticity G' seems to be accompanied by a shift of the local minimum in G'' to larger frequencies. This shift suggests a faster relaxation process for stiffer gels, possibly related with a finer network structure with smaller voids. G' remains larger than G'' in the whole range of tested temperatures indicating that melting, i.e. gel-to-solution phase transition does not to occur during heating. Instead, structural enhancement of the gel elasticity is seen for some hydrogels (suc-PheNapΔPheOMe (**16**), suc-NapΔPheOMe (**13**) and suc-PheΔPheOMe (**5**)) after a thermal cycle, as evidenced by the negative values of the parameter G_{eq}-G_0. In contrast, the thermal cycle weakens significantelly some hydrogels: suc-NapPheΔPheOMe (**8**), suc-NapPheΔPheOH (**9**) and suc-PheNapΔPheOH (**17**), by around one order of magnitude, and to a lesser extent the hydrogel suc-NapΔPheOH (**14**). Overall, the *C*-terminal methyl ester hydrogelators seem to build stronger hydrogels than their *C*-deprotected dicarboxylic acid counterparts. The hydrogelator suc-PheNapΔPheOMe (**16**) is an exception to this trend.

The *C*-protected methyl ester hydrogelators (**5**, **8**, **13** and **16**) originate gel structures more resistant to shear strain than their *C*-deprotected counterparts (**6**, **9**, **14** and **17**), as evidenced by their larger S_c values. The nonlinear viscoelastic behavior of all hydrogels is qualitatively similar: the onset of nonlinearity is signaled by a strain softening where the onset of decrease in G' with strain is associated with a broad local maximum in G'' (**Figure 50d**) reminiscent of the Payne effect, which is the hallmark of many charged elastic matrices.[83] This strain softening is followed by an abrupt drop in both moduli at larger strain. The drop is more pronounced for G' which eventually leads to a crossover point with G'' indicating the fluid-like behavior of the strained gel at a strain S_c. The suc-NapΔPheOH (**14**) hydrogel is an exception to this trend not exhibiting a crossover point between G' and G'' (see in **annex Figure A5.2**).

Interestingly, after the strain-induced structural break down, all samples recover an elastic gel structure within one hour. The *TMH* data overall confirm that the methyl ester hydrogels display higher thermal and mechanical resistance than their *C*-deprotected counterpart hydrogels. Moreover, the thermo-mechanical treatment has very little impact on the structure of the hydrogels showing the best *TMH* values, since the corresponding mechanical spectra can nearly be superimposed by a vertical shift (see **annex figure A5.3**). In contrast, for the hydrogels formed by the *C*-deprotected hydrogelators and the suc-NapPheΔPheOMe (**8**) hydrogel, the structural change induced by the thermo-mechanical treatment relates to a significant shift in the minimum of G'' towards lower frequencies.

The comprehensive rheological characterization of the focused library of dehydropeptide hydrogels prepared in this work demonstrates all hydrogelators, except the dicarboxylic acid suc-PheΔPheOH (**6**), are good candidates for injectable gel applications: the hydrogels rebuild after shear-induced breakup and remain solid-like for temperatures over 37 °C. As a general trend, the *C*-protected methyl ester hydrogels display stronger elasticity, better thermal stability and structural healing after breakup than their dicarboxylic acid *C*-deprotected counterparts. One exception to this trend is the suc-PheNapΔPheOMe (**16**) hydrogel, which exhibits the smallest elastic modulus in the *C*-protected hydrogelator series. However, this hydrogel showed the fastest gellation kinetics, excellent thermal stability (G' and G'' are insensitive to the thermal cycle) and best mechanical healing, within a minute.

The PheΔPhe sequence is a privileged sequence for building hydrogels. Extending the PheΔPhe *motif* with the naphthylalanine amino acid residue significantly improves the hydrogel properties in sharp contrast to the *scrambled* peptide sequence PheNapΔPhe.

The magnetic hydrogels SPION@hydrogels (0.4 *wt* %, 14 *wt* % SPION) were analysed regarding elasticity, thermal behavior and structural healing after break-up (**Table 4**). The results in **Table 4** show that the incorporation of SPION into the succinate *N*-capped hydrogels has a profound effect on their rheological properties. In general, the incorporation of SPION results in significantly slower gel setting kinetics. This effect was reported previously for naproxen *N*-capped hydrogels.[15] SPION incorporation into the *C*-protected hydrogels, suc-NapΔPheOMe (**13**) and suc-NapPheΔPheOMe (**8**), with *N*-terminal 2-naphthylalanine, accelerates gel setting. As a general trend, the mechanical properties (G´) of the hydrogels are weakened by the incorporation of SPION. The hydrogels suc-NapPheΔPheOH (**9**) and suc-PheΔPheOMe (**5**), bearing the PheΔPhe *motif,* are reinforced by incorporation of SPION. While this effect is moderate for the hydrogel suc-PheΔPheOMe (**5**), the elasticity value (G´) for hydrogel suc-NapPheΔPheOH (**9**) is enhanced by a factor *circa* 4 by SPION incorporation. Interestingly, the incorporation of SPION seems not to affect the fibrilar gel structure since the frequency dependence of the shear moduli remains unchanged. The thermal stability is unchanged except for hydrogel suc-NapPheΔPheOH (**9**), where SPION have a stabilizing effect on a hydrogel structure which showed a significant loss of elasticity after the thermal cycle.

Overall, the data set does not allows inferring any peculiar interplay between the chemical structure of the hydrogelator molecules and the effect of SPION on the properties of the hydrogels. Only the hydrogel suc-NapPheΔPheOH (**9**) shows enhanced hydrogel elastic and thermal properties in the presence of SPION.

The effect of hydrogelator concentration (0.2, 0.4 and 0.6 *wt* %) on the rheological properties was studied for the hydrogelator suc-NapPheΔPheOMe (**8**) (see **annex Figure A5.5**) to gain insight into the hydrogel's nano-microstructure. For hydrogelator suc-NapPheΔPheOMe (**8**) higher hydrogelator concentrations result in faster gelation kinetics. A direct relation between hydrogel concentration and elastic modulus G' (at 1 Hz) could not be established - the highest elasticity is attained at 0.4 *wt* % hydrogelator concentration. Nonetheless, the mechanical spectra of the hydrogels at different concentrations, can be superimposed on a single master curve by vertical shifts (*a*) of both storage and loss moduli, indicating the same structure irrespective concentration.

Strain sweeps show softening under large strain, meaning that the hydrogel is composed of a dual network with non-permanent crosslinks between semiflexible fibres with lifetime of the order or faster than the shearing time (1 sec). An alternative hydrogel picture points to flexible filaments giving rise to topological inter connections like entanglements.

2.7 Characterization of (para)magnetic hydrogels as CAs for MRI

The efficacy of magnetic hydrogels, with incorporated SPION, as CAs for T_{2w} MRI was studied by ^{1}H relaxometry (1.5 T, 60 MHz; 37 °C) and MRI (3 T, 120 MHz; 37 °C) measurements- $T_{1,2}$ phantoms and relaxation maps. Paramagnetic hydrogels, with incorporated Gd(Npx) and Gd(DOTA) complexes, were also characterized as potential CAs for T_{1w} MRI by ^{1}H relaxometry (1.5 T, 60 MHz; 37 °C) and MRI (3 T, 120 MHz; 37 °C) measurements - $T_{1,2}$ phantoms and relaxation maps measurements. Water proton longitudinal (T_1) and transverse (T_2) relaxation times were determined for the magnetic and paramagnetic self-assembled hydrogels and for agarose gels (0.5 *wt* %) containing SPION and Gd chelates in the same concentration range.

Relaxivities $r_{1,2}$ (mM^{-1}s^{-1}) were calculated for the (para)magnetic hydrogels from the graphical representation of the concentration dependence of the relaxations rates $R_{1,2}$ (s^{-1}) ($R_{1,2} = 1/T_{1,2}$) on the Fe and Gd concentration in the composite hydrogels. The parameter relaxivity ($r_{1,2}$) measures the enhancement of the relaxations rates $R_{1,2}$ brought about by 1 mM concentration of active centres (Fe or Gd).

2.7.1 Relaxometric measurements

Hydrogels with incorporated SPION

Relaxivity values ($r_{1,2}$ mM^{-1}s^{-1}) were calculated for the magnetic hydrogels, with incorporated SPION, from the concentration dependence of the relaxation rates ($R_{1,2}$) on the Fe concentration 1.4 – 27.9 mM (**Figure 51**).

Figure 51 illustrates the relaxivity determination for the SPION and for magnetic hydrogels suc-NapPheΔPheOMe/H (**8**, **9**) in the Fe concentration range (1.4 – 27.9 mM). The full set of relaxivity values, for all magnetic hydrogels, is summarized in **Table 5** (see **annex figure A8**).

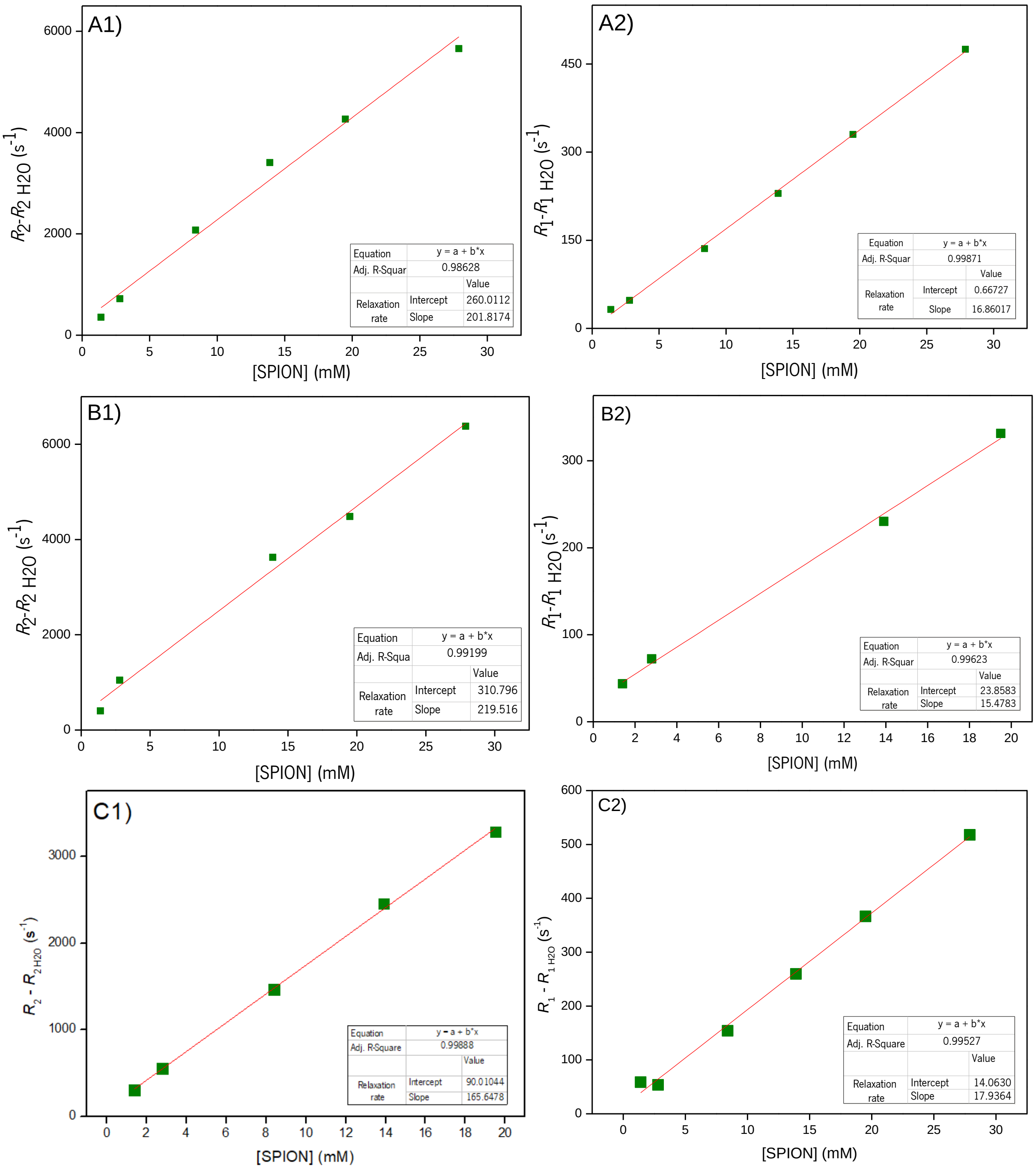

Equation	y = a + b*x	
Adj. R-Squar	0.98628	
		Value
Relaxation rate	Intercept	260.0112
	Slope	201.8174

Equation	y = a + b*x	
Adj. R-Squar	0.99871	
		Value
Relaxation rate	Intercept	0.66727
	Slope	16.86017

Equation	y = a + b*x	
Adj. R-Squa	0.99199	
		Value
Relaxation rate	Intercept	310.796
	Slope	219.516

Equation	y = a + b*x	
Adj. R-Squar	0.99623	
		Value
Relaxation rate	Intercept	23.8583
	Slope	15.4783

Equation	y = a + b*x	
Adj. R-Square	0.99888	
		Value
Relaxation rate	Intercept	90.01044
	Slope	165.6478

Equation	y = a + b*x	
Adj. R-Square	0.99527	
		Value
Relaxation rate	Intercept	14.0630
	Slope	17.9364

Figure 51 Illustration of the procedure used to determine the relaxivities (r_1 and r_2) for the magnetic hydrogels: **A1** and **A2**) suc-NapPheΔPheOH (**9**); and **B1** and **B2**) suc-NapPheΔPheOMe (**8**) (1.4 – 27.9 mM); **C1** and **C2**) SPION (1.4 – 27.9 mM) in water.

Table 5 Relaxivity ($r_{1,2}$ mM^{-1}s^{-1}; 60 MHz; 37 °C) for hydrogels **5**, **6**, **8**, **9**, **13**, **14**, **16** and **17** with incorporated SPION, [Fe] (1.4 – 27.9 mM).

SPION@hydrogel (0.4 *wt* %)	r_1 (mM^{-1}s^{-1})	r_2 (mM^{-1}s^{-1})	r_2/r_1	Δ r_2 (%)
suc-PheΔPheOMe (5)	17.5±0.6	154.3±6.9	8.8	-6.9
suc-PheΔPheOH^a (6)	17.3±2.9	148.2±23.1	8.6	-10.5
suc-NapΔPheOMe (13)	17.6±1.0	194.1±11.9	11.0	17.2
suc-NapΔPheOH (14)	17.6±0.2	160.6±4.0	9.1	-3.1
suc-NapPheΔPheOMe (8)	15.5±2.0	219.5±9.9	14.2	32.5
suc-NapPheΔPheOH (9)	16.9±0.3	201.8±10.6	12.0	21.8
suc-PheNaΔPheOMe (16)	20.8±1.3	190.2±17.6	9.2	14.8
suc-PheNaΔPheOH (17)	19.3±0.3	183.1±5.2	9.5	10.5
Agarose	20.4±0.5	220.3±2.9	10.8	33.0
SPION	18.0±0.6	165.7±2.8	9.2	-
^{a}measured in solution				

The SPION used in this work can be classified as a typical T_2 contrast agent: high r_2 value (165.7 mM^{-1}s^{-1}, 60 MHz, 37 °C) associated to a r_2/r_1 ratio, approximately 10.[84] The r_2 relaxivity value determined for the SPION used throughout this Thesis is comparable to other CA, e.g. Ferucarbotran (Resovist) (179 mM^{-1}s^{-1}, 60 MHz, 37 °C), originally developed for human uses.[32] These first generation CA consist of dynamically rearranging discrete polydisperse assemblies, containing multiple polydisperse iron oxide cores (diameter around 10 nm) embedded into matrix-like structures formed by polysacharide dextran-derived polymers physically adsorbed to the iron oxide cores.[85] Their high relaxivity can be modeled as that of a nanoparticle with an iron oxide core equivalent to the aggregated individual cores together with high water volume near the magnetic cores and a diffusion-retarding hydrophilic polymer matrix. In contrast, SPION with small iron oxide cores (around 10 nm diameter) individually stabilized by well-defined chemically anchored hydrophilic PEG-type polymers display much lower relaxivity due to the limiting effect of the low magnetic moment of the non-aggregated nanopaticles on the relaxivity.[47] The hydrodynamic diameter of the SPION (HD = 108 nm) used in this Thesis being much higher than the nominal nanoparticles core size (8 nm diameter) suggests a multicore matrix like structure for the PAA-stabilised SPION.

The effect of SPION incorporation into the hydrogels on the r_2 relaxivity was computed as % variation in relation to the relaxivity of the SPION in water (**Table 5** and **Figure 52**).

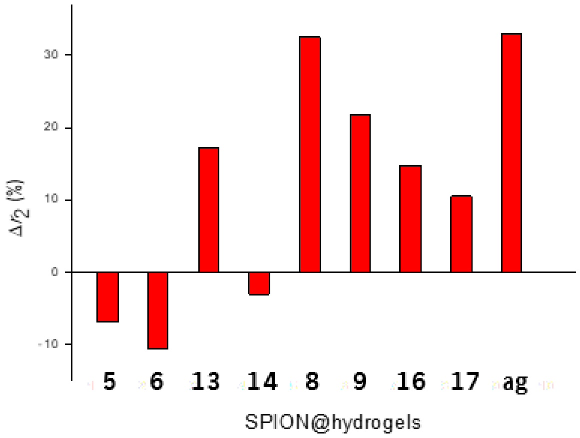

Figure 52 Percentage variation of the SPION relaxivity Δr_2 (%) upon incorporation into the hydrogels.

As a general trend, SPION incorporation into the hydrogels results in enhancement of the transversal relaxivity (**Figure 52**). The dipeptide-based hydrogel suc-PheΔPheOMe (**5**) (r_2= 154.3 mM^{-1}s^{-1}; - 6.9 %) and the suc-NapΔPheOH (**14**) (160.6 mM^{-1}s^{-1}; - 3.1 %) are an exception to this trend. Hydrogelator suc-PheΔPheOH (**6**) does not gellates, showing that the relaxivity enhancement observed for the hydrogels is related to the gels phase properties. In general, the effects on the longitudinal relaxivity r_1 are less pronounced than those observed for r_2 and follow the same trend as r_2. Interestingly, excluding the "anomalous" suc-PheΔPheOMe/H (**5**/**6**) hydrogelators couple, the *C*-terminal methyl ester hydrogels consistently display higher transversal relaxivity r_2 than the dicarboxylic acid-based hydrogels. This suggests a correlation with the relative hydrophobicity of the methyl ester/dicarboxylic acid couples. Among the tripeptide hydrogelators, the ones containing the PheΔPhe sequence (with the *N*-terminal Nap residue) (**8**/**9**) display higher relaxivity than its scrambled isomer (**16**/**17**). Beyond hydrophobicity, peptide sequence seems to play an important role on relaxivity. The tri-peptide-based hydrogel suc-NapPheΔPheOMe (**8**) exhibits the most pronounced r_2 enhancement (219.5 mM^{-1}s^{-1}, 32.5 %), of the same order of magnitude as that produced by SPION incorporation into agarose hydrogel (0.5 *wt* %) (220.3 mM^{-1}s^{-1}, 33.0 %). Agarose hydrogel has been extensively used as a matrix for incorporation of contrast agents for signal reproducibility and accuracy quality control purposes in NMR and MRI.[86] The relaxivity increase observed for the SPION in the agarose hydrogel is likely to be the result of slower water diffusion in the SPION vicinity within the agarose hydrophilic matrix. A longer residence time of the water protons inside the SPION dephasing magnetic field, results in faster water proton relaxation rates comparing to bulk water.[87] The entangled network structure observed for the hydrogels (see STEM images) suggest that restricted water diffusion is the likely cause for the observed relaxivity enhancement. Higher fiber density and entanglement could therefore be correlated with slower water diffusion and higher relaxivities. However, a clear correlation between relaxivity and the rheology properties and STEM images can not be clearly established.

Effect of hydrogelator concentration on the relaxivity

The effect of hydrogelator concentration (0.1 - 0.6 *wt* %) on the transversal water proton relaxation rate (R_2, 60 MHz, 37 °C) of hydrogels loaded with a fixed amount of SPION (0.467 *wt* %, 16.7 mM) was studied (**Figure 53**).

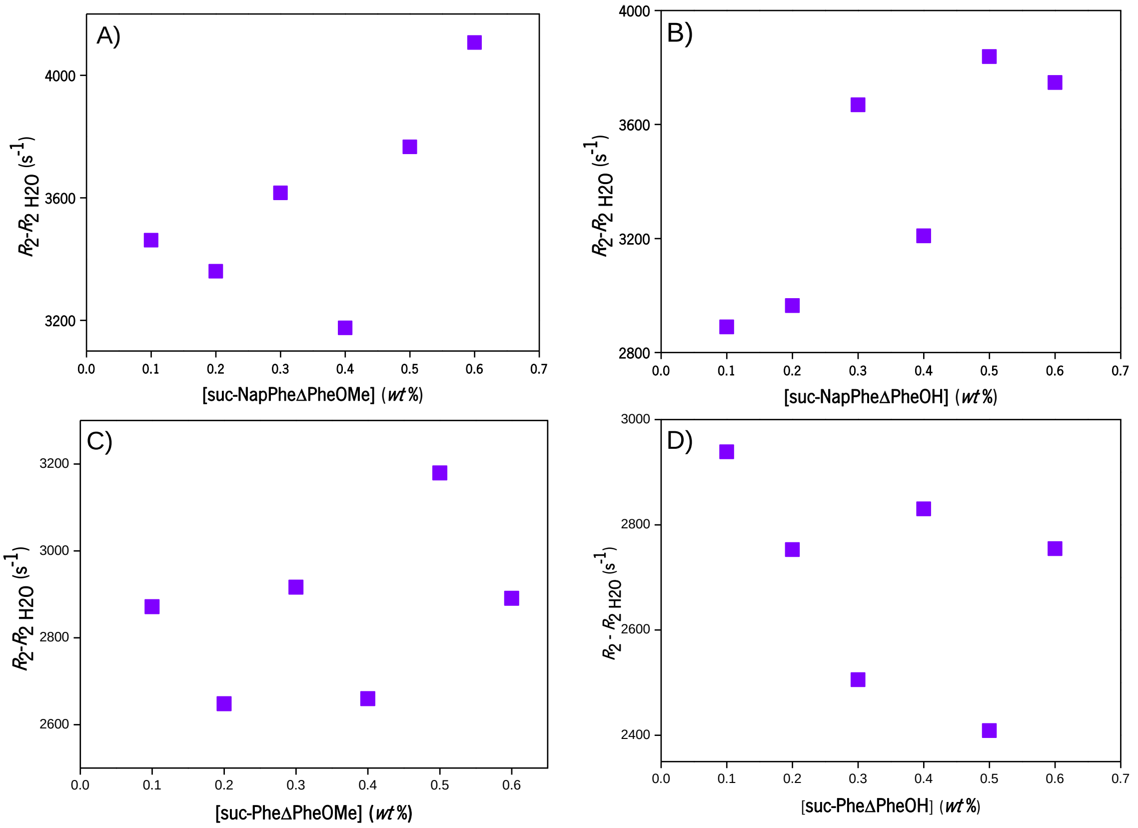

Figure 53 Hydrogelator concentration dependence of the transversal water proton relaxation rate R_2 (60 MHz, 37 °C) for hydrogels (0.1 - 0.6 *wt* %) with incorporated SPION (0.467 *wt* %, 16.7 mM SPION$_{Fe}$): **A)** suc-NapPheΔPheOMe (**8**); **B)** suc-NapPheΔPheOH (**9**); **C)** suc-PheΔPheOMe (**5**); **D)** suc-PheΔPheOH (**6**).

The tripeptide and dipeptide hydrogelator couples suc-NapPheΔPheOMe/H (**8**/**9**) and suc-PheΔPheOMe/H (**5**/**6**), bearing the PheΔPhe *motif*, were selected for this study. In general, SPION incorporation did not abolish gelation ability for hydrogelator concentrations above the *cgc*. Hydrogelator concentrations, bellow the *cgc*, were also included in this study to evaluate the effect of self-assembled fibres in solution on the relaxivity properties. In general, the effect of hydrogelator concentration on R_2 is weak. The data suggest a liner trend for increasing of R_2 with increasing hydrogelator concentration, more pronounced for the tripeptide hydrogelators (**8**/**9**).

The study of the effect of hydrogelator concentration on the rheological properties of the suc-NapPheΔPheOMe (**8**) hydrogel (see rheology section) indicates that the hydrogels display the same structure irrespective of hydrogelator concentration. An increase on the hydrogelator concentration above the *cgc* is likely to result in a denser hydrogel fibril network, which imposes higher restrictions to water diffusion.

Hydrogels with incorporated Gd complexes

Hydrogels with incorporated Gd(Npx) complex were studied as potential CA for MRI. Relaxivity values ($r_{1,2}$, $mM^{-1}s^{-1}$) were determined for the Gd(Npx) complex and for the paramagnetic hydrogels, with incorporated chelate (0.33 – 1.67 mM), from the graphical representation of the chelate concentration dependence of the water proton relaxation rates ($R_{1,2}$, s^{-1}). The relaxivity determination is illustrated in **Figure 54** for the paramagnetic hydrogels suc- NapPheΔPheOMe/H (**8**/**9**).

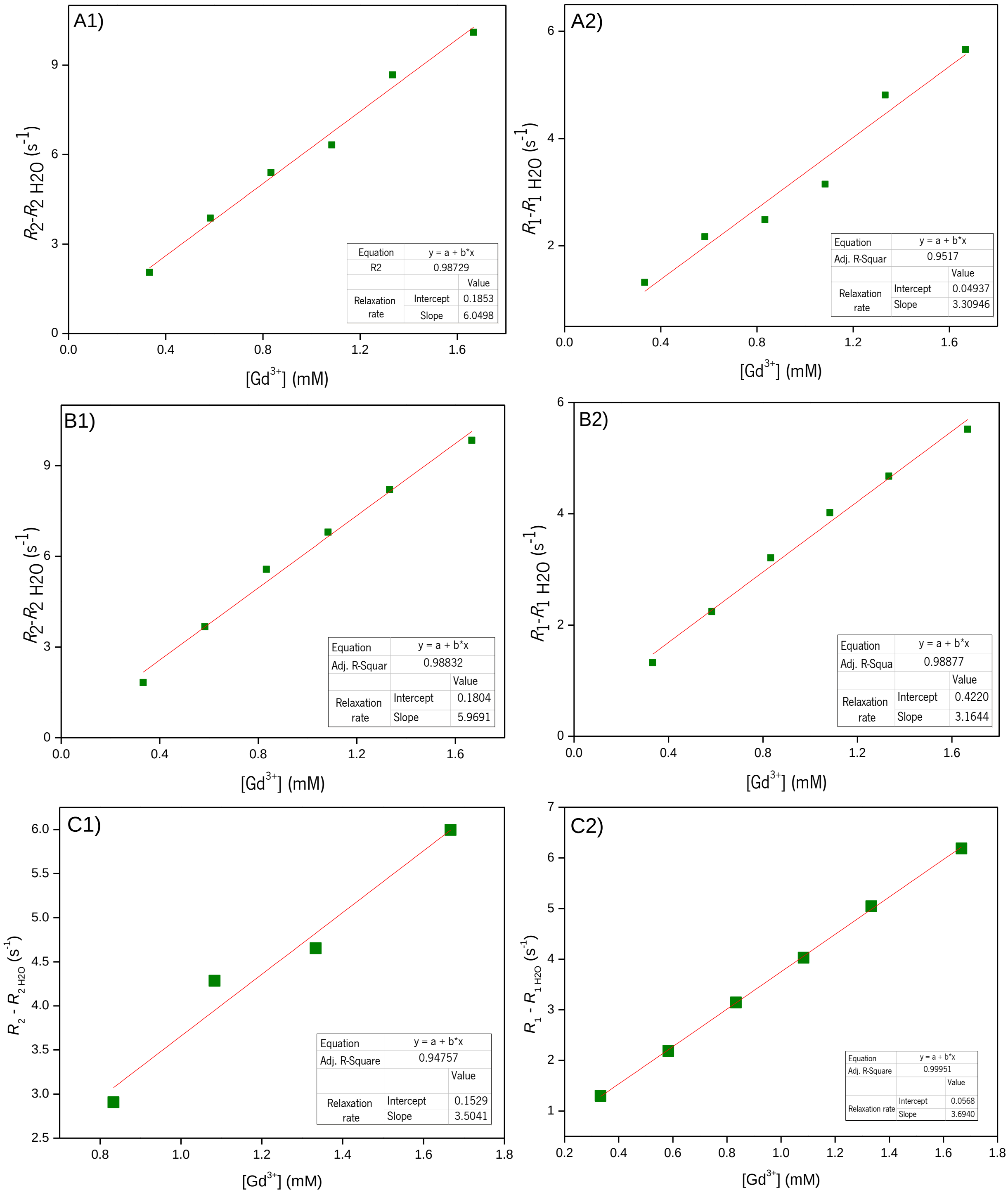

Figure 54 Illustration of the procedure used to determine the water proton relaxivities (r_1 and r_2) for the paramagnetic hydrogels: **A1** and **A2**) suc-NapPheΔPheOMe (**8**); and **B1** and **B2**) suc-NapPheΔPheOH (**9**) (0.33 – 1.67 mM); **C1** and **C2**) Gd-Npx complex (0.33 – 1.67 mM) in water**.** Data for the remaining hydrogels can be found in **annex Figure A7**.

The full set of relaxivity values for the magnetic hydrogels is summarized in **Table 6**.

Table 6 Relaxivity values ($r_{1,2}$ mM^{-1}s^{-1}; 60 MHz; 37 °C) for hydrogels **5**, **6**, **8**, **9**, **13**, **14**, **16** and **17** with incorporated Gd-Npx complex.

Gd(Npx)@hydrogel	r_1 (mM^{-1}s^{-1})	r_2 (mM^{-1}s^{-1})	r_2/r_1	$\Delta\ r_1$ (%)
suc-PheΔPheOMe (5)	3.8±0.1	3.5±0.2	0.9	1.6
suc-PheΔPheOH^a (6)	3.6±0.04	3.2±0.3	0.9	-3.5
suc-NapΔPheOMe (13)	4.2±0.1	5.8±0.3	1.4	14.9
suc-NapΔPheOH (14)	4.2±0.2	5.9±0.6	1.4	14.6
suc-NapPheΔPheOMe (8)	3.2±0.2	6.0±0.3	1.9	-14.4
suc-NapPheΔPheOH (9)	3.3±0.3	6.1±0.3	1.8	-10.3
suc-PheNapΔPheOMe (16)	4.0±0.2	4.5±0.1	1.1	8.4
suc-PheNapΔPheOH (17)	6.2±0.2	10.2±0.6	1.7	68.3
Agarose gel (1%)	2.2±0.4	2.0±0.4	0.9	-41.7
Gd(Npx)	3.7±0.04	3.5±0.5	1.0	0

The complex Gd(Npx), in aqueous solution, displays a r_1 value (3.7 mM^{-1}s^{-1}, 60 MHz, 37 °C) and a ratio r_2/r_1 close to the unit qualifying as T_1 contrast agent. The relaxivity displayed by the Gd(Npx) complex is characteristic of intermediate molecular weight complexes, in fast rotation in solution.[84] Moreover, good linear fitting of the relaxation rate data to a single linear trend, indicates that the complex does not undergoes self-assembly in the concentration range studied (0.33 - 1.67 mM), despite its lipophilicity.[88]

The effect of incorporation of the Gd(Npx) complex into the hydrogels, on their performance as T_{1w} CA for MRI, was evaluated by the % variation of the longitudinal relaxivity in relation to the complex in water (**Table 7**, **Figure 55**).

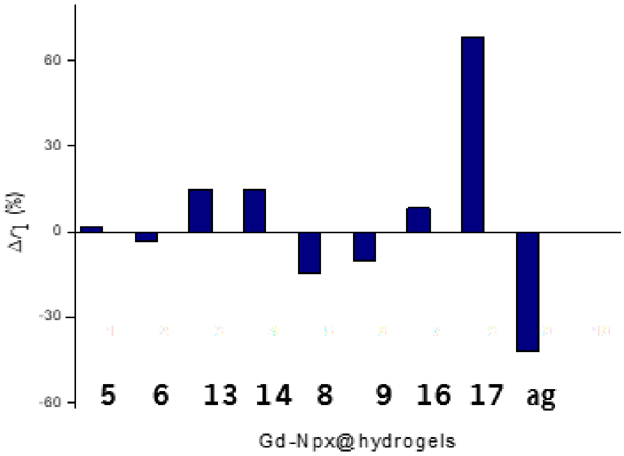

Figure 55 Percentage variation of the longitudinal relaxivity of the Gd-Npx complex (Δr_1 (%)) upon incorporation into hydrogels, in relation to complex relaxivity in water.

Overall, incorporation of the complex Gd(Npx) into the hydrogels results in a increase of longitudinal relaxivity r_1, most noticeable (68.3 %) for the dicarboxylic acid tripeptide suc-PheNapΔPheOH (**17**). Although, the effect of hydrogel incorporation on the longitudinal relaxivity is much weaker and hydrogel dependent - a unic trend can not be identified. Interestingly, incorporation of the chelate into agarose gel (0.5 *wt* %) leads to a significant reduction, around 40 %, of longitudinal relaxivity.

The SBM model identifies the parameters rotational correlation time- τ_R and water exchange rate- k_{ex} ($k_{ex}= 1/\tau_M$) as the main modulators of the inner sphere relaxation mechanism. High relaxivity can be attained at intermediate fields (20 - 60 MHz) by simultaneous optimization of τ_R and k_{ex}. Complex Gd(Npx), belonging to the DO3A-*N*-(α-aminopropionate) chelator family, is likely to display optimized water exchange rate for attaining high relaxivity at intermediate fields, thanks to steric compression around the water binding site.[75] Preliminary data (not shown) reveal that non-covalent association of the Gd(Npx) chelate to human serum albumin results in relaxivities, of the order of magnitude 45 $mM^{-1}s^{-1}$ (20 MHz, 37 °C). Slow complex tumbling (long τ_R) upon binding to HSA, associated to fast optimized water exchange leads to the observed high relaxivity. The longitudinal relaxivity of the Gd(Npx) complex in solution (r_1= 3.7±0.04 $mM^{-1}s^{-1}$, 60 MHz, 37 °C) is limited by fast tumbing in solution, short τ_R value. The longitudinal relaxivity enhancements observed for the Gd(Npx) complex incorporated into the hydrogels, especially for the suc-PheNapΔPheOH (**17**) hydrogel (70 % enhancement), is likely related to effects of the hydrogel network on the rotational dynamics of the complex. In previous works the research group demonstrated by Forster Resonance Energy Transfer (FRET) experiments that hydrophobic molecules (e.g. curcumin) interact with the hydrogel fibres of similar self-assembed hydrogels, with FRET distances similar to the ones measured for the binding of curcumin to BSA.[89] Moreover, the fluorescence studies reveal that the curcumin molecules experience a local environment with polarity equivalent to acetonitrile.The modest relaxivity enhancement attained upon chelate incorporation into the hydrogels suggests a much lower affinity interaction of the chelate with hydrogel fibres comparing to Gd(Npx) chelate-BSA non-covalent binding. The relaxivity reduction observed for the complex included in agarose gel is probably related to restricted water diffusion in the hydrophilic hydrogel matrix. The consistently higher enhancement of the transversal relaxivity, comparing to longitudinal relaxivity, observed for most hydrogels indicates self-assembly/aggregation of the Gd(Npx) complex on the surface of the hydrogel fibres. A similar phenomenon was reported for peptide based Gd^{3+} complexes that undergo self-assembly into fibrilar structures and hydrogels.[90] The weak effects of the suc-PheΔPheOH (**6**) hydrogelator solution on the relaxivities confirms that the relaxivity changes are linked to hydrogel formation.

Effect of hydrogelator concentration on the relaxation rates

The effect of hydrogelator concentration (0.1 – 0.6 *wt* %) on the water proton longitudinal relaxation rate R_1 (s^{-1}) (60 MHz, 37 °C) was determined for the paramagnetic hydrogels suc-NapPheΔPheOMe/H (**8**/**9**) using a fixed concentration of the Gd(Npx) complex (0.5 mM). (**Figure 56**).

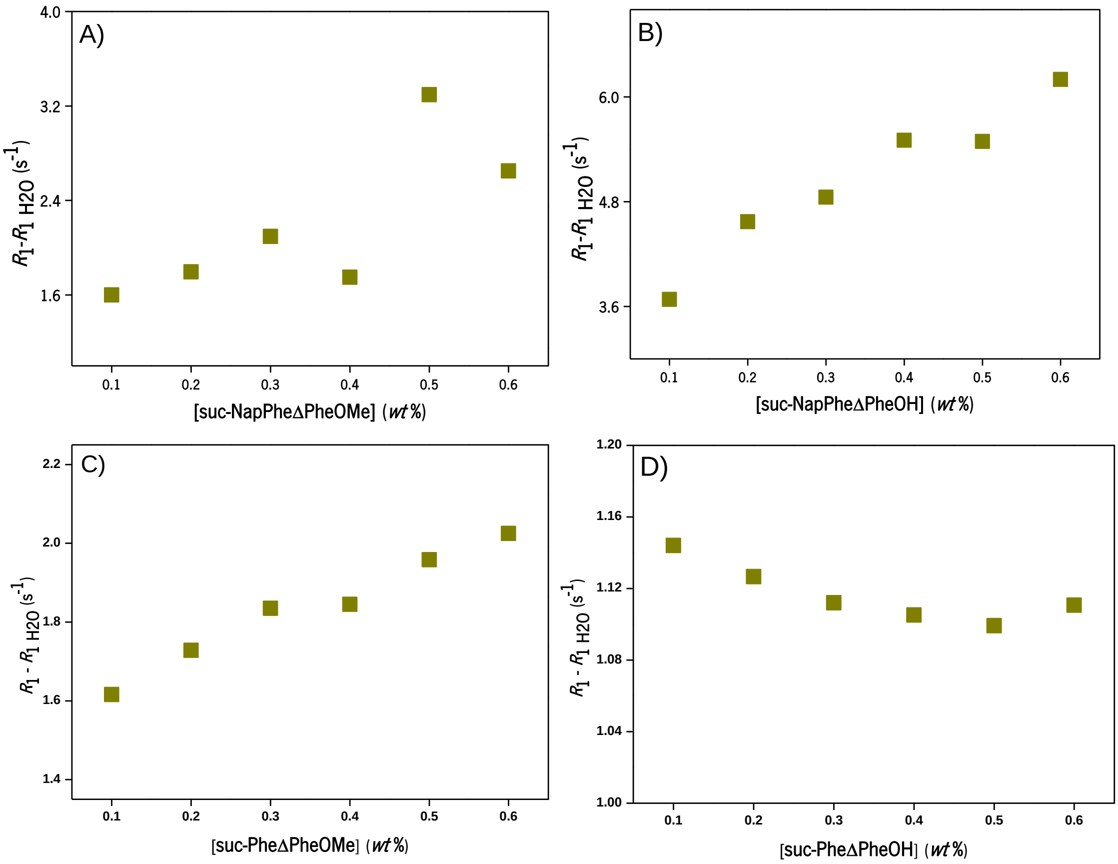

Figure 56 Effect of hydrogelator concentration on the water proton longitudinal relaxation rate R_1 (60 MHz, 37 °C) for paramagnetic hydrogels, with incorporated Gd(Npx) complex (0.5 mM Gd): **A**) suc-NapPheΔPheOMe (**8**); **B**) suc-NapPheΔPheOH (**9**); **C**) suc-PheΔPheOMe (**5**); **D**) suc-PheΔPheOH (**6**).

The incorporation of Gd(Npx) complex (0.5 mM) does not to change the gelation ability of the studied hydrogelators at concentrations above the *cgc* (*circa* 0.3 *wt* %). Hydrogels with incorporated Gd(Npx) complex (0.5 mM) were obtained for the tripeptide hydrogelator couple suc-NapPheΔPheOMe/H (**8**/**9**) and for the dipeptide hydrogelator suc-PheΔPheOMe (**5**). Despite not forming a gel, relaxivity measurements were performed also for the suc-PheΔPheOH (**6**) hydrogelator.

In general, the longitudinal relaxation rate R_1 of the water protons in the hydrogels increases "linearly" with the hydrogelator concentration. The increase of hydrogelator concentration beyond the *cgc* value is likely to result in an increase of the density of the entangled hydrogel´s network. The increase in R_1 suggests progressive association of the complex with the hydrogel fibres as the hydrogelator´s concentration increases. The higher concentration dependence of R_1 observed for the dicarboxylic acid hydrogel suc-NapPheΔPheOH (**9**) suggests higher affinity of the complex for this hydrogel. The R_1 concentration dependence for hydrogel suc-PheΔPheOMe (**5**) shows also a "linear" trend, although less pronounced than that hydrogelator **9**. The R_1 concentration dependence for the suc-PheΔPheOH (**6**) hydrogelator, which does not form a hydrogel in the concentration range studied, is different from the one observed for the hydrogels, suggesting that the effect of the hydrogels on R_1 is related to the entangled fibrilar structure and association of the complex to the hydrogel fibres.

2.7.2 Magnetic resonance imaging (MRI)

Magnetic resonance imaging (MRI, 3 T, 120 MHz, 37 °C) was used to evaluate the efficacy of the hydrogels with incorporated SPION and Gd(Npx) complex as CAs for $T_{1,2}$-weighted MRI. MRI $T_{1,2}$ relaxation maps were determined using the MEMS (multi-echo-multi-spin) sequence, the MPRAGE (Magnetization Prepared Rapid Acquisition Gradient Echo) sequence and the MRI calculator tool. Contrast agent efficacy was assessed by the parameter relaxivity $r_{1,2}$ ($mM^{-1}s^{-1}$), calculated from the dependence of the experimental relaxation rates $R_{1,2}$ (s^{-1}) = $1/T_{1,2}$ (s) on the concentration of active centres (Fe and Gd).

SPION was incorporated into hydrogels (0.4 *wt* %) in the Fe concentration range 0.02 - 0.12 mM to ascertain the effect of the hydrogel network on their performance as potential CA for MRI. Phantoms and $T_{1,2}$ relaxation maps (3 T, 120 MHz, 37 °C) were acquired for the SPION preparation and for all magnetic hydrogels. Illustrative data are shown for the tripeptide hydrogels suc-NapPheΔPheOMe/H (**8** and **9**) (0.4 *wt* %) with incorporated SPION (0.02 - 0.12 mM Fe) (**Figure 57**, see also **annex Figure A8** for the complete set of phantoms and relaxation maps).

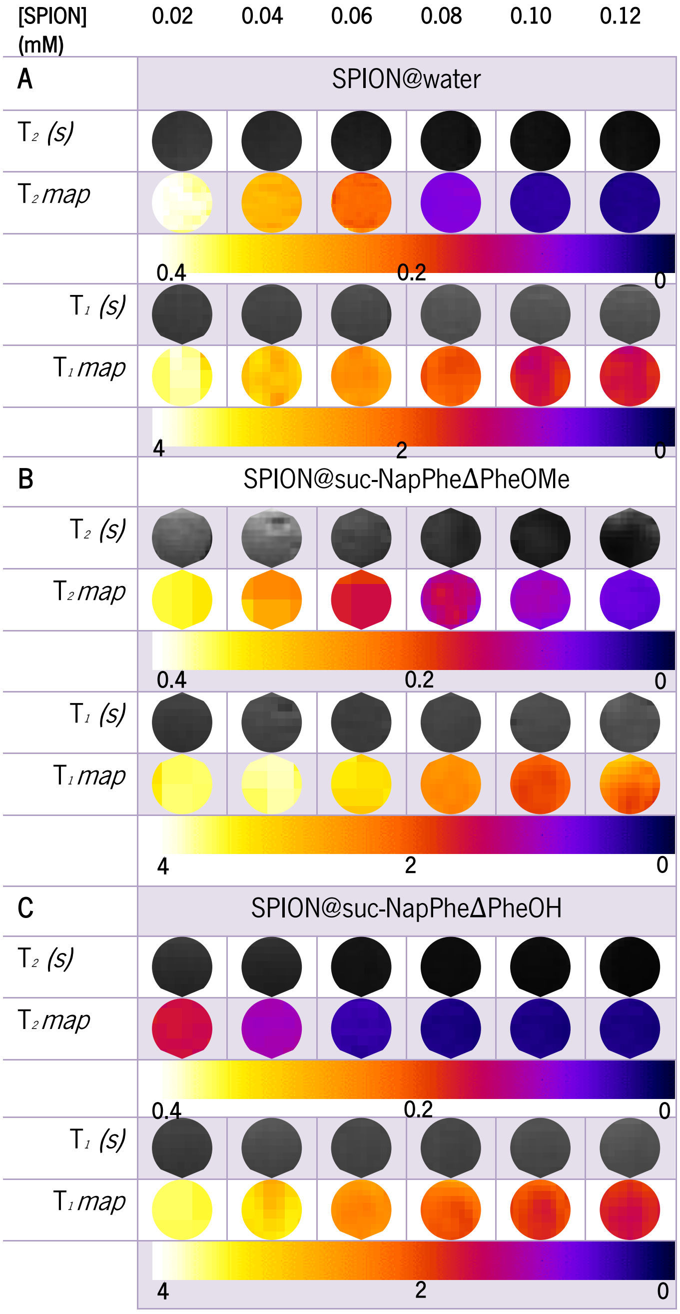

Figure 57 $T_{1,2}$ MRI images (phantoms) and relaxation maps for: (**A**) SPION (0.02 - 1.2 mM) and for the tripeptide hydrogel couple (**B**) suc-NapPheΔPheOMe and (**C**) suc-NapPheΔPheOH ((0.4 *wt* %) with incorporated SPION (0.02 - 1.2 mM).

As can be seen in the phantoms and MRI relaxation maps, the SPION generates strong concentration-dependent T_2 dark signal enhancement. T_1 concentration dependent bright signal enhancement is comparatively lower. The SPION used in this work qualifies as a contrast agent for T_2 weight MRI. Relaxivity ($r_{1,2}$) values were calculated for the SPION and for the magnetic hydrogels (with incorporated SPION) from the dependence of the relaxation rates $R_{1,2}$ (s^{-1}) on the $SPION_{Fe}$ concentration

(**Figure 58**).

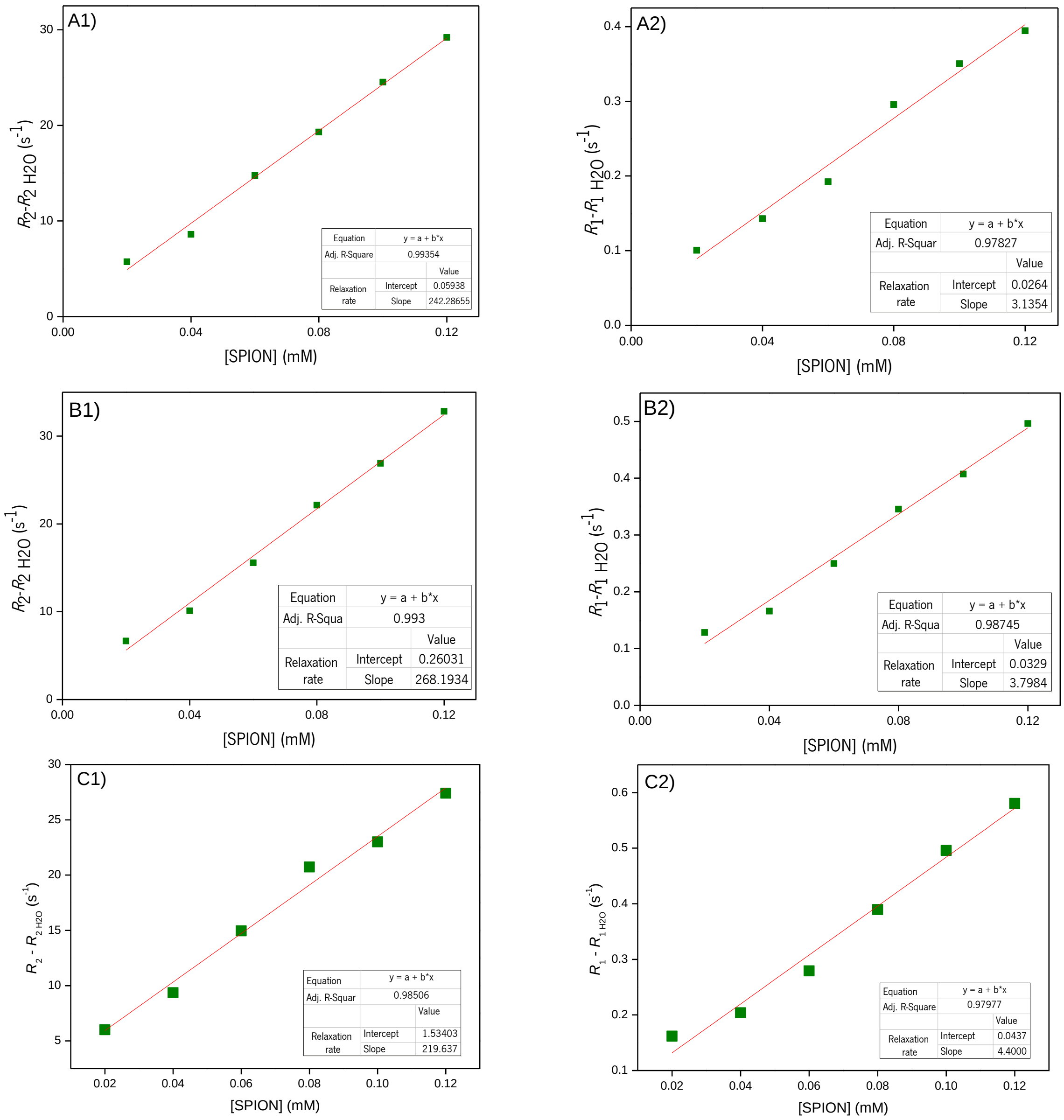

Figure 58 Concentration dependence of the water proton relaxation rates $R_{1,2}$ (120 MHz, 37 °C) for SPION (0.02 – 0.12 mM) on magnetic hydrogels (0.4 *wt* %, 0.02 - 0.12 mM Fe) for: (**A1**) and (**A2**) hydrogel suc-NapPheΔPheOMe (**8**) (0.4 *wt* %) and (**B1**) and (**B2**) hydrogel suc-NapPheΔPheOH (**9**) (0.4 *wt* %); (**C1**) and (**C2**) SPION in water (0.02 - 0.12 mM Fe). The full data set is presented in **annex Figure A9**.

The r_2 relaxivity value calculated for SPION (219.5 mM^{-1}s^{-1}, 120 MHz, 37 °C) is comparable to the value reported for Ferucarbotran (Resovist) (186 mM^{-1}s^{-1}, 120 MHz, 37 °C) in agarose gel (0.5 *wt* %).[32] MRI T_2 signal saturation is attained at 0.10 mM Fe concentration. The r_2 value calculated for the SPION by MRI (219.5 mM^{-1}s^{-1}, 120 MHz, 37 °C), is in good accordance with the one calculated by ^{1}H relaxometry, at 60 MHz, (165.7 mM^{-1}s^{-1}, 37 °C). The apparent discrepancy between the relaxivity values is related to the Larmour frequency (120 and 60 MHz, for MRI and relaxometry respectively) at which measurements were performed. As the magnetic moment of SPION is determined by the external magnetic field, higher relaxivities are expected at higher magnetic fields, until reaching the saturation magnetization. Moreover, the SPION concentration range used for the relaxivity measurements at 60 MHz is over an order of magnitude higher than that used for the MRI measurements, according to the detection sensitivity of both techniques. The r_1 value measured for the SPION at 120 MHz (4.4 mM^{-1}s^{-1}) is much lower than the one measured at 60 MHz (18.0 mM^{-1}s^{-1}), reflecting the effect of the higher magnetic moment of the nanoparticles at the magnetic field 3 T on the longitudinal water proton relaxation. Accordingly, SPION displays a much higher r_2/r_1 ratio at 120 MHz comparing to 60 MHz (50.0 and 9.2 respectively).

Analysis of the $T_{1,2}$ phantoms and relaxation maps reveal that the magnetic tripeptide-based hydrogels suc-NapPheΔPheOMe/H (**8** and **9**) (**Figure 59**) display strong concentration-dependent T_2 signal enhancement and much weaker T_1 signal contrast enhancement. Relaxivity $r_{1,2}$ values were calculated for the magnetic hydrogels (**Table 7**).

Table 7 Calculated relaxivity values (mM^{-1}s^{-1}, 120 MHz, 37 °C) for magnetic hydrogels.

SPION@hydrogel	r_1 (mM^{-1}s^{-1})	r_2 (mM^{-1}s^{-1})	r_2/r_1	Δ r_2 (%)
suc-PheΔPheOMe (5)	3.8±0.2	260.6±14.9	69.3	18.7
suc-PheΔPheOH^a (6)	1.9±0.1	115.5±8.1	60.5	-47.4
suc-NapΔPheOMe (13)	2.5±0.1	170.0±11.9	67.7	-22.6
suc-NapΔPheOH (14)	2.4±0.2	151.2±9.4	64.1	-31.2
suc-NapPheΔPheOMe (8)	3.1±0.2	242.3±8.7	77.2	10.3
suc-NapPheΔPheOH (9)	3.8±0.2	268.2±10.1	70.6	22.1
suc-PheNapΔPheOMe (16)	1.9±0.1	145.4±6.3	76.1	-33.8
suc-PheNapΔPheOH (17)	3.8±0.2	283.3±12.8	73.8	29.0
SPION	4.4±0.3	219.6±12.1	49.9	0

^{a}Measured as viscous solution

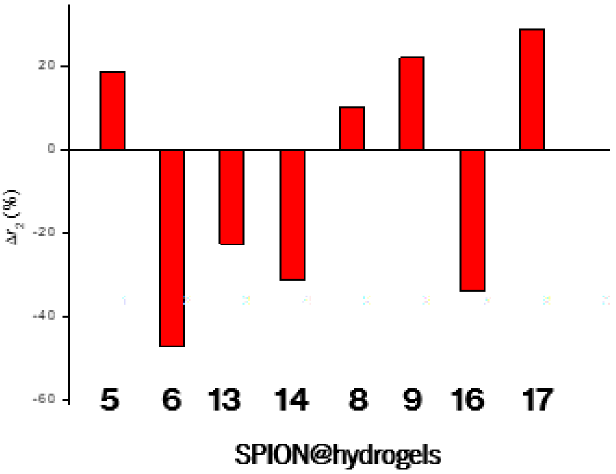

Figure 59 Percentage variation of r_2 for magnetic hydrogels in relation to SPION water.

In general, SPION incorporation into the hydrogels results in a considerable reduction of transversal relaxivity r_2 for all hydrogels. The dipeptide hydrogel suc-PheΔPheOMe (**5**) and the tripeptide hydrogels suc-NapPheΔPheOMe/H (**8** and **9**), containing the PheΔPhe motif, and the dicarboxylic acid tripeptide suc-PheNapΔPheOH (**17**) display a moderate increment of transverse relaxivity. This trend suggests a rough qualitative correlation between transversal relaxivity and gel elasticity, well appearent for the hydrogel couple suc-PheNapΔPheOMe/H (**16** and **17**). In fact, the dicarboxylic acid hydrogel (**17**) which displays much higher elasticity (G´= 102 kPa) than the methyl ester analogue (1.2 kPa), exhibits also the highest relaxivity enhancement. Higher hydrogel elasticity is likely to be the result of an increase of hydrogels' network density and fibre entanglement, which in turn can impose limitations on water diffusion inside the gel. Slower water diffusion imposed by a denser hydrogel network is likely to result in higher transversal relaxivity. It is noteworthy that the SPION concentration used for the MRI studies (0.02 - 1.2 mM$_{Fe}$) is unlikely to change the rheological properties and the microstructure of the hydrogels. In contrast, the much higher SPION concentration used for the relaxometric studies (1.4 - 27.9 mM$_{Fe}$) is prone to influence the rheological properties and microstructure of the gels (**Table 4**, rheology section).

Besides magnetic field strength, SPION concentration effects on the hydrogel´s microstructure can explain the disparate results obtained by relaxometry and MRI studies.

Effect of hydrogelator concentration on the properties of magnetic hydrogels

The effect of hydrogelator concentration on the properties of the magnetic hydrogels as MRI CA was studied for the dipeptide hydrogelator couple suc-PheΔPheOMe/H (**5** and **6**) and the tripeptide hydrogelator pair suc-NapPheΔPheOMe/H (**8** and **9**) in the concentration range 0.5 – 5 *wt* %. $T_{1,2}$ MRI phantoms and relaxation maps were obtained for the magnetic hydrogels (**annex Figure A12**).

The dependence of the R_2 relaxation rate on the hydrogelator concentration is represented on **Figure 60**.

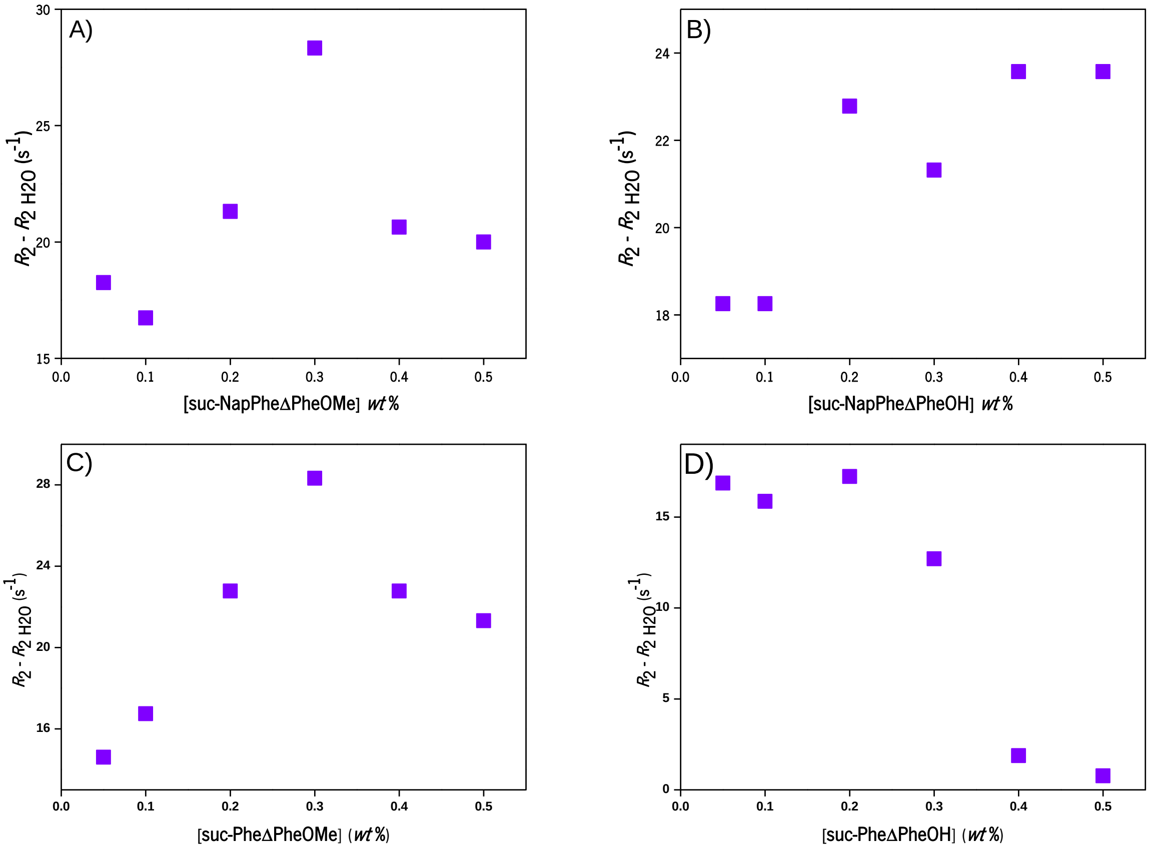

Figure 60 Dependence of the transversal relaxation rate R_2 on hydrogelators' concentration for hydrogels with incorporated SPION (0.08 mM): **A)** suc-NapPheΔPheOMe (**8**); **B)** suc-NapPheΔPheOH (**9**); **C)** suc-PheΔPheOMe (**5**); **D)** suc-PheΔPheOH (**6**).

For hydrogelators suc-PheΔPheOMe (**5**) and suc-NapPheΔPheOMe (**8**) (**Figure 60C** and **60A**, respectively), R_2 reaches a maximum for hydrogelator concentrations of the order of magnitude of the *cgc* (0.3 *wt* %). At concentrations bellow the *cgc*, the relaxivity seems to be proportional to the hydrogelators concentration suggesting that the increase on the concentration of fibre in solution has a restricting effect on the water diffusion. The reduction of R_2 above the *cgc* suggests nanoparticles aggregation due to the increase of the density of the hydrogels' network. For hydrogelator suc-NapPheΔPheOH (**9**) the transversal relaxivity reaches a plateau around the *cgc* (**Figure 60B**). This hydrogel displays much lower elasticity (G´) than its protected counterpart suggesting a less dense network which possibly does not induce aggregation. Hydrogelator suc-PheΔPheOH (**6**) (**Figure 60D**), which fails to gel in the concentration range studied, shows a R_2 behaviour different from that seen for the hydrogels - a decrease of R_2 for hydrogelator concentrations above 0.2 *wt*%. This suggests that the concentration effects on R_2 observed for the hydrogels are specific of the hydrogel fibrillar network.

Paramagnetic hydrogels with incorporated Gd(Npx) and Gd(DOTA) complexes

$T_{1,2}$ MRI phantoms and relaxation maps (120 MHz, 37 °C) were acquired in water for the Gd(Npx) and Gd(DOTA) chelates in the concentration range 0.1 - 1.2 mM (**Figure 61**).

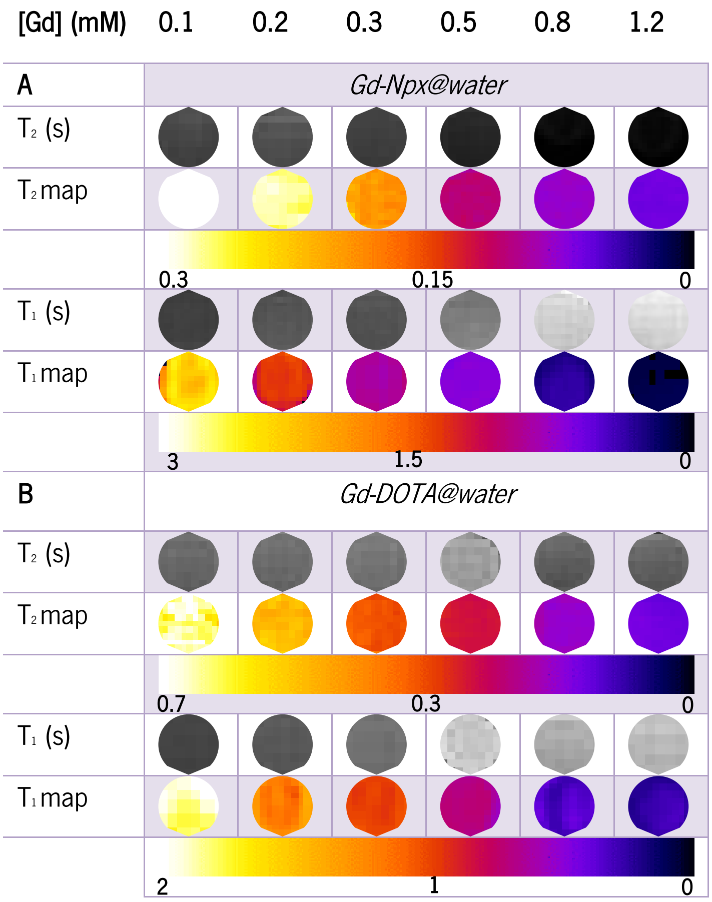

Figure 61 $T_{1,2}$ MRI images and relaxation maps (120 MHz, 37 °C) for the (**A**) Gd(Npx) and (**B**) Gd(DOTA) complexes in the concentration range 0.1 - 1.2 mM$_{Gd}$ in water solution.

The MRI phantoms and the relaxation maps for the Gd(Npx) and Gd(DOTA) complexes show a concentration-dependent effect on T_1 relaxation time reduction, which translates in progressively brighter images seen in the MRI phantoms. As expected, no shortening effect is observed for T_{2w} confirming that both complexes behave effective as CA for T_{1w} MRI. The phantoms and the relaxation maps indicate higher T_{1w} MRI contrast enhancement for the Gd(Npx) complex comparing to the Gd(DOTA) complex. This is confirmed by the relaxivity values (r_1= 3.1 and 5.7 mM^{-1}s^{-1}, 120 MHz, 37 °C) obtained for the Gd(DOTA) and Gd(Npx) complexes, respectively (**Table 8**, **Figure 62**).

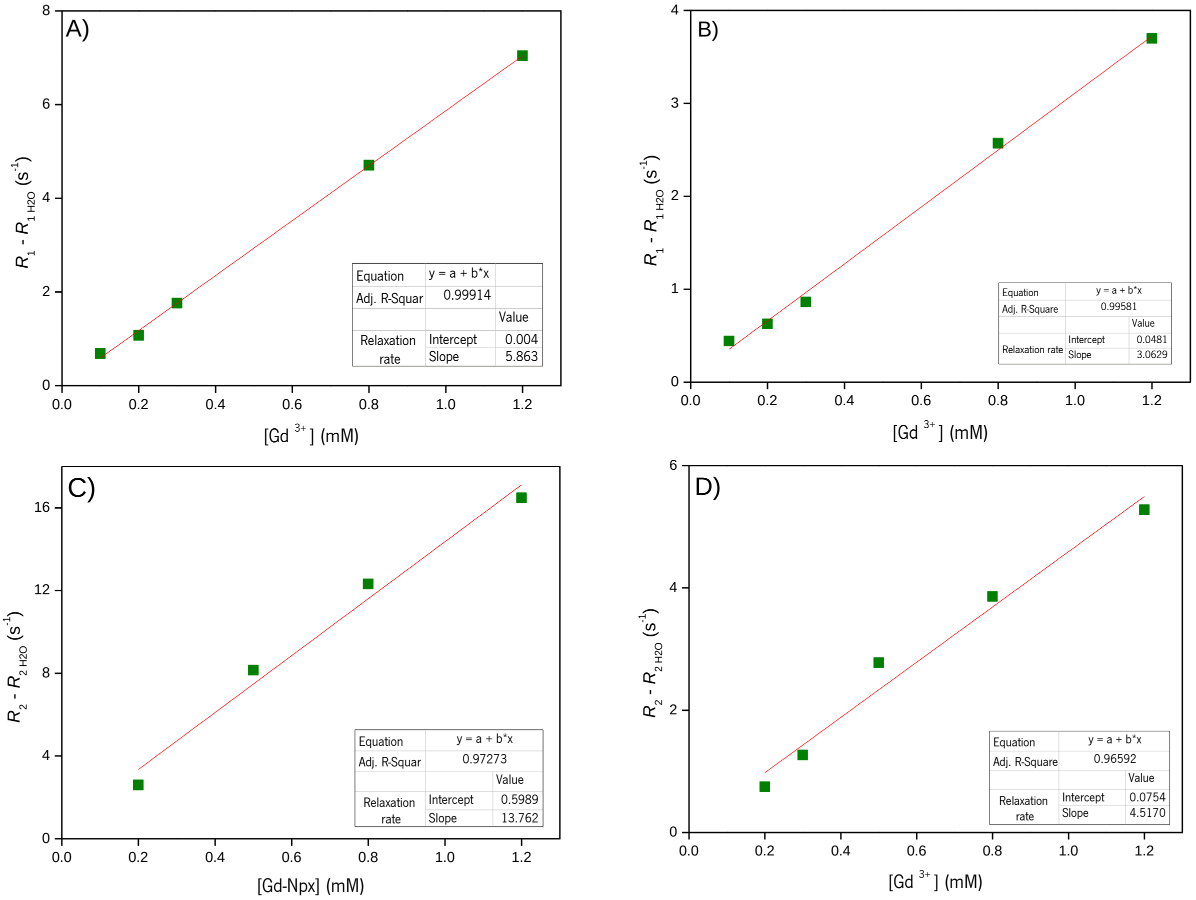

Figure 62 Dependence of the longitudinal and transversal water proton $R_{1,2}$ (s^{-1}) relaxation rate on chelate (Gd) concentration (mM): **A)** R_1 Gd(Npx)@water; **B)** R_1 Gd(DOTA) @water; **C)** R_2 Gd(Npx)@water; **D)** R_2 Gd(DOTA)@water.

The relaxivity value and the linear fitting of the Gd concentration dependence of R_1 indicate that complex association does not takes place in the concentration range studied. The higher relaxivity value determined for the Gd(Npx) complex, comparing to the Gd(DOTA) chelate, is determined by its higher molecular weight, which results in a longer rotational correlation time, τ_R. The relaxivity of the Gd(Npx) and Gd(DOTA) complexes is limited by fast tumbling in solution.[91] The relaxivity determined for the Gd(DOTA) complex is in accordance to the literature values (3.1 mM^{-1}s^{-1}, 120 MHz, 37 °C) (**Figure 62**).[92]

In the concentration range studied, the Gd(Npx) and Gd(DOTA) complexes show contrast saturation at 0.8 and 0.5 mM, respectively.

Paramagnetic hydrogels, with incorporated Gd(Npx) and Gd(DOTA) chelates, were prepared at fixed hydrogelator concentration (0.4 *wt* %) by varying the Gd concentration in the range 0.1 - 1.2 mM. MRI $T_{1,2}$ phantoms and relaxation maps were acquired for all hydrogelators. **Figure 63** shows illustrative MRI $T_{1,2}$ phantoms and relaxation maps for the paramagnetic hydrogels suc-NapPheΔPheOMe/H (**8** and **9**) with incorporated Gd(Npx) and Gd(DOTA) complexes.

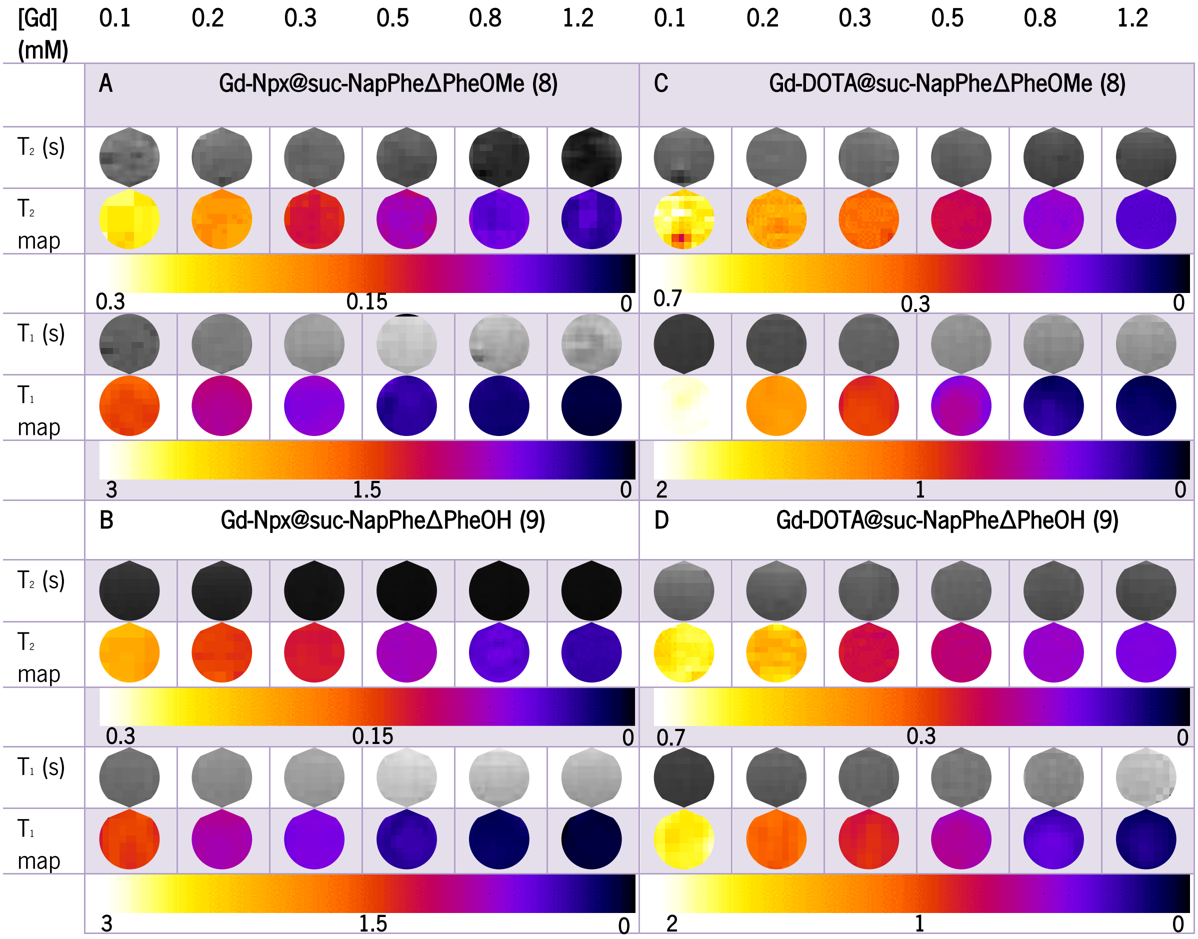

Figure 63 Illustrative MRI $T_{1,2}$ phantoms and relaxation maps (120 MHz, 37 °C) for paramagnetic hydrogels (0.4 *wt* %), with incorporated Gd(DOTA) and Gd(Npx) chelates (0.1 - 1.2 mM): **A)** Gd(Npx)@suc-NapΔPheOMe (**8**); **B)** Gd(Npx)@suc-NapPheΔPheOH (**9**); **C)** Gd(DOTA)@suc-NapPheΔPheOMe (**8**); **D)** Gd(DOTA)@sucNapPheΔPheOH (**9**). The full set is presented in **annex Figure A10**.

The MRI phantoms and relaxation maps demonstrate concentration-dependent T_1 contrast enhancement for the paramagnetic hydrogels, more pronounced for the hydrogels with incorporated Gd(Npx) complex than for the Gd(DOTA) hydrogels. Moreover, the paramagnetic hydrogel Gd(Npx)@suc-

NapPheΔPheOH (**9**) displays strong concentration-dependent T_1 and T_2 contrast enhancement, suggesting applications as dual $T_{1,2}$ contrast agent for MRI.

Relaxivities values ($r_{1,2}$, mM^{-1}s^{-1}) were calculated for the Gd(Npx)@suc-NapPheΔPheOMe/H (**8** and **9**) paramagnetic hydrogels from the Gd concentration dependence of the paramagnetic relaxation rates (**Figure 64** and **Table 8**).

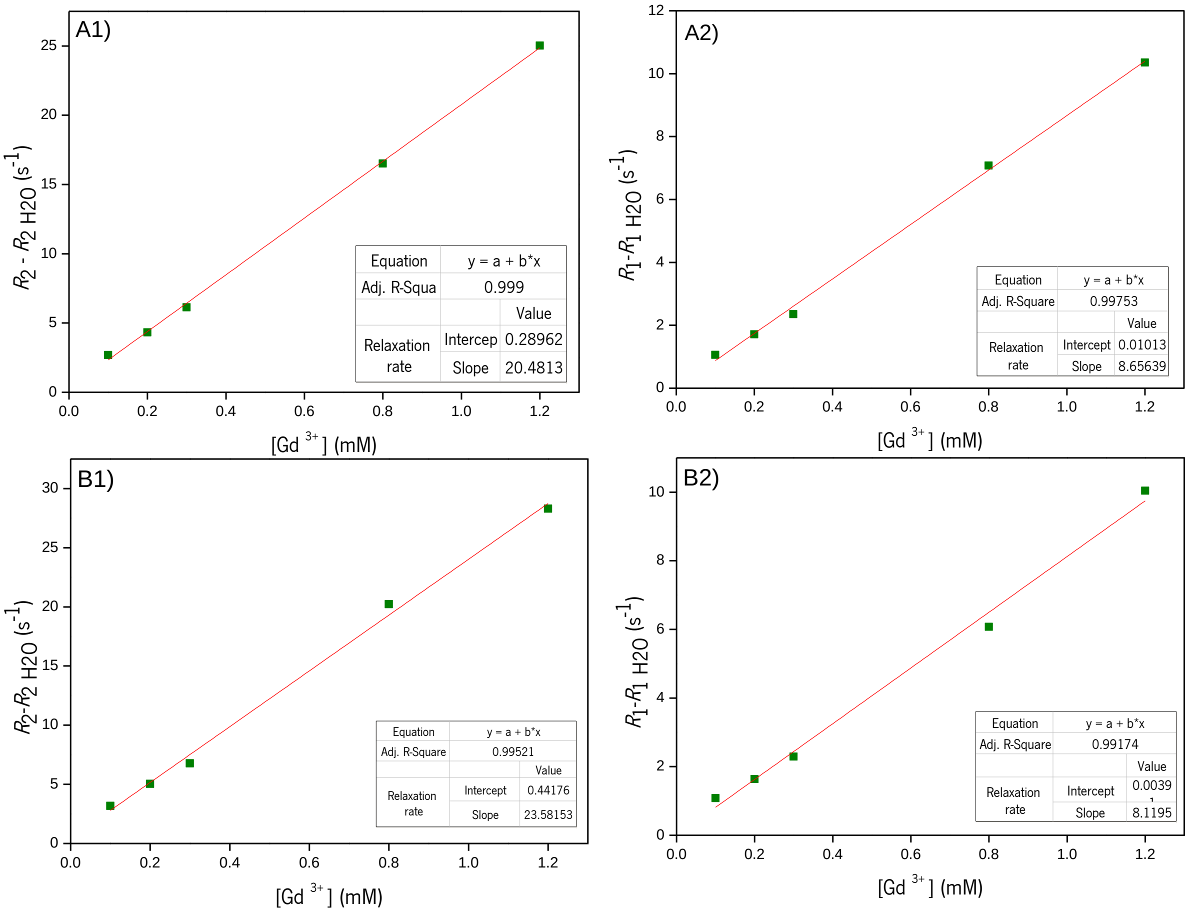

Figure 64 Gd concentration dependence of the paramagnetic relaxation rates $R_{1,2}$ (120 MHz, 37 °C) for paramagnetic hydrogels suc-NapPheΔPheOMe/H (**8** and **9**) (0.4 *wt* %): **A1)** R_2 Gd(Npx)@suc-NapPheΔPheOMe (**8**); **A2)** R_1 Gd(Npx)@suc-NapPheΔPheOMe (**8**); **B1)** R_2 Gd(Npx)@suc-NapPheΔPheOH (**9**); **B2)** R_1 Gd(Npx)@suc-NapPheΔPheOH (**9**). The full data set is presented in **annex Figure A11.1** (Gd(Npx)@hydrogels) and **annex Figure A11.2** (Gd(DOTA)@hydrogels).

The full data set of measured relaxivities ($r_{1,2}$) is summarized in **Table 8**.

Table 8 Relaxivity values (120 MHz, 37 °C) for paramagnetic hydrogels (0.4 *wt*%), with incorporated Gd(Npx) and Gd(DOTA) complexes (0.1 - 1.2 mM).

	r_1 ($mM^{-1}s^{-1}$)		r_2 ($mM^{-1}s^{-1}$)		r_2/r_1		Δr_1 (%)	
Complex@hydrogel	Gd(Npx)	Gd(DOTA)	Gd(Npx)	Gd(DOTA)	Gd(Npx)	Gd(DOTA)	Gd(Npx)	Gd(DOTA)
suc-PheΔPheOMe (5)	7.6±0.2	5.0±0.2	9.4±0.4	4.8±0.2	1.2	1.0	31.9	63.5
suc-PheΔPheOH^a (6)	5.7±0.2	5.1±0.3	7.2±0.5	3.8±0.2	1.3	0.8	-1.2	64.5
suc-NapΔPheOMe (13)	7.0±0.3	5.7±0.2	13.0±0.7	4.8±0.4	1.9	0.8	20.9	85.0
suc-NapΔPheOH (14)	8.8±0.2	4.7±0.3	21.0±1.2	4.3±0.2	2.4	0.9	53.7	52.4
suc-NapPheΔPheOMe (8)	8.7±0.22	5.9±0.4	20.5±0.3	5.3±0.1	2.4	0.9	50.9	92.2
suc-NapPheΔPheOH (9)	8.1±0.4	4.6±0.4	23.6±0.8	4.1±0.2	2.9	0.9	41.5	49.2
suc-PheNapΔPheOMe(16)	6.4±0.5	5.3±0.2	12.6±0.6	4.7±0.2	2.0	0.9	10.8	71.0
suc-PheNapΔPheOH (17)	7.9±0.2	3.7±0.3	22.7±1.2	4.1±0.3	2.9	1.1	37.8	20.2
H_2O	5.7±0.3	3.1±0.2	14.71±0.5	4.8±0.3	2.6	1.6	0	0

^{a}Measured as viscous solution

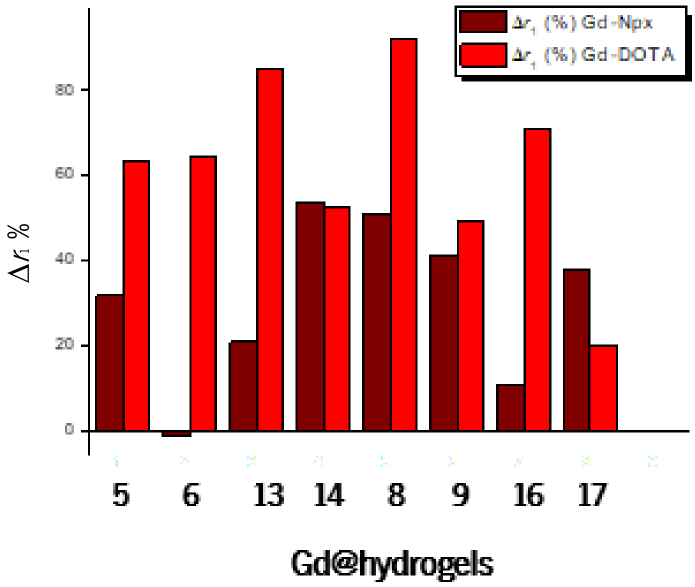

Figure 65 Percentage variation of longitudinal relaxivity r_1 for the paramagnetic hydrogels in relation to the Gd(Npx) and Gd(DOTA) complexes in aqueous solution: Gd(DOTA)@hydrogel (red bars); Gd(Npx)@hydrogel (bourdoux bars).

In general, both series of paramagnetic hydrogels, with incorporated Gd(Npx) and Gd(DOTA) complexes show a significant enhancement of longitudinal relaxivity upon incorporation into the hydrogels (**Figure 65**). The r_1 enhancement observed for the Gd(DOTA) complex in the suc-PheΔPheOH (**6**) hydrogelator solution suggests longer chelate tumbling times possibly associated to viscosity effects derived from hydrogelator fibres in solution. Within each ester/dicarboxylic acid hydrogelator pair, the methyl ester hydrogel shows consistently higher r_1 relaxivity, suggesting a rough correlation with hydrogel elasticity. As the hydrophilic Gd(DOTA) complex is not prone to undergo association (co-assembly) with the hydrogel fibres it is likely that the observed hydrogel effects on the relaxivity derive from chelate slower tumbing rates in the entangled hydrogel matrix. Interestingly, incorporation of the Gd(Npx) complex in the suc-PheΔPheOH (**6**) hydrogelator solution has a negligible effect on the longitudinal relaxivity. The relaxivity effects observed for the hydrogels with incorporated Gd(Npx) are related to hydrogel microstructure and properties. Overall, the moderate enhancement of longitudinal relaxivity observed for all gels, can not be correlated with gel elasticity. It is noteworthy, that the enhancement of longitudinal relaxivity observed for the hydrogels with incorporated Gd(Npx) complex is accompanied by a substantial enhancement of transversal relaxivity. For the hydrogels with incorporated Gd(DOTA) complex the enhancement of tranversal relaxivity is insignificant. This suggests that the increase of longitudinal relaxivity observed for the hydrogels with incorporated Gd(Npx) complex results from complex self-assembly on the surface of the hydrogel fibers and its effect on the tumbling rate.

Effect of hydrogelator concentration on the properties of paramagnetic hydrogels Gd(Npx)@hydrogel as CA for MRI

The effect of hydrogelator concentration on the properties of the paramagnetic hydrogels as MRI CA was studied at a fixed complex concentration ([Gd]= 0.8 mM) by varying the concentration of the dipeptide hydrogelators couple suc-PheΔPheOMe/H (**5** and **6**) and the tripeptide hydrogelators pair suc-NapPheΔPheOMe/H (**8** and **9**) in the range 0.5 - 5 *wt* %. MRI $T_{1,2}$ phantoms and relaxation maps (120 MHz, 37 °C) were obtained for the paramagnetic hydrogels (see **annex Figure A12**). The dependence of the longitudinal water proton R_1 relaxation rates on hydrogelator concentration is represented in **Figure 66**.

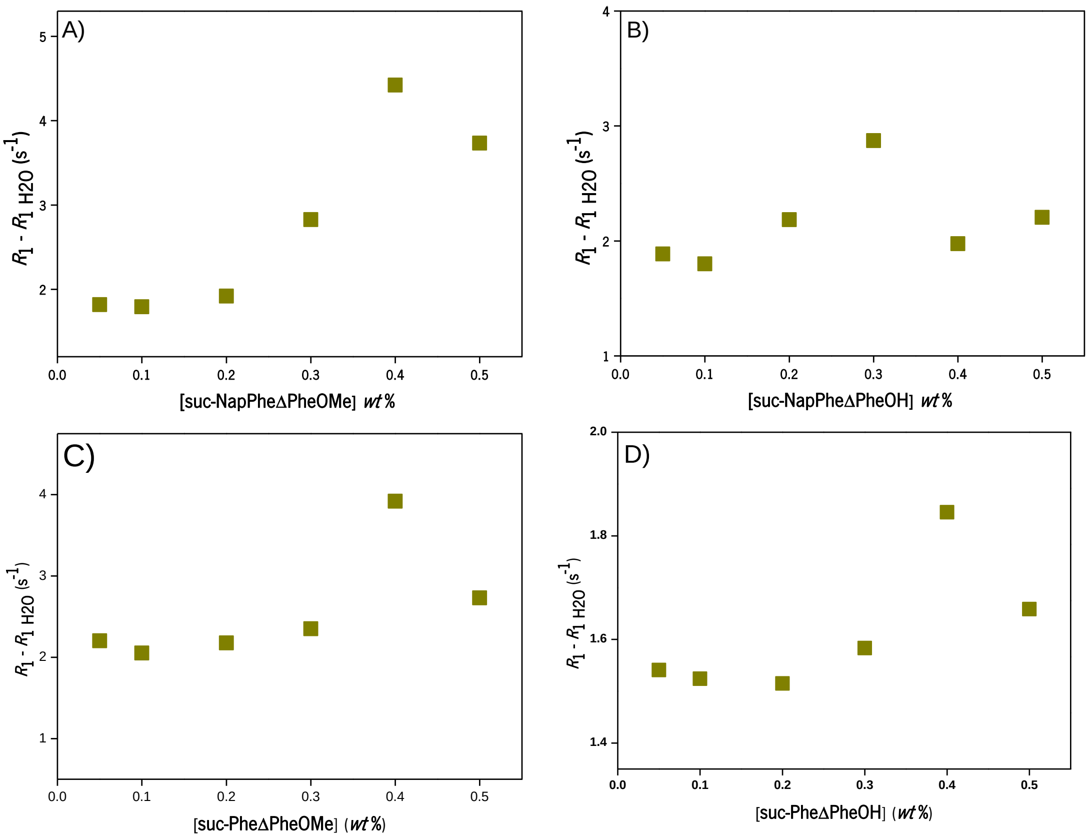

Figure 66 Hydrogelator concentration dependence of the longitudinal water proton relaxation rate R_1 (s^{-1}) for hydrogels with incorporated Gd complex (0.8 mM): **A)** suc-NapPheΔPheOMe (**8**); **B)** suc-NapPheΔPheOH (**9**), **C)** suc-PheΔPheOMe (**5**), **D)** suc-PheΔPheOH (**6**).

Overall, the longitudinal relaxation rate seems to follow the same trend for all hydrogelators. In solution, bellow hydrogelator concentration 0.3 *wt* %, R_1 seems to be concentration independent. Thereafter, R_1 increases, reaching a maximum for hydrogelator concentrations around the *cgc* (0.3 - 0.4 *wt* %) (**Figure 66**). Interestingly, hydrogelator suc-PheΔPheOH (**6**), which fails to gellate follows the same trend. The rheology studies indicate that although a direct relation between hydrogel concentration and elastic modulus G' (at 1 Hz) can not be established gels display the same structure irrespective of concentration. It is likely that increasing hydrogelator´s concentration leads to higher hydrogel network density, which can restrict complex rotation or promote hydrogel association with the fibre. Limited water diffusion above the *cgc* can lead to relaxivity reduction.

2.8 Hyperthermia studies

In previous studies our research group demonstrated that self-assembled hydrogels based on naproxen *N*-capped dehydrodipeptides could be made responsive to external magnetic fields by incorporation of SPION. The magnetic hydrogels displayed MRI reporting properties allied to magnetic hyperthermia.[57]

The library of hydrogels produced in this work displays interesting rheological properties, especially thermal-mechanical recovery, which suggests *in vivo* applications as injectable materials for magnetic hyperthermia-activated drug delivery applications.

In this thesis, the hyperthermia properties of magnetic hydrogels (0.4 *wt* %), with incorporated SPION (14 and 42 *wt* %$_{Fe}$; equivalent to 0.56 and 1.68 mg/ml of SPION Fe, respectively) were evaluated under magnetic excitation with an alternating field (H= 250 G, *f* = 869 kHz) (**Figure 67** and **Table 9** and **10**).

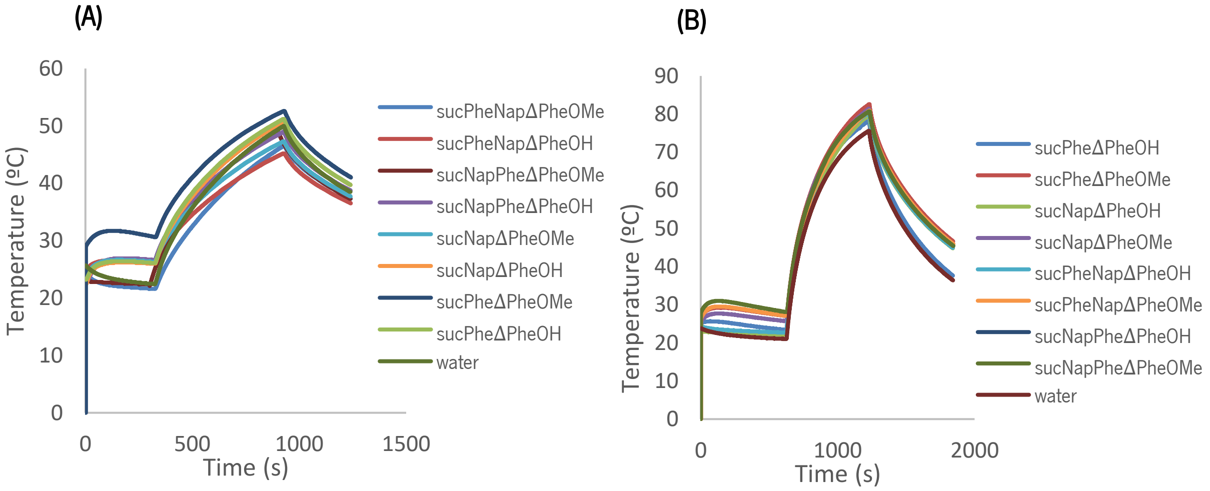

Figure 67 Hyperthermia curves for hydrogels (0.4 *wt* %) under excitation with an AC magnetic field (H=250 G, f = 869 kHz): **A**) 14 *wt* % SPION; **B**) 42 *wt* % SPION.

The hyperthermia heating curves display the characteristic shape of the calorimetric method.[93] The hydrogels loaded with higher SPION concentration (42 *wt* %$_{Fe}$) reach much higher temperatures (around 85 °C) than the hydrogels loaded with 14 *wt* %$_{Fe}$ (around 50 °C). In general, temperatures around 42 °C are sufficient to induce apoptosis of cancer cells. The parameter specific absorption rate (*SAR*) measures the transduction efficiency of the magnetic field energy into heat by magnetic nanoparticles (**Equation 15**).

$$SAR = \frac{C}{m(\frac{Fe}{sol})}\frac{dT}{dt}$$

Equation 15

C (J/(cm^3.°C)) represents the specific heat capacity of the magnetic nanoparticles solution; *m* (g) represents the mass fraction of iron in the hydrogel; d*T*/d*t* is the slope of the initial rate of temperature rise obtained from the temperature (°C) *vs* time (s) curve.

SAR values were calculated using the specific heat capacity of pure water (4.186 J/(cm^3.°C)). The hydrogelator (0.4 *wt* %) is unlikely to change significantly the specific heat capacity of water as the hydrogels are more than 99.5 *wt* % water. A preliminary DSC experiment (results not shown) with a hydrogel (0.4 *wt* %) loaded with 14 *wt* % SPION supports this assumption. The calculation of the parameter d*T*/d*t* from the hyperthermia heating curves is illustrated in **Figure 68**.

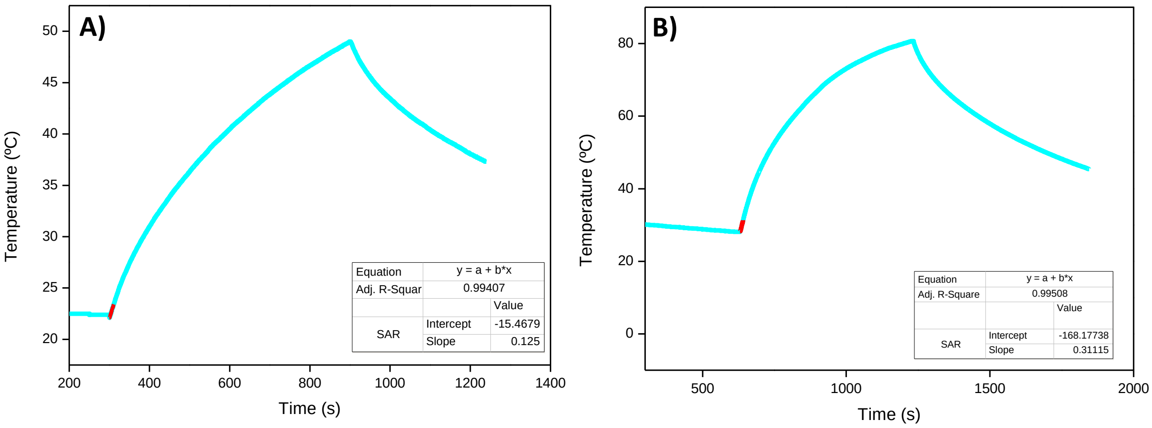

Figure 68 Methodology employed to calculate the parameter d*T*/d*t* from hyperthermia heating curves. Illustrative examples of hyperthermia heating curves are shown for the magnetic hydrogel suc-NapPheΔPheOMe (**8**) with: **A**) 14 *wt* % incorporated SPION; **B**) 42 *wt* % incorporated SPION. Data for the remaining hydrogels can be found in **annex Figure A13.1** and **13.2**.

The results of the hyperthermia experiments for the hydrogel´s library (0.4 *wt* %) loaded with SPION, 14 *wt* % and 42 *wt* % are summarised in **Table 9** and **10**, respectively.

Table 9 Hyperthermia characterization of hydrogels (0.4 *wt* %) loaded with SPION (14 *wt* %).

Hydrogelator 0.4 *wt* %	m Fe (g)	m Fe/m sol (g)	dT/dt (°C/s)	⊿T(°C)	SAR (W/g)	ΔSAR (%)
suc-PheΔPheOMe (5)	0.00056	0.000888	0.0969±0.00030	22	456.91	-19.782
suc-PheΔPheOH^a (6)	0.00056	0.000865	0.1096±0.00038	25	530.31	-6.8951
suc-NapΔPheOMe (13)	0.00056	0.000906	0.0903±0.00038	20.9	417.28	-26.739
suc-NapΔPheOH (14)	0.00056	0.000881	0.1180±0.00044	24.6	560.72	-1.5557
suc-NapPheΔPheOMe (8)	0.00056	0.000877	0.1250±0.00029	23.7	596.79	4.77637
suc-NapPheΔPheOH (9)	0.00056	0.000874	0.0910±0.00045	22.2	435.96	-23.46
suc-PheNapΔPheOMe (16)	0.00056	0.000892	0.0880±0.00027	24.8	412.84	-27.519
suc-PheNapΔPheOH (17)	0.00056	0.000884	0.0753±0.00026	19.2	356.69	-37.377
SPION (aqueous solution)	0.00056	0.000931	0.1240±0.00054	27.5	569.58	0

*SPION concentration expressed as % (m/m) in relation to hydrogelator´s weight, equivalent to *circa* 0.088 *wt* % in relation to hydrogel´s weight.
^{a}Measured as viscous solution

Table 10 Hyperthermia characterization of hydrogels (0.4 *wt* %) loaded with SPION (42 *wt* %).

Hydrogelator 0.4 *wt* %	m Fe (g)	m Fe/ m sol (g)	dT/dt (°C/s)	⊿T(°C)	SAR (W/g)	ΔSAR (%)
suc-PheΔPheOMe (5)	0.00168	0.002709	0.3441±0.0016	54.8	531.75	13.28
suc-PheΔPheOH^a (6)	0.00168	0.002695	0.3678±0.0014	53.1	571.21	21.69
suc-NapΔPheOMe (13)	0.00168	0.002733	0.3216±0.0012	54.2	492.49	4.92
suc-NapΔPheOH (14)	0.00168	0.002812	0.3657±0.0016	56	544.44	15.98
suc-NapPheΔPheOMe (8)	0.00168	0.002849	0.3115±0.0012	52.4	457.62	-2.51
suc-NapPheΔPheOH (9)	0.00168	0.002835	0.3130±0.0012	52.5	462.16	-1.54
suc-PheNapΔPheOMe (16)	0.00168	0.002809	0.3097±0.0011	53.7	461.46	-1.69
suc-PheNapΔPheOH (17)	0.00168	0.002781	0.3472±0.0013	56.1	522.52	11.31
SPION (aqueous solution)	0.00168	0.002840	0.3185±0.0017	52.9	469.41	0

*SPION concentration expressed as % (m/m) in relation to hydrogelator´s weight, equivalent to *circa* 0.28 *wt* % in relation to the hydrogel weight.
^{a}Measured as viscous solution

A higher *SAR* value was determined for SPION (in water) at 14 *wt* % Fe concentration (569.58 W/g) comparing to the 42 *wt* % SPION concentration (469.41 W/g). The hydrogels with incorporated 14 *wt* % SPION reach a temperature in the range 47 - 52 °C (ΔT ~ 30 °C) while the hydrogels loaded with 42 *wt* % SPION attain temperatures of the order of magnitude 75 °C (ΔT ~50 °C) upon magnetic irradiation (H= 250 G, *f* = 869 kHz) for 10 minutes. (**Figure 68**, **Table 9** and **10**).

The *SAR* dependence on the SPION concentration suggests SPION aggregation, more noticeable for the higher SPION concentration, under magnetic field excitation.[94] The *SAR* value obtained for the SPION concentration 14 *wt* $\%_{Fe}$ (569.58 W/g) is within the range expected for spherical magnetite multicore nanoparticle assembles with a nominal nanoparticle size *circa* 8 nm.[95] The effect of

SPION (14 and 42 *wt* %) incorporation into the hydrogels (0.4 *wt* %) on the efficacy of the nanoparticles as heat generators was evaluated as percentage variation of *SAR* in relation to SPION in water (**Figure 69**).

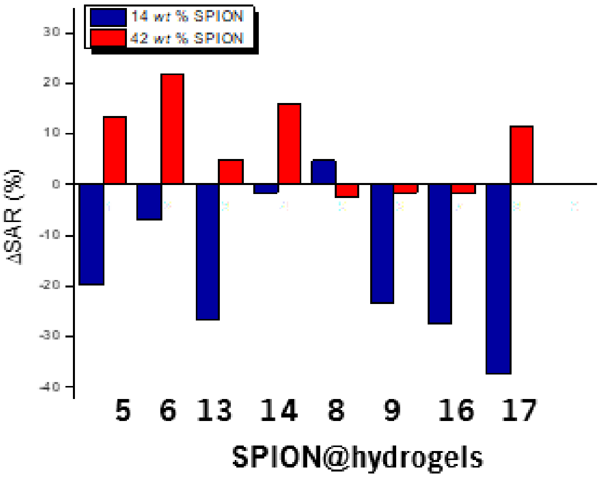

Figure 69 Percentage variation of the parameter *SAR* for hydrogels (0.4 *wt* %) with incorporated SPION in relation to SPION in water. **Blue bars**: 14 *wt* % SPION; **Red bars**: 42 *wt* % SPION.

The effect of the hydrogels on the *SAR* parameter is determined by the SPION concentration. For the SPION concentration 14 *wt* % there is a clear trend for a significant reduction of *SAR* for the magnetic hydrogels, except for the hydrogel suc-NapPheΔPheOMe (**8**). For the 42 *wt* % SPION concentration, the dipeptide and tripeptide suc-PheNapΔPheOH (**17**) hydrogels show a moderate *SAR* enhancement in relation to SPION. The tripeptide hydrogels suc-NapPheΔPheOMe (**8**), suc-NapPheΔPheOH (**9**) and suc-PheNapΔPheOMe (**16**) have an insignificant negative effect (lower than - 3 %). It is noteworthy that, for the dipeptides (**5**, **6**, **13** and **14**) hydrogels with 14 *wt* % SPION incorporated, the methyl ester hydrogels provoke a higher *SAR* reduction than that observed for their dicarboxylic acid *C*-deprotected counterparts, while to the tripeptides (**8**, **9**, **16** and **17**) hydrogels the *SAR* reduction is higher with the *C*-deprotected hydrogels. For the hydrogels with 42 *wt* % SPION concentration is observed a general trend, where the *C*-deprotected hydrogels (**6**, **9**, **14** and **17**) have a higher *SAR* positive effect comparatively to their *C*-protected counterparts (**5**, **8**, **13** and **16**). The rheology experiments reveal that, in general, SPION incorporation (14 *wt* %) into the hydrogels (0.4 *wt* %) results in a considerable reduction of hydrogel elasticity (G´) (**Table 4** rheology). The most noticeable exception to this trend is the hydrogel suc-NapPheΔPheOH (**9**) for which a considerable increase of elasticity occurs upon SPION incorporation. A correlation between *SAR* and hydrogel elasticity can not be unambiguously established. The hydrogel pair suc-NapPheΔPheOMe/H (**8** and **9**), at 14 *wt* % SPION concentration, displays different *SAR* value, 596.79 and 435.96 W/g, respectively, despite similar elasticity (116 and 175 kPa, respectively). It is also relevant to point out that the hydrogelator suc-PheΔPheOH (**6**) display a similar extent of reduction of *SAR*, similar to other gels, despite not forming a hydrogel. SPION *SAR* reduction is generally associated to nanoparticle aggregation.[95] This suggests that there is a higher extent of nanoparticles aggregation for the hydrogels with the lower concentration of incorporated SPION. The effect of the 42 *wt* % SPION concentration on the rheological properties and hydrogel microstructure has not studied. The heating properties of SPION under an oscillating magnetic field are due two main magnetic relaxation mechanisms for the nanoparticle's magnetic moment: Nèel and Brownian relaxation. Nèel relaxation consists of the rotation of the nanoparticles magnetic moment between the magnetization easy directions, under the influence of the applied alternate magnetic field, without overall nanoparticle rotation in solution. The Nèel relaxation contribution to the *SAR* of a dispersion of magnetic nanoparticles is determined by their saturation magnetization (Ms), which is in turn determined by the nanoparticles ferrite spinel structure, size and anisotropy. Brownian relaxation is related to friction between suspended nanoparticles and the solvent, due to rotation of the whole nanoparticles as consequence of the torque forced by the alignment of the magnetic moment of the nanoparticles with the direction of the applied magnetic field. The *SAR* reduction observed for the hydrogels with 14 *wt* % SPION suggests that interaction of the nanoparticles with the hydrogel fibres reduces the contribution of Brownian relaxation to heat generation. This hypothesis is supported by the STEM images obtained for hydrogels (0.4 *wt* %) with 14 *wt* % incorporated SPION, which indicate association of the nanoparticles with the hydrogel fibers.

Effect of hydrogelator concentration on the hydrogels hyperthermia properties

The effect of the concentration of the tripeptide hydrogelators (**8**/**9**) and the dipeptides (**5**/**6**) on the hyperthermia properties of hydrogels loaded with 14 *wt* % SPION was studied in concentration range 0.05 - 0.6 *wt* % (**Figure 70**).

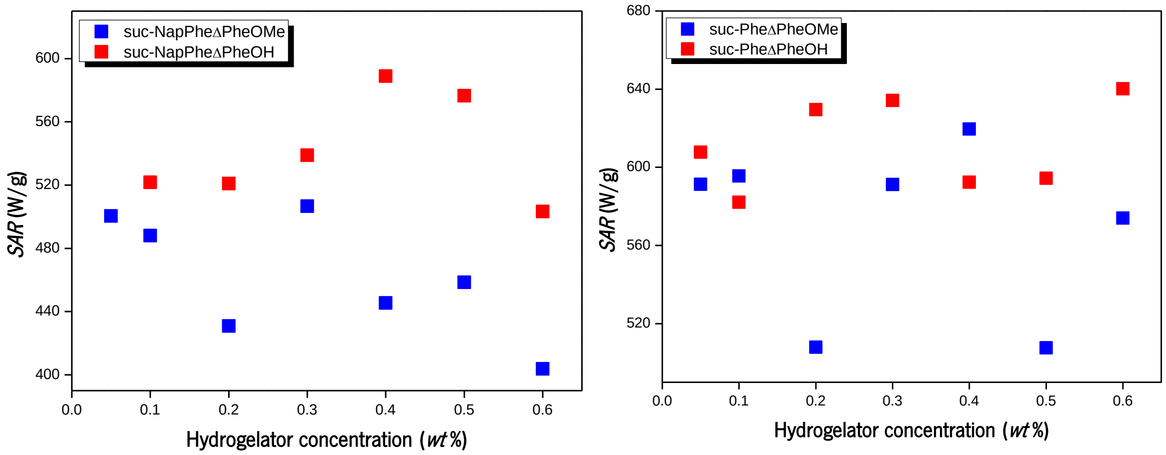

Figure 70 Hydrogelator concentration dependence of *SAR* (W/g) for hydrogels with incorporated SPION (14 *wt* %) in the hydrogelator concentration range 0.05 – 0.6 *wt* %: **A**) hydrogel couple suc-NapPheΔPheOMe/H (**8** - blue squares; **9**- red squares); **B**) hydrogel pair suc-PheΔPheOMe/H (**5** - blue squares; **6**- red squares).

The *SAR* dependence of the hydrogelator´s concentration shows curves with maximum *SAR* at hydrogelator concentrations around 0.3 *wt* % and 0.4 *wt* % - of the *cgc* order of magnitude. The STEM images of the magnetic hydrogels (0.4 *wt* %, 14 *wt* % SPION) suggest SPION association with the hydrogel fibers. Moreover, the hydrogelator suc-PheΔPheOH (**6**), despite not forming a hydrogel, shows a *SAR vs* hydrogelator concentration curve similar to the hydrogels. STEM images of solutions of this hydrogelator (0.4 *wt* %, 14 *wt* % SPION) show also self-assembled fibrilar structures with associated nanoparticles. The association of nanoparticles with hydrogel fibres in solution seems to have a *SAR* enhancing effect until reaching the *cgc.* Further fiber density increase of the hydrogel network above the *cgc* seems to reduce the Brownian contribution to *SAR* and lead to *SAR* reduction.

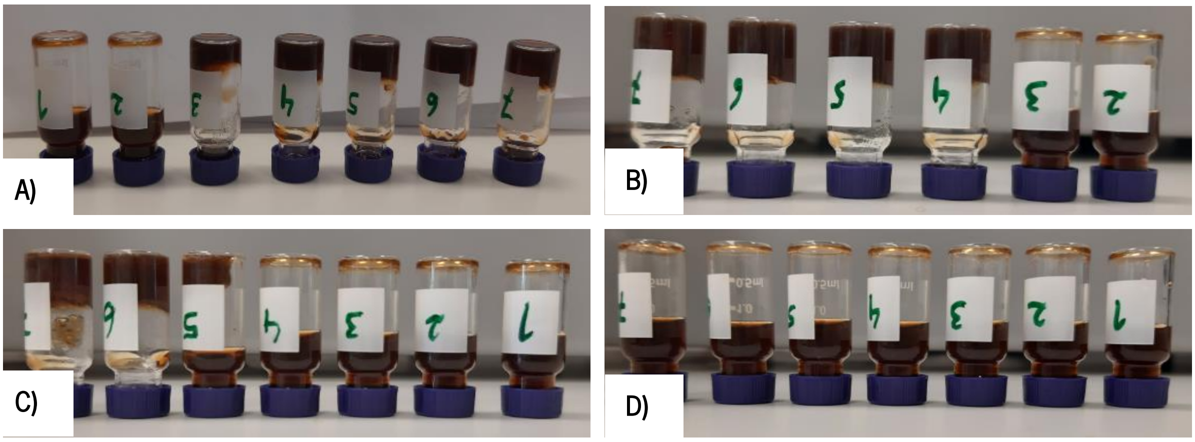

Figure 71 Photographs of hydrogel containing SPION (14 *wt* %) after hyperthermia measurements: **A**) suc-NapPheΔPheOMe (**8**); **B**) suc-NapPheΔPheOH (**9**); **C**) suc-PheΔPheOMe (**5**); **D**) suc-PheΔPheOH (**6**). The labels indicate hydrogelator concentration (*wt* %): **1**- 0.05 *wt* %; **2**- 0.1 *wt* %; **3**- 0.2 *wt* %; **4**- 0.3 *wt* %; **5**- 0.4 *wt* %; **6**- 0.5 *wt* %; **7**- 0.6 *wt* %.

Photographs of the suc-NapPheΔPheOMe (**8**) (**Figure 71A**) and suc-NapPheΔPheOH (**9**) (**Figure 71B**) hydrogels after hyperthermia, show that these hydrogels, at concentrations above the *cgc*, do not undergo gel-to-solution phase transition for temperatures of the order of magnitude 50 °C. The suc-PheΔPheOMe (**5**) (**Figure 71C**) hydrogel is thermally stable for hydrogelator concentrations above 0.4 *wt* %. Thermal stability has meaningful implications for *in vivo* applications of hydrogels as drug carriers for hyperthermia-triggered drug delivery. A gel-to-solution phase transition *in vivo* upon magnetic stimulation is undesirable, even for thermally reversible hydrogels, due to burst release of incorporated cargos and hydrogel loss. It is likely that thermally stable hydrogels can undergo temperature triggered structural changes that promote drug release without gel-to-solution transition, due to the nanoscale heating character of the MNPs-based hyperthermia.[95]

2.9 Hydrogels as nanocarriers for drug-delivery

Previous works from the research group established that naproxen and Cbz *N*-protected dehydropeptide-based hydrogels are effective drug carriers for drug-delivery applications.[24,15]

Pristine hydrogels (0.4 *wt* %) and magnetic hydrogels (0.4 *wt* % hydrogelator, 14 *wt* %$_{Fe}$ SPION) were studied as potential nanocarriers for drug delivery applications. The tripeptide couple suc-NapPheΔPheOMe/H (**8** and **9**) was selected as drug carrier owing to formation of highly elastic (strong) hydrogels (G´= 151 and 45.7 kPa, respectively). Moreover, their magnetic hydrogels (0.4 *wt* %

hydrogelator; 14 *wt* % SPION) not only (partially) retaim the elasticity of the pristine hydrogels but display enhanced elasticity (G' = 116 and 175 kPa, respectively). A panel of drug model molecules was selected for testing: methyl orange and methylene blue dyes and the antibiotic ciprofloxacin (**Figure 72**).

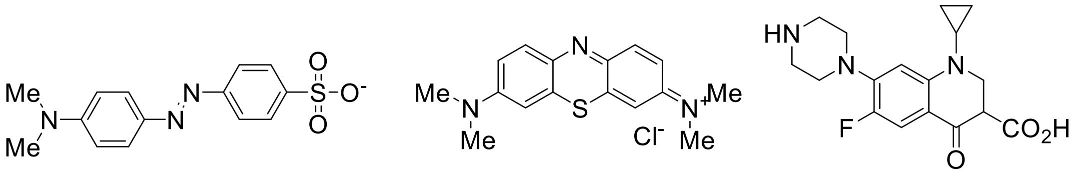

Metyl orange
MW= 301.45
LogP= 0.17

Methylene blue
MW= 284.41
LogP= 0.09

Ciprofloxacin
MW= 333.36
LogP= 0.82

Figure 72 Structure and molecular properties for the model drugs, methyl orange and methylene blue dyes and the antibiotic ciprofloxacin, selected for drug-delivery assays. Molecular properties calculated with the molinspiration online tool https://molinspiration.com/cgi-bin/properties.

This panel of hydrophilic drug model molecules allows exploring charge effects on the drug delivery properties of the hydrogels. The methyl orange dye, bearing a strong sulfonic acid functional group, display pH-independent negative charge. The methylene blue displays pH-independent positive charge. The ciprofloxacin antibiotic has both acidic, carboxylic acid (pKa = 6.09) and basic sites - nitrogen on piperazinyl ring (pKa = 8.74). The isoelectric point of ciprofloxacin is around 7.4, meaning that at pH 7.4 ciprofloxacin displays zwiterionic structure and overall neutral charge.[96] The methyl ester and the dicarboxylic acid hydrogelators suc-NapPheΔPheOMe/H (**8** and **9**) together with the drug panel can give insight into the interplay between hydrogel and drug charge on the drug delivery properties of the hydrogels. The effect of SPION on the drug delivery properties of the magnetic hydrogels is studied as well.

The dyes, methyl orange and methylene blue and the antibiotic ciprofloxacin, were loaded into hydrogels during the gelation procedure: hydrogelator suspensions, in an aqueous "drug" solution, were made soluble by adjustement to pH 9 - 10 with NaOH (1 M) followed by GdL triggered gelation. For drug release assays, drug-loaded hydrogels (0.85 ml) were prepared inside Pur-A-Lyser mini dialysis tubes (MWCO 12-14 kDa) and immersed into PBS buffer 10X (pH 7.4) (7 ml). Aliquots (200 µl) were removed at set time points and replaced with same volume of PBS buffer. (see annex **Figure A14**). Strong absorption in the visible region (λ_{max} = 465 and 666 nm for methyl orange and methylene blue, respectively) allows measuring the concentration of the released dyes by UV-Vis spectrophotometry without potential interference from released hydrogelator molecules. Ciprofloxacin was quantified by

HPLC with iscocratic elution (MeCN:H_2O, 0.1 *wt* % TFA) and UV-Vis detection at 280 nm. Drug release profiles were obtained for pristine hydrogels suc-NapPheΔPheOMe/H (**8** and **9**) (0.4 *wt* %) and for their magnetic equivalents (0.4 *wt* % hydrogelator, 14 *wt* %$_{Fe}$ SPION) loaded with the dyes methyl orange (0.0066 *wt* %) and methylene blue (0.0064 *wt* %) and the antibiotic ciprofloxacin (0.0067 *wt* %). **Figure 73.**

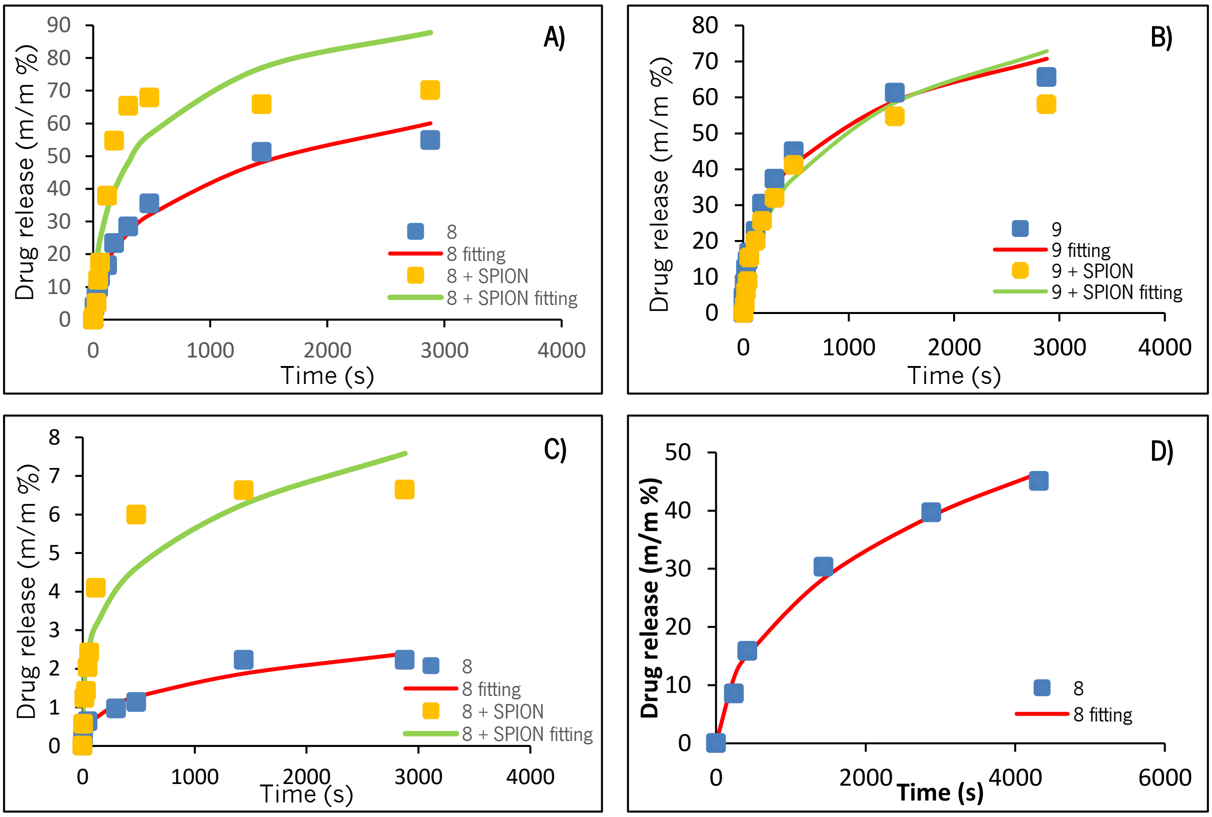

Figure 73 Drug release profiles for hydrogels suc-NapPheΔPheOMe/H (**8**/**9**) (0.4 *wt* %): **A)** pristine hydrogel **8** and its magnetic hydrogel equivalent (14 *wt* % SPION) with methyl orande dye; **B)** pristine hydrogel **9** and its magnetic hydrogel equivalent (14 *wt* % SPION) with methyl orande dye; **C)** pristine hydrogel **8** and its magnetic hydrogel equivalent (14 *wt* % SPION) with methylene blue dye; **D)** pristine hydrogel **8** with ciprofloxacin. The continuous lines are the fitting of the Weibull model to the experimental data.

Analysis of the release profile of the methyl orange-loaded hydrogels suc-NapPheΔPheOMe/H (**8**/**9**) (**Figure 73A** and **73B**) reveals initial burst release, aproximatelly 40 % of the methyl orange cargo is released after 8 hours, followed by a slower release phase, reaching 60 % cumulative release after 48 hours. The magnetic hydrogel suc-NapPheΔPheOMe (**8**) (14 *wt* % SPION), shows a more pronounced burst release phase releasing almost 70 % of the methy orange cargo after 8 hours. These results reflect the hydrophilicity and the negative charge of the methyl orange dye. Electrostatic repulsion presumably precludes tight association between the hydrogel fibres and the methylene orange molecule. The faster burst release observed for the magnetic hydrogel suc-NapPheΔPheOMe (**8**) (14 *wt* % SPION) suggests that the negatively charged SPION nanoparticles further contribute to methyl orange release through electrostatic repulsion. Interestingly, the release profiles for the hydrogels with incorporated methylene blue dye (**Figure 73C**) show very slow release: aproximatelly 2 % release for the non-magnetic hydrogel and around 7 % for the magnetic hydrogel (14 *wt* % SPION) after 24 hours. This suggests that attractive electrostatic interactions between the hydrogel fibres and the dye preclude release. Ciprofloxacin (**Figure 73D**) release displays an intermediate behaviour, between that seen for methyl orange and methylene blue: 16 % release after 7 hours, followed by a slower release phase, attaining 45 % cumulative releasing after 72 hours. This behaviour seems in accordance with the zwiterionic, overall neutral, structure of ciprofloxacin at pH 7.4.

The drug release model Weibull was used to fit the experimental drug release profiles to get insight into the drug release mechanisms.[97]

The Weibull mathemathic model is extensively used also to model drug release processes with polymer and self-assembled-based hydrogels (**Equation 15**).[97]

$$y = 1 - EXP(-a * x^b) \qquad \textbf{Equation 15}$$

a is the scale factor and *b* is the shape factor.

The value of *b* is an indicator of the drug transport mechanism: b < 0.75 indicates Fickian diffusion in the fractal or Euclidian spaces; 0.75 < *b* < 1 indicates a combination of Fickian difusian and Case II transport; b > 1 indicates a complex drug transport mechanism.[97]

The results of the drug release experiments for the non-magnetic (0.4 *wt* % hydrogelator) and magnetic hydrogels (0.4 *wt* % hydrogelator; 14 *wt* % SPION) with incorporated methyl orange dye, methylene blue dye and ciprofloxacin antibiotic are summarized in **Table 11**.

Table 11 Weibull release parameters for non-magnetic (0.4 *wt* % hydrogelator) and magnetic hydrogels (0.4 *wt* % hydrogelator; 14 *wt* % SPION) with incorporated methyl orange and methylene blue dyes and ciprofloxacin antibiotic (0.006 *wt* %).

			Weibull		
Drug	**Hydrogelator**	**SPION**	**a**	**b**	**R^2**
Methyl Orange	**8**	No	0.0195	0.4835	0.95
		Yes	0.0343	0.5167	0.80
	9	No	0.0302	0.4654	0.97
		Yes	0.0141	0.5687	0.92
Methylene blue	**8**	No	0.0014	0.3545	0.96
		Yes	0.0081	0.2854	0.93
Ciprofloxacin	**8**	No	0.0052	0.5732	0.99

Acceptable fittings of the Weibull model of the experimental drug-delivery data were obtained (R^2 values above 0.80). The magnetic hydrogels have a worst adjustment with this model than their non-magnetic hydrogel equivalent. The parameter *b* suggests that all the hydrogels have a transport mechanism that obeys to Fickian diffusion ($b < 0.75$).

The hydrogels are not suitable for sustained delivery of negatively charged drugs. The very slow release of the methylene blue suggests that the magnetic hydrogels are likely to be suitable vehicules for hyperthermia trigged drug delivery of positively charged drugs, for example doxorubicin.[98]

2.10 Cell Viability studies

The injectable properties of the hydrogels, established by rheological characterization, suggest many potential applications *in vivo*. Hydrogel nontoxicity and biocompatibility are essential requisites for relevant *in vivo* applications. Hydrogelators **5**, **6**, **8**, **9**, **13**, **14**, **16** and **17** were evaluated for their potential toxicity against the keratynocyte cell line HaCat (**Figure 74**).

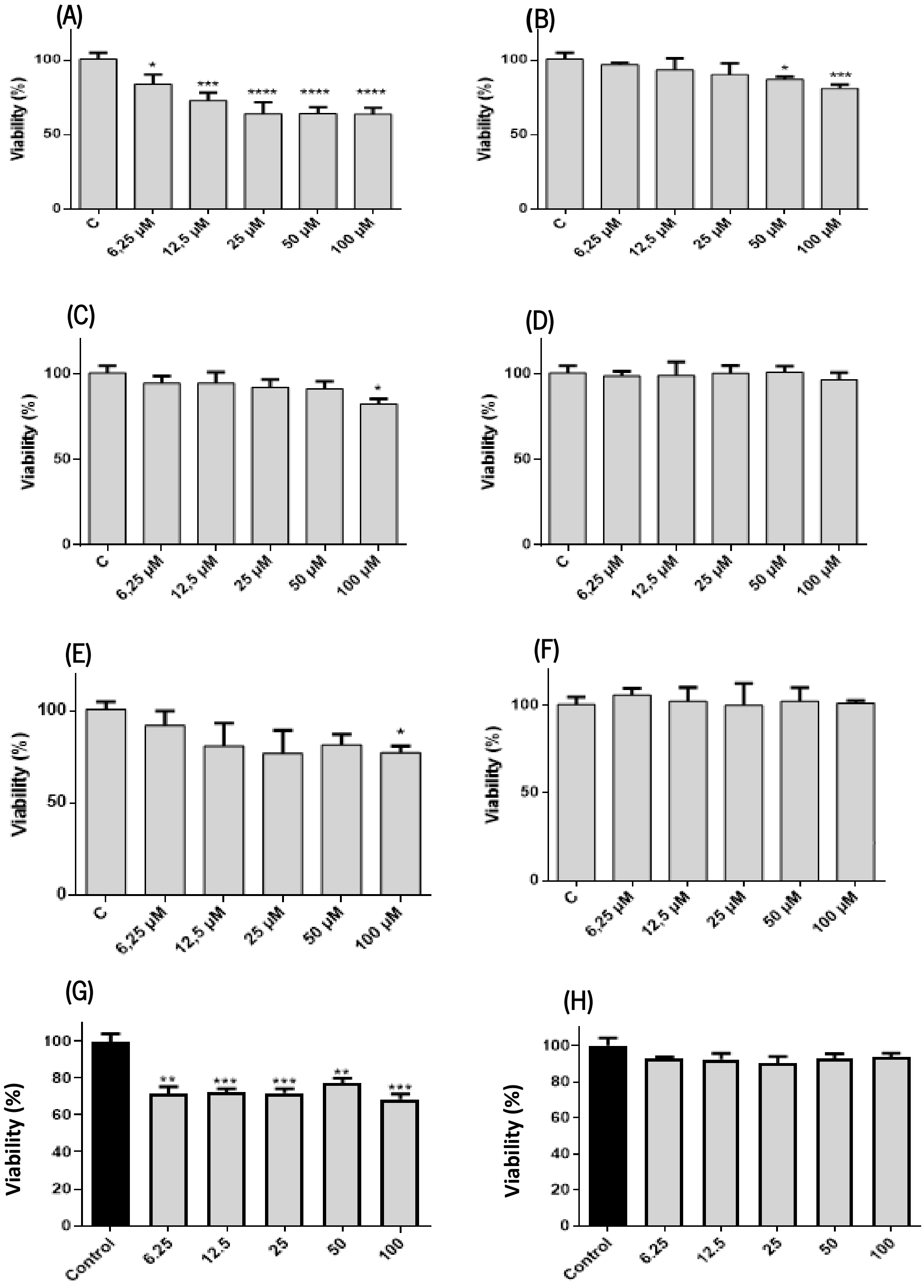

Figure 74 Viability of the keratinocyte cell line HaCat assessed with the MTT assay after for 24 hours incubation with hydrogelators: (**A**) suc-PheΔPheOMe (**5**); (**B**) suc-PheΔPheOH (**6**); (**C**) suc-NapΔPheOMe (**13**); (**D**) suc-NapΔPheOH (**14**); (**E**) suc-NapPheΔPheOMe (**8**); (**F**) suc-NapPheΔPheOH (**9**); (**G**) suc-PheNapΔPheOMe (**16**); (**H**) suc-PheNapΔPheOH (**17**).

As a general trend, the *C*-protected hydrogelators (**Figure 74A, 74C, 74E** and **74G**) show non-negligible, concentration dependent, effects on cell viability, while their dicarboxylic acid counterparts exhibit negligible toxicity. This effect can be related to the higher hydrophobicity of the *C*-protected hydrogelators, comparing to their dicarboxilic acid counterparts. Moreover, while the *C*-protected hydrogelators have a "detergent-like" structure, the dicarboxylic acid hydrogelators have "bolaamphiphile-type" structures. A detergente-like structure can presumably contribute to membrane diffusion and cell internalisation. Interestingly, the increase in hydrophobicity in the dicarboxylic acid hydrogelator series (from dipeptide to tripeptide) seems not to have any effect on the cell viability. In the *C*-deprotected hydrogelator series it is interesting to note the concentration independent loss of viability observed for the tripeptide suc-PheNapΔPheOMe (**16**) suggesting a toxicity mechanism different from the one lecited by the other hydrogelators.

2.11 *In vivo* studies - proof of concept

The concept of using magnetic hydrogels as theranostic agents, combining synergistic hyperthermia-activated thermal-chemotherapy with MRI imaging can be realized either by direct tumour injection or by hydrogel implantation into the resection cavity after surgery.[77,78]

Intratumoural hydrogel injection is appropriate for non-resectable tumours and for tumour size reduction before surgery. Tumour implantation is proposed for preventing tumour recurrence and metastases due to incomplete tumour removal during surgery.[77]

Injectable hydrogel-based theranostic platforms are challenging. The effect of incorporation of nanoparticles and drugs on the rheological properties of hydrogels is difficult to predict.[77]

Apart from the work described by our research group, reports on magneto-responsive self-assembled hydrogels are rare. Bing Xu originally reported a magneto-responsive hydrogel, obtained by co-assembly of a naphthalene acetic acid *N*-capped diphenylalanine hydrogelator with SPION decorated with cathecol-functionalised diphenylalanine. Very recently Ravoo and co-works reported a magnetoresponsive hydrogel by incorporation of unfunctionalised SPION into the hydrogel NapGlyPheTyrGlu. Both hydrogels display gel-to-solution phase transition upon exposure to a permanent magnet (static magnetic field). Bing Xu ascribed the hydrogel magnetic properties and responsiveness to co-assembly of the hydrogelator-functionalised SPION with the hydrogel fibres and to strong magnetic dipole interactions between the nanoparticles in the gel phase.[99] Ravoo attributed the magneto responsiveness to SPION mediated crosslinking of the hydrogel network, which resulted in improved hydrogel elasticity. Static magnetic field-enhanced drug delivery was demonstrated *in vitro* by Ravoo and co-workers.[100]

As far as we are aware peptide-based self-assembled magnetic hydrogels with self-healing (injectable) properties have not been reported.

Magnetic hydrogel suc-NapPheΔPheOMe (**8**) (0.4 *wt* % hydrogelator, 14 *wt* % SPION) was directly injected into a xenographt (cancer cell line CT26) mouse tumour model (**Figure 75**).

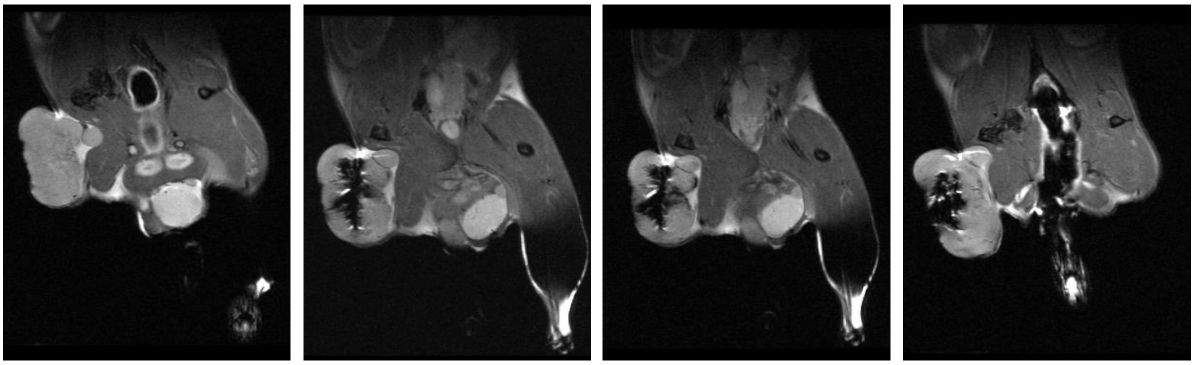

Before injection **20 minutes pi** **5 hours** **3 day pi**

Figure 75 MRI images (9.7 T) of mice with a xenograft tumour (cel line CT26) after intratumoural injection (50 µl) of magnetic hydrogel suc-NapPheΔPheOMe (**8**) (0.4 *wt* % hydrogel, 14 *wt* % SPION): top row- injected gel.

The *in vivo* MRI experiments with magnetic hydrogel suc-NapPheΔPheOMe (**8**) were performed at ICNAS (Coimbra, Portugal) by Dr. José Sereno and Professor Dr. Antero Abrunhosa.

Tumor and hydrogel volume were followed over time by $T_{2\text{-w}}$ MRI (9.7 T) at specified time points (**Figure 75**, **Table 12**).

Table 12 MRI time evolution of tumour size and hydrogel volume for a mouse injected with 50 µl of magnetic hydrogel suc-NapPheΔPheOMe (**8**) (0.4 *wt* % hydrogelator, 14 *wt* % SPION).

Time (hours)	Tumour (mm^3)	Hydrogel (mm^3)	Tumour/Hydrogel
Before injection	362.86	0	-
After injection	391	30.4	12.9
5	393.4	45	8.74
24	420	37	11.35
72		-	-

The objective of this study was to assess the feasibility of hydrogel injection and gelation *in vivo* and hydrogel retention in the tumour.

The T_{2w} MRI images in **Figure 75** outline the tumour as a clear mass. The injected hydrogel is clearly visible as a dark region corresponding to T_2 SPION-enhanced contrast. The hydrogel remains in the tumour for the time duration of the experiment, up to 3 days. The time evolution of the hydrogel volume suggests that the hydrogel is likely to remain in the tumour for an extended period. The initial increase of hydrogel volume following injection suggests *in vivo* hydrogel gelation.

These results indicate that intratumoural hydrogel injection is feasible and that the injected hydrogel remains in the tumour. The incorporated SPION allows following the fate of the hydrogel by T_{2w} MRI.

These results are a very promising step forward towards the full proof of concept of self-assembled magnetic hydrogels as cancer theranostic agents.

Chapter 3

Conclusions

3.1 Conclusions

Self-assembled peptide-based hydrogels are the novel paradigm biomaterials: synthetic versatility and amenability to automation, high water content and fibril structure reminiscent of the extracellular matrix, biocompatibility and degradability and responsiveness to environmental stimuli.

This Thesis contributes a new class of di- and tri-peptide succinic acid *N*-capped dehydropeptide hydrogelators (suc-Xaa-ΔPheOR and suc-Xaa-Xaa-ΔPheOR; suc - succinic acid, Xaa - Phe or 3-(2-naphthyl)-L-alanine; R- Me or H) to the growing field of self-assembled peptide hydrogels.

We envisaged that replacing the aromatic *N*-capping groups, usually used in the design of low molecular weight peptide self-assembled hydrogelators, by a succinic acid moiety would generate a new class of hydrogelators with “reversed polarity” and “bolamphiphile like” structure. The molecular design generated a focused library of hydrogelators which allowed us to explore the effect of peptide composition and sequence on the self-assembly, gelation and rheological properties of the hydrogels.

Self-assembly (UV-Vis, fluorescence and CD spectroscopy) studies revealed onset of molecular aggregation around pH 5, likely trigged by carboxylate protonation. The CD study indicates that the hydrogelator molecules in the self-assembled fibres display β-sheet and random coil secondary structure. All hydrogelators, except the least hydrophobic one (suc-PheΔPheOH (**6**)) afforded hydrogels at 0.3 *wt* % concentration via the GdL pH dropping methodology. The hydrogels display pH values around pH 5 in accordance with the fluorescence self-assembly studies.

Magnetic hydrogels (0.4 *wt* %) were prepared by incorporation of SPION (14 and 42 *wt* % Fe) during the gelation step. The incorporation of SPION did not abolish the gelation ability of the hydrogelators in the SPION concentrations studied.

The fibrillar nature of the non-magnetic (pristine) (0.4 *wt* %) and of the magnetic (with incorporated SPION) hydrogels (0.4 *wt* %, 14 *wt* % SPION_{Fe}) was confirmed by STEM microscopy studies. Both non-magnetic and magnetic hydrogels are made of fiber networks with different fiber thickness (around 20 - 30 nm) and length on the micrometer scale and variable fiber density. The STEM images suggest association of the SPION with the hydrogel fibers.

Rheological characterization of the non-magnetic (0.4 *wt* %) hydrogels revealed that the *C*-protected methyl ester hydrogels display stronger elasticity, better thermal stability and structural healing after breakup than their dicarboxylic acid *C*-deprotected counterparts. The PheΔPhe *motif* emerged as a privileged sequence for building hydrogels.

Incorporation of SPION (14 *wt* %) results in significantly slower gel setting kinetics and both weakening and reinforcing effects. All non-magnetic and magnetic hydrogels (0.4 *wt* %, 14 *wt* % SPION_{Fe})

are good candidates for injectable gel applications: the hydrogels rebuild after shear-induced breakup and remain solid-like for temperatures over 37 °C. A correlation between the chemical structure of the hydrogelator molecules and the effect of SPION on the rheological of the hydrogels could not be established.

The magnetic hydrogels (0.4 *wt* %) were characterized as potential contrast agents for T_{2w} MRI by relaxometry (1.5 T, 60 MHz, 37 °C) and MRI (3 T, 120 MHz, 37 °C) phantoms an $T_{1,2}$ relaxation maps. Despite subtle differences arising from the different magnetic field strengths and SPION concentrations used for both techniques, the magnetic hydrogels display significant concentration-dependent T_{2w} (dark) contrast enhancement and transversal relaxivity (r_2, mM^{-1}s^{-1}) values similar to the SPION in water. Paramagnetic hydrogels, with incorporated Gd(DOTA) and Gd(Npx) complexes were also studied as potential contrast agents for T_{1w} MRI, revealing concentration-dependent T_{1w} (bright) contrast enhancement and longitudinal relaxivity (r_1, mM^{-1}s^{-1}) values similar to the complexes in water. Therefore, both magnetic (with incorporated SPION) and paramagnetic (with incorporated Gd complexes) hydrogels are promising injectable contrast agents for MRI.

The heating efficacy of the magnetic hydrogels (0.4 *wt* %, 14 *wt* % SPION$_{Fe}$) was evaluated by the parameter Specific Absorption Rate (SAR, H = 250 G, f = 869 Hz). In general, the magnetic hydrogels display SAR values comparable to the SPION preparation in water. Hydrogel temperatures around 50 °C, suitable for cancer hyperthermia treatment, were attained upon magnetic excitation over 10 minutes. The non-magnetic (0.4 *wt* %) and magnetic hydrogels (0.4 *wt* %, 14 *wt* % SPION$_{Fe}$) were evaluated also as nano-carriers for drug-delivery using dyes (methyl orange and methylene blue) and the antibiotic ciprofloxacin as model drugs. Fickian diffusion was identified as the transport mechanism for all drugs incorporated both in non-magnetic and magnetic hydrogels. The hydrogels are not suitable for sustained delivery of negatively charged drugs due to burst release, as seen for the methyl orange cargo. However, the hydrogels revealed very slow release of the positively charged methylene blue dye, suggesting that magnetic hyperthermia could be used for on-demand drug delivery of positively charged drugs such as doxorubicin. Anny relevant biomedical application of the hydrogels are likely to be hampered by biocompatibility issue. Preliminary studies with the cell line HaCat revealed that the dicarboxylic acid *C*-deprotected hydrogelators are essentially nontoxic. The ester protected hydrogelators showed a low level of concentration-dependent toxicity. Further studies are necessary to understand the interplay between structure and toxicity mechanism.

As a step forward towards the *in vivo* proof-of-principle of "injectable magnetic hydrogels as theranostic cancer platforms", the magnetic hydrogel suc-NapPheΔPheOMe (**8**) (0.4 *wt* %, 14 *wt* %

SPION) was directly injected into a xenograft (cell line CT26) tumour bearing mouse. T_{2w} MRI monitoring confirmed the injectable properties and *in situ* recovery of the hydrogel and its tumour retention over 3 days.

This thesis sets the basis for development of "injectable magnetic hydrogels as theranostic cancer platforms".

Further studies require extensive *in vivo* experimentation. It is necessary to demonstrate hydrogels´ biocompatibility and establish their elimination route. It is also fundamental to demonstrate hyperthermia-triggered drug delivery from the hydrogels and synergistic thermo-chemotherapeutic capabilities. The MRI reporting properties of SPION are ideal to monitor the thermo-chemotherapeutic efficacy of the injected hydrogel platform and to adjust the therapeutic regime by external magnetic hyperthermia.

Chapter 4

Experimental procedures

4.1 Reagents and instrumentation

Analytical grade reagents were purchased from Sigma-Aldrich and Acros and used without further purification. Analytical grade solvents were used and dried by the usual methods when was needed. The petroleum ether used refers to the fraction having a boiling point of 40-60°C. Distilled water was always used for the reactions when aqueous medium was needed. The reactions were monitored by thin layer chromatography (TLC) on Merck-Kieselgel plates 60 F254 and detection was made by examination under UV light (240 nm) or by adsorption of iodine vapour. The organic phases were dried using anhydrous magnesium sulphate (Riedel) and carbonate of anhydrous potassium (Merck). Chromatographic separations were performed on silica MN Kieselgel 60 M (230-400 mesh). When solvent gradient was used, the increase of polarity was made from neat petroleum ether to mixtures of diethyl ether/petroleum ether, increasing 10% of diethyl ether each time until the isolation of the product.

The ^{1}H and ^{13}C NMR spectra (assigned by DEPT, HSQC and HMBC techniques) were recorded on a Bruker Avance III 400 spectrometer, operating at 400.13 MHz and 100.62 MHz, for ^{1}H and ^{13}C NMR respectively. The NMR spectra were recorded at 25°C and in some cases at 75°C, using the residual solvent signals as reference. Deuterated dimethyl sulfoxide (DMSO-d$_6$) and deuterated chloroform (CDCl$_3$-d$_1$) were used as solvents. Chemical shifts are given in parts per million (ppm) and the coupling constants in Hertz (Hz). HRMS data were recorded by the mass spectrometry service of the University of Vigo, Spain.
MS was recorded by a Thermo Finnigan LxQ (Linear Ion Trap) Mass Detector with Electro Spray Ionization (ESI).

CD spectra were recorded under N$_2$ on a Jasco J815 CD spectrometer. The samples used were solutions from dilutions of the preparation of the hydrogels.

MR imaging was performed in a 3.0 T horizontal bore MR Solutions Benchtop MRI system equipped with 48 G/cm actively shielded gradients. To image the samples, a 56 mm diameter quadrature birdcage coil was used in transmit/receive mode. For the phantom measurements, the samples at different concentrations (between 0-0.43 mM Fe) were dissolved in 200 µL of Milli-Q water in 300 µL tubes. All MR images of the phantoms were acquired with an image matrix 256 252, field of view (FOV) 60 60 mm, 3 slices with a slice thickness of 1 mm and 1 mm slice gap. For T2-weighted imaging, fast spin echo (FSE) sequences with the following parameters were used: TE = 15 ms, TR = 1500 ms, NA = 12, AT = 24m 48s. For T1-weighted imaging a FSE sequence with TE = 11 ms, TR = 400 ms, NA = 12 and AT= 7m 34s was used.

Relaxometre studies were carried out with a rheometer (MCR300, Anton Paar). Liquid samples were loaded into the Couette geometry of the rheometer and temperature was kept at 25 °C during testing. For the hydrogels kinetics, small amplitude oscillatory shear was applied during 60 000 seconds, with a frequency of 1 Hz and an amplitude varying from 0.0001% to 1 %, depending on the NP loading in sample. After the kinetics, mechanical spectra were recorded using the same strain amplitude as in the kinetics tests, by ramping the frequency from 100 Hz down to 0.01 Hz.

Scanning transmission electron microscopy images (STEM) were obtained on a JEOL JEM-2100 microscope at an accelerating voltage of 200 kV. The samples were prepared using a uranyLess staining. Using a carbon coated grid, 10µL of the hydrogel was placed and left for 30 seconds. The excess of water was removed using filter paper. The grid was washed with 10µL of uranyLess and water (2 times), always removing the excess with filter paper after 30 seconds.

4.2 Hydrogellators synthesis

Synthesis of Boc-Phe-Phe-OMe (3)

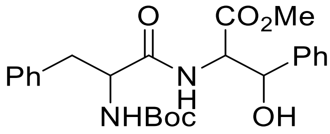

Boc-Phenilalanine (1.24 g, 4.67 mmol) was dissolved in MeCN (50 mL), in an ice bath. HBTU (4.77 mmol, 1.81 g), phenilserine methyl ester (in hydrochloride form) (1.08 g, 4.66 mmol) and TEA (13.95 mmol, 1.94 mL) were added. The solution was kept under magnetic stirring for 23 h. The solution was filtrated and the solvent was evaporated under reduced pressure. The residue was dissolved in ethyl acetate (100 mL) and it was filtrated. The filtrated was washed with $KHSO_4$ (3 x 50 mL), $NaHCO_3$ (3 x 50 mL) and brine (50 mL). The organic phase was dried with $MgSO_4$, filtrated and the solvent was evaporated under reduced pressure. It was obtained the compound (**3**) as a white foam (1.98 g, 4.47 mmol, 96.1 %).

^{1}H-NMR (400 MHz, DMSO): δ=1.27 (s,9H, Boc), 2.37-2.79 (m, 2H, CH_2β Phe), 3.66 (s, 3H, OMe), 4.58 (m, 1H, CHα PheSer), 5.17 (t, *J* = 3.8 Hz, 1H, CHα Phe), 5.97 (dd, *J* = 4.8 Hz and *J* = 8.8 Hz, 1H, OH), 6.70 (d, *J* = 8.8 Hz, 1H, CHβ PheSer), 6.99-7.29 (m, 10H, CH ar), 8.01 (d, *J* = 8.4 Hz, 1H, NH Phe), 8.22 (d, *J* = 8.8 Hz, 1H, NH PheSer).

Synthesis of Boc-PheΔPhe-OMe (4)

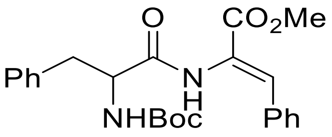

Compound (**3**) (1.97 g, 4.45 mmol) was dissolved in dry MeCN (10 mL). Boc$_2$O (5.54 mmol, 1.21 g) and DMAP (0.57 mmol, 0.07 g) were added. The solution was kept under magnetic stirring, at room temperature, and the reaction was followed by ^{1}H-NMR until all the reagents had been consumed (18 h). The *N,N,N',N'*-tetramethylguadinine (2 % in volume) was added, magnetic stirring was continued, and the reaction was followed by ^{1}H-NMR until all the reagent had been consumed (19 h). The solvent was evaporated under reduced pressure, the residue was dissolved in ethyl acetate (100 mL) and it was washed with KHSO$_4$ (3 x 50 mL), NaHCO$_3$ (3 x 50 mL) and brine (50 mL). The organic phase was dried with MgSO$_4$, filtrated and the solvent was evaporated under reduced pressure. It was obtained the compound (**4**) as a white solid (1.76 g, 4.15 mmol, 93.5 %).

^{1}H-NMR (400 MHz, DMSO): δ=1.31 (s, 9H, Boc), 2.79 (dd, *J* = 10.6 Hz and *J* = 13.6 Hz, 1H, CHβ Phe), 3.04 (dd, *J* = 3.6 Hz and *J* = 13.6 Hz, 1H, CHβ Phe), 3.69 (s, 3H, OMe), 4.33 (ddd, *J* = 4 Hz, 10.8 Hz and 14.4 Hz, 1H, CHα Phe), 7.07 (d, *J* = 8.4 Hz, 1H, CHβ PheSer), 7.19-7.37 (m, 10H, CH ar), 7.67 (m, 1H, NH Phe), 9.79 (s, 1H, NH PheSer).

Synthesis of suc-PheΔPhe-OMe (5)

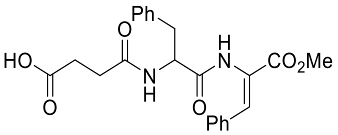

Compound (**4**) (0.72 g, 1.64 mmol) was dissolved in TFA (1 mL/mmol) and the solution was kept under stirring for 25 min. DCM (~5 mL) was added and the solvent was evaporated under reduced pressure. The same procedure was applied twice to obtain an oil. The residue was dissolved in pyridine (49.20 mmol, 3.98 mL) and succinic anhydrous (0.27 g, 2.70 mmol) was added. The solution was kept under magnetic stirring, at room temperature and under a N$_2$ atmosphere, for 22 h. DCM (100 mL) was added and the solution was washed with HCl (0.1 M) (3 x 50 mL) and brine (50 mL). The organic phase was dried with MgSO$_4$, filtrated and the solvent was evaporated under reduced pressure. The residue was dissolved in diethyl ether (~5 mL) and the solvent was evaporated under reduced pressure, obtaining the compound (**5**) as a white solid (0.58 g, 1.37 mmol, 83.5 %). Global yield: 75.0 %.

^{1}H NMR (400 MHz, DMSO, δ): 2.36 (m, 4H, CH$_2$ Suc), 2.81 (dd, *J* = 10.0 Hz and 14.0 Hz, 1H, CH$_2$β), 3.12 (dd, *J* = 4.4 Hz and 14.0 Hz, 1H, CH$_2$β), 3.71 (s, 3H, OMe), 4.67 (ddd, *J* = 4.8 Hz, 10.0 Hz and 12.8 Hz, 1H, CHα), 7.20 - 7.40 (m, 9H, CHβΔPhe and CH ar (meta and ortho)), 7.63 (t, *J* = 3.8 Hz, 2H, CH ar (para)), 8.27 (d, *J* = 8.4 Hz, 1H, NH), 9.80 (s, 1H, NH ΔPhe), 12.08 (brs, 1H, CO_2H).

^{13}C NMR (100.6 MHz, DMSO, δ): 29.10 (CH_2 Suc), 36.99 (CH_2β), 52.15 (OMe), 54.06 (CHα), 125.90 (CHβ ΔPhe), 126.30-131.89 (CH ar (*meta* and *ortho*)), 130.10 (CH ar (*para*)), 165.35 (C=O), 171.14 (C=O), 171.44 (CO_2Me), 173.67 (CO_2H).

HRMS (ESI) m/z: $[M + H]^+$ calc for $C_{23}H_{25}N_2O_6^+$, 425.1707; found, 425.1718.

Synthesis of suc-PheΔPhe-OH (6)

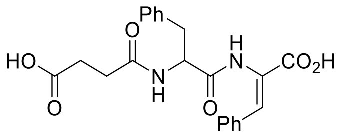

Compound (**5**) (0.25 g, 0.59 mmol) was dissolved in dioxane (5 mL) and NaOH (1 M) (2.30 mL) (pH~11). The solution was kept under magnetic stirring, at room temperature, for 18 h. The solvent was evaporated under reduced pressure, the residue was dissolved in water (~5 mL) and it was triggered the precipitation with HCl (6 M) (0.09 mL). The precipitated was filtrated, washed with ethanol and the solvent was evaporated under reduced pressure. The residue was dissolved in diethyl ether and the solvent was evaporated under reduced pressure. It was obtained the compound (**6**) as a white solid (0.19 g, 0.46 mmol, 78 %). Global yield: 58.5 %.

^{1}H NMR (400 MHz, DMSO, δ): 2.32 (m, 4H, CH_2Succ), 2.80 (dd, *J* = 10.4 Hz and 13.8 Hz, 1H, CH_2β), 3.12 (dd, *J* = 4.0 Hz and 13.8 Hz, 1H, CH_2β), 4.62 (ddd, *J* = 4.0 Hz, 8.4 Hz and 10.0 Hz, 1H, CHα), 7.16 - 7.36 (m, 9H, CHβΔPhe and CH Ph (meta and ortho)), 7.61 (dd, *J* = 2.4 Hz and 7.6 Hz, 2H, CH Ph (para)), 8.31 (d, *J* = 8.4 Hz, 1H, NH), 9.67 (s, 1H, NH ΔPhe), 12.39 (brs, 1H, CO_2H).

^{13}C NMR (100.6 MHz, DMSO, δ): 29.58 (CH_2 Suc), 37.00 (CH_2β), 54.27 (CHα), 126.24 (CHβ ΔPhe), 126.61-129.43 (CH ar (*meta* and *ortho*)), 130.02 (CH ar (*para*)), 131.91 (CO_2H), 166.16 (C=O), 171.12 (C=O), 171.18 (CO_2H), 173.76 (CO_2H).

HRMS (ESI) m/z: $[M + H]^+$ calc for $C_{22}H_{23}N_2O_6^+$, 411.1551; found, 411.1562.

Synthesis of Boc-NaphthylAla-PheΔPhe-OMe (7)

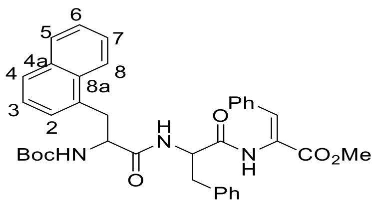

Compound (**4**) (1.05 g, 2.40 mmol) was dissolved in TFA (1 mL/mmol) and the solution was kept under stirring for 25 min. DCM (~5 mL) was added and the solvent was evaporated under reduced pressure. The same procedure was applied twice to obtain an oil. Compound (**10**) (0.78 g, 2.47 mmol) was dissolved in MeCN (30 mL), in an ice bath, and HBTU (0.7 g, 1.85 mmol), the oil solution (dissolved in MeCN (10 mL)) and TEA (7.17 mmol, 1 mL) were added with about 2 min between each addition. The solution was kept under magnetic stirring for 23 h (pH~7). The solution was put in an ice bath (30 min) and the precipitated was filtrated, obtaining the compound (**7**) as a white solid (0.82 g, 1.32 mmol, 55 %).

^{1}H NMR (400 MHz, DMSO, δ): 1.20 (s, 9H, Boc), 2.91 (dd, *J* = 9.8 Hz and *J* = 13.8 Hz, 1H, CHβ Phe), 3.05 (dd, *J* = 10.2 Hz and *J* = 13.8 Hz, 1H, CHβ Phe), 3.17 (dd, *J* = 4.2 Hz and *J* = 13.8 Hz, 1H, CHβ Nap), 3.31 (dd, *J* = 4.6 Hz and *J* = 13.8 Hz, 1H, CHβ Nap), 3.70 (s, 3H, OMe), 4.30 (dd, *J* = 5.6 Hz and *J* = 9.2 Hz, 1H, CHα Phe), 4.79 (dd, *J* = 8.8 Hz and *J* = 13.2 Hz, 1H, CHα Nap), 7.01 (d, *J* = 9.2 Hz, 1H, CHβ ΔPhe), 7.19-7.55 (m, 14H, ar, H2,H3, H6 and H7), 7.60 (d, *J* = 6.4 Hz, 1H, H4), 7.74 (d, *J* = 8 Hz, 1H, H5), 7.88 (d, *J* = 8 Hz, 1H, H8), 8.06 (d, *J* = 8 Hz, 1H, NH), 8.15 (d, *J* = 8.4 Hz, 1H, NH), 9.93 (s, 1H, NH ΔPhe).

^{13}C NMR (100.6 MHz, DMSO, δ): 28 (Boc), 34 (Cβ Nap), 37 (Cβ Phe), 50.1 (C OMe), 53 (Cα Nap), 55.2 (Cα Phe), 126.7 (C5), 128.3 (C8), 129.8 (C4), 154.9 (C=O), 165.3 (C=O), 171.1 (CO$_2$Me), 171.7 (C=O Boc).

HRMS (ESI) m/z: [M + H]$^+$ calc for C37H40N3O6$^+$, 622.2912; found, 622.2942.

Synthesis of suc-NaphthylAla-PheΔPhe-OMe (8)

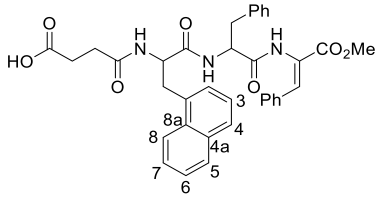

Compound (**7**) (0.69 g, 1.11 mmol) was dissolved in TFA (1 mL/mmol) and the solution was kept under stirring for 25 min. DCM (~5 mL) was added and the solvent was evaporated under reduced pressure. The same procedure was applied twice to obtain an oil. The residue was dissolved in pyridine (33.40 mmol, 2.70 mL) and succinic anhydrous (0.24 g, 2.40 mmol) was added. The solution was kept under magnetic stirring, at room temperature and under a N$_2$ atmosphere, for 24 h. DCM (100 mL) was added and the solution was washed with HCl (0.1 M) (3 x 50 mL) and brine (50 mL). The organic phase was dried with MgSO$_4$, filtrated and the solvent was evaporated under reduced pressure. The residue was dissolved in diethyl ether (~5 mL) and the solvent was evaporated under reduced pressure. It was obtained the compound (**8**) as a white solid (0.63 g, 1.01 mmol, 91 %). Global yield: 45.0 %.

^{1}H NMR (400 MHz, DMSO, δ): 2.16-2.29 (m, 4H, CH suc), 2.93(dd, *J* = 9.8 Hz and 13.8 Hz, 1H, CHβ Phe), 3.10 (dd, *J* = 9.8 Hz and 14.2 Hz, 1H, CHβ Nap), 3.16 (dd, *J* = 4.4 Hz and 14.0 Hz, 1H, CHβ Phe), 3.45 (dd, *J* = 4.2 Hz and 14.2 Hz, 1H, CHβ Nap), 3.70 (s, 3H, OMe), 4.65 (ddd, *J* = 4.4 Hz, 9.0 Hz and 13.0 Hz, 1H, CHα Phe), 4.72 (ddd, *J* = 4.6 Hz, 8.6 Hz and 12.6 Hz, 1H, CHα Nap), 7.21-7.37 (m, 11H, ar and H7), 7.62 (d, *J* = 7.6 Hz, 2H, H3 and H6), 7.73 (d, *J* = 8.0 Hz, 1H, H4), 7.87 (d, *J* = 7.6 Hz, 1H, Cβ ΔPhe), 8.10 (d, *J* = 8.4 Hz, 1H, NH), 8.19 (d, *J* = 8.4 Hz, 1H, NH), 8.27 (d, *J* = 8.0 Hz, 1H, H8), 9.83 (s, 1H, NH ΔPhe).

^{13}C NMR (100.6 MHz, DMSO, δ): 29.07 (C succ), 34.59 (Cβ Phe), 36.91 (Cβ Naph), 52.22 (Cα Naph), 53.18 (Cα Phe), 127.2 (C4), 128.5 (Cβ ΔPhe), 130.3 (C8), 165.37 (C=O), 171.06-171.40 (2 x C=O and CO_2Me), 173.80 (CO_2H).

HRMS (ESI) m/z: $[M + H]^+$ calc for C36H36N3O7$^+$, 622.2548; found, 622.2540.

Synthesis of suc-NaphthylAla-PheΔPhe-OH (9)

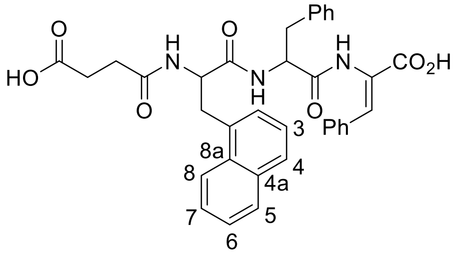

Compound (**8**) (0.1 g, 0.165 mmol) was dissolved in dioxane (5 mL) and NaOH (1 M) (1 mL) (pH~11). The solution was kept under magnetic stirring, at room temperature, for 18 h. The solvent was evaporated under reduced pressure, the residue was dissolved in water (~5 mL) and it was triggered the precipitation with HCl (6 M) (0.12 mL). The precipitated was filtrated and washed with ethanol. The solvent was evaporated under reduced pressure and the residue was dissolved in diethyl ether. The solvent was evaporated under reduced pressure and it was obtained the compound (**9**) as a white solid (0.09 g, 0.15 mmol, 97.4 %). Global yield: 43.8 %.

^{1}H NMR (400 MHz, DMSO, δ): 2.18 (s, 4H, CH$_2$Suc), 2.86-2.95 (m, 1H, CHβ Phe), 3.04-3.20 (m, 2H, CHβ Phe and CHβ Nap), 3.38-3.42 (m, 1H, CHβ Nap), 4.59-4.71 (m, 2H, CHα Phe and CHα Nap), 7.16-7.35 (m, 10H, ar), 7.50 (m, 1H, Cβ ΔPhe), 7.62 (s, 2H, H6 and H3), 7.71 (d, *J* = 6.8 Hz, 1H, H7), 7.86 (d, *J* = 5.6 Hz, 1H, H4), 8.04 (dd, *J* = 8.0 Hz and 16.0 Hz, 1H, H5), 8.27 (dd, *J* = 8.4 Hz and 12.0 Hz, 1H, H8), 8.58 (d, *J* = 8.4 Hz, 1H, NH), 9.67 and 9.71 (s, 1H, NH ΔPhe), 12.29 (brs, 1H, CO_2H).

^{13}C NMR (100.6 MHz, DMSO, δ): 29.07 (C succ), 34.70 (Cβ Nap), 37.00 (Cβ Phe), 53.27 (Cα Phe), 54.35 (Cα Nap), 123.80 (C7), 125.91 (C2), 127.33 (C4), 128.43 (C5), 129.99 (C8), 131.57 (Cβ ΔPhe), 166.13 (C=O), 170.96 (CO_2H), 173.70 (CO_2H).

HRMS (ESI) m/z: $[M + H]^+$ calc for C35H34N3O7$^+$, 608.2391; found, 608.2395.

Synthesis of Boc-NaphthylAla-Phe-OMe (11)

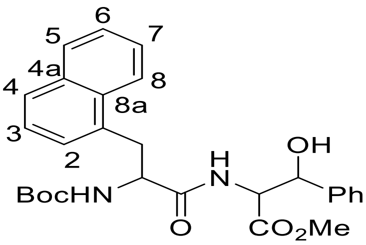

Boc-Naphtylalanine (1.70 g, 5.39 mmol) was dissolved in MeCN (50 mL), in an ice bath, and HBTU (2.34 g, 6.17 mmol), esther-phenilserine (1.22 g, 5.27 mmol) and TEA (15.73 mmol, 2.19 mL) were added. The solution was kept under magnetic stirring for 21 h. The solvent was evaporated under reduced pressure, the residue was dissolved in ethyl acetate (120 mL) and it was washed with $KHSO_4$ (3 x 50 mL), $NaHCO_3$ (3 x 50 mL) and brine (50 mL). The organic phase was dried with $MgSO_4$, filtrated and the solvent was evaporated under reduced pressure. It was obtained the compound (**11**) as a white solid (2.56 g, 5.20 mmol, 98.7 %).

^{1}H NMR (400 MHz, DMSO, δ): 1.26 (s, 9H, Boc), 2.87-3.02 (m, 1H, CHβ Nap), 3.11-3.22 (m, 1H, CHβ Nap), 3.63 (s, 3H, OMe), 4.64 (m, 1H, CHα Phe), 5.18 (m, 1H, CHα Nap), 6.01 (dd, *J* = 4.8 Hz and 6.8 Hz, 1H,OH), 7.14 (d, *J* = 6.8 Hz, 1H, CHβ Phe), 7.22-7.57 (m, 9H, H2, H3, H4, H6, H7 and ar), 7.89 (d, *J* = 8.4 Hz, 1H, H5), 8.00 (d, *J* =8 Hz, 1H, H8), 8.17 (d, *J* = 8.8 Hz, 1H, NH), 8.40 (d, *J* = 8.4 Hz, 1H, NH).

^{13}C NMR (100.6 MHz, DMSO, δ): 28 (C Boc), 35.1 (Cβ Nap), 52.2 (C OMe), 57.2 (Cα Phe)78.2 (Cα Nap), 123.5 (Cβ Phe), 127.3 (C5), 128.5 (C8), 170.4 (C=O), 171.8 (CO_2Me), 172.2 (C=O Boc).

HRMS (ESI) m/z: $[M + H]^+$ calc for $C28H33N2O6^+$,493.2333; found, 493.2327.

Synthesis of Boc-NaphthylAlaΔPhe-OMe (12)

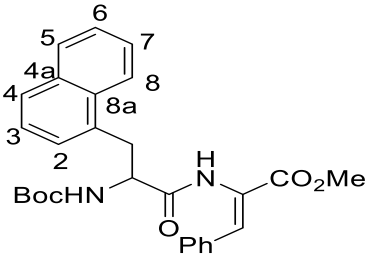

Compound (**11**) (2.10 g, 4.26 mmol) was dissolved in dry MeCN (15 mL) and Boc_2O (5.11 mmol, 1.12 g) and DMAP (0.51 mmol, 0.06 g) were added. The solution was kept under magnetic stirring, at room temperature, and the reaction was followed by ^{1}H-NMR until all the reactants had been consumed (19 h). The *N,N,N',N'*-tetramethylguadinine (2 % in volume) was added, magnetic stirring was continued, and the reaction was followed by ^{1}H-NMR until all the reactant had been consumed (22 h). The solvent was evaporated under reduced pressure, the residue was dissolved in ethyl acetate (100 mL) and it was washed with $KHSO_4$ (3 x 50 mL), $NaHCO_3$ (3 x 50 mL) and brine (50 mL). The organic phase was dried with $MgSO_4$, filtrated and the solvent was evaporated under reduced pressure. The compound (**12**) was obtained as a white foam (1. 66 g, 3.50 mmol, 82.2

%).

^{1}H NMR (400 MHz, DMSO, δ): 1.29 (s, 9H, Boc), 3.21 (dd, *J* = 10.4 Hz and *J* = 14.2 Hz, 1H, CHβ), 3.57 (dd, *J* = 3.6 Hz and *J* = 14.2 Hz, 1H, CHβ), 3.72 (s, 3H, OMe), 4.50 (ddd, *J* = 4.0 Hz, 10.2 Hz and *J* = 12.6 Hz, 1H, CHα), 7.18 (d, *J* = 8.8 Hz, 1H, CHβ ΔPhe), 7.29-7.59 (m, 9H, ar, H2, H3, H6 and H7), 7.67 (d, *J* = 7.6 Hz 1H, H4), 7.80 (d, *J* = 8 Hz, 1H, H5), 7.93 (d, *J* = 8 Hz, 1H, H8), 8.21 (d, *J* = 8.4 Hz, 1H, NH), 9.86 (s, 1H, NH ΔPhe).

^{13}C NMR (100.6 MHz, DMSO, δ): 28.1 (C Boc), 34.1 (Cβ Nap), 52.2 (C OMe), 78.2 (Cα), 123.7 (Cβ ΔPhe), 127 (C5), 128.5 (C8), 130.2 (C4), 155.4 (C=O), 165.3 (CO$_2$Me), 172.2 (C=O Boc).

HRMS (ESI) m/z: [M + H]$^{+}$ calc for C28H31N2O5^{+} ,475.2227; found, 475.2227.

Synthesis of suc-NaphthylAlaΔPhe-OMe (13)

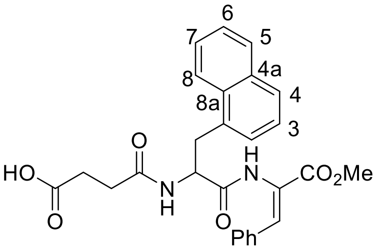

Compound (**12**) (0.6 g,1.26 mmol) was dissolved in TFA (1 mL/mmol) and the solution was kept under stirring for 25 min. DCM (~5 mL) was added and the solvent was evaporated under reduced pressure. The same procedure was applied twice to obtain an oil. The oil was dissolved in pyridine (37.09 mmol, 3 mL) and the succinic anhydrous (0.33 g, 3.33 mmol) was added. The solution was kept under magnetic stirring, at room temperature and under a N$_2$ atmosphere, for 24 h. DCM (100 mL) was added and it was washed with HCl (0.5 M) (3 x 50 mL) and brine (2 x 50 mL). The organic phase was dried, filtrated, the solvent was evaporated under reduced pressure. The residue was dissolved in diethyl ether, filtrated and compound (**13**) was obtained as a white solid (0.42 g, 0.89 mmol, 70.6 %). Global yield: 57.3 %.

^{1}H NMR (400 MHz, DMSO, δ): 2.28-2.41 (m, 4H, CH$_2$suc), 3.21-3.27 (dd, *J* = 9.0 Hz and 14.4 Hz, 1H, CH$_2$β), 3.58-3.62 (dd, *J* = 5.4 Hz and 14.4 Hz, 1H, CH$_2$β), 3.70 (s, 3H, OMe), 4.81 (ddd, *J* = 5.4 Hz, 8.4 Hz and 13.8 Hz, 1H, CHα), 7.24 (s, 1H, CHβ ΔPhe), 7.28-759 (m, 9H, H2, H3, H6, H7, CH ar), 7.81 (d, *J* = 7.6 Hz, 1H, H4), 7.93 (d, *J* = 8.0 Hz, 1H, H5), 8.24 (d, *J* = 8.4 Hz, 1H, H8), 8.28 (d, *J* = 8.0 Hz, 1H, NH), 9.81 (s, 1H, NH ΔPhe).

^{13}C NMR (100.6 MHz, DMSO, δ): 29.20 (C suc), 34.40 (Cβ Nap), 52. 3 (OMe), 53.56 (Cα), 123.87 (C8), 127.27 (C4), 128.57 (C5), 132.3 (Cβ ΔPhe), 165.15 (C=O), 171.29 (CO$_2$Me), 173.81 (CO$_2$H).

HRMS (ESI) m/z: [M + H]$^{+}$ calc for C27H27N2O6^{+}, 475.1864; found, 475.1860.

Synthesis of suc-NaphthylAlaΔPhe-OH (14)

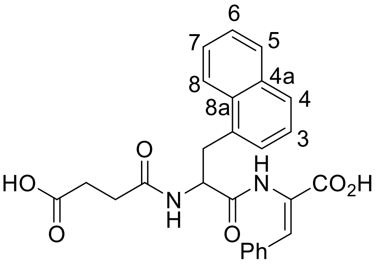

Compound (**13**) (0.09 g, 0.19 mmol) was dissolved in 1,4-dioxane (5 mL) and NaOH (1 M) (500 µL) (pH~11). The solution was kept under magnetic stirring, at room temperature, for 18 h. The solvent was evaporated, the residue was dissolved in water (~5 mL) and it was triggered the precipitation with HCl (6 M) (0.07 mL). The precipitated was filtrated and washed with ethanol. The solvent was evaporated under reduced pressure and the residue was dissolved in diethyl ether. The solvent was evaporated under reduced pressure and it was obtained the compound (**14**) as a white solid (0.08 g, 0.17 mmol, 89 %). Global yield: 51.0 %.

^{1}H NMR (400 MHz, DMSO, δ): 2.23-2.39 (m, 4H, CH$_2$suc), 3.20 (dd, *J* = 10 Hz and 14.4 Hz, 1H, CH$_2$β), 3.63 (dd, *J* = 4 Hz and 14.4 Hz, 1H, CH$_2$β), 4.79 (ddd, *J* = 4.4 Hz, *J* = 9.2 Hz and 13.2 Hz, 1H, CHα), 7.79 (d, *J* = 8 Hz, 1H, H4), 7.92 (d, *J* = 7.6 Hz, 1H, H5), 8.22 (d, *J* = 8 Hz, 1H, H8), 8.38 (d, *J* = 8.4 Hz, 1H, NH), 9.65 (s, 1H, NHΔPhe), 12.40 (brs, 1H, OH).

^{13}C NMR (100.6 MHz, DMSO, δ): 29.50 (Csuc), 34.38 (Cβ), 53.35 (Cα), 123.66 (C8), 127.07 (C4), 127.47 (C5), 166.15 (C=O), 171.19 (CO$_2$H), 173.81 (CO$_2$H).

HRMS (ESI) m/z: [M + H]$^+$ calc for C26H25N2O6$^+$, 461.1707; found, 461.1709.

Synthesis of Boc-PheNaphΔPheOMe (15)

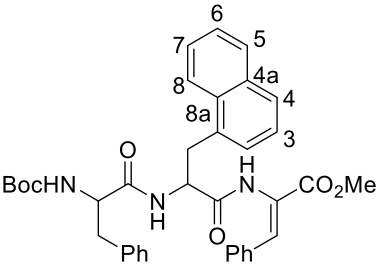

Compound (**12**) (1.426 g, 3.0 mmol) was dissolved in MeCN (40 mL), in an ice bath, and HBTU (1.28 g, 3.38 mmol), compound (**2**) (0.80 g, 3.02 mmol) and TEA (10.76 mmol, 1.50 mL) were added. The solution was kept under magnetic stirring for 20 h. The solvent was evaporated under reduced pressure, the residue was dissolved in ethyl acetate (120 mL) and it was washed with KHSO$_4$ (3 x 50 mL), NaHCO$_3$ (3 x 50 mL) and brine (50 mL). The organic phase was dried with MgSO$_4$, filtrated and the solvent was evaporated under reduced pressure. It was obtained the compound (**15**) as a white solid (1.449 g, 2.33 mmol, 78 %).

^{1}H NMR (400 MHz, DMSO, δ): 1.26 (s, 9H, Boc), 2.65 (m, 1H, CHβ Phe), 2.83 (dd, *J* = 3.6 Hz and 13.6 Hz, 1H, CHβ Phe), 3.32 (m, 1H, CHβ Nap), 3.58 (dd, *J* = 5.6 Hz and 14 Hz, 1H, CHβ Nap), 3.68 (s, 3H, OMe), 4.17 (ddd, *J* = 4 Hz, 9 Hz and 14 Hz, 1H, CHα Nap), 4.89 (dd, *J* = 7.8 Hz and 13.6 Hz, 1H, CHα Phe), 6.88 (d, *J* = 8.8. Hz, 1H, CHβ ΔPhe), 7.14-7.59

(m, 15H, H2, H3, H4, H6, H7 and ar), 7.82 (d, *J* = 8 Hz, 1H, NH), 7.95 (d, *J* = 7.6 Hz, 1H, H5), 8.30 (t, *J* = 7.4 Hz, 1H, H8), 9.92 (s, 1H, NH ΔPhe).

HRMS (ESI) m/z: $[M + H]^+$ calc for C37H40N3O6$^+$, 622.2912; found, 622.2935.

Synthesis of suc-PheNaphΔPheOMe (16)

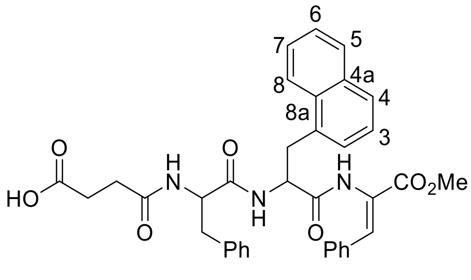

Compound (**15**) (1.023 g, 1.65 mmol) was dissolved in TFA (1 mL/mmol) and the solution was kept under stirring for 25 min. DCM (~5 mL) was added and the solvent was evaporated under reduced pressure. The same procedure was applied twice to obtain an oil. The oil was dissolved in pyridine (49.46 mmol, 4 mL), succinic anhydrous (0.302 g, 3.02 mmol) was added and the solution was kept under magnetic stirring, at 40 °C and under a N_2 atmosphere, for 20 min. Temperature was removed and the solution was going on under magnetic stirring and N_2 atmosphere for 20 h. DCM (100 mL) was added and it was washed with HCl (0.5 M) (3 x 50 mL) and brine (2 x 50 mL). The organic phase was dried, filtrated, the solvent was evaporated under reduced pressure. The residue was dissolved in diethyl ether, filtrated and compound (**16**) was obtained as a white solid (0.729 g, 1.17 mmol, 71 %). Global yield: 45.0 %.

^{1}H NMR (400 MHz, DMSO, δ): 2.27 (m, 4H, CH_2suc), 2.69 (dd, *J* = 9.8 Hz and 13.8 Hz, 1H, CH_2β Phe), 2.95 (dd, *J* = 4.4 Hz and 14.0 Hz, 1H, CH_2β Phe), 3.31 (dd, *J* = 8.6 Hz and 14.2 Hz, 1H, CH_2β Nap), 3.52 (m, 1H, CH_2β Nap), 3.69 (s, 3H, OMe), 4.51 (ddd, *J* = 4.4 Hz, 9.4 Hz and 13 Hz, 1H, CHα Nap), 4.84 (dd, *J* = 8.4 Hz and 14 Hz, 1H, CHα Phe), 7.15-7.59 (m, 15H, CHβ ΔPhe, H2, H3, H6, H7 and ar), 7.81 (m, 1H, H4), 7.95 (d, *J* = 7.2 Hz, 1H, H5), 8.03 (d, *J* = 8.4 Hz, 1H, NH), 8.28 (d, *J* = 8.4 Hz, 1H, H8), 8.38 (d, *J* = 8.0 Hz, 1H, NH), 9.84 (s, 1H, NHΔPhe).

^{13}C NMR (100.6 MHz, DMSO, δ): 29.6 (C suc), 34.8 (Cβ Nap), 37.90 (Cβ Phe), 51.5 (C OMe), 53.70 (Cα Phe), 54.80 (Cα Nap), 123.7 (C8), 127.3 (C4), 128.6 (C5), 129.2 (Cβ ΔPhe), 165.30 (C=O), 170.92 (C=O), 171.38 (CO_2Me), 173.77 (CO_2H).

HRMS (ESI) m/z: $[M + H]^+$ calc for C36H36N3O7$^+$, 622.2548; found, 622.2561.

Synthesis of suc-PheNaphΔPheOH (17)

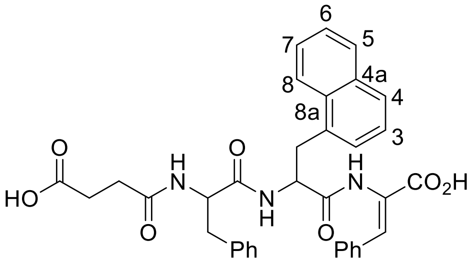

Compound (**16**) (0.371 g, 0.596 mmol) was dissolved in dioxane (5 mL) and NaOH (1 M) (5.96 mmol, 3 mL) (pH~11). The solution was kept under magnetic stirring, at room temperature, for 18 h. The solvent was evaporated, the residue was dissolved in water (~5 mL) and it was triggered the precipitation with HCl (6 M) (0.07 mL). The precipitated was filtrated and washed with ethanol. The solvent was evaporated under reduced pressure and the residue was dissolved in diethyl ether. The solvent was evaporated under reduced pressure and it was obtained the compound (**17**) as a white solid (0.342 g, 0.563 mmol, 94 %). Global yield: 42.2 %.

^{1}H NMR (400 MHz, DMSO, δ): 2.26 (m, 4H, CH_2suc), 2.66 (m, 1H, CH_2Phe), 2.93 (dd, *J* = 4 Hz and 13.6 Hz, 1H, CH_2Phe), 3.21 (dd, *J* = 10.8 Hz and 13.6 Hz, 1H, CH_2Nap), 3.67 (m, 1H, CH_2Nap), 4.48 (m, 1H, CHα Nap), 4.81 (m, 1H, CHα Phe), 6.89 (d, *J* = 6.4 Hz, 1H, CHβ ΔPhe), 7.06-7.15 (m, 4H, H2, H3, H6, and H7), 7.30-7.59 (m, 10H, ar), 7.79 (t, *J* = 8 Hz, 1H, H4), 7.94 (t, *J* = 7.6 Hz, 1H, H5), 8.09 (d, *J* = 8.4 Hz, 1H, NH), 8.24 (d, *J* = 8 Hz, 1H, H8), 8.46 (d, *J* = 8.0 Hz, 1H, NH), 9.68 (s, 1H, NH ΔPhe), 12.41 (brs, 2H, OH).

^{13}C NMR (100.6 MHz, DMSO, δ): 29.05 (C suc), 34.45 (CH_2 Nap), 37.50 (CH_2 Phe), 53.40 (Cα Phe), 53.87 (Cα Nap), 123.7 (C8), 126.2 (C2), 127.1 (C4), 127.5 (C7), 127.9 (C6), 128.5 (C5), 129.0 (C3), 129.2 (Cβ ΔPhe), 166.08 (C=O), 170.81 (CO_2H), 173.73 (CO_2H).

HRMS (ESI) m/z: $[M + H]^+$ calc for $C_{35}H_{34}N_3O_7^+$, 608.2391; found, 608.2398.

4.3 Synthesis of the Gd-Npx complex

Synthesis of methyl (2-(6-methoxynaphthalen-2-yl)propanoyl)serinate (20)

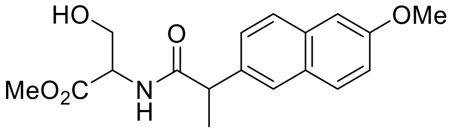

Naproxen (3,27 mmol, 754 mg) was dissolved in dichloromethane (70 mL) in an ice bath. HOBt (1 eq., 3,27 mmol, 441 mg), DCC (1 eq., 3,27 mmol, 675 mg), triethylamine (3 eq., 9,81 mmol, 1,4 mL) and serine methyl ester hydrochloride (1 eq., 3,27 mmol, 506,9 mg) were added to the solution. The solution was kept under magnetic stirring overnight at room temperature. The precipitated urea was filtered, and the solvent was evaporated under reduced pressure. The solid was dissolved in acetone and the solution was stored in the freezer for 2h. The urea was filtered again, and the solvent was evaporated under reduced pressure. The solid obtained was dissolved in ethyl acetate (70 mL) and organic phase was washed with $KHSO_4$ (1M) (3x50 mL), $NaHCO_3$ (1M) (3x50 mL) and brine (3x50 mL) and dried with $MgSO_4$. After filtration, the solvent was evaporated under reduced pressure to afford the product (**20**) as white solid as a diastereomeric mixture (1,04 g, 96%).

^{1}H NMR (400 MHz, $CDCl_3$): δ= 1.39 (d, 3H, *J*= 7,2 Hz, CH_3 Npx), 3.64 (s, 3H, OMe), 3.84 (m, 3H, OMe Npx;), 3.90 (m, 1H, CH Npx), 4.29 (m, 1H, αCH), 5,01 (m, 2H, βCH_2 ΔSer), 6.42 (d, 1H, *J*=7,2 Hz, NH), 7.10-7.13 (m,2H, Ar), 7.39-7.42 (m, 1H, Ar), 7.64-7.68 (m, 3H, Ar).

HRMS (ESI) m/z: $[M + H]^+$ calc for C18H22NO5, 332.1492; found, 332.1494.

Synthesis of methyl 2-(*N*-(*tert*-butoxycarbonyl)-2-(6-methoxynaphthalen-2-yl)propanamido)acrylate (21)

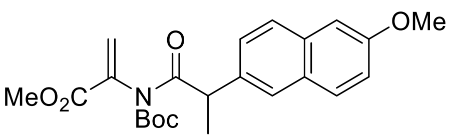

Compound **20** (1,00 g, 3,02 mmol) was dissolved in dry acetonitrile (10 mL). To the solution was added Boc_2O (3 eq., 9,06 mmol, 1,975 g) and DMAP (0,1 eq. Boc_2O, 0,906 mmol, 110,5 g). The solution was kept under magnetic stirring overnight at room temperature. Dehydration was confirmed by ^{1}H NMR. The solvent was evaporated under reduced pressure, dissolved in ethyl acetate (150 mL) and washed with $KHSO_4$ (1M) (3x30 mL), $NaHCO_3$ (1M) (3x30 mL) and brine (3x30 mL) and dried with $MgSO_4$. After evaporating the solvent, the product was obtained a yellow crystal as a diastereomeric mixture (1,054 g, 2,55 mmol, 84,4 %).

^{1}H NMR (400 MHz, $CDCl_3$): δ= 1.35 (s, 9H, CH_3Boc), 1.57 (d, 3H, *J*=7,2 Hz, CH_3 Npx), 3.61 (s, 3H, OMe), 3.85 (s, 3H, OMe Npx), 5.66 (s, 1H, βCH), 6.32 (s, 1H, βCH), 7.12-7.15 (m,2H, Ar), 7.34-7.37 (m, 1H, Ar), 7.76-7.79 (m, 3H, Ar).

HRMS (ESI) m/z: $[M + H]^+$ calc for C23H27NNaO6, 436.1731; found, 436.1732.

Synthesis of methyl 2-(N-(*tert*-butoxycarbonyl)-2-(6–methoxynaphthalen-2-yl)propanamido)-3-(1,4,7,10-tetraazacyclododecan-1-yl)propanoate (22)

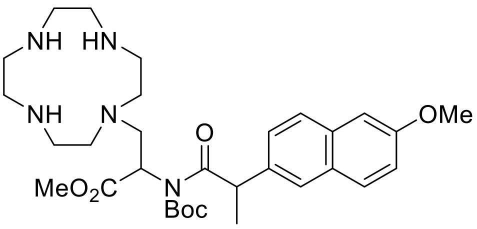

Cyclen (1 eq., 2,24 mmol, 388 mg) was dissolved in acetonitrile (30 mL) for 1h. To this solution was added K_2CO_3 (4 eq., 8,96 mmol, 1,24 g).

Compound **21** (924 mg, 2,24 mmol) was dissolved in dry acetonitrile (10 mL) and added to the cyclen solution solution drop by drop. The solution was kept under magnetic stirring overnight at room temperature. The solvent was evaporated under reduced pressure. The oil was purified by flash chromatography using as eluent a mixture dichloromethane:ethanol (35:15) followed by a mixture dichloromethane : ethanol : NH_3 : H_2O (35: 15: 1: 4). The chromatography fractions were analysed by TLC with revelation by iodine adsorption. The relevant fractions were pooled, and the solvent was evaporated under reduced pressure. The reaction product was obtained a yellow oil (905 mg, 1,58 mmol, 70,5%).

^1H NMR (400 MHz, $CDCl_3$): δ= 1.29 (s, 9H, CH_3Boc), 1.48 (m, 3H, CH_3 Npx), 2.55-2.85 (m, 18 H, $N(CH_2CH_2)N$ and βCH_2), 3.70 (s, 3H, OMe), 3.91 (s, 3H, OMe Npx), 5.20 (m, 1H, CH Npx), 5,37 (m, 1H, αCH), 7.10-7.13 (m,2H, Ar), 7.39-7.42 (m, 1H, Ar), 7.64-7.68 (m, 3H, Ar).

HRMS (ESI) m/z: $[M + H]^+$ calc for C31H48N5O6, 586.3599; found, 586.3577.

Synthesis of triethyl 2,2`,2``-(10-(3-methoxy-2-(2-(6-methoxynaphthalen-2-yl)propanamido)-3-oxopropyl)-1,4,7,10- tetraazacyclododecane-1,4,7-triyl)triacetate (23).

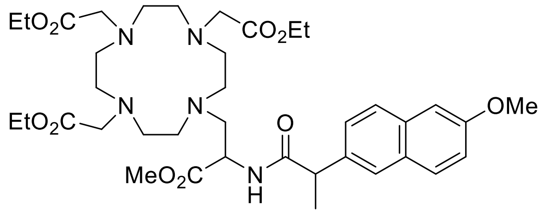

Compound **22** (892 mg, 1,56 mmol) was dissolved in a mixture dichloromethane: trifluoroacetic acid (5:1) and the solution was under magnetic agitation during 4h. The solvent was evaporated and the solid was dissolved in acetonitrile (30 mL). To this solution was added K_2CO_3 (10 eq., 15,6 mmol, 2,155 g) and ethyl bromoacetate (3,6 eq., 5,62 mmol, 626 μL). The solution was kept under magnetic stirring overnight at room temperature. The reaction was followed by TLC using as eluent dichloromethane: ethanol (10: 1). The insoluble salts were filtered out, and the solvent was evaporated under reduced pressure. The solid was dissolved in ethyl acetate (150 mL) and washed with $KHSO_4$ (1M) (3x30 mL), $NaHCO_3$ (1M) (3x30 mL) and brine (3x30 mL) and dried with $MgSO_4$. The solvent was evaporated under reduced pressure to give the product as a yellow solid (875 mg, 1,18 mmol, 75,6%).

^1H NMR (400 MHz, $CDCl_3$): δ= 1,19-1,57 (m, 12H, $CO_2CH_2\underline{CH_3}$, CH_3 Npx), 2,32-3,2 (m, 24H, cyclene CH_2, CH_2-N, $CH_2\beta$), 3,67 (s, 3H, OMe), 4,0-4,25 (m, 6H, $CO_2\underline{CH_2}CH_3$), 3,88 (s, 3H, OMe Npx), 4,2 (m, 1H, CH Npx), 4,4 (m, 1H, CHα), 7,08 (m, 2H, Ar), 7,62 (m, 1H, Ar), 7,69 (m, 3H, Ar).

HRMS (ESI) m/z: $[M + H]^+$ calc for C38H58N5O10, 744.4178; found, 744.4178.

Synthesis of 2,2`,2``-(10-(2-carboxy-2-(2-(6-methoxynaphthalen-2-yl)propanamido)ethyl)-1,4,7,10-tetraazacyclododecane-1,4,7-triyl)triacetic acid (24).

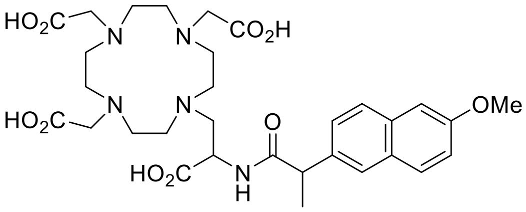

Compound **23** (790 mg, 1,06 mmol) was dissolved in a mixture water/ethanol (20/30). Strongly basic resin Dowex-1X2-OH^- was added until pH ~ 8-9 (pH paper). The mixture was kept under gentle shaking for 4 hrs at room temperature. The resin was transferred to a column, washed with water and eluted with HCl (0,1 M). The fractions from the column were analysed by TLC using as eluent a mixture of dichloromethane: ethanol: ammonia: water (5: 2: 1: 1) with revelation by iodine vapour adsorption. The relevant fractions were put together and the solvent was evaporated under reduced pressure. The metal chelator (**24**) was obtained in the hydrochloride form as a white solid (540 mg, 0,84 mmol, 79,2%). Global yield: 34.2 %.

^1H NMR (400 MHz, $CDCl_3$): δ= 1,56 (d, 3H, *J*= 6,8 Hz, CH_3 Npx), 2,32-3,9 (m, 24H, cyclene CH_2, CH_2-N, $CH_2\beta$), 3,97 (s, 3H, OMe Npx), 4,65(m, 1H, CH Npx), 4,90 (m, 1H, $CH\alpha$), 7,27 (m, 2H, Ar), 7,41 (m, 2H, Ar), 7,52 (m, 2H, Ar), 7,87 (m, 3H, CO_2H).

HRMS (ESI) m/z: $[M + H]^+$ calc for C31H44N5O10, 646.3083; found, 646.3081.

Preparation of the complex Gd-Npx (25)

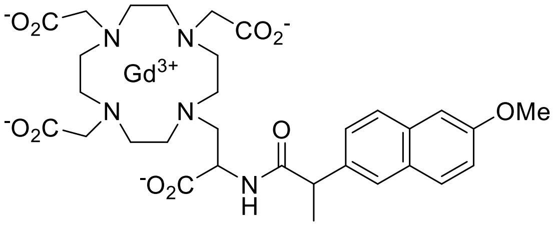

Chelator **24** (6,8 mg, 0,0085 mmol) was dissolved in water (5 mL) and adjusted to pH 5,8 with NaOH (1M). A solution of $GdCl_3$ (1,5 eq., 0,013 mmol, 3,4 mg) was added the chelator solution in small portions. The solution was kept at pH 5,8 by addition of NaOH (1 M) after addition of each $GdCl_3$ aliquot. The solution was kept under stirring at room temperature for 12 hrs. The solution was quantitatively transferred to a 10 ml volumetric flask. Aliquots of the complex solution in acetate buffer (0,1 M, pH 5,8) were titrated with standardised EDTA solution (1 mM) in the presence of the complexometric indicator xylenol orange. The purity of the chelator (93 %) was computed from the titration results.

Complex Gd-Npx **25** was prepared, taking into consideration the calculated purity of the chelator **24** (92 %), following the procedure described above. Chelator **24** (40 mg, 0,05 mmol) and a $GdCl_3$ solution (0,93 eq., 12,3 mg, 0,047 mmol were used to prepare a Gd-Npx solution (10 ml, 5 mM). A small excess of chelator is used to ensure complete complexation of the Gd^{3+} ion.

4.4 Preparation of the hydrogels

The hydrogelators (**5**, **6**, **8**, **9**, **13**, **14**, **16** and **17**) (0.4 *wt* %) were dissolved in water (1 mL), and the pH was increased to 11 with NaOH 1 M (20 μL). After dissolved, it was added the glucono-δ-lactone (GdL) (0.4 *wt* %) and the solution stayed in rest until the gelation.

4.5 Hydrogelators spectroscopy characterization

UV- Visivel characterization

It was prepared samples with the different hydrogelators with a concentration of 0.1 *wt* %. The solutions were diluted to ½ and they were measured in the range 200-400 nm.

Fluorescence characterization

Preparation of the pH buffers

The pH buffer solutions in the pH range 2–10 were prepared from a sodium phosphate 0.1 M solution and a mixed citric and boric acid solution at 0.05 M and 0.2 M, respectively, in ultrapure water (Milli-Qgrade), for a final volume of 50 mL.

The pH was measured with a pH meter NiCd-1 and the required adjustments were made using HCl or NaOH 1 M.

Preparation of the solutions to self-assembly dependence on pH

It was prepared ethanolic solutions of the different hydrogelators with a final concentration of 1 mM, to a final volume of 1 mL. These solutions were used to prepare aqueous solutions of each hydrogelators at concentration of 0.02 mM and to the pH range 2-10. The solutions were sonicated and kept by 1 day before the fluorescence measure.

Preparation of the microplate

To determine the critical concentration of each hydrogelator, it was prepared a microplate, in which different concentrations of hydrogelators (0.05 - 0.3 *wt* %) and GdL (0.1-0.4 *wt* %) were scanned. The hydrogelators solutions were prepared, previously, in water (900 μL) and aqueous solution of NaOH 1M (20 μL) and then it was added to GdL. The solutions were kept overnight in order to form hydrogels. The hydrogel pH was measured with a pH meter.

CD assays

Circular Dichroism (CD) spectra were recorded at 20 °C on a spectropolarimeter Jasco model J-1500 spectropolarimeter (JASCO, Tokyo, Japan), at 25 °C, under a constant flow of nitrogen gas. Peptide hydrogelator 0.01 *wt* % solutions were loaded into 0.1 mm quartz cells. Spectra were acquired with 1 nm steps, 1 nm bandwidth and 1 second collection time per step, taking three averages. The obtained data was smoothed by an 11-point Savitsky-Golay filter, to remove random noise elements from the averaged spectra.

4.6 Structural characterization

STEM

The STEM samples were prepared with 0.4 *wt* % of the hydrogelators or with 0.4 *wt* % of the hydrogelators incorporating 14 *wt* % of SPION. STEM images were recorded using a NanoSEM – FEI Nova 200 (FEI Technologies, Inc., Hillsboro, Oregon, USA), operating at 15 kV, coupled to an Electron Dispersive Spectroscopic analyzer (EDS) and Electron Backscatter Diffraction EDAX - Pegasus X4M analyser and detection system (EBSD) at SEMAT (Serviços de Caracterização de Materiais), Guimarães, Portugal. A small portion of hydrogel was placed onto a TEM 400 mesh copper grid with Formvar/Carbon (ref. S162-4 from Agar Scientific Ltd, Essex, UK), held by tweezers and the excess solution was cleaned. The processing of STEM images was performed using ImageJ software (National Institutes of Health- NIH, Bethesda, MD, USA), which consisted in enhancing local contrast and adjusting brightness followed by manual selection of fibres.

Rheology

Samples (hydrogelator 0. 4 *wt* % and hydrogelator 0.4 *wt* % with 14 *wt* % SPION incorporated) are loaded in liquid form in the Couette geometry (gap 0.5 mm) of a stress control rotational rheometer (MCR300, Anton Paar). After a pre-shear (steady shear rate of 5 s^{-1} applied during 60 s), the sample is left to gel for 10 h, whereas the gel setting is monitored by applying a small amplitude oscillatory strain of 10^{-3} % at 1 Hz. A quantitative estimate of the kinetics of the gel setting is given by measuring the time t_{half} at which the elastic shear modulus G’ reaches half of the value measured at equilibrium G_{eq}. The latter is measured from the frequency sweep performed on the equilibrated gel, by picking up the value of *G'* at 1 Hz. After the thermal cycle which is followed by an equilibrium period of 2 h at 25 °C, the thermal reversibility of gels is quantified by computing the difference $G_{eq} - G_0$, where G_0 is the elastic modulus of gels measured in the linear viscoelastic regime of the strain sweep performed right after the 2 h rest at 25 °C. The strain sweep is also used to compute the critical strain for gel break-up, S_c, which is defined by the strain where $G'' = G'$, thereby corresponding to the fluidization of the elastic network in gel. The gel break-up is followed by a structural recovery which is monitored for 1 h. The time at which G' reaches 50 % of its equilibrated recovered value defines the recovery time t_r of the gel. Eventually, the elasticity of the healed gel is measured by the elastic modulus G_r measured at 1 Hz during the frequency sweep presented in Figure 1f and the healing *H* of the gel is quantified by computing $H = G_r / G_0$.

4.7 Relaxation Characterization

MRI relaxation maps

Stock solutions of the different hydrogelators and of the Gd-complex solution (2.5 mM) or the SPIONs (83.6 mM) were used to prepare the hydrogel phantoms for the MRI studies. The final concentration of the hydrogelator was kept constant at 0,4 *wt* % while the Gd-complex was varied in the concentration range 0 - 1.2 mM and the SPIONs were varied in the concentration range 0 -0.18 mM. The hydrogelator solution (0,8 *wt* %) was prepared by adjusting the solution pH to *circa* 11 with aqueous NaOH (1 M) to make the hydrogelator soluble. Gelation was triggered by addition of GdL (0,8 *wt* % (OMe *terminal*) or 0.12 *wt* % (OH *terminal*)). Aliquots of the hydrogelator solution (100 µL) were immediately transferred into *Eppendorf* tubes containing the Gd-Npx or Gd(DOTA). The final volume of the hydrogel phantom was 200 µl. Gelation was allowed for 24 h before the MRI measurements.

To the concentrations variations samples, the procedure was similar, with the hydrogelator concentration range 0 – 0.6 *wt* % and the SPIONs concentration fixed at 0.08 mM (19 µl) or the Gd-Npx complex fixed at 0.8 mM (64 µl).

Relaxometry

It was measured to a relaxometry tube, the GdL complex, in a concentration range 0 – 1.67 mM or the SPIONs, in the concentration range 0 – 1.4 mM. The hydrogelators, with an initial concentration of 1.2 *wt* %, were prepared and it was added the volume correspond to the hydrogel have a final concentration of 0.4 *wt* % in a final volume of 300 µl. Gelation was allowed for 24 h before the relaxometry measurements.

To the concentrations variations samples, the procedure was similar, with the hydrogelator concentration range 0 – 0.6 *wt* % and the SPION concentration fixed (60 µl) or the Gd-Npx complex fixed (60 µl).

4.8 Hyperthermia characterization

It was measured to a tube the SPION concentration of 14 *wt* % (120 µl) and 42 *wt* % (360 µl) (m/m), relatively to the hydrogelator mass. The hydrogelators were prepared with the concentration of 0.4 *wt* % and they were added to the SPION solution, to a final volume of 600 µl. Gelation was allowed for 24 hours before the hyperthermia measurements.

To the concentrations variations samples, the procedure was similar, with the hydrogelator concentration range 0 – 0.6 *wt* % and the SPION concentration fixed at 14 *wt* % (120 µl).

4.9 Nanocarriers characterization

Drug delivery

Hydrogelators (0.4 *wt* %) were dissolved in 1 mL of the colouring (to a final concentration of 0.06 mg/mL) and dissolved with NaOH (1M). The GDL (0.4 *wt* %) was added and the samples was transferred to a membrane tube. Gelation was allowed for 24 hours. It was measured 5 mL of PBS pH 7.2 to a tube and the hydrogel was submersed in the PBS, during 48 h, taking of aliquots of 130 l over the time. When it was incorporated SPION, the procedure was similar, but with 800 µl of dye and 200 µl of SPION.

Cell viability

Human keratinocytes cell line HaCaT was from ATCC. Cells were cultured in DMEM supplemented with 10 % FBS and 1 % penicillin/streptomycin, and were incubated in an incubator at 37 °C, in a humidified atmosphere of 5 % CO_2. Cells were seeded in 96-well plates (1.5×10^4 cells/well) and left to attach for 24h. After this period, cells were incubated with different concentrations of the molecules under study for another 24 h. After this period, cell viability was evaluated based on the ability of metabolically active cells to convert MTT to formazan over the course of 2 hours. Absorbances were measured at 570 nm in a Multiskan GO plate reader (Thermo Fisher Scientific; Waltham, MA, USA) and results were expressed as percentage of the respective control and correspond to the mean ± standard error of the mean (SEM) of at least three independent experiments performed in triplicate.

Chapter 5

Annex

A)

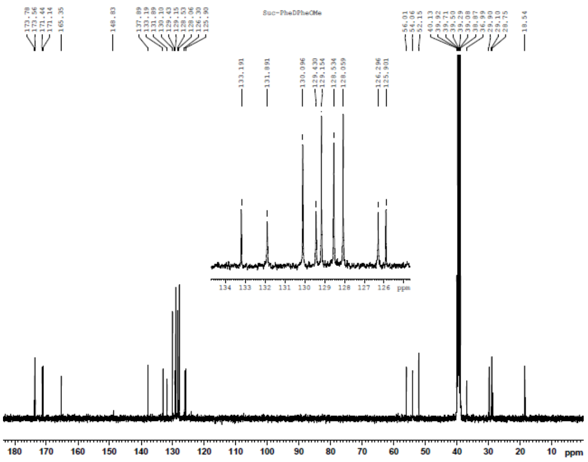
Suc-PheDPheOMe
ppm

B)

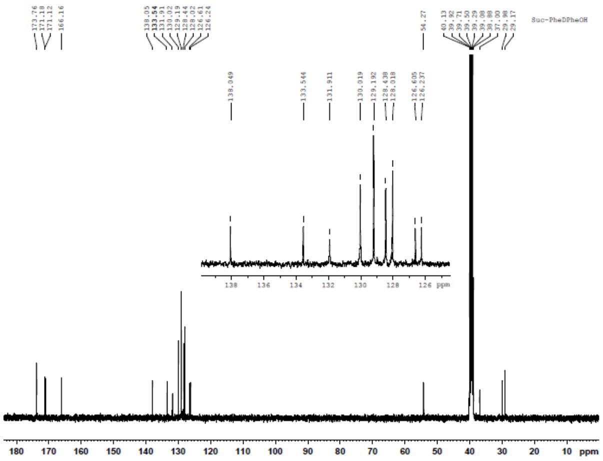
Suc-PheDPheOH
ppm

C)

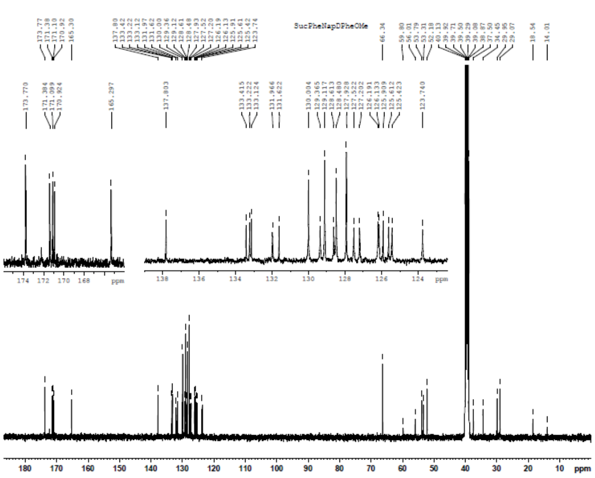
SucPheNapDPheOMe
ppm

D)

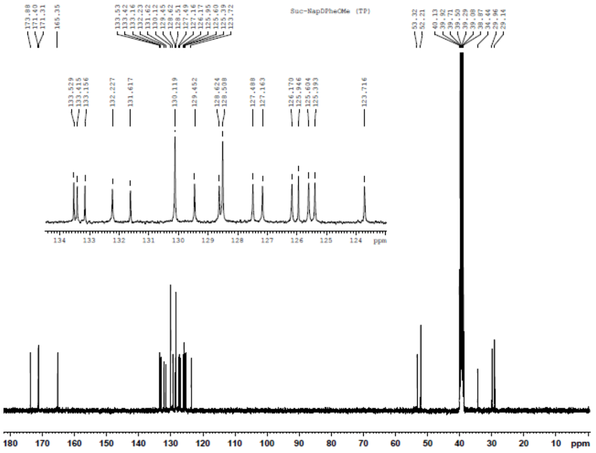
Suc-NapDPheOMe (TP)
ppm

E)

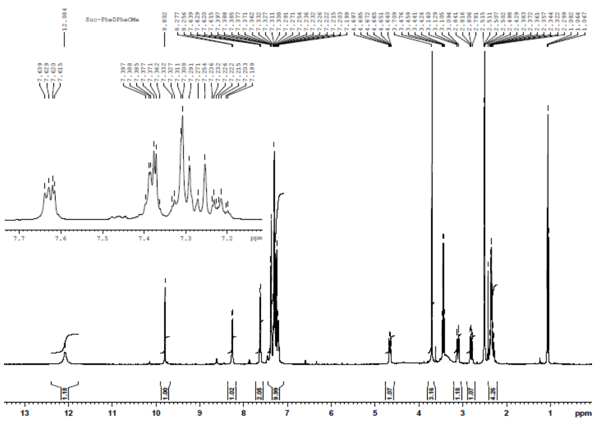
Suc-PheDPheOMe
ppm

F)

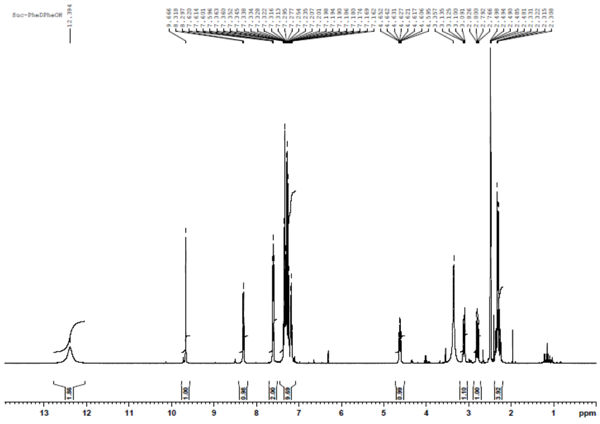
Suc-PheDPheOH
ppm

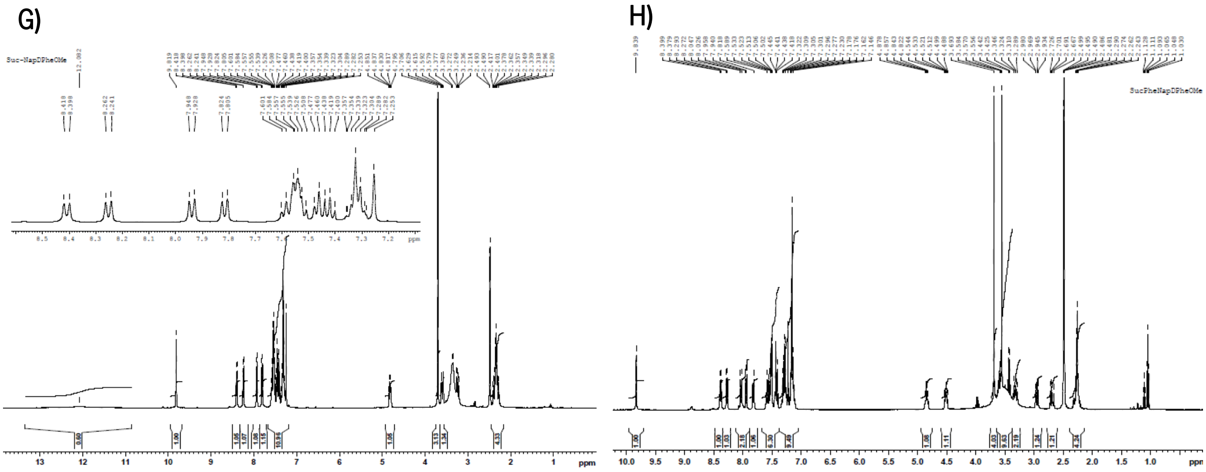

Figure A1 ^{13}C and ^{1}H NMR spectra of hydrogelators **(A)** 5, **(B)** 6, **(C)** 13, **(D)** 16, and **(E)** 5, **(F)** 6, **(G)**13, **(H)** 16, respectively.

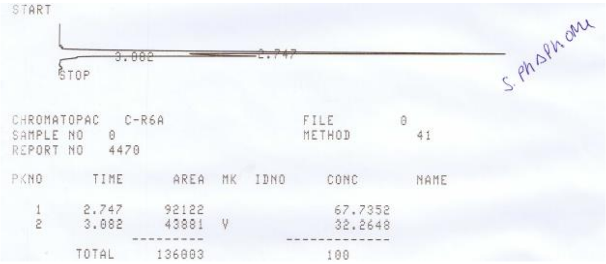

S. PhΔPh OMe

```
CHROMATOPAC   C-R6A                    FILE        0
SAMPLE NO   0                          METHOD        41
REPORT NO   4470

PKNO      TIME      AREA  MK  IDNO      CONC        NAME

  1      2.747     92122                 67.7352
  2      3.082     43881  V              32.2648
                 ---------          -------------
        TOTAL     136003                  100
```

Suc. NaΔPh OMe

```
CHROMATOPAC   C-R6A                    FILE        0
SAMPLE NO   0                          METHOD        41
REPORT NO   4465

PKNO      TIME      AREA  MK  IDNO      CONC        NAME

  1      3.342    135036                  100
                 ---------          -------------
        TOTAL     135036                  100
```

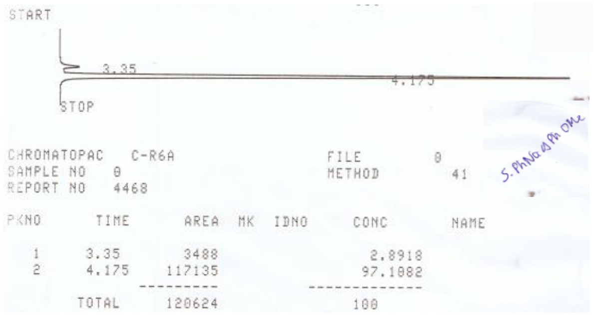

S. PhNaΔPh OMe

```
CHROMATOPAC   C-R6A                    FILE        0
SAMPLE NO   0                          METHOD        41
REPORT NO   4468

PKNO      TIME      AREA  MK  IDNO      CONC        NAME

  1      3.35       3488                  2.8918
  2      4.175    117135                 97.1082
                 ---------          -------------
        TOTAL     120624                  100
```

S. PhΔPh OH

```
CHROMATOPAC   C-R6A                    FILE        0
SAMPLE NO   0                          METHOD        41
REPORT NO   4469

PKNO      TIME      AREA  MK  IDNO      CONC        NAME

  1      2.29      14532                 21.2318
  2      2.445     16979  V              24.806
  3      2.607     18286  V              26.7163
  4      2.8       13774  V              20.124
  5      3.305      4875  V               7.1218
                 ---------          -------------
        TOTAL      68446                  100
```

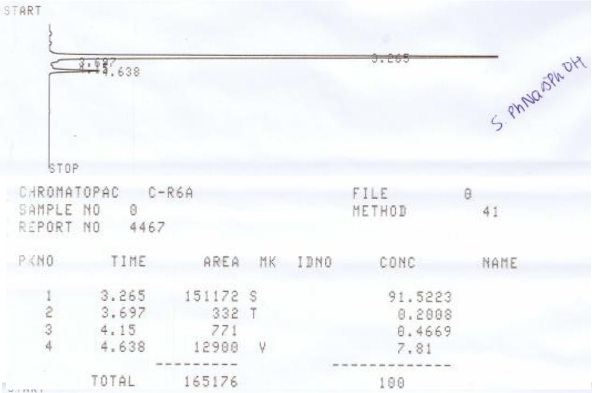

S PhNaΔPh OH

```
CHROMATOPAC   C-R6A                    FILE        0
SAMPLE NO   0                          METHOD        41
REPORT NO   4467

PKNO      TIME      AREA  MK  IDNO      CONC        NAME

  1      3.265    151172 S               91.5223
  2      3.697       332 T                0.2008
  3      4.15        771                  0.4669
  4      4.638     12900  V               7.81
                 ---------          -------------
        TOTAL     165176                  100
```

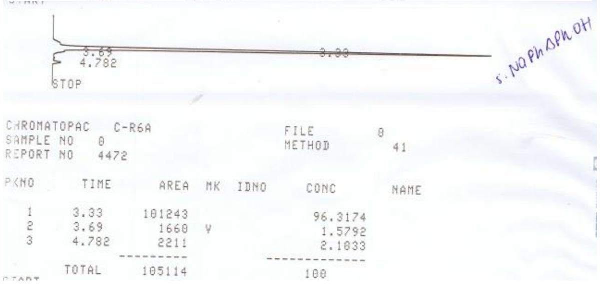

s. NaPhΔPh OH

```
CHROMATOPAC   C-R6A                    FILE        0
SAMPLE NO   0                          METHOD        41
REPORT NO   4472

PKNO      TIME      AREA  MK  IDNO      CONC        NAME

  1      3.33     101243                 96.3174
  2      3.69       1660  V               1.5792
  3      4.782      2211                  2.1033
                 ---------          -------------
        TOTAL     105114                  100
```

```
START



STOP

CHROMATOPAC   C-R6A                    FILE       0
SAMPLE NO   0                          METHOD       41
REPORT NO   4471

PKNO    TIME       AREA  MK  IDNO      CONC       NAME

  1     3.325       950                  1.3358
  2     4.312     70157                 98.6642
               ---------          -------------
        TOTAL     71107                100
```

```
START



STOP

CHROMATOPAC   C-R6A                    FILE       0
SAMPLE NO   0                          METHOD       41
REPORT NO   4461

PKNO     TIME      AREA  MK  IDNO      CONC       NAME

  1      2.8     131418                  79.2913
  2      3.08     29633  V               17.8788
  3      3.308     3005  V                1.8131
  4      3.702     1685  V                1.0167
               ---------          -------------
        TOTAL    165741                100
```

Figure A2 HPLC to the hydrogels: **A)** suc-PheΔPheOMe; **B)** suc-PheΔPheOH; **C)** suc-NapΔPheOMe; **D)** suc-NapΔPheOH; **E)** suc-NapPheΔPheOMe; **F)** suc-NapPheΔPheOH; **G)** suc-PheNapΔPheOMe; **H)** suc-PheNapΔPheOH.

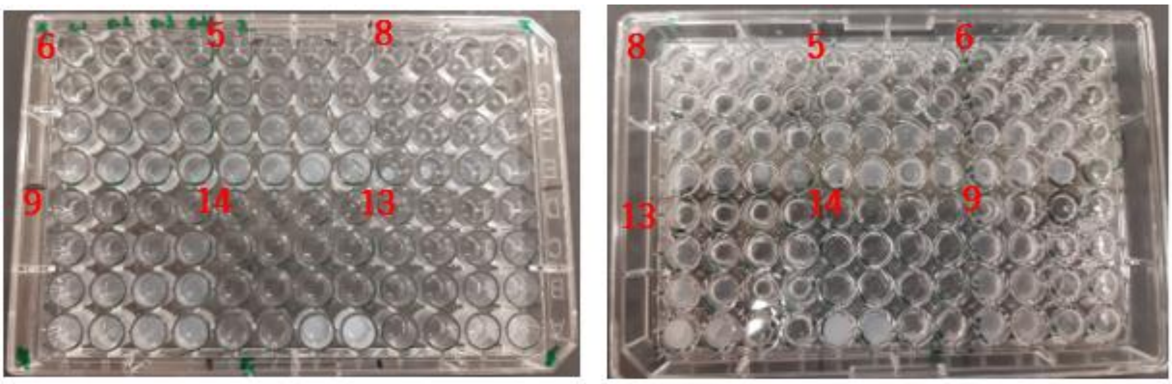

Figure A3 96 wee-plate to the gelation studies: **A)** normal plate **B)** inverted plate.

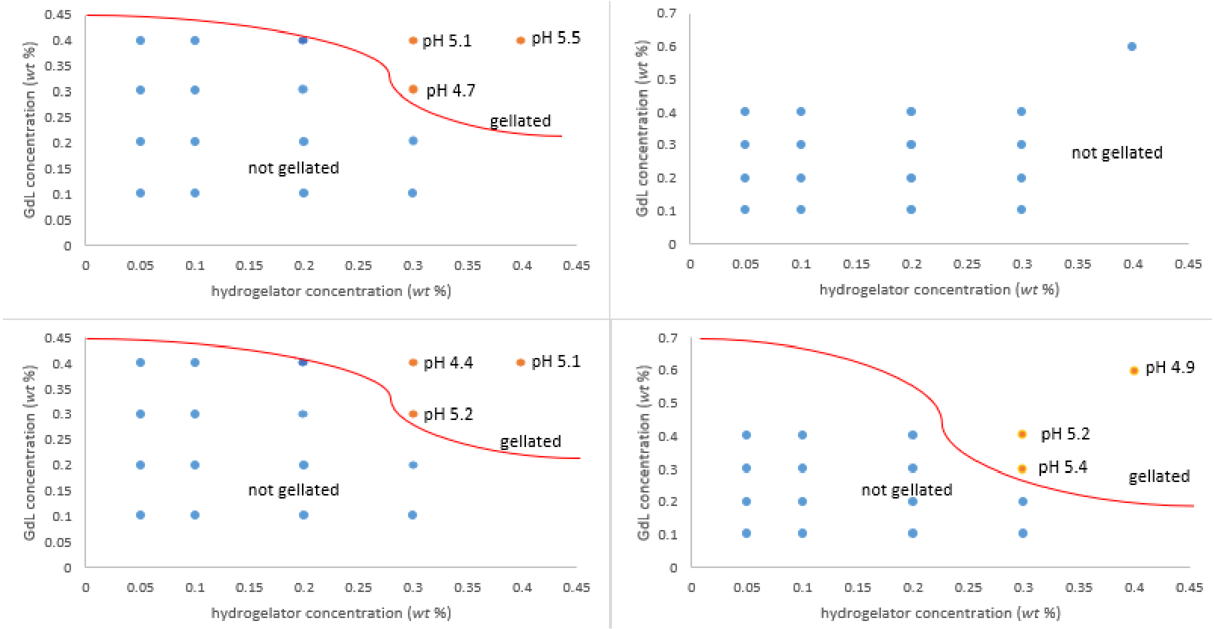

Figure A4 Illustrative phase diagrams for gelation of the hydrogelators: **A)** suc-PheΔPheOMe (**5**); **B)** suc-PheΔPheOH (**6**); **C)** suc-NapΔPheOMe (**13**); **D)** suc-NapΔPheOH (**14**).

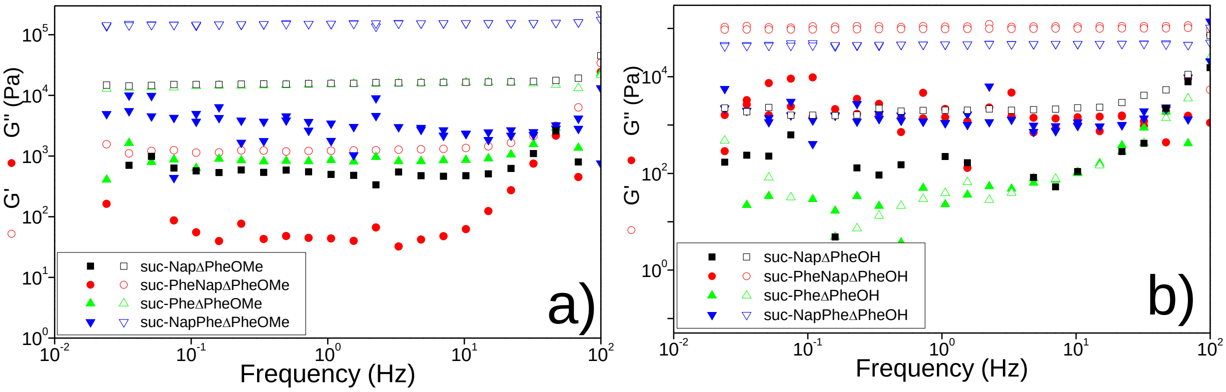

Figure A5.1 Mechanical spectra of equilibrated hydrogels after complete gel setting. **a**) to the *C*-protected methyl ester hydrogelators (**5**, **8**, **13** and **16**); **b**) and to the *C*-deprotected hydrogelators (**6**, **9**, **14** and **17**).

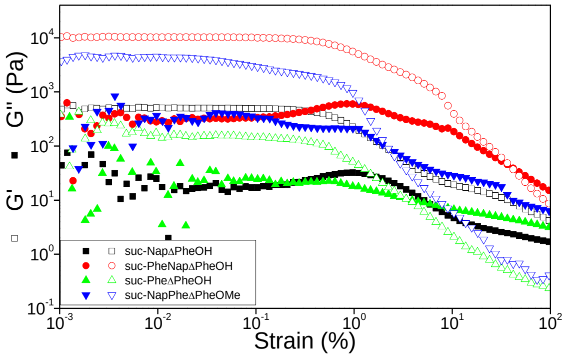

Figure A5.2 Nonlinear viscoelastic behaviour of hydrogels made with *C*-deprotected hydrogelators (**6**, **14** and **17**) and made with *C*-protected methyl ester (**8**).

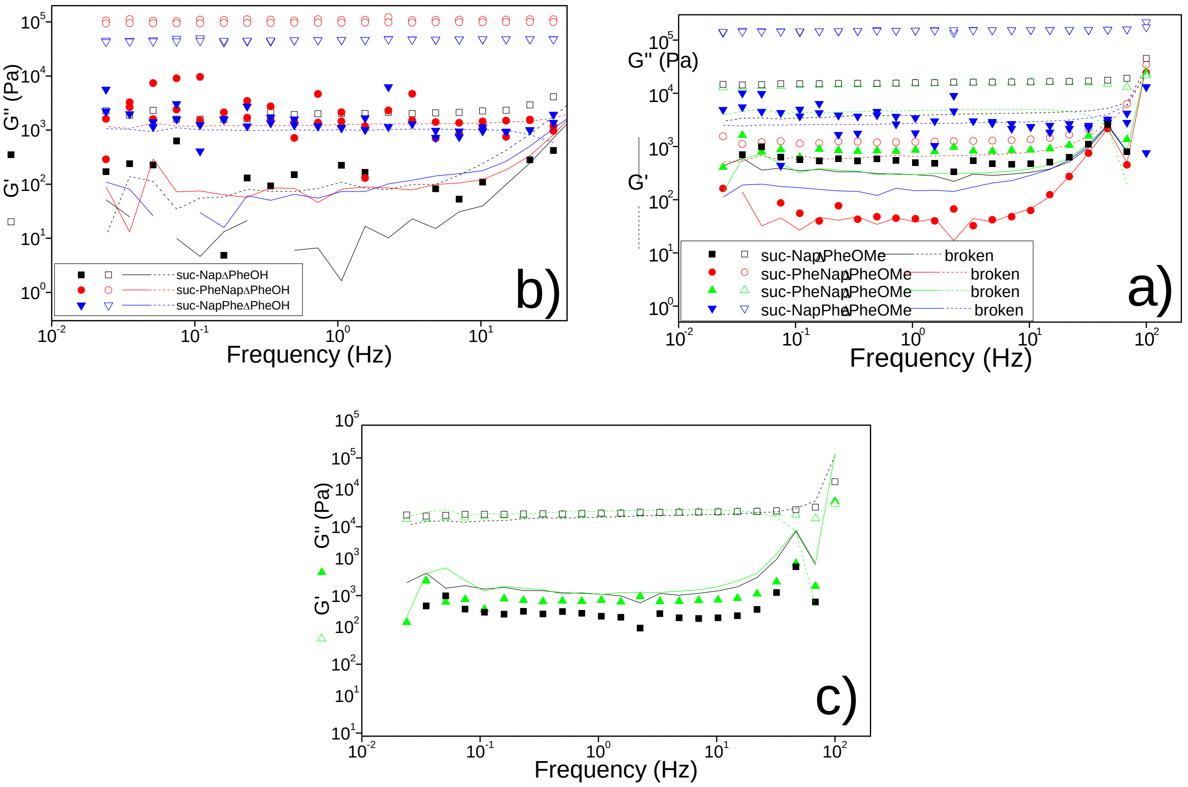

Figure A5.3 Mechanical spectra of "fresh" (symbols) and thermo-mechanically treated (lines) hydrogels made from compounds (**a**) *C*-protected and (**b**) *C*-deprotected. Solid lines and symbols: G''; empty symbols and dashed lines: G'. In (**c**), the mechanical spectra of healed gels have been vertically shifted to superimpose on those of initial gels.

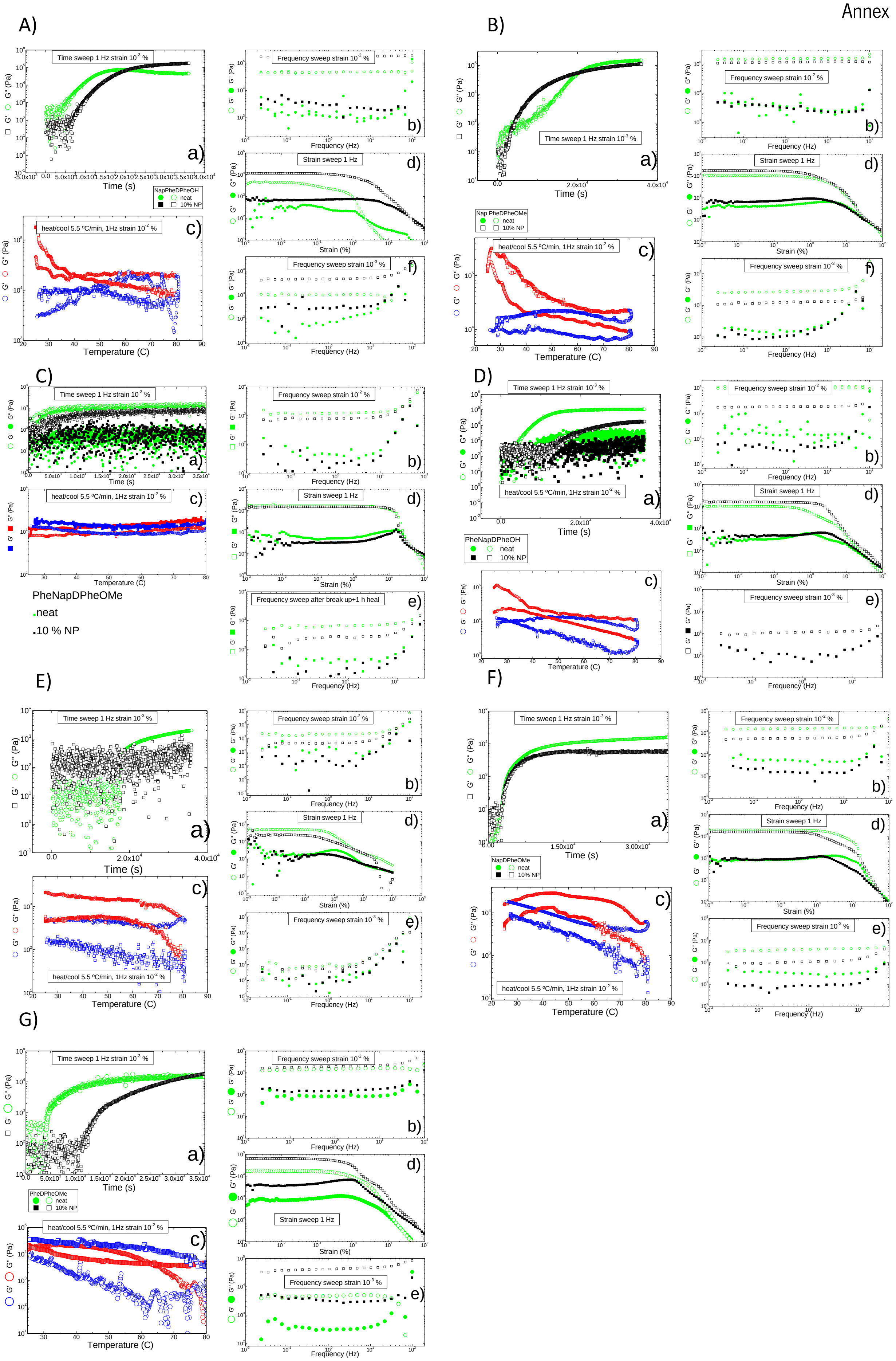

Figure A5.4 Data for the hydrogelators with and without SPION: **A)** suc-NapPheΔPheOH, **B)** suc-NapPheΔPheOMe, **C)** suc-PheNapΔPheOMe, **D)** suc-PheNapΔPheOH, **E)**suc-NapΔPheOH, **F)**suc-NapΔPheOMe, **G)**suc-PheΔPheOMe.

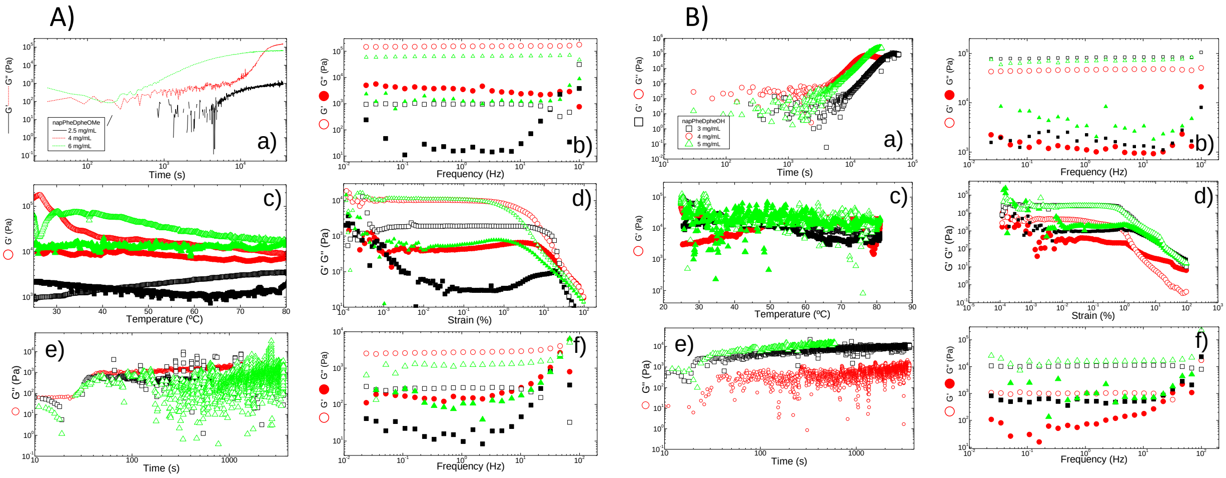

Figure A5.5 Effect of the hydrogelator concentration on the rheological properties: **A)** suc-NapPheΔPheOMe, **B)** suc-NapPheΔPheOH.

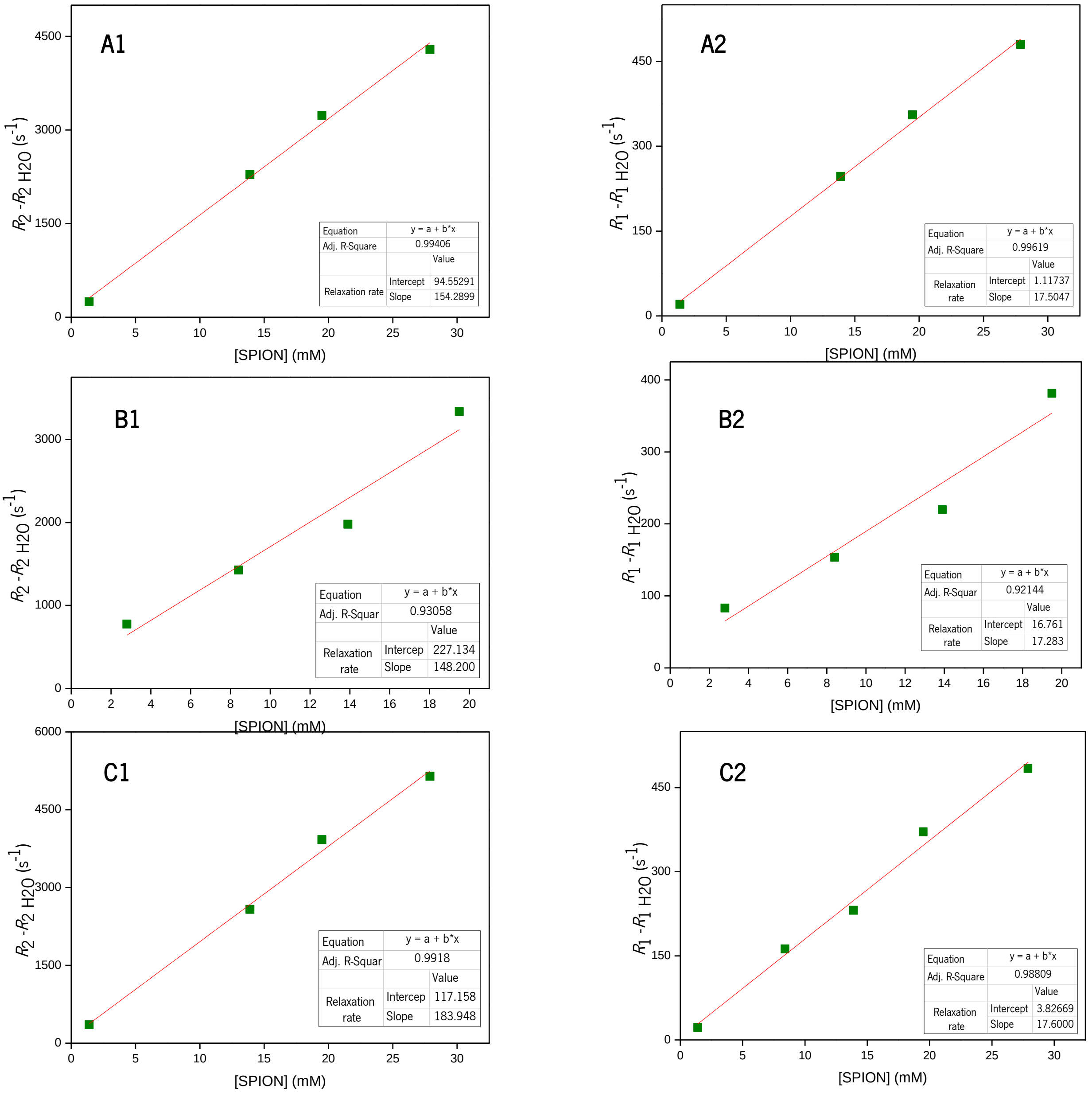

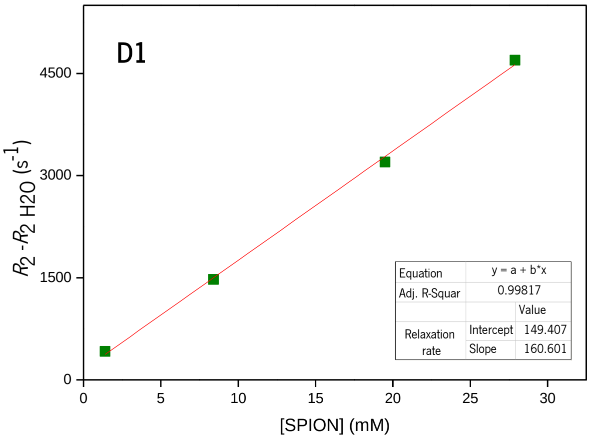
D1
R2 -R2 H20 (s-1)
4500
3000
1500
0
0
5
10
15
20
25
30
[SPION] (mM)
Equation | y = a + b*x
Adj. R-Squar | 0.99817
Value
Relaxation rate | Intercept | 149.407
Slope | 160.601

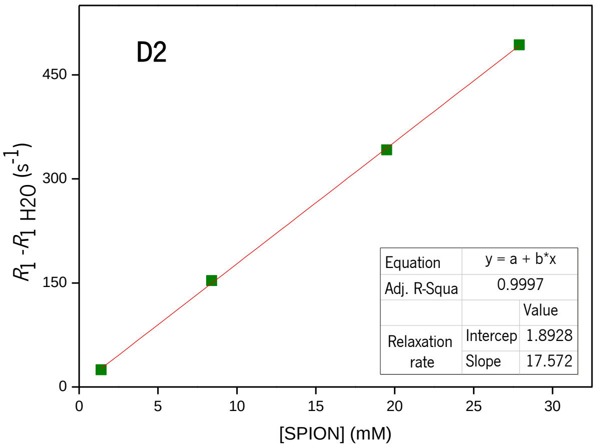
D2
R1 -R1 H20 (s-1)
450
300
150
0
0
5
10
15
20
25
30
[SPION] (mM)
Equation | y = a + b*x
Adj. R-Squa | 0.9997
Value
Relaxation rate | Intercep | 1.8928
Slope | 17.572

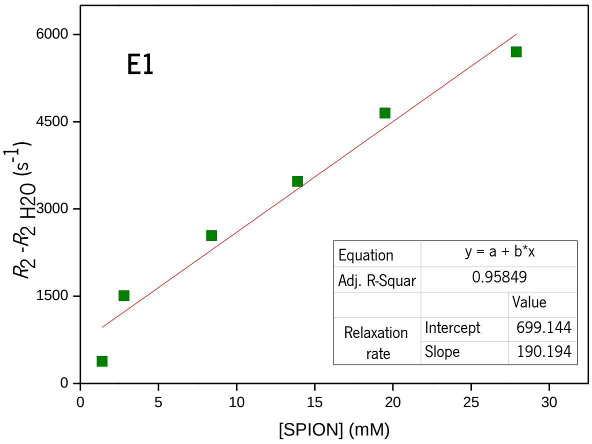
E1
R2 -R2 H20 (s-1)
6000
4500
3000
1500
0
0
5
10
15
20
25
30
[SPION] (mM)
Equation | y = a + b*x
Adj. R-Squar | 0.95849
Value
Relaxation rate | Intercept | 699.144
Slope | 190.194

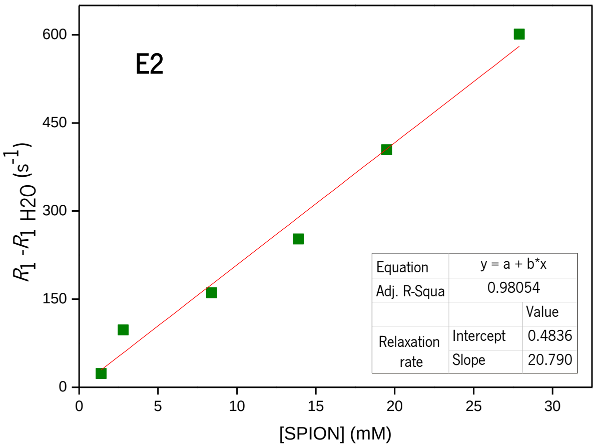
E2
R1 -R1 H20 (s-1)
600
450
300
150
0
0
5
10
15
20
25
30
[SPION] (mM)
Equation | y = a + b*x
Adj. R-Squa | 0.98054
Value
Relaxation rate | Intercept | 0.4836
Slope | 20.790

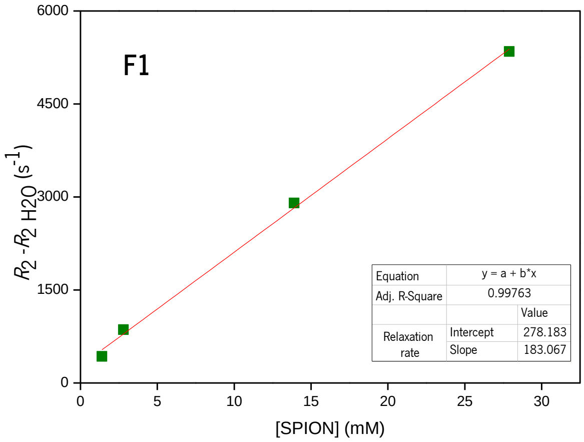
F1
R2 -R2 H20 (s-1)
6000
4500
3000
1500
0
0
5
10
15
20
25
30
[SPION] (mM)
Equation | y = a + b*x
Adj. R-Square | 0.99763
Value
Relaxation rate | Intercept | 278.183
Slope | 183.067

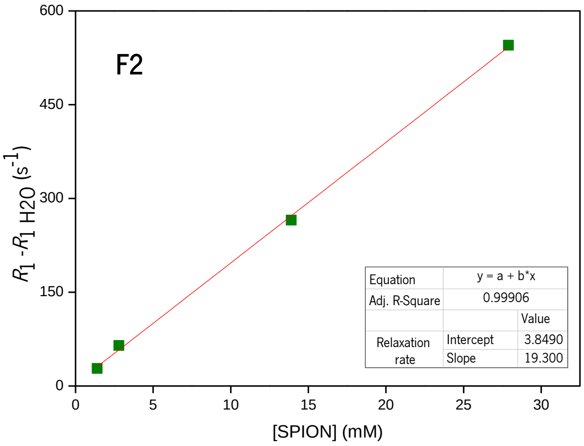
F2
R1 -R1 H20 (s-1)
600
450
300
150
0
0
5
10
15
20
25
30
[SPION] (mM)
Equation | y = a + b*x
Adj. R-Square | 0.99906
Value
Relaxation rate | Intercept | 3.8490
Slope | 19.300

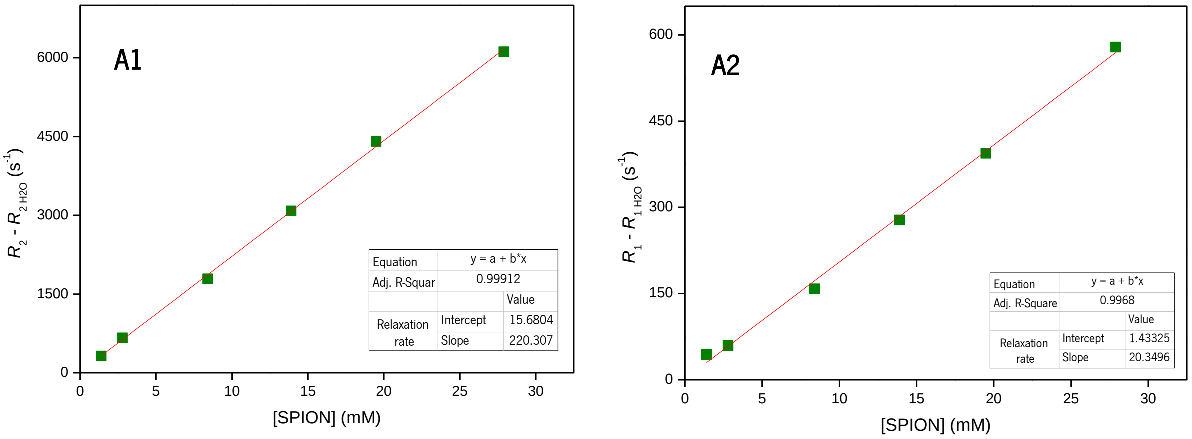

Figure A6 Illustration of the procedure used to determine the relaxivities for the magnetic hydrogels, using the hydrogelators: **A1** and **A2**) suc-PheΔPheOMe (**5**); **B1** and **B2**) suc-PheΔPheOH (**6**); **C1** and **C2**) hydrogelator suc-NapΔPheOMe (**13**); **D1** and **D2**) hydrogelator suc-NapΔPheOH (**14**); **E1** and **E2**) hydrogelator suc-PheNapΔPheOMe (**16**); **F1** and **F2**) hydrogelator suc-PheNapΔPheOH (**17**); **G1** and **G2**) agarose.

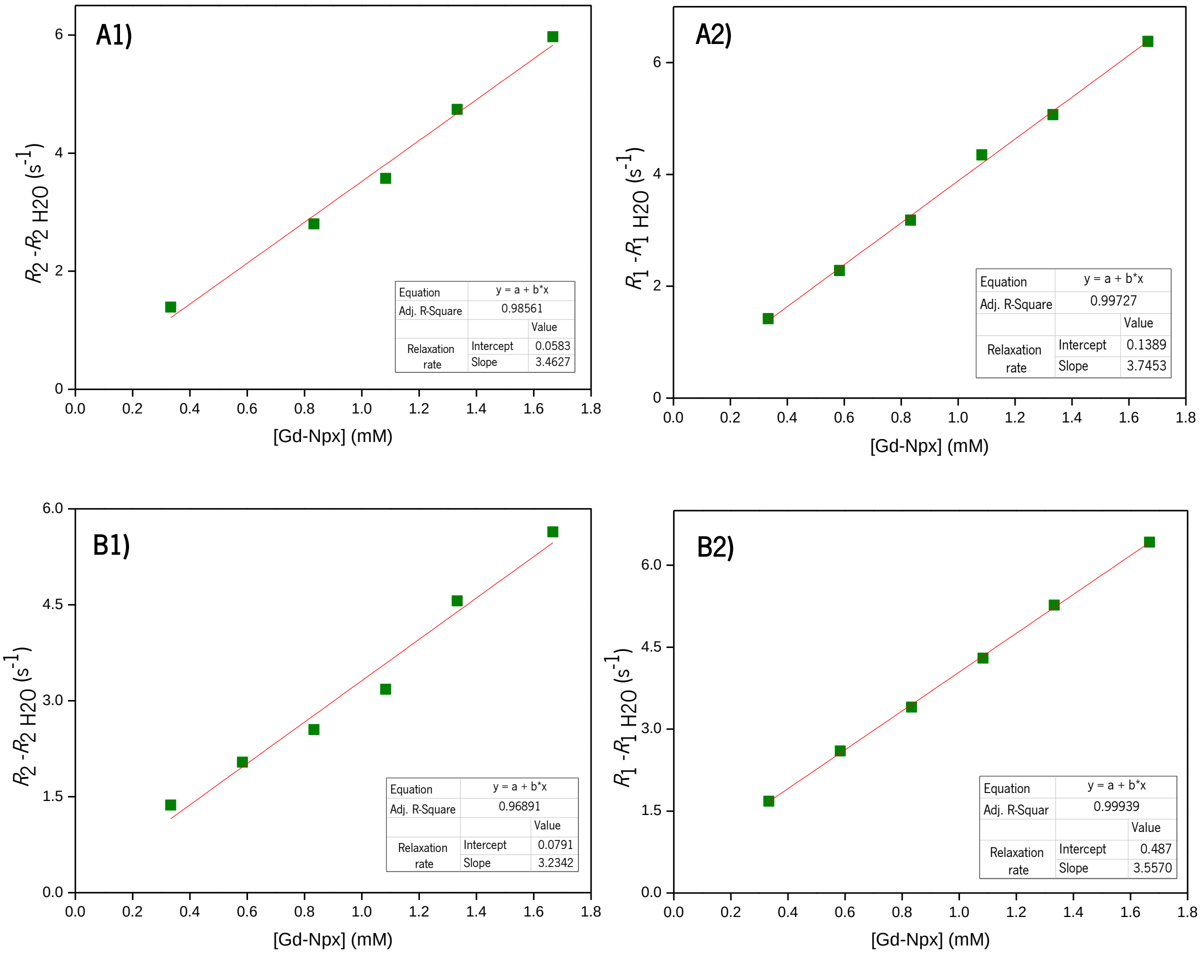

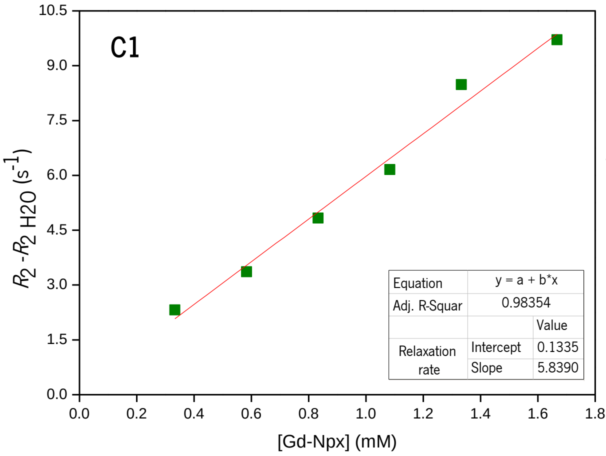
C1
R_2 -R_2 H2O (s^{-1})
[Gd-Npx] (mM)
0.0
1.5
3.0
4.5
6.0
7.5
9.0
10.5
0.0
0.2
0.4
0.6
0.8
1.0
1.2
1.4
1.6
1.8
Equation
y = a + b*x
Adj. R-Squar
0.98354
Value
Relaxation rate
Intercept
0.1335
Slope
5.8390

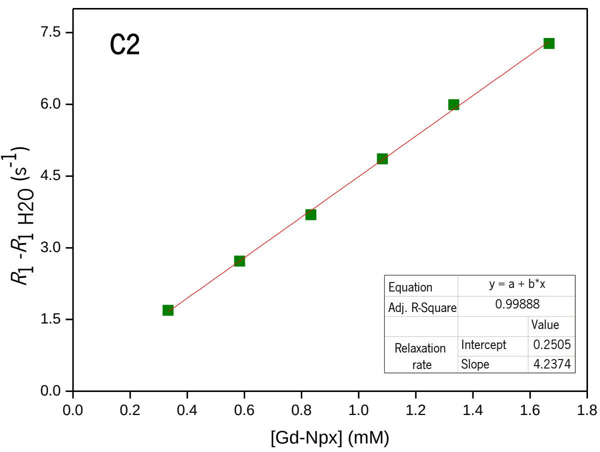
C2
R_1 -R_1 H2O (s^{-1})
[Gd-Npx] (mM)
0.0
1.5
3.0
4.5
6.0
7.5
0.0
0.2
0.4
0.6
0.8
1.0
1.2
1.4
1.6
1.8
Equation
y = a + b*x
Adj. R-Square
0.99888
Value
Relaxation rate
Intercept
0.2505
Slope
4.2374

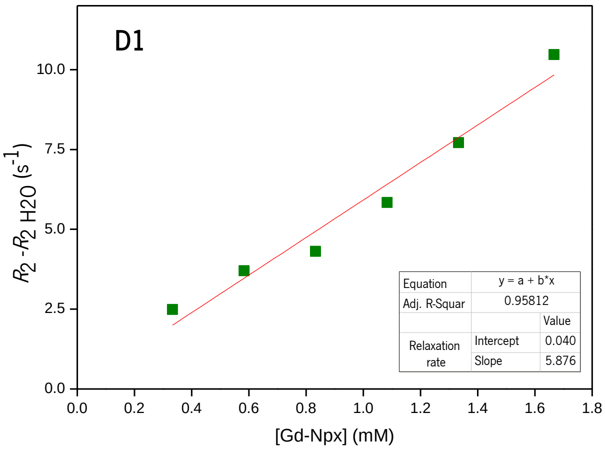
D1
R_2 -R_2 H2O (s^{-1})
[Gd-Npx] (mM)
0.0
2.5
5.0
7.5
10.0
0.0
0.2
0.4
0.6
0.8
1.0
1.2
1.4
1.6
1.8
Equation
y = a + b*x
Adj. R-Squar
0.95812
Value
Relaxation rate
Intercept
0.040
Slope
5.876

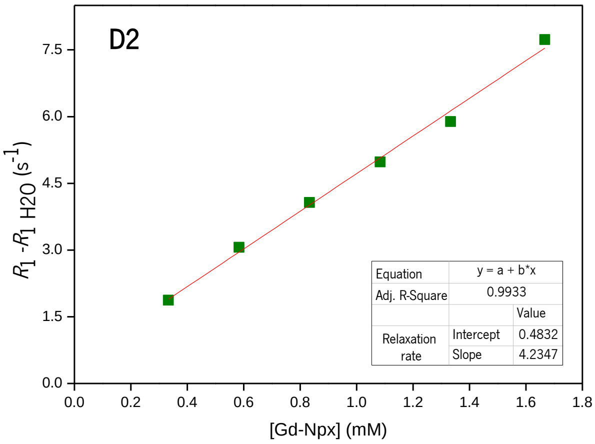
D2
R_1 -R_1 H2O (s^{-1})
[Gd-Npx] (mM)
0.0
1.5
3.0
4.5
6.0
7.5
0.0
0.2
0.4
0.6
0.8
1.0
1.2
1.4
1.6
1.8
Equation
y = a + b*x
Adj. R-Square
0.9933
Value
Relaxation rate
Intercept
0.4832
Slope
4.2347

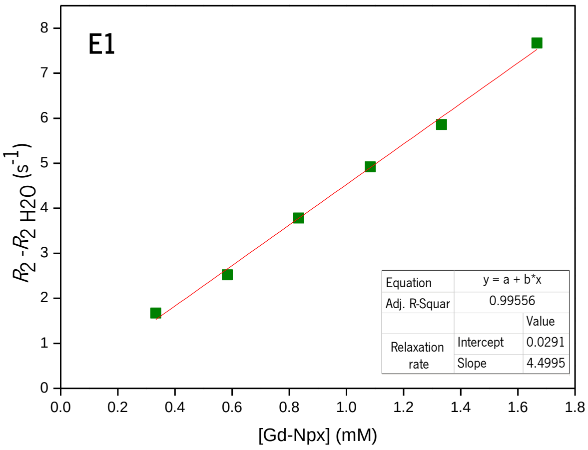
E1
R_2 -R_2 H2O (s^{-1})
[Gd-Npx] (mM)
0
1
2
3
4
5
6
7
8
0.0
0.2
0.4
0.6
0.8
1.0
1.2
1.4
1.6
1.8
Equation
y = a + b*x
Adj. R-Squar
0.99556
Value
Relaxation rate
Intercept
0.0291
Slope
4.4995

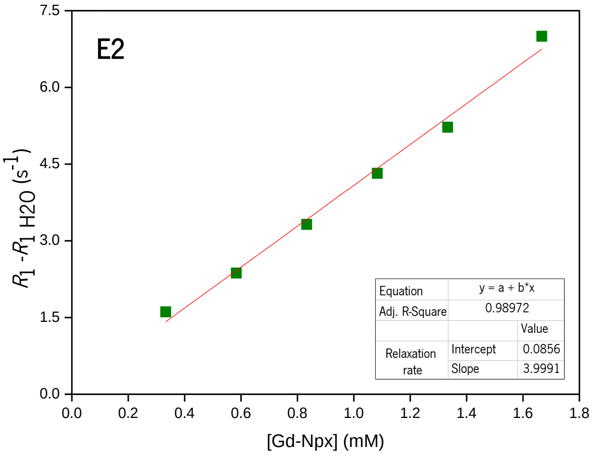
E2
R_1 -R_1 H2O (s^{-1})
[Gd-Npx] (mM)
0.0
1.5
3.0
4.5
6.0
7.5
0.0
0.2
0.4
0.6
0.8
1.0
1.2
1.4
1.6
1.8
Equation
y = a + b*x
Adj. R-Square
0.98972
Value
Relaxation rate
Intercept
0.0856
Slope
3.9991

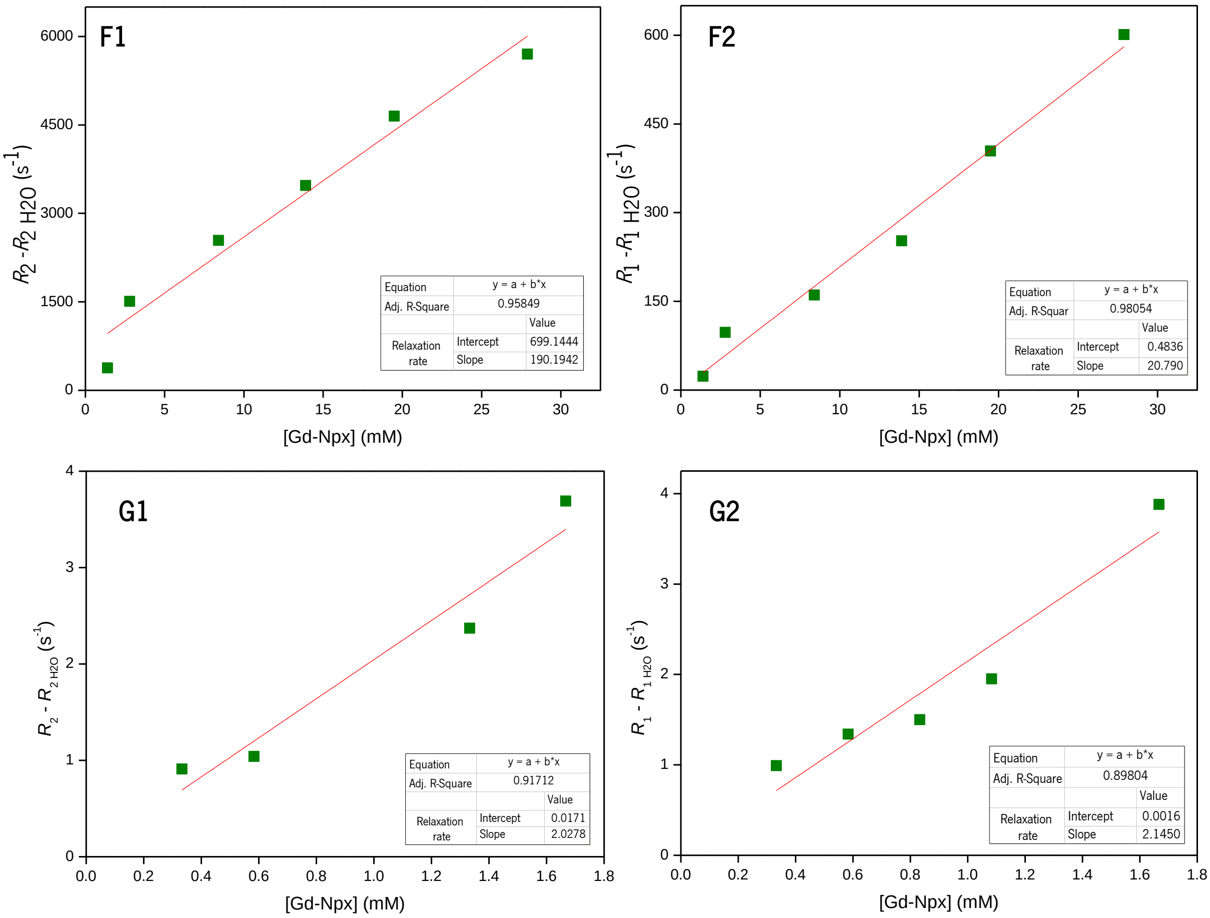

Figure A7 Illustration of the procedure used to determine the relaxivities for the paramagnetic hydrogels, using the hydrogelators: **A1** and **A2**) suc-PheΔPheOMe (**5**); **B1** and **B2**) suc-PheΔPheOH (**6**); **C1** and **C2**) hydrogelator suc-NapΔPheOMe (**13**); **D1** and **D2**) hydrogelator suc-NapΔPheOH (**14**); **E1** and **E2**) hydrogelator suc-PheNapΔPheOMe (**16**); **F1** and **F2**) hydrogelator suc-PheNapΔPheOH (**17**); **G1** and **G2**) agarose.

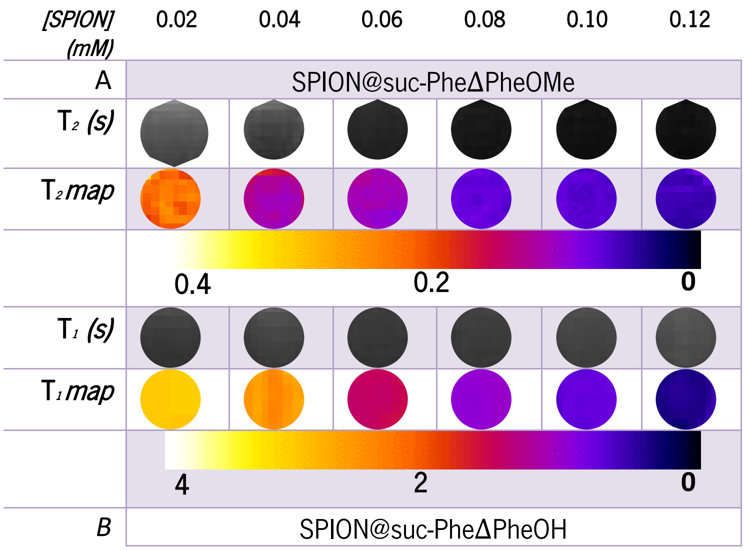

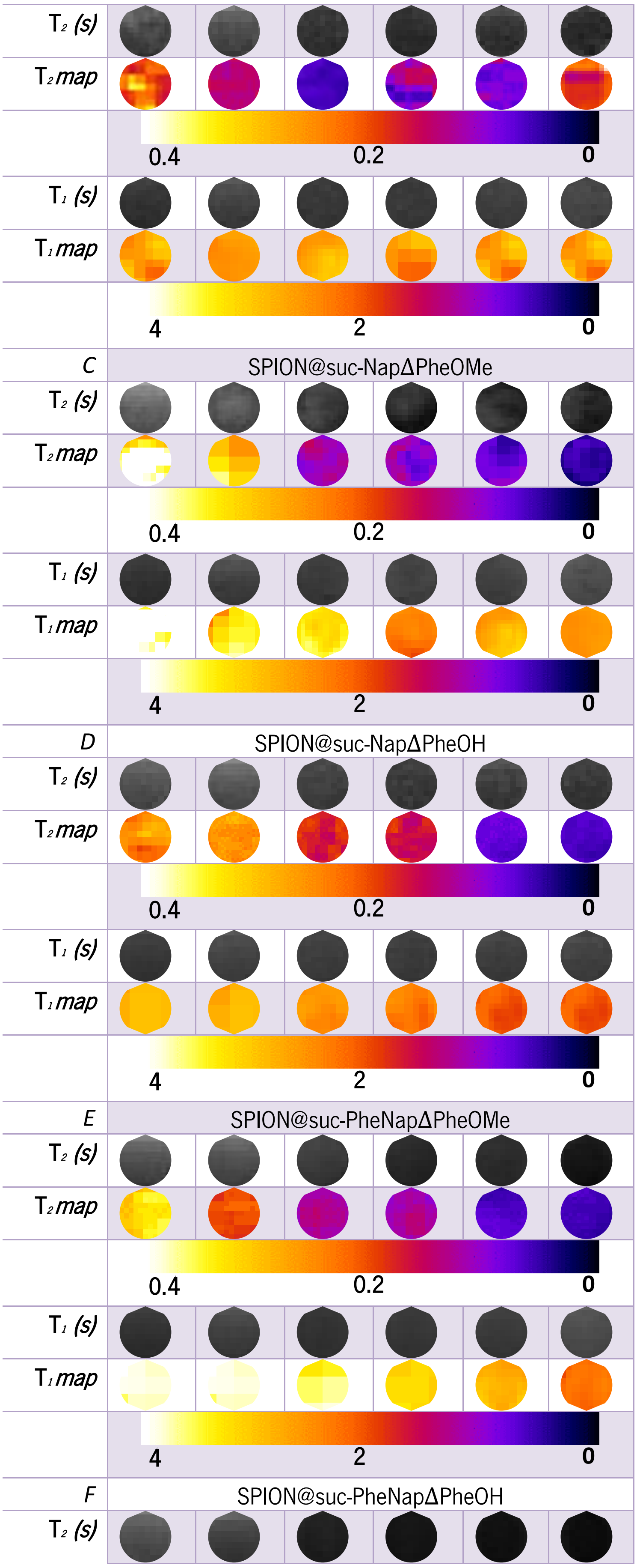
T2 (s)
T2 map
0.4
0.2
0
T1 (s)
T1 map
4
2
0
C
SPION@suc-NapΔPheOMe
T2 (s)
T2 map
0.4
0.2
0
T1 (s)
T1 map
4
2
0
D
SPION@suc-NapΔPheOH
T2 (s)
T2 map
0.4
0.2
0
T1 (s)
T1 map
4
2
0
E
SPION@suc-PheNapΔPheOMe
T2 (s)
T2 map
0.4
0.2
0
T1 (s)
T1 map
4
2
0
F
SPION@suc-PheNapΔPheOH
T2 (s)

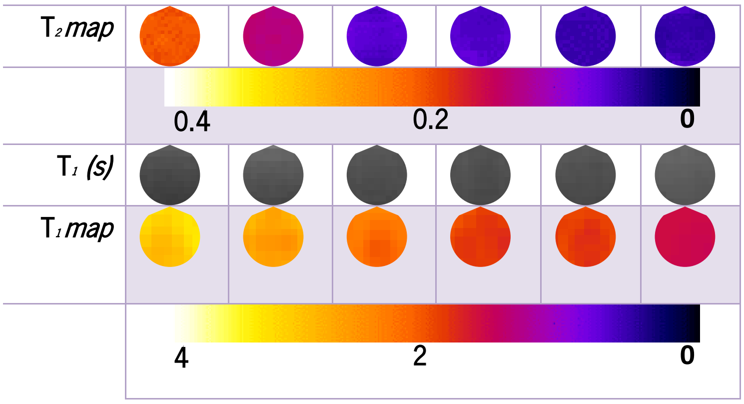

Figure A8 $T_{1,2}$ relaxation maps (120 MHz, 37 °C): **A)** and **B)** hydrogels suc-PheΔPheOMe (**5**) and suc-PheΔPheOH (**6**); **C)** and **D)** suc-NapΔPheOMe (**13**) and suc-NapΔPheOH (**14**); **E)** and **F)** hydrogels suc-PheNapΔPheOMe (**16**) and suc-PheNapΔPheOH (**17**); (0.4 *wt* %), with incorporated SPION in the Fe concentration range (0 - 0.12 m).

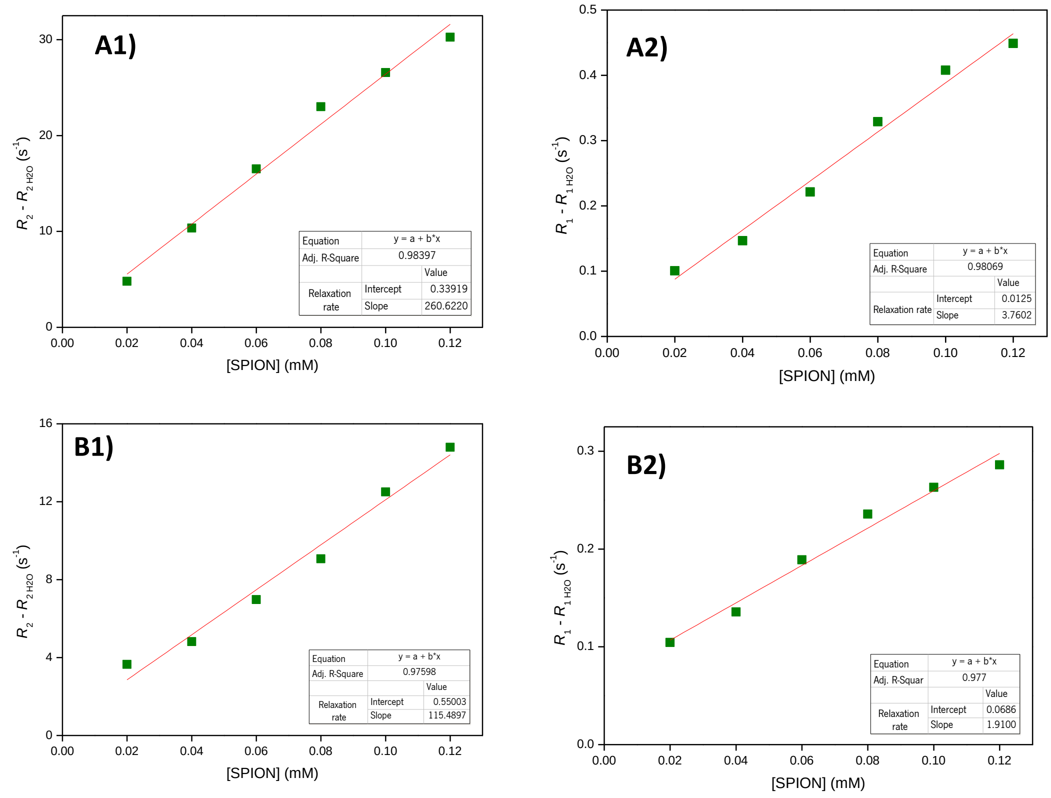

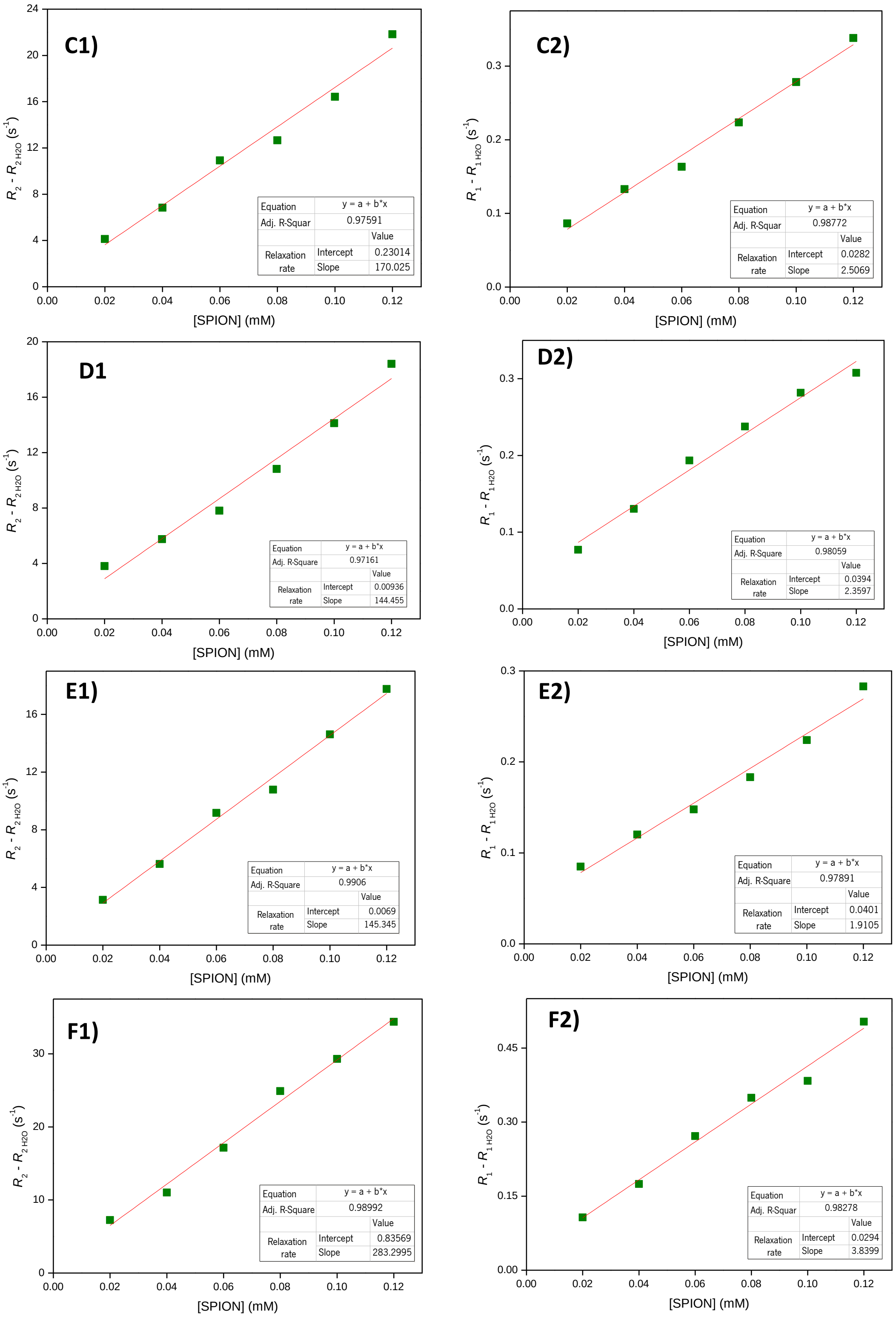

Figure A9 Illustration of the procedure used to determine the relaxivities for the magnetic hydrogels, using the hydrogelators: **A1** and **A2**) suc-PheΔPheOMe (**5**); **B1** and **B2**) suc-PheΔPheOH (**6**); **C1** and **C2**) hydrogelator suc-NapΔPheOMe (**13**); **D1** and **D2**) hydrogelator suc-NapΔPheOH (**14**); **E1** and **E2**) hydrogelator suc-PheNapΔPheOMe (**16**); **F1** and **F2**) hydrogelator suc-PheNapΔPheOH (**17**).

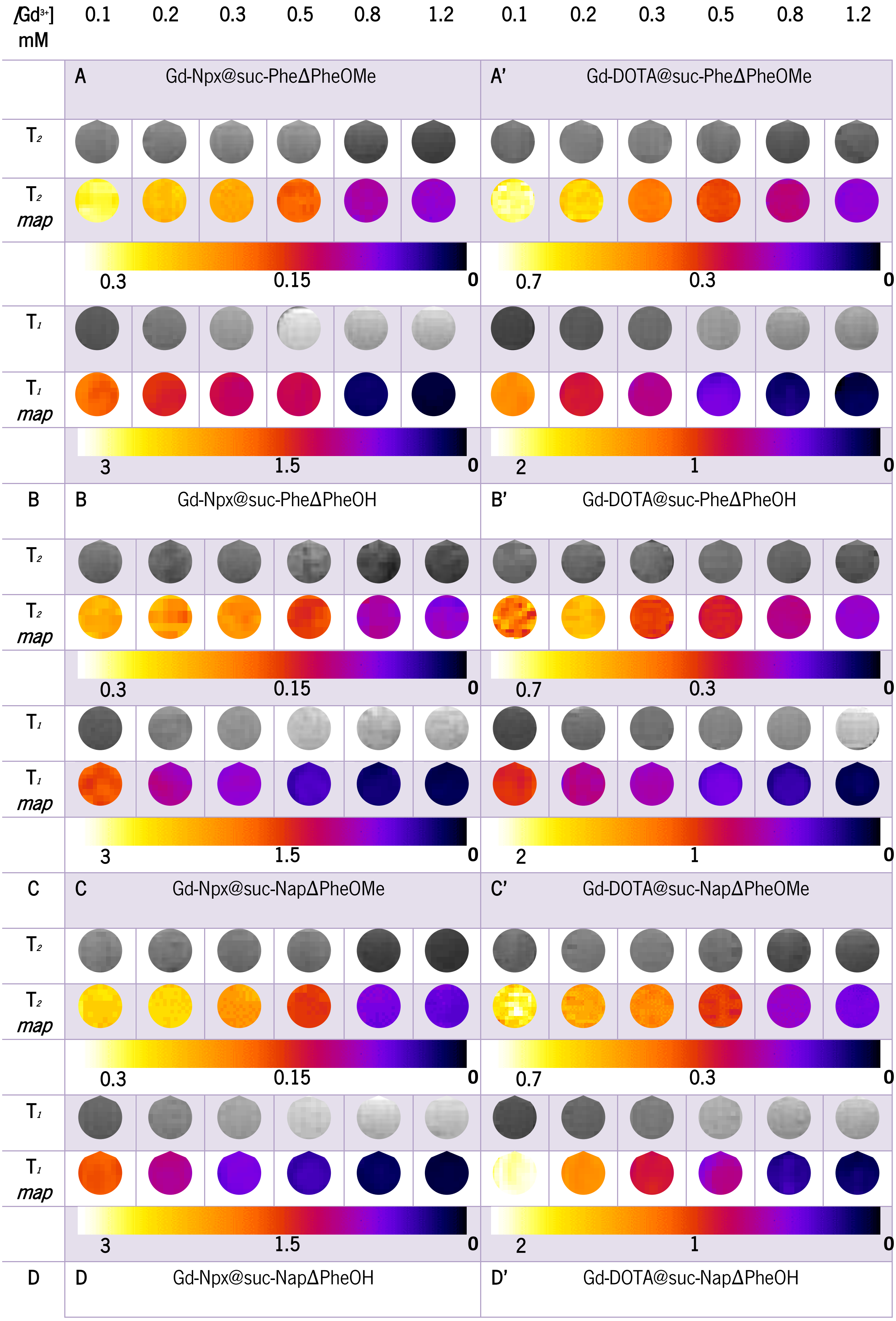
[Gd3+] mM
0.1 0.2 0.3 0.5 0.8 1.2 0.1 0.2 0.3 0.5 0.8 1.2
A Gd-Npx@suc-PheΔPheOMe
A' Gd-DOTA@suc-PheΔPheOMe
T2
T2 map
0.3 0.15 0
0.7 0.3 0
T1
T1 map
3 1.5 0
2 1 0
B
B Gd-Npx@suc-PheΔPheOH
B' Gd-DOTA@suc-PheΔPheOH
T2
T2 map
0.3 0.15 0
0.7 0.3 0
T1
T1 map
3 1.5 0
2 1 0
C
C Gd-Npx@suc-NapΔPheOMe
C' Gd-DOTA@suc-NapΔPheOMe
T2
T2 map
0.3 0.15 0
0.7 0.3 0
T1
T1 map
3 1.5 0
2 1 0
D
D Gd-Npx@suc-NapΔPheOH
D' Gd-DOTA@suc-NapΔPheOH

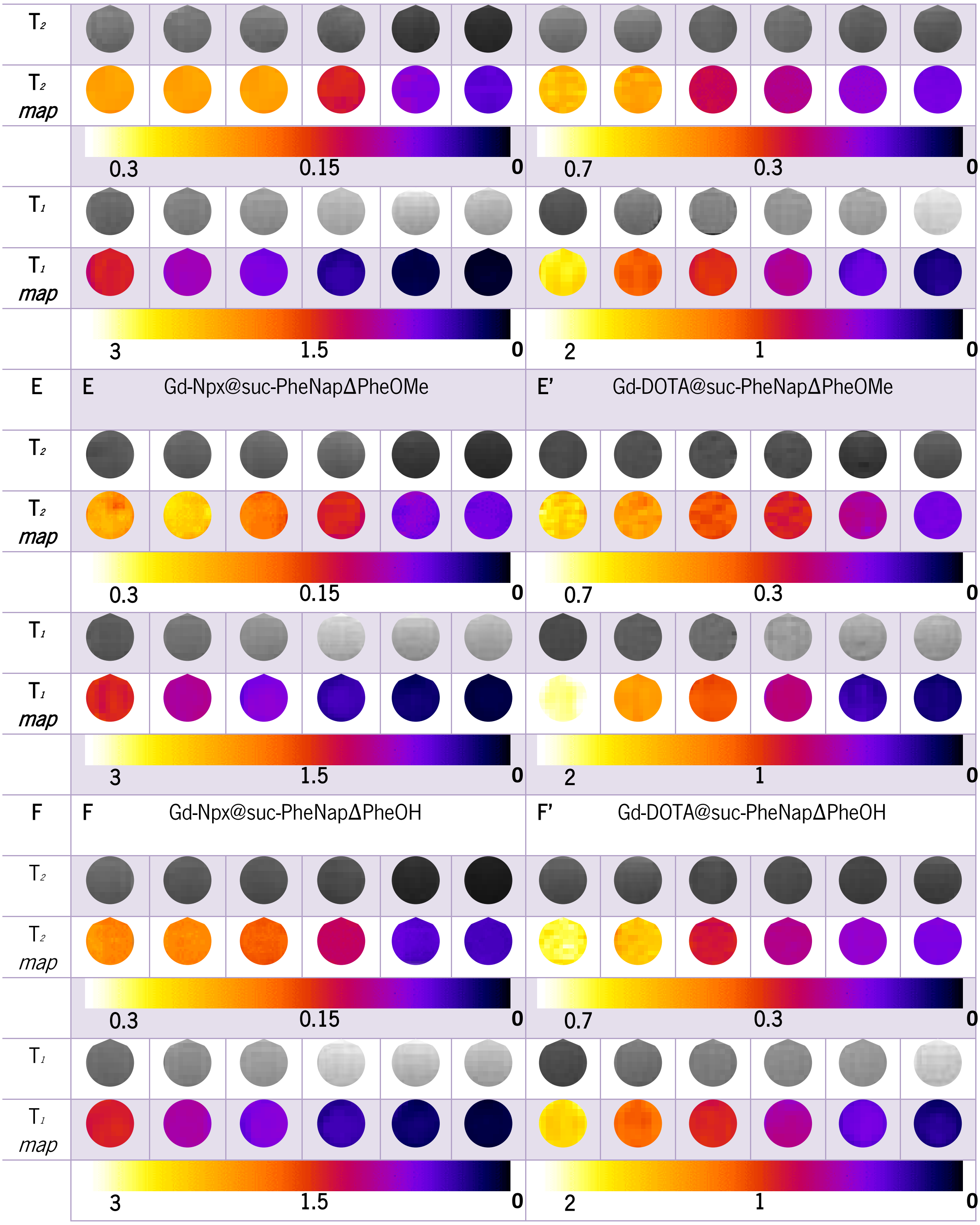

Figure A10 $T_{1,2}$ relaxation maps (120 MHz, 37 °C): Illustrative relaxation maps for hydrogels **A)** and **A')** suc-PheΔPheOMe (**5**); **B)** and **B')** suc-PheΔPheOH (**6**), **C)** and **C')** suc-NapΔPheOMe (**13**); **D)** and **D')** suc-NapΔPheOH (**14**), **E)** and **E')** suc-PheNapΔPheOMe (**16**), **F)** and **F')** suc-PheNapΔPheOH (**17**), (0.4 *wt* %), with incorporated Gd-Npx and Gd-DOTA, respectively, in the Gd concentration range (0 – 1.2 mM).

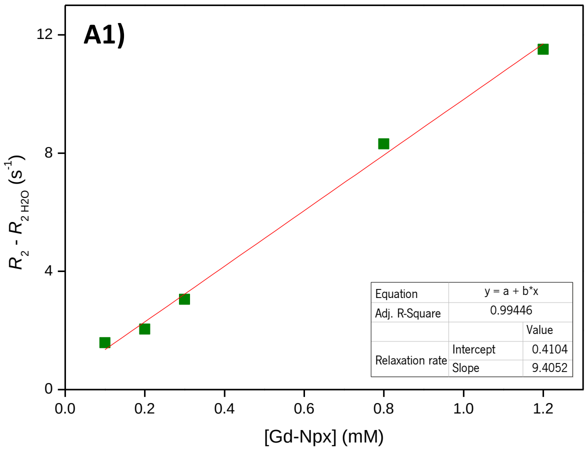
A1)
$R_2 - R_{2\,H2O}$ (s^{-1})
[Gd-Npx] (mM)
0
4
8
12
0.0
0.2
0.4
0.6
0.8
1.0
1.2
Equation
y = a + b*x
Adj. R-Square
0.99446
Value
Relaxation rate
Intercept
0.4104
Slope
9.4052

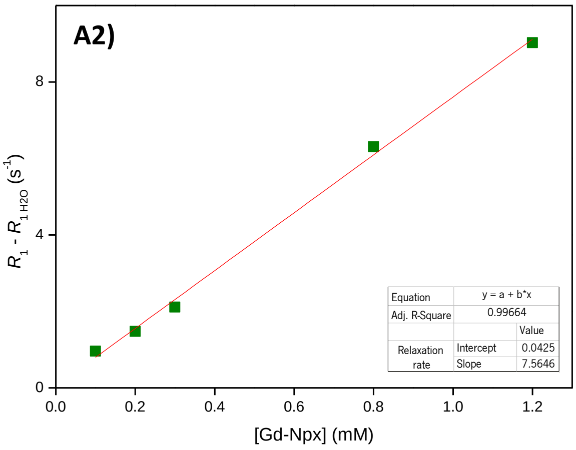
A2)
$R_1 - R_{1\,H2O}$ (s^{-1})
[Gd-Npx] (mM)
0
4
8
0.0
0.2
0.4
0.6
0.8
1.0
1.2
Equation
y = a + b*x
Adj. R-Square
0.99664
Value
Relaxation rate
Intercept
0.0425
Slope
7.5646

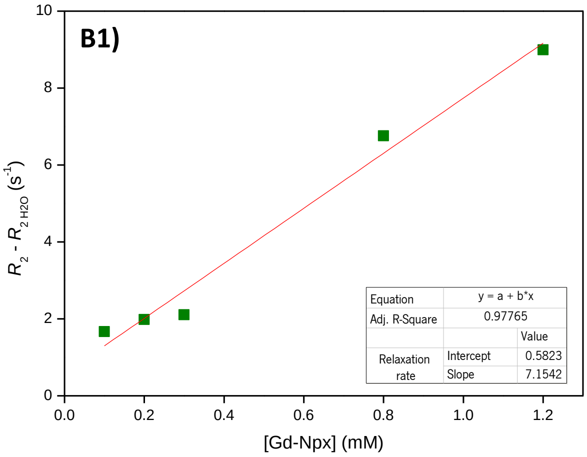
B1)
$R_2 - R_{2\,H2O}$ (s^{-1})
[Gd-Npx] (mM)
0
2
4
6
8
10
0.0
0.2
0.4
0.6
0.8
1.0
1.2
Equation
y = a + b*x
Adj. R-Square
0.97765
Value
Relaxation rate
Intercept
0.5823
Slope
7.1542

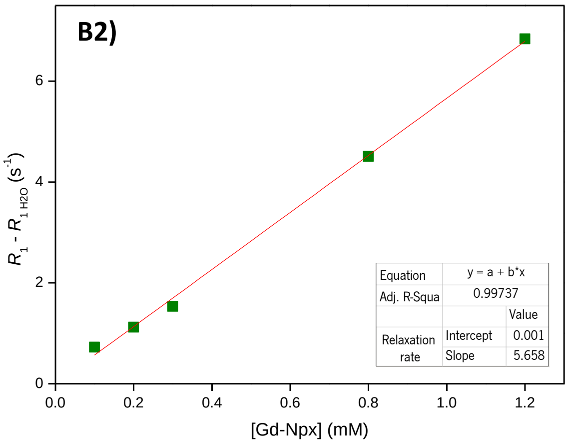
B2)
$R_1 - R_{1\,H2O}$ (s^{-1})
[Gd-Npx] (mM)
0
2
4
6
0.0
0.2
0.4
0.6
0.8
1.0
1.2
Equation
y = a + b*x
Adj. R-Squa
0.99737
Value
Relaxation rate
Intercept
0.001
Slope
5.658

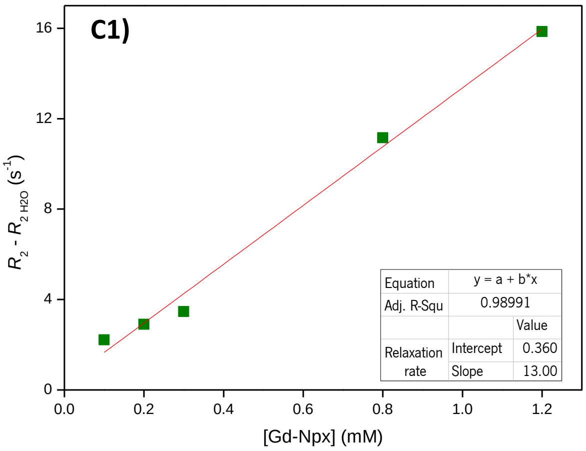
C1)
$R_2 - R_{2\,H2O}$ (s^{-1})
[Gd-Npx] (mM)
0
4
8
12
16
0.0
0.2
0.4
0.6
0.8
1.0
1.2
Equation
y = a + b*x
Adj. R-Squ
0.98991
Value
Relaxation rate
Intercept
0.360
Slope
13.00

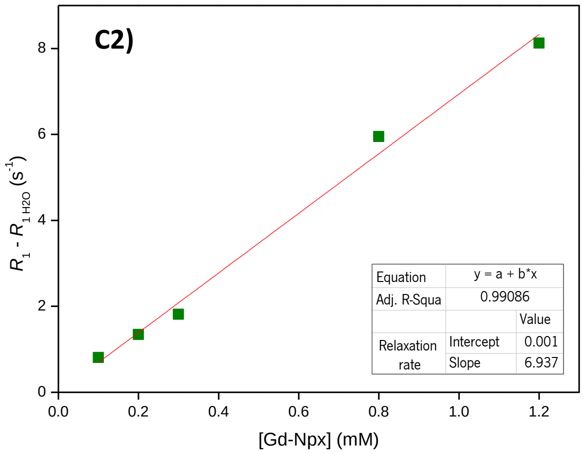
C2)
$R_1 - R_{1\,H2O}$ (s^{-1})
[Gd-Npx] (mM)
0
2
4
6
8
0.0
0.2
0.4
0.6
0.8
1.0
1.2
Equation
y = a + b*x
Adj. R-Squa
0.99086
Value
Relaxation rate
Intercept
0.001
Slope
6.937

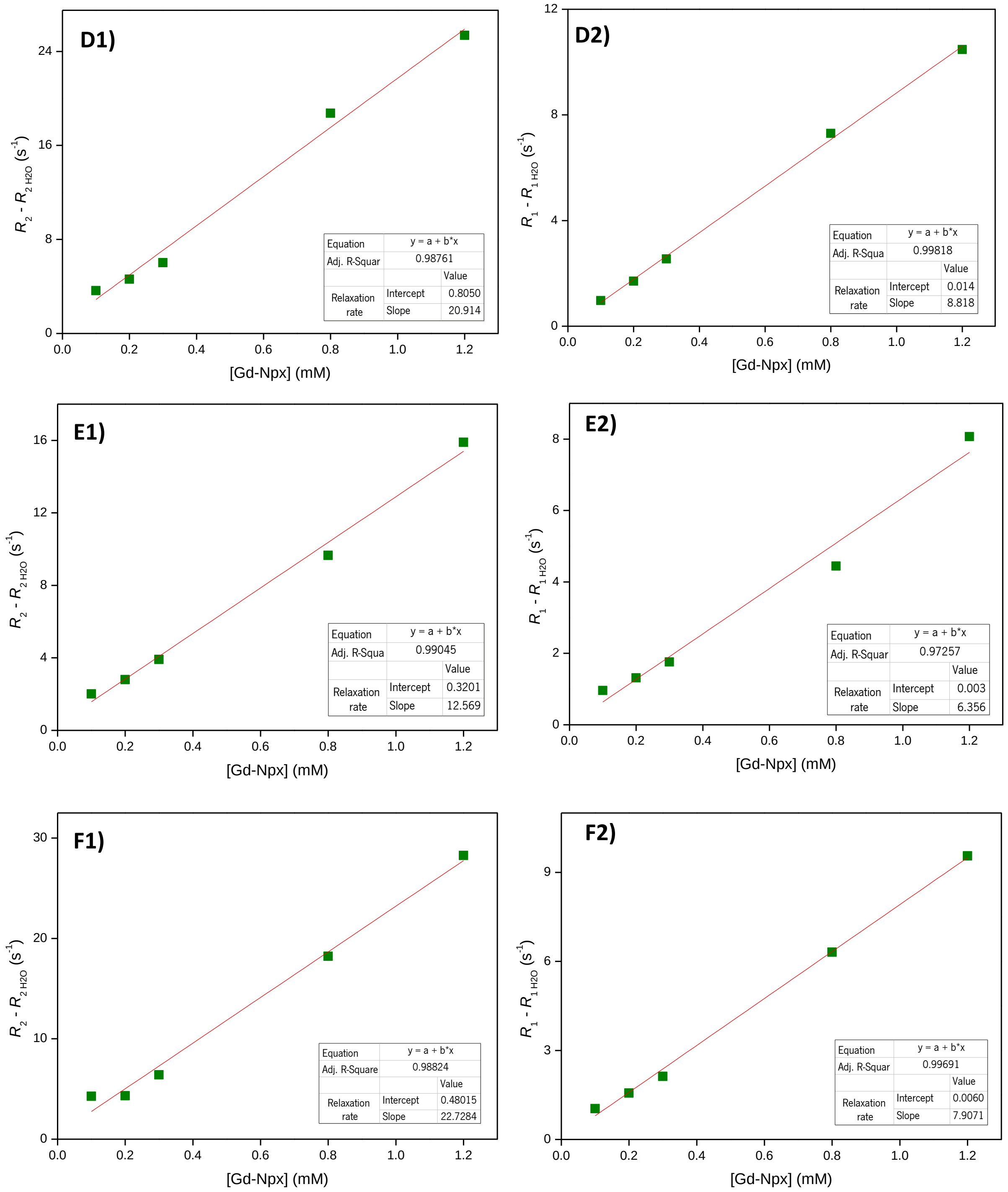

Figure A11.1 Illustration of the procedure used to determine the relaxivities for the paramagnetic (Gd-Npx) hydrogels, using the hydrogelators: **A1** and **A2**) suc-PheΔPheOMe (**5**); **B1** and **B2**) suc-PheΔPheOH (**6**); **C1** and **C2**) hydrogelator suc-NapΔPheOMe (**13**); **D1** and **D2**) hydrogelator suc-NapΔPheOH (**14**); **E1** and **E2**) hydrogelator suc-PheNapΔPheOMe (**16**); **F1** and **F2**) hydrogelator suc-PheNapΔPheOH (**17**).

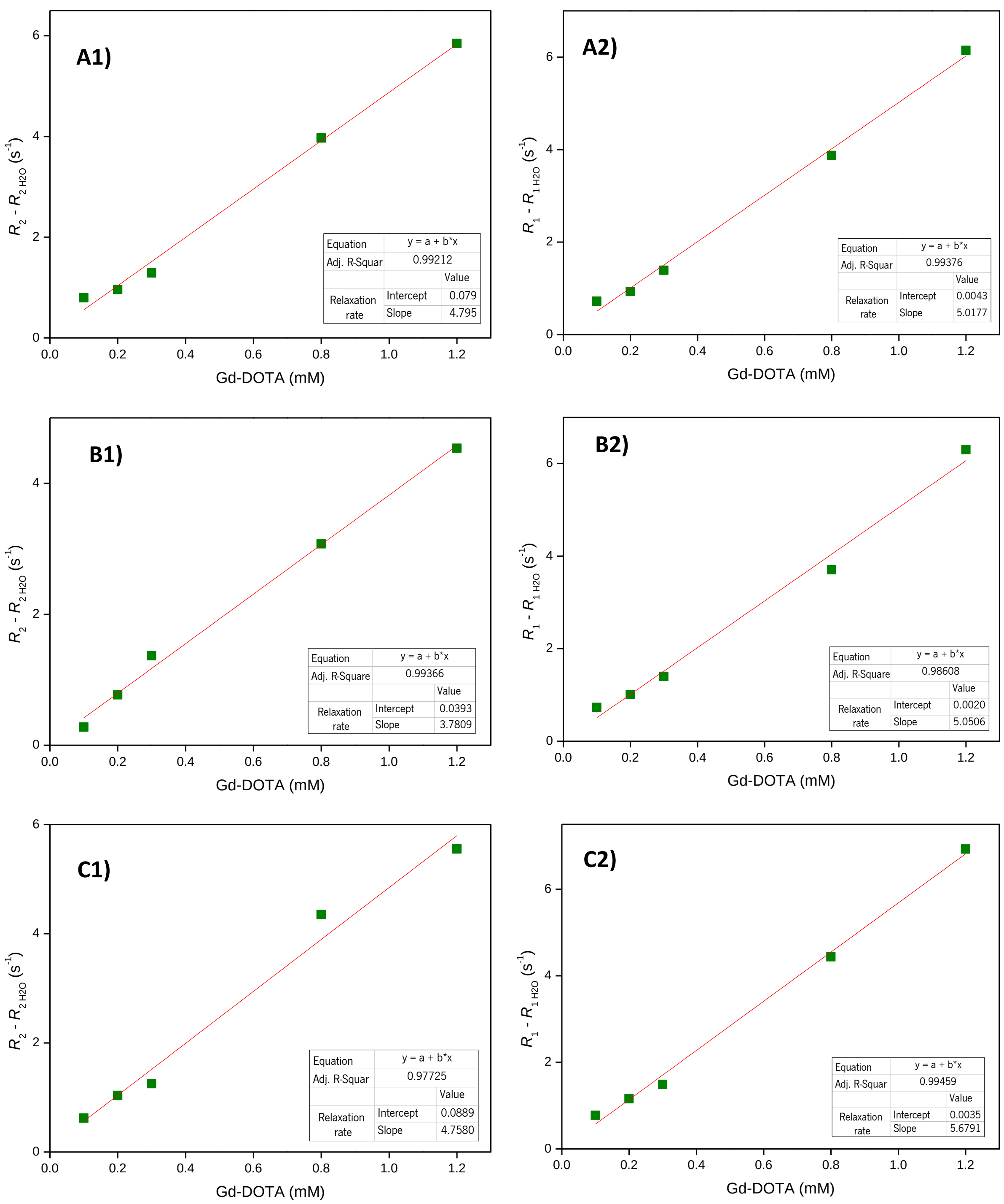
A1)
$R_2 - R_{2\,H2O}$ (s^{-1})
Gd-DOTA (mM)
0
2
4
6
0.0
0.2
0.4
0.6
0.8
1.0
1.2
Equation
y = a + b*x
Adj. R-Squar
0.99212
Value
Relaxation rate
Intercept
0.079
Slope
4.795
A2)
$R_1 - R_{1\,H2O}$ (s^{-1})
Gd-DOTA (mM)
Equation
y = a + b*x
Adj. R-Squar
0.99376
Value
Relaxation rate
Intercept
0.0043
Slope
5.0177
B1)
$R_2 - R_{2\,H2O}$ (s^{-1})
Gd-DOTA (mM)
Equation
y = a + b*x
Adj. R-Square
0.99366
Value
Relaxation rate
Intercept
0.0393
Slope
3.7809
B2)
$R_1 - R_{1\,H2O}$ (s^{-1})
Gd-DOTA (mM)
Equation
y = a + b*x
Adj. R-Square
0.98608
Value
Relaxation rate
Intercept
0.0020
Slope
5.0506
C1)
$R_2 - R_{2\,H2O}$ (s^{-1})
Gd-DOTA (mM)
Equation
y = a + b*x
Adj. R-Squar
0.97725
Value
Relaxation rate
Intercept
0.0889
Slope
4.7580
C2)
$R_1 - R_{1\,H2O}$ (s^{-1})
Gd-DOTA (mM)
Equation
y = a + b*x
Adj. R-Squar
0.99459
Value
Relaxation rate
Intercept
0.0035
Slope
5.6791

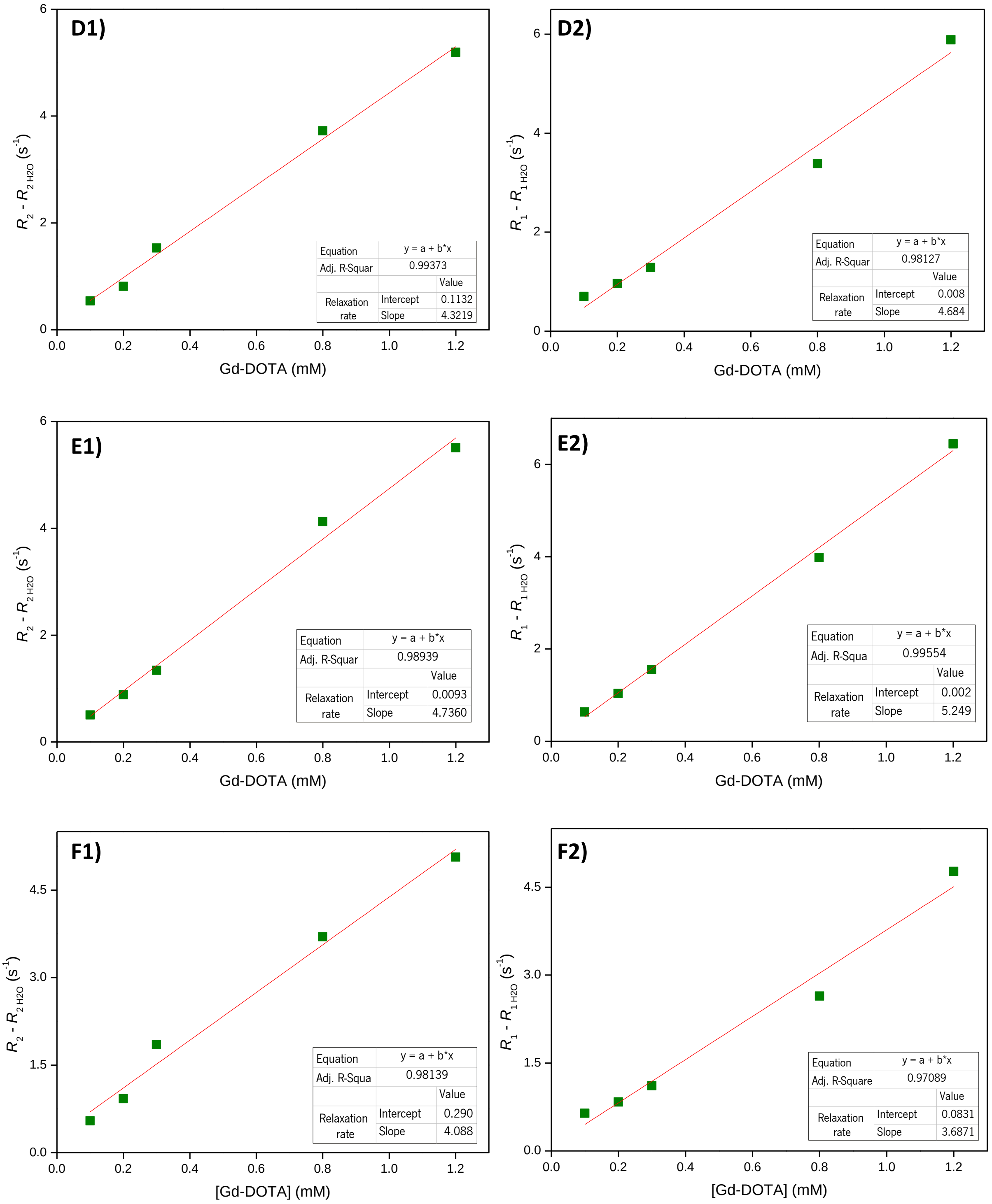

Figure A11.2 Illustration of the procedure used to determine the relaxivities for the paramagnetic (Gd-DOTA) hydrogels, using the hydrogelators: **A1** and **A2**) suc-PheΔPheOMe (**5**); **B1** and **B2**) suc-PheΔPheOH (**6**); **C1** and **C2**) hydrogelator suc-NapΔPheOMe (**13**); **D1** and **D2**) hydrogelator suc-NapΔPheOH (**14**); **E1** and **E2**) hydrogelator suc-PheNapΔPheOMe (**16**); **F1** and **F2**) hydrogelator suc-PheNapΔPheOH (**17**).

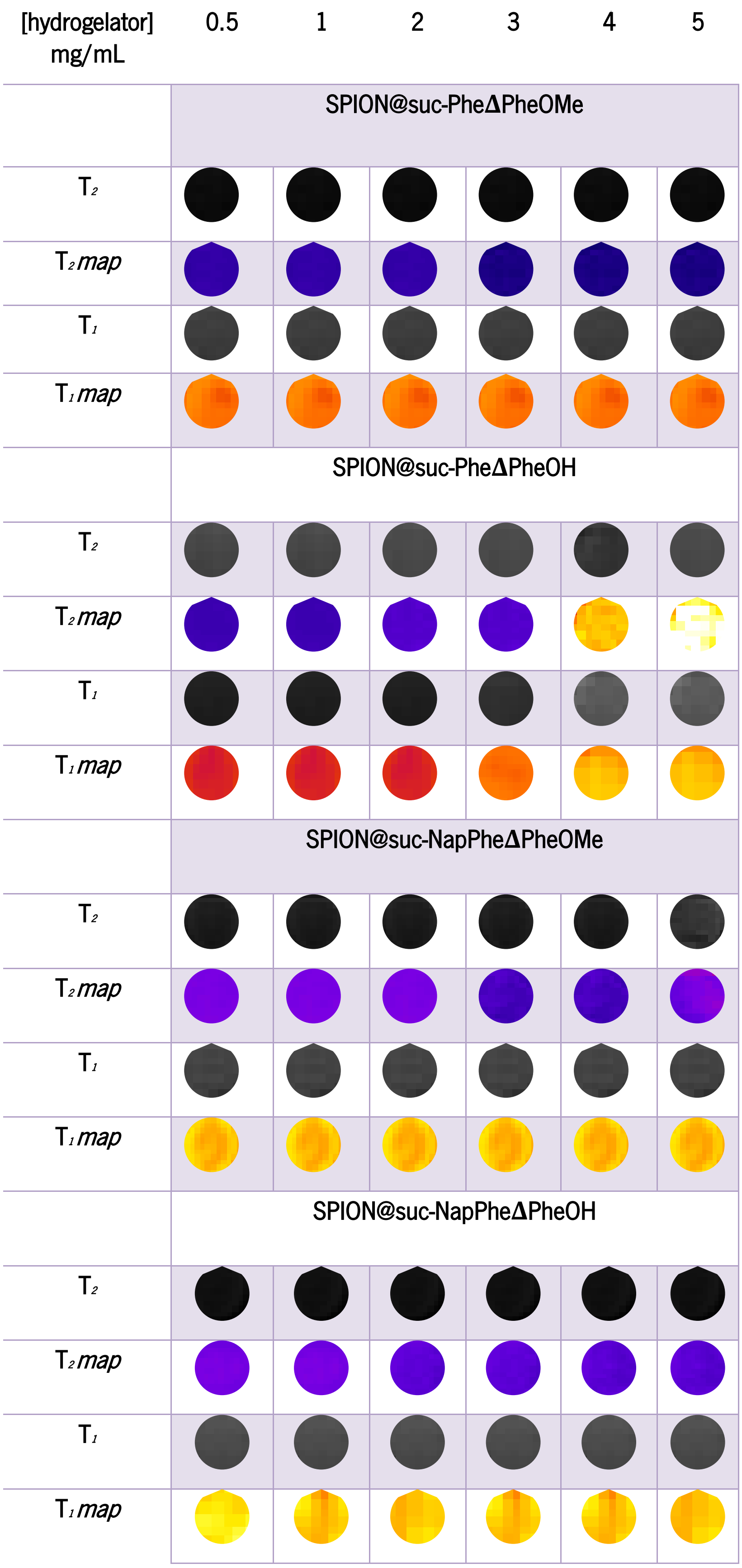

Figure A12 $T_{1,2}$ relaxation maps (120 MHz, 37 °C): Illustrative relaxation maps for hydrogels **A)** suc-PheΔPheOMe (**5**); **B)** suc-PheΔPheOH (**6**), **C) E)** and **E')** suc-PheNapΔPheOMe (**16**), **F)** and **F')** suc-PheNapΔPheOH (**17**), (0.4 *wt* %), with incorporated Gd-Npx and Gd-DOTA, respectively, in the Gd concentration range (0 – 1.2 mM).

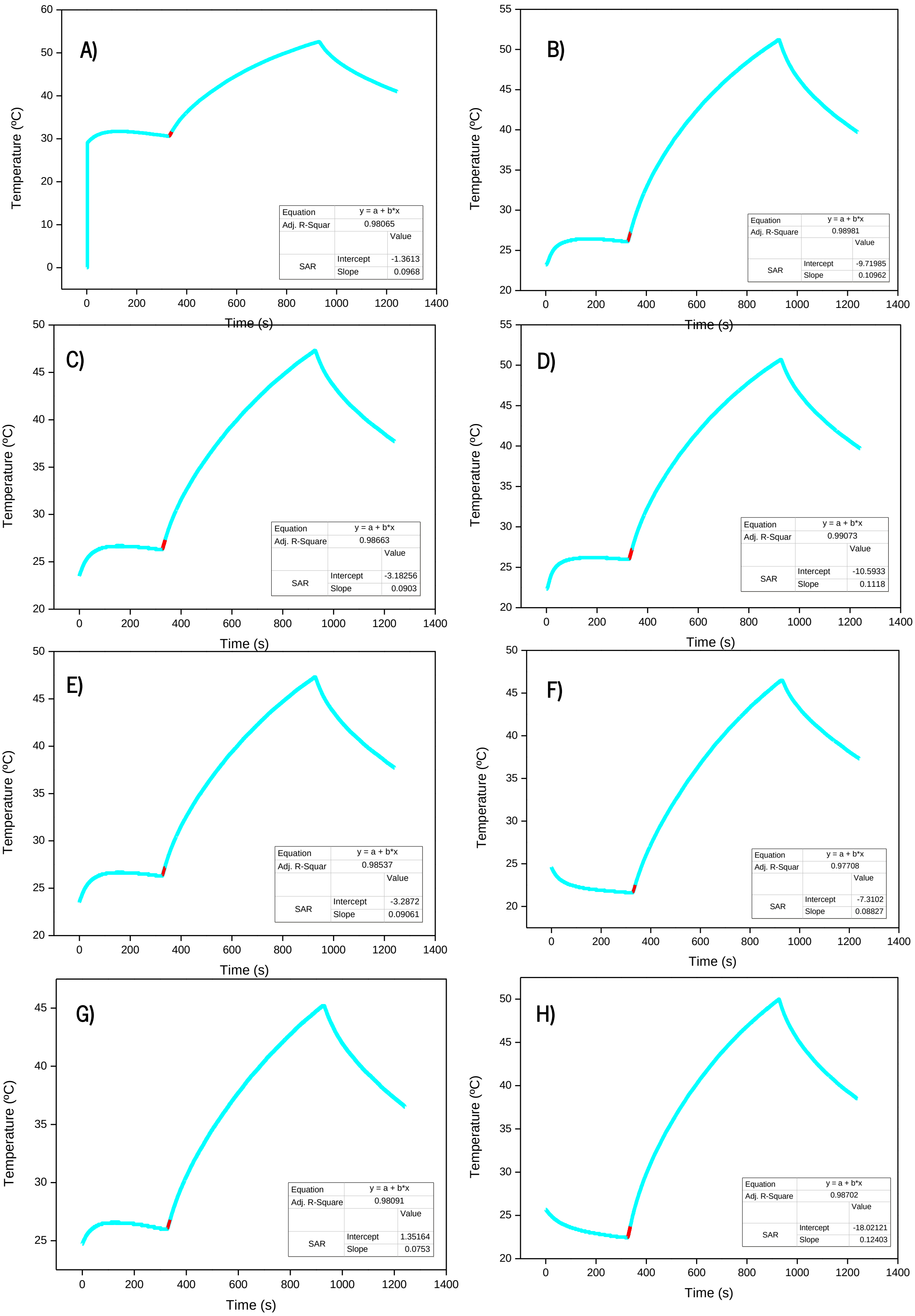

Figure A13.1 Procedure used to determine the hyperthermia (14 *wt* %) for the magnetic hydrogels, using the hydrogelators: **A)** suc-PheΔPheOMe (**5**); **B)** suc-PheΔPheOH (**6**); **C)** suc-NapΔPheOMe (**13**); **D)** suc-NapΔPheOH (**14**); **E)** suc-NapPheΔPheOH (**9**); **F)** suc-PheNapΔPheOMe (**16**); **G)** suc-PheNapΔPheOH (**17**); **H)** water.

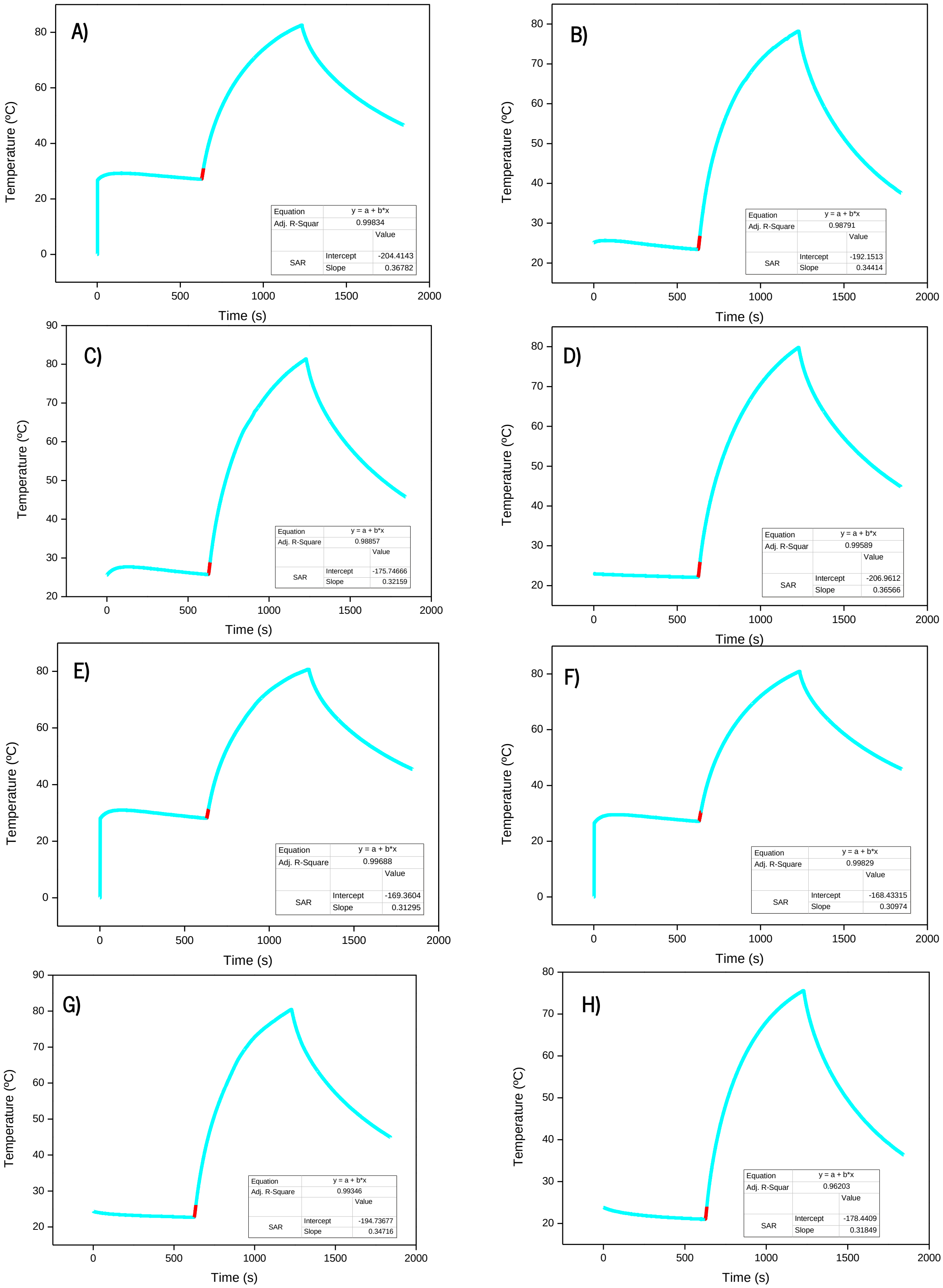

Figure A13.2 Procedure used to determine the hyperthermia (14 *wt* %) for the magnetic hydrogels, using the hydrogelators: **A)** suc-PheΔPheOMe (**5**); **B)** suc-PheΔPheOH (**6**); **C)** suc-NapΔPheOMe (**13**); **D)** suc-NapΔPheOH (**14**); **E)** suc-NapPheΔPheOH (**9**); **F)** suc-PheNapΔPheOMe (**16**); **G)** suc-PheNapΔPheOH (**17**); **H)** water.

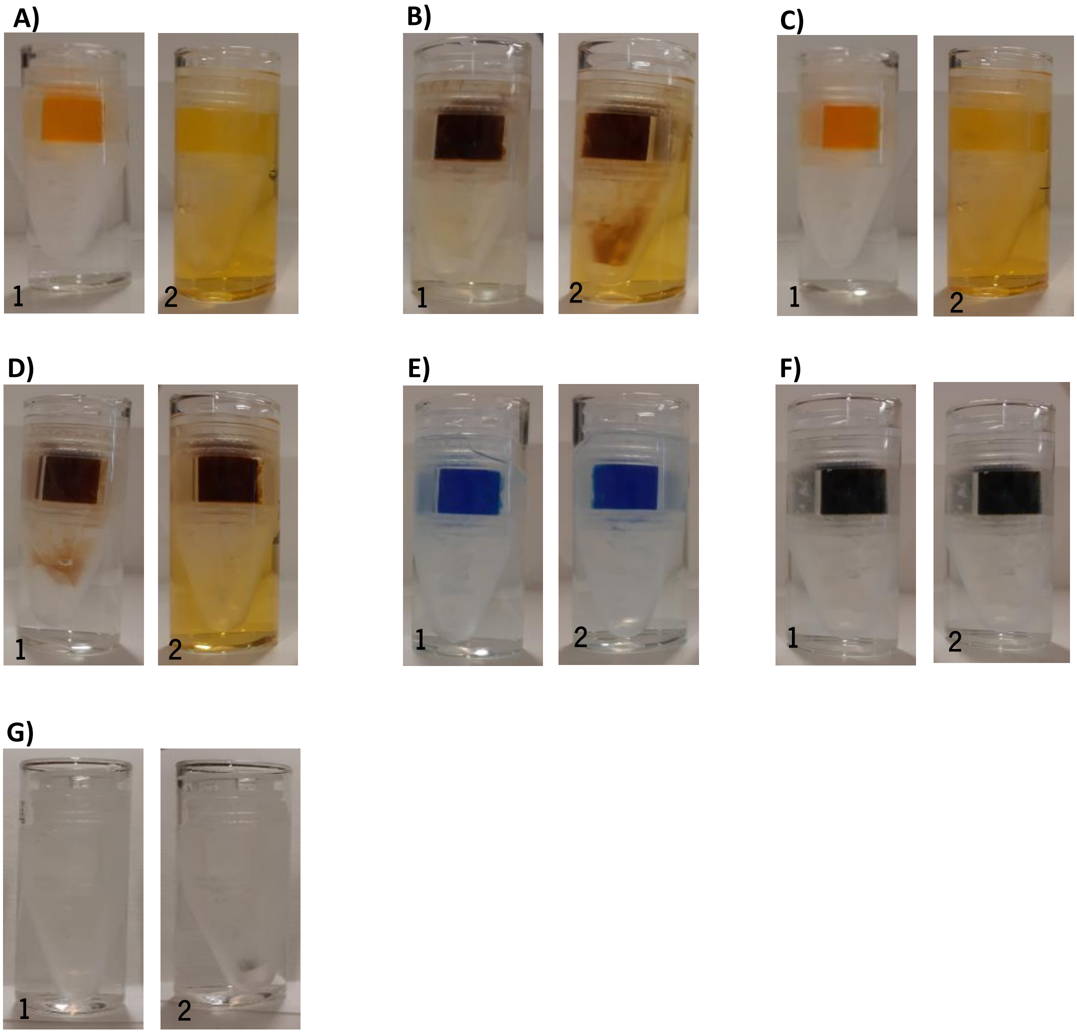

Figure A14 Illustration of the preparation of the drug delivery assays: **A**) suc-NapPheΔPheOMe (**8**) incorporating methyl orange dye (0.0066 *wt* %); **B**) suc-NapPheΔPheOMe (**8**) incorporating methyl orange dye and SPION (14 *wt* %); **C**) suc-NapPheΔPheOH (**9**) incorporating methyl orange dye (0.0066 *wt* %); **D**) suc-NapPheΔPheOH (**9**) incorporating methyl orange dye and SPION (14 *wt* %); **E**) suc-NapPheΔPheOMe (**8**) incorporating methylene blue dye (0.0064 *wt* %); **F**) suc-NapPheΔPheOMe (**8**) incorporating methylene blue dye and SPION (14 *wt* %); **G**) suc-NapPheΔPheOMe (**8**) incorporating ciprofloxacin (0.0068 *wt* %). The letters on the figure corresponde: 1- initial time; 2- final time.

Chapter 6

References

1. Lowry G V., Avellan A, Gilbertson LM. Opportunities and challenges for nanotechnology in the agri-tech revolution. *Nat Nanotechnol*. 2019;14(6):517-522. doi:10.1038/s41565-019-0461-7
2. Ariga K, Shrestha LK. Supramolecular nanoarchitectonics for functional materials. *APL Mater*. 2019;7(12). doi:10.1063/1.5134530
3. Talebian S, Mehrali M, Taebnia N, et al. Self-Healing Hydrogels: The Next Paradigm Shift in Tissue Engineering? *Adv Sci*. 2019;6(16). doi:10.1002/advs.201801664
4. Means AK, Grunlan MA. Modern Strategies to Achieve Tissue-Mimetic, Mechanically Robust Hydrogels. *ACS Macro Lett*. 2019;8(6):705-713. doi:10.1021/acsmacrolett.9b00276
5. Caló E, Khutoryanskiy V V. Biomedical applications of hydrogels: A review of patents and commercial products. *Eur Polym J*. 2015;65:252-267. doi:10.1016/j.eurpolymj.2014.11.024
6. Tu Y, Chen N, Li C, et al. Advances in injectable self-healing biomedical hydrogels. *Acta Biomater*. 2019;90:1-20. doi:10.1016/j.actbio.2019.03.057
7. Zidan G, Greene CA, Seyfoddin A. *Formulation Design in Drug Delivery*. Elsevier LTD.; 2019. doi:10.1016/B978-0-08-102548-2.00002-0
8. Shiraishi K, Yokoyama M. Toxicity and immunogenicity concerns related to PEGylated-micelle carrier systems: a review. *Sci Technol Adv Mater*. 2019;20(1):324-336. doi:10.1080/14686996.2019.1590126
9. Dong R, Pang Y, Su Y, Zhu X. Supramolecular hydrogels: synthesis, properties and their biomedical applications. *Biomater Sci*. 2015;3(7):937-954. doi:10.1039/c4bm00448e
10. Habibi N, Kamaly N, Memic A, Shafiee H. Self-assembled peptide-based nanostructures: Smart nanomaterials toward targeted drug delivery. *Nano Today*. 2016;11(1):41-60. doi:10.1016/j.nantod.2016.02.004
11. Liu K. Chem Soc Rev and kinetics. *Chem Soc Rev*. 2016. doi:10.1039/C6CS00176A
12. Singh N, Kumar M, Miravet JF, Ulijn R V., Escuder B. Peptide-Based Molecular Hydrogels as Supramolecular Protein Mimics. *Chem - A Eur J*. 2017;23(5):981-993. doi:10.1002/chem.201602624
13. Raeburn J, Cardoso AZ, Adams DJ. The importance of the self-assembly process to control mechanical properties of low molecular weight hydrogels. *Chem Soc Rev*. 2013;42(12):5143-5156. doi:10.1039/c3cs60030k

14. Lim JYC, Lin Q, Xue K, Loh XJ. Recent advances in supramolecular hydrogels for biomedical applications. *Mater Today Adv*. 2019;3:100021. doi:10.1016/j.mtadv.2019.100021
15. Carvalho A, Gallo J, Pereira DM, et al. Magnetic dehydrodipeptide-based self-assembled Hydrogels for Theragnostic applications. *Nanomaterials*. 2019;9(4). doi:10.3390/nano9040541
16. Han J, Lei T, Wu Q. High-water-content mouldable polyvinyl alcohol-borax hydrogels reinforced by well-dispersed cellulose nanoparticles: Dynamic rheological properties and hydrogel formation mechanism. *Carbohydr Polym*. 2014;102(1):306-316. doi:10.1016/j.carbpol.2013.11.045
17. Rasayan P, Dash SS. Hierarchical self-assembly of amphiphilic building blocks into various supramolecular architectures Prayogik Rasayan. 2018;2(1):1-4.
18. Yan X, Zhu P, Li J. Self-assembly and application of diphenylalanine-based nanostructures. *Chem Soc Rev*. 2010;39(6):1877-1890. doi:10.1039/b915765b
19. Porter SL, Coulter SM, Pentlavalli S, Thompson TP, Laverty G. Self-assembling diphenylalanine peptide nanotubes selectively eradicate bacterial biofilm infection. *Acta Biomater*. 2018;77:96-105. doi:10.1016/j.actbio.2018.07.033
20. Zhang Y, Kuang Y, Gao Y, Xu B. Versatile small-molecule motifs for self-assembly in water and the formation of biofunctional supramolecular hydrogels. *Langmuir*. 2011;27(2):529-537. doi:10.1021/la1020324
21. Reches M, Gazit E. Self-assembly of peptide nanotubes and amyloid-like structures by charged-termini-capped diphenylalanine peptide analogues. *Isr J Chem*. 2005;45(3):363-371. doi:10.1560/5mc0-v3dx-ke0b-yf3j
22. Marchesan S, Vargiu A V., Styan KE. The Phe-Phe motif for peptide self-assembly in nanomedicine. *Molecules*. 2015;20(11):19775-19788. doi:10.3390/molecules201119658
23. Vilaça H, Hortelão ACL, Castanheira EMS, et al. Dehydrodipeptide Hydrogelators Containing Naproxen N-Capped Tryptophan: Self-Assembly, Hydrogel Characterization, and Evaluation as Potential Drug Nanocarriers. *Biomacromolecules*. 2015;16(11):3562-3573. doi:10.1021/acs.biomac.5b01006
24. Veloso SRS, Jervis PJ, Silva JFG, et al. Supramolecular ultra-short carboxybenzyl-protected dehydropeptide-based hydrogels for drug delivery. *Mater Sci Eng C*. 2021;122(December

2020). doi:10.1016/j.msec.2021.111869

25. Jervis PJ, Amorim C, Pereira T, Martins JA, Ferreira PMT. Exploring the properties and potential biomedical applications of NSAID-capped peptide hydrogels. *Soft Matter*. 2020;16(44):10001-10012. doi:10.1039/d0sm01198c
26. Vilaça H, Castro T, Costa FMG, et al. Self-assembled RGD dehydropeptide hydrogels for drug delivery applications. *J Mater Chem B*. 2017;5(43):8607-8617. doi:10.1039/c7tb01883e
27. Moreira R, Jervis PJ, Carvalho A, et al. Biological evaluation of naproxen–dehydrodipeptide conjugates with self-hydrogelation capacity as dual LOX/COX inhibitors. *Pharmaceutics*. 2020;12(2). doi:10.3390/pharmaceutics12020122
28. Belanova AA, Gavalas N, Makarenko YM, Belousova MM, Soldatov A V., Zolotukhin P V. Physicochemical Properties of Magnetic Nanoparticles: Implications for Biomedical Applications in Vitro and in Vivo. *Oncol Res Treat*. 2018;41(3):139-143. doi:10.1159/000485020
29. Keasberry NA, Bañobre-López M, Wood C, Stasiuk GJ, Gallo J, Long NJ. Tuning the relaxation rates of dual-mode T1/T2 nanoparticle contrast agents: a study into the ideal system. *Nanoscale*. 2015;7(38):16119-16128. doi:10.1039/c5nr04400f
30. Ahmad T, Phulb R. Magnetic iron oxide nanoparticles as contrast agents: Hydrothermal synthesis, characterization and properties. *Solid State Phenom*. 2015;232:111-145. doi:10.4028/www.scientific.net/SSP.232.111
31. Jin R, Lin B, Li D, Ai H. Superparamagnetic iron oxide nanoparticles for MR imaging and therapy: Design considerations and clinical applications. *Curr Opin Pharmacol*. 2014;18:18-27. doi:10.1016/j.coph.2014.08.002
32. Thorek DLJ, Chen AK, Czupryna J, Tsourkas A. Superparamagnetic iron oxide nanoparticle probes for molecular imaging. *Ann Biomed Eng*. 2006;34(1):23-38. doi:10.1007/s10439-005-9002-7
33. Sharifi Dehsari H, Ksenofontov V, Möller A, Jakob G, Asadi K. Determining Magnetite/Maghemite Composition and Core-Shell Nanostructure from Magnetization Curve for Iron Oxide Nanoparticles. *J Phys Chem C*. 2018;122(49):28292-28301. doi:10.1021/acs.jpcc.8b06927
34. Laurent S, Forge D, Port M, et al. Magnetic iron oxide nanoparticles: Synthesis, stabilization, vectorization, physicochemical characterizations and biological applications.

Chem Rev. 2008;108(6):2064-2110. doi:10.1021/cr068445e

35. Institutet K. Long-term neurodevelopmental outcome after moderate neonatal encephalopathy and after post-term birth From CLINTEC , Department of Paediatrics Karolinska Institutet , Stockholm , Sweden; 2015.
36. Ilg P, Kröger M. Dynamics of interacting magnetic nanoparticles: Effective behavior from competition between Brownian and Néel relaxation. *Phys Chem Chem Phys*. 2020;22(39):22244-22259. doi:10.1039/d0cp04377j
37. Deissler RJ, Wu Y, Martens MA. Dependence of Brownian and Néel relaxation times on magnetic field strength. *Med Phys*. 2014;41(1). doi:10.1118/1.4837216
38. Ludwig F, Eberbeck D, Löwa N, et al. Characterization of magnetic nanoparticle systems with respect to their magnetic particle imaging performance. *Biomed Tech*. 2013;58(6):535-545. doi:10.1515/bmt-2013-0013
39. Aliofkhazraei M. *Handbook of Nanoparticles*.; 2015. doi:10.1007/978-3-319-15338-4_24
40. Myrovali E, Maniotis N, Makridis A, et al. Arrangement at the nanoscale: Effect on magnetic particle hyperthermia. *Sci Rep*. 2016;6(November):1-11. doi:10.1038/srep37934
41. Tu L, Klein T, Wang W, Feng Y, Wang Y, Wang JP. Measurement of brownian and Néel relaxation of magnetic nanoparticles by a mixing-frequency method. *IEEE Trans Magn*. 2013;49(1):227-230. doi:10.1109/TMAG.2012.2224853
42. Kemp SJ, Ferguson RM, Khandhar AP, Krishnan KM. Monodisperse magnetite nanoparticles with nearly ideal saturation magnetization. *RSC Adv*. 2016;6(81):77452-77464. doi:10.1039/c6ra12072e
43. Anjum S, Fayyaz J, Khurram R, Zia R. Tuning of Magnetic and Optical Properties of Co0.8Zn0.2Fe2O4 Spinel Ferrite Thin Films Based on Post Annealing Temperature. *J Supercond Nov Magn*. 2018;31(12):4095-4106. doi:10.1007/s10948-018-4662-3
44. Tatarchuk T, Bououdina M, Judith Vijaya J, John Kennedy L. Spinel ferrite nanoparticles: Synthesis, crystal structure, properties, and perspective applications. *Springer Proc Phys*. 2017;195:305-325. doi:10.1007/978-3-319-56422-7_22
45. Mohapatra J, Mitra A, Bahadur D, Aslam M. Surface controlled synthesis of MFe2O4 (M = Mn, Fe, Co, Ni and Zn) nanoparticles and their magnetic characteristics. *CrystEngComm*. 2013;15(3):524-532. doi:10.1039/c2ce25957e

46. Hu P, Kang L, Chang T, et al. High saturation magnetization Fe3O4 nanoparticles prepared by one-step reduction method in autoclave. *J Alloys Compd*. 2017;728:88-92. doi:10.1016/j.jallcom.2017.08.290

47. Zhou Z, Yang L, Gao J, Chen X. Structure–Relaxivity Relationships of Magnetic Nanoparticles for Magnetic Resonance Imaging. *Adv Mater*. 2019;31(8):1-32. doi:10.1002/adma.201804567

48. Sharma R, Thakur P, Sharma P, Sharma V. Ferrimagnetic Ni2+doped Mg-Zn spinel ferrite nanoparticles for high density information storage. *J Alloys Compd*. 2017;704:7-17. doi:10.1016/j.jallcom.2017.02.021

49. Cao Y, Xu L, Kuang Y, Xiong D, Pei R. Gadolinium-based nanoscale MRI contrast agents for tumor imaging. *J Mater Chem B*. 2017;5(19):3431-3461. doi:10.1039/c7tb00382j

50. Lee N, Hyeon T. Magnetic Nanoparticles for Magnetic Resonance Imaging Contrast Agents. *Magn Nanoparticles Biosensing Med*. 2019:228-250. doi:10.1017/9781139381222.008

51. Ridgway JP. Cardiovascular magnetic resonance physics for clinicians: Part i. *J Cardiovasc Magn Reson*. 2010;12(1):1-28. doi:10.1186/1532-429X-12-71

52. Sharon M, Oza G, Gupta A, Pandey S. Super-Paramagnetic Iron Oxide Nanoparticles (Spions) As Nano-Flotillas for Hyperthermia. *Adv Nanomater*. 2014;(August 2017). doi:10.1201/b16966-14

53. Caravan, Peter; Ellison, Jeffrey J.; McMurry, Thomas J.; Lauffer – Gadolinium(III) Chelates as MRI Contrast Agents-B Structure, .pdf. *Chem Rev*. 1999;99(Iii):2293-2352. [doi 10.1021%2Fcr980440x]

54. Zhou Z, Lu ZR. Gadolinium-based contrast agents for magnetic resonance cancer imaging. *Wiley Interdiscip Rev Nanomedicine Nanobiotechnology*. 2013;5(1):1-18. doi:10.1002/wnan.1198

55. Kaewlai R, Abujudeh H. Nephrogenic systemic fibrosis. *Am J Roentgenol*. 2012;199(1):17-23. doi:10.2214/AJR.11.8144

56. Gale EM, Atanasova IP, Blasi F, Ay I, Caravan P. A Manganese Alternative to Gadolinium for MRI Contrast. *J Am Chem Soc*. 2015;137(49):15548-15557. doi:10.1021/jacs.5b10748

57. Blanco-Andujar C, Walter A, Cotin G, et al. Design of iron oxide-based nanoparticles for MRI and magnetic hyperthermia. *Nanomedicine*. 2016;11(14):1889-1910.

doi:10.2217/nnm-2016-5001

58. Ferreira MF, Mousavi B, Ferreira PM, et al. Gold nanoparticles functionalised with stable, fast water exchanging Gd 3+ chelates as high relaxivity contrast agents for MRI. *Dalt Trans*. 2012;41(18):5472-5475. doi:10.1039/c2dt30388d
59. Ferreira MF, Pereira G, Martins AF, et al. Ln[DO3A-N-α-(pyrenebutanamido)propionate] complexes: Optimized relaxivity and NIR optical properties. *Dalt Trans*. 2014;43(8):3162-3173. doi:10.1039/c3dt52958d
60. Ferreira MF, Martins AF, Martins CIO, et al. Amide conjugates of the DO3A-N-(α-amino)propionate ligand: Leads for stable, high relaxivity contrast agents for MRI? *Contrast Media Mol Imaging*. 2013;8(1):40-49. doi:10.1002/cmmi.1492
61. Etheridge ML, Hurley KR, Zhang J, et al. Accounting for biological aggregation in heating and imaging of magnetic nanoparticles. *Technology*. 2014;02(03):214-228. doi:10.1142/s2339547814500198
62. Lu AH, Salabas EL, Schüth F. Magnetic nanoparticles: Synthesis, protection, functionalization, and application. *Angew Chemie - Int Ed*. 2007;46(8):1222-1244. doi:10.1002/anie.200602866
63. Abenojar EC, Wickramasinghe S, Bas-Concepcion J, Samia ACS. Structural effects on the magnetic hyperthermia properties of iron oxide nanoparticles. *Prog Nat Sci Mater Int*. 2016;26(5):440-448. doi:10.1016/j.pnsc.2016.09.004
64. Kumar CSSR. *Nanotechnology Characterization Tools for Tissue Engineering and Medical Therapy*.; 2019. doi:10.1007/978-3-662-59596-1
65. He S, Zhang H, Liu Y, et al. Maximizing specific loss power for magnetic hyperthermia by hard-soft mixed ferrites. *arXiv*. 2018:1-35.
66. Veloso SRS, Martins JA, Hilliou L, et al. Dehydropeptide-based plasmonic magnetogels: a supramolecular composite nanosystem for multimodal cancer therapy. *J Mater Chem B*. 2020;8(1):45-64. doi:10.1039/C9TB01900F
67. Johnson EK, Adams DJ, Cameron PJ. Peptide based low molecular weight gelators. *J Mater Chem*. 2011;21(7):2024-2027. doi:10.1039/c0jm03099f
68. Chakraborty P, Gazit E. Amino Acid Based Self-assembled Nanostructures: Complex Structures from Remarkably Simple Building Blocks. *ChemNanoMat*. 2018;4(8):730-740. doi:10.1002/cnma.201800147
69. Qiu F, Tang C, Chen Y. Amyloid-like aggregation of designer bolaamphiphilic peptides:

Effect of hydrophobic section and hydrophilic heads. *J Pept Sci*. 2018;24(2):1-9. doi:10.1002/psc.3062

70. Zhou J, Du X, Wang J, Yamagata N, Xu B. Enzyme-instructed self-assembly of peptides containing phosphoserine to form supramolecular hydrogels as potential soft biomaterials. *Front Chem Sci Eng*. 2017;11(4):509-515. doi:10.1007/s11705-017-1613-7
71. Ferreira PMT, Monteiro LS, Pereira G. Synthesis and electrochemical behaviour of β-halodehydroamino acid derivatives. *Amino Acids*. 2010;39(2):499-513. doi:10.1007/s00726-009-0466-x
72. Bowerman CJ, Nilsson BL. Self-assembly of amphipathic β-sheet peptides: insights and applications. *Biopolymers*. 2012;98(3):169-184. doi:10.1002/bip.22058
73. Laverty G, McCloskey AP, Gilmore BF, Jones DS, Zhou J, Xu B. Ultrashort cationic naphthalene-derived self-assembled peptides as antimicrobial nanomaterials. *Biomacromolecules*. 2014;15(9):3429-3439. doi:10.1021/bm500981y
74. Fukukawa KI, Rossin R, Hagooly A, et al. Synthesis and characterization of core-shell star copolymers for in vivo PET imaging applications. *Biomacromolecules*. 2008;9(4):1329-1339. doi:10.1021/bm7014152
75. Ferreira MF, Martins AF, Martins JA, Ferreira PM, Tóth É, Geraldes CFGC. Gd(DO3A-N-α-aminopropionate): A versatile and easily available synthon with optimized water exchange for the synthesis of high relaxivity, targeted MRI contrast agents. *Chem Commun*. 2009;(42):6475-6477. doi:10.1039/b912201j
76. Adams DJ, Mullen LM, Berta M, Chen L, Frith WJ. Relationship between molecular structure, gelation behaviour and gel properties of Fmoc-dipeptides. *Soft Matter*. 2010;6(9):1971-1980. doi:10.1039/b921863g
77. Shen H, Gao Q, Ye Q, et al. Peritumoral implantation of hydrogel-containing nanoparticles and losartan for enhanced nanoparticle penetration and antitumor effect. *Int J Nanomedicine*. 2018;13:7409-7426. doi:10.2147/IJN.S178585
78. Han X, Huang J, To AKW, et al. CEST MRI detectable liposomal hydrogels for multiparametric monitoring in the brain at 3T. *Theranostics*. 2020;10(5):2215-2228. doi:10.7150/thno.40146
79. Poustchi F, Amani H, Ahmadian Z, et al. Combination Therapy of Killing Diseases by Injectable Hydrogels: From Concept to Medical Applications. *Adv Healthc Mater*. 2020;2001571:1-30. doi:10.1002/adhm.202001571

80. Miles AJ, Wallace BA. Circular dichroism spectroscopy of membrane proteins. *Chem Soc Rev*. 2016;45(18):4859-4872. doi:10.1039/c5cs00084j

81. Mulens-Arias V, Nicolás-Boluda A, Gehanno A, Balfourier A, Carn F, Gazeau F. Polyethyleneimine-assisted one-pot synthesis of quasi-fractal plasmonic gold nanocomposites as a photothermal theranostic agent. *Nanoscale*. 2019;11(7):3186-3192. doi:10.1039/c8nr09849b

82. Geissberger R, Maldonado J, Bahamonde N, Keller A, Dransfeld C, Masania K. Rheological modelling of thermoset composite processing. *Compos Part B Eng*. 2017;124:182-189. doi:10.1016/j.compositesb.2017.05.040

83. Sorokin V V, Ecker E, Stepanov G V, et al. Experimental study of the magnetic fi eld enhanced Payne e ff ect in magnetorheological elastomers. *Soft Matter*. 2014:8765-8776. doi:10.1039/c4sm01738b

84. Wang G, Zhang X, Skallberg A, et al. One-step synthesis of water-dispersible ultra-small Fe3O 4 nanoparticles as contrast agents for T1 and T 2 magnetic resonance imaging. *Nanoscale*. 2014;6(5):2953-2963. doi:10.1039/c3nr05550g

85. Na H Bin, Song IC, Hyeon T. Inorganic nanoparticles for MRI contrast agents. *Adv Mater*. 2009;21(21):2133-2148. doi:10.1002/adma.200802366

86. Yang Y, Dreessen de Gervai P, Sun J, Glogowski M, Gussakovsky E, Kupriyanov V. MRI studies of cryoinjury infarction in pig hearts: II. Effects of intrapericardial delivery of adipose-derived stem cells (ADSC) embedded in agarose gel. *NMR Biomed*. 2012;25(2):227-235. doi:10.1002/nbm.1735

87. Kostevšek N. A review on the optimal design of magnetic nanoparticle-based t2 mri contrast agents. *Magnetochemistry*. 2020;6(1):1-12. doi:10.3390/magnetochemistry6010011

88. Braun GA, Ary BE, Dear AJ, et al. On the Mechanism of Self-Assembly by a Hydrogel-Forming Peptide. *Biomacromolecules*. 2020. doi:10.1021/acs.biomac.0c00989

89. Veloso SRS, Magalhães CAB, Rodrigues ARO, et al. Novel dehydropeptide-based magnetogels containing manganese ferrite nanoparticles as antitumor drug nanocarriers. *Phys Chem Chem Phys*. 2019;21(20):10377-10390. doi:10.1039/C9CP00352E

90. Diaferia C, Accardo A. Peptide - based building blocks as structural elements for supramolecular Gd - containing MRI contrast agents. 2019;(December 2018):1-13. doi:10.1002/psc.3157

91. Raymond KN, Pierre VC. Next generation, high relaxivity gadolinium MRI agents. *Bioconjug Chem*. 2005;16(1):3-8. doi:10.1021/bc049817y

92. Shen Y, Goerner FL, Snyder C, et al. T1 relaxivities of gadolinium-based magnetic resonance contrast agents in human whole blood at 1.5, 3, and 7T. *Invest Radiol*. 2015;50(5):330-338. doi:10.1097/RLI.0000000000000132

93. Andreu I, Natividad E. Accuracy of available methods for quantifying the heat power generation of nanoparticles for magnetic hyperthermia. *Int J Hyperth*. 2013;29(8):739-751. doi:10.3109/02656736.2013.826825

94. Hajduová J, Uchman M, Šafařík I, et al. Aggregation of superparamagnetic iron oxide nanoparticles in dilute aqueous dispersions: Effect of coating by double-hydrophilic block polyelectrolyte. *Colloids Surfaces A Physicochem Eng Asp*. 2015;483:1-7. doi:10.1016/j.colsurfa.2015.07.008

95. Mohapatra J, Zeng F, Elkins K, et al. Size-dependent magnetic and inductive heating properties of Fe3O4 nanoparticles: Scaling laws across the superparamagnetic size. *Phys Chem Chem Phys*. 2018;20(18):12879-12887. doi:10.1039/c7cp08631h

96. Torniainen K, Tammilehto S, Ulvi V. The effect of pH, buffer type and drug concentration on the photodegradation of ciprofloxacin. *Int J Pharm*. 1996;132(1-2):53-61. doi:10.1016/0378-5173(95)04332-2

97. Papadopoulou V, Kosmidis K, Vlachou M, Macheras P. On the use of the Weibull function for the discernment of drug release mechanisms. *Int J Pharm*. 2006;309(1-2):44-50. doi:10.1016/j.ijpharm.2005.10.044

98. Liao J, Huang H. Review on Magnetic Natural Polymer Constructed Hydrogels as Vehicles for Drug Delivery. *Biomacromolecules*. 2020. doi:https://dx.doi.org/10.1021/acs.biomac.0c00566

99. Yang Z, Gu H, Du J, et al. Self-assembled hybrid nanofibers confer a magnetorheological supramolecular hydrogel. *Tetrahedron*. 2007;63(31):7349-7357. doi:10.1016/j.tet.2007.02.009

100. Benedikt P. Nowak MN and BJR, Hydrogels. Magneto-responsive hydrogels by self-assembly of low molecular weight peptides and crosslinking with iron oxide nanoparticles. *R Soc Chem*. 2019;2019-Novem. doi:10.1039/x0xx00000x

101. Okesola BO, Smith DK. Applying low-molecular weight supramolecular gelators in an environmental setting-self-assembled gels as smart materials for pollutant removal. *Chem*

Soc Rev. 2016;45(15):4226-4251. doi:10.1039/c6cs00124f

102. Edwards-Gayle CJC, Hamley IW. Self-assembly of bioactive peptides, peptide conjugates, and peptide mimetic materials. *Org Biomol Chem*. 2017;15(28):5867-5876. doi:10.1039/c7ob01092c

103. Dodero VI, Quirolo ZB, Sequeira MA. Biomolecular studies by circular dichroism. *Front Biosci*. 2011;16(1):61-73. doi:10.2741/3676